1. EUROfusion

1.1 ITER Physics

1.1.1 - FTU machine and additional systems

FTU Operations

During 2015 two experimental campaigns have been carried out on FTU, first one (C1-2015) starting from early March to the end of June, while the second campaign foreseen in Autumn has started at the beginning of September, but has been stopped after few days because of an excessive level of vibrations on MFG3 generator.

The C1-2015 campaign has started with a new IC1A switch installed, but due to some assembling issues it has not been released for the operation, so that, as a consequence, the maximum toroidal field of FTU has been limited to 4T. This switch swaps the current flowing into the toroidal field coils, at the end of discharge, into an external resistance where it is dissipated. Without this switch the magnetic energy stored in toroidal field is dissipated inside the magnetic field coils directly, increasing the coils temperature excessively, and as consequence maximum operation magnetic field in FTU needed to be limited. Only experimental programs compatible with such limitations have then been carried out.

In June FTU reached the goal of extending the pulse up to 4.5s (shot no. 40052) with a flat top of 3.5 sec to 0.25 MA and 4T magnetic field, which was made in preparation for the second experimental campaign (C2-2015) in favour of lithium limiter.

Table 1.1 - FTU Operational Delays for the year 2015

	January	February	March	April	May	June	July	August	September	October	November	December	Total	
Total pulses			207	336	335	274	56		78				1286	
Successful pulses (sp)			184	313	304	246	47		63				1157	
I(sp)			0,89	0,93	0,91	0,90	0,84		0,81				0,90	
Real experimental days			10,0	13,5	14,5	12,0	2,0		4,5				56,5	
Experimental minutes			4037	5912	6468	4640	921		1646				23624	
Delay minutes			2947	3065	2637	2873	386		1199				13107	
I(et)			0,58	0,66	0,71	0,62	0,70		0,58				0,64	
A(sp/d)			18,40	23,19	20,97	20,50	23,50		14,00				20,48	
A(p/d)			20,70	24,89	23,10	22,83	28,00		17,33				22,76	
DELAY FOR SYSTEM (minutes)														
	January	February	March	April	May	June	July	August	September	October	November	December	Total	%
MACHINE			265	106	168	204	40		61				844	6,4
POWER SUPPLIES			1505	1292	909	1014	33		694				5447	41,6
CONTROL SYSTEM			155	0	54	156	52		27				444	3,4
DAS			91	0	215	52	22		159				539	4,1
FEEDBACK			33	32	67	19	5		0				156	1,2
NETWORK			0	269	163	32	0		0				464	3,5
DIAGNOSTIC SYSTEMS			237	94	16	11	5		51				414	3,2
ANALYSIS			82	477	724	1310	229		109				2931	22,4
OTHERS			579	795	321	75	0		98				1868	14,3
TOTAL	0	0	2947	3065	2637	2873	386	0	1199	0	0	0	13107	100,0

In July 2015, IC1A switches, after some assembling modifications, have been positively tested within a set of dedicated discharges, and finally released at the end of the test.

The second experimental campaign (C2-2015) was allocated for cooled lithium limiter experiments, but due to a leak in cooling system it has not been possible to carried out such program. The campaign started anyway to complete other urgent program, which required full performance of FTU, but a problem of excessive vibration alarm on the poloidal generator (MFG3), recommended to stop the experimental session with more than 2 weeks in advance.

Inspection of MFG3 by Ansaldo Energia, the company that built the generator, confirmed the need to halt the experimental campaign and open the generator for a closer inspection.

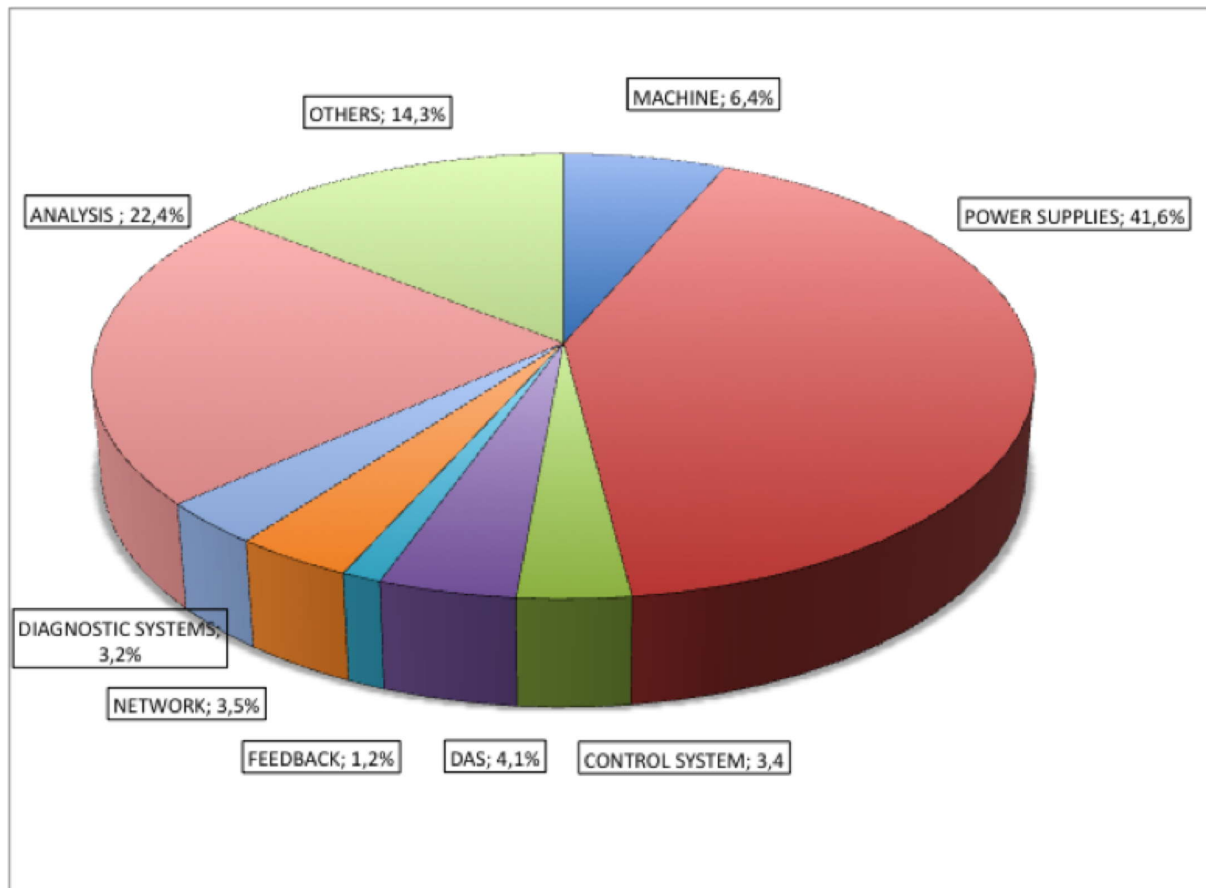In 2015, 1157 shots were successfully completed during the two experimental campaigns out

Figure 1.1 - Source of downtime in FTU for the year 2015

of a total of 1286 performed in 56.5 experimental days (by the way shot # 40000 was a good discharge with 0.5 MA and 4T). The average number of successful daily pulses was 20.5. *Table 1* reports the summary data. *Figure 1.1* reports the source of downtime for 2015: Power Supplies is the greatest cause of delay with 41,6% of the total.

FTU Data Acquisition and Control

The FSN CODAS team provides its expertise on Control, Data Acquisition and Information technology to several FSN projects, from FTU experiments to F4E and EUROfusion work packages.

Data acquisition systems and plant control. Most of the activities this year have been done to upgrade the Control and Data Acquisition systems performance and usability to support FTU long (4s) plasma discharges, while several enhancements on plant control are under way:

- two new ECRH data acquisition systems have been developed, based on a compact PXI based acquisition unit standard, granting configurable data acquisition time windows and an enhanced local data HMI.
- the integration in the FTU supervisor of a new cRIO-based Fast Sequence Controller has been done.
- the development of a new cPCI acquisition unit, capable of simultaneous acquisition of 80 channels up to 500 kHz for the soft-x tomography diagnostic has been completed.
- the development of a cPCI/PXI system for the data acquisition and reference generation of the FTU poloidal coils, based on the ITER CODAC Core System package, is under way in the framework of the ITER CODAC – FTU CODAS collaboration.
- The new liquid nitrogen control system, based on ITER CODAC software framework, is ongoing.

- A new vibration detection system is being implemented on FTU poloidal coils power generator MFG3

Information technology. A new network Extreme S8 matrix has been installed, realizing 1 Gb link towards any FTU host and foreseeing 10 Gb uplinks in view of remote experiment control projects.

A virtual VMware ESXi environment has been put in place. The system is based on a Supermicro X7BDU (Xeon 5160 @ 3GHz / 32 GB RAM) node and two Fiberchannel EonStore storage systems, one of which devoted to virtual machines backup. Its aim is hosting test and production systems avoiding the proliferation of dedicated hardware resources. The following virtual machines have been installed:
- Backend FSC, based on Windows 7 Professional, hosting the Basestar Open client to handle FSC configuration;
- Zabbix Server, a CentOS 6.7 node monitoring the availability and the performance of FTU IT infrastructure (network switches, WiFi access points, servers, HMI thin clients)
- Wiki server, a CentOS 6.7 node running MediaWiki to host operating procedures and documents produced by CODAS team
- Webftu, a new version under test of the web based environment supporting FTU technical activities.

The FTU buiding wireless infrastructure has been enhanced installing managed access points (Aruba iAP-205).

Real Time systems. The development of real time systems has reached the following goals:
- Enhancement of the FTU feedback system with a user programmable impurity feedback, based on the pressure readout ahead of the impurity valve. The session leader can specify – through the specialized GUI – the amount of impurities to be injected into the torus. The system can read and react to measurement variations with a sensitivity of one millibar.
- Density cycles in runaway generation and gas puffing suppression experiments.
- Upgrade of the feedback GUI for density reference and gas prefill readout from FTU archive.
- Realization of a real time data acquisition system for a scanning interferometer, within the framework of the Eurofusion work package MST2-Runaway Control. Based on MARTe middleware, the system acquires and processes data from the CO-CO2 interferometer calculating the density profile inversion. Data is shared with the real time control system through reflecting memories to perform density feedback and runaway monitoring.

F4E projects and grants. The CODAS team has contributed to the Radial Neutron Camera System Level Design (System requirement assessment – Instrumentation and Control functional analysis) within the framework of FPA 327 specific grants 01 and 03.

LH System

In 2015, the Lower Hybrid (LH) system has undergone ordinary and extraordinary maintenance. With reference to the latter, the displays showing the access conditions of the tube room have been reprogrammed after finding and buying a compatible remote controller. Much effort has been put in the reactivation of gyrotrons serving LH modules 3 and 8. Concerning the former, extreme attempts based on cleaning ion pumps by means of heating tapes have been unsuccessfully tried. After significant efforts of conditioning with no increase of the beam current, the tube was definitely reckoned unusable. Regarding the gyrotron of LH module 8, many units were broken and have been repaired, e.g., power supply of the gun field, electronic boards of the modulator, optical switches in the high voltage power supply, BiRa-based acquisition system, etc. After reactivating enough module units to perform a pulse at high voltage with no power, the occurrence of electrical discharges inside the gyrotron tank were recorded due to the detachment of some resistances in oil from their

places. The tube has thus undergone an intense activity consisting on disassembling, replacement of resistance series and reassembling; oil has been filtered and treated. Subsequently a monitoring activity of the gyrotron, with its auxiliary systems under working conditions, has been undertaken. Preliminary indications regarding tube behaviour are promising. In autumn, maintenance activities slowed down because of the unavailability of the 20 kV AC, namely the high power from the electrical substation of the Frascati research center. Several investigations were carried out in December, when, nevertheless, no further alarm events occurred.

ECRH System
At the beginning of 2015 the FTU ECRH system was prepared to operate with 3 gyrotrons (140Ghz-400kW-0.5s) connected at the two EC launchers. During the conditioning activities of the first FTU campaign, 2 gyrotrons broke, one for a window damage (due to the failure in the arc detector protection system) and the other for a short circuit in the filament. These two gyrotrons were then prepared for the shipment to GYCOM factory for repair.

Nevertheless the ECRH system operated satisfactorily during the FTU campaign with one gyrotron only. The available EC power was used in different experiments as MHD control, run-away electrons formation in EC assisted breakdown plasma, density limit studies, MARFE stabilization, assistance for LH in high density and for the Enabling Research programme on the experimental investigation of PDIs and wave excitation by non-resonant mm-wave beams.

1.1.2 - FTU experimental Activity

WP15-MST2-9 Mitigation of runaways, validation of runaway generation models studies and related diagnostics in support of MST and JET activities
The WP15-MST2-9 project addresses the position control of disruption-generated runaway electrons (RE) [see also next Paragraph on RE Control] and the determination of the critical electric field for RE generation.
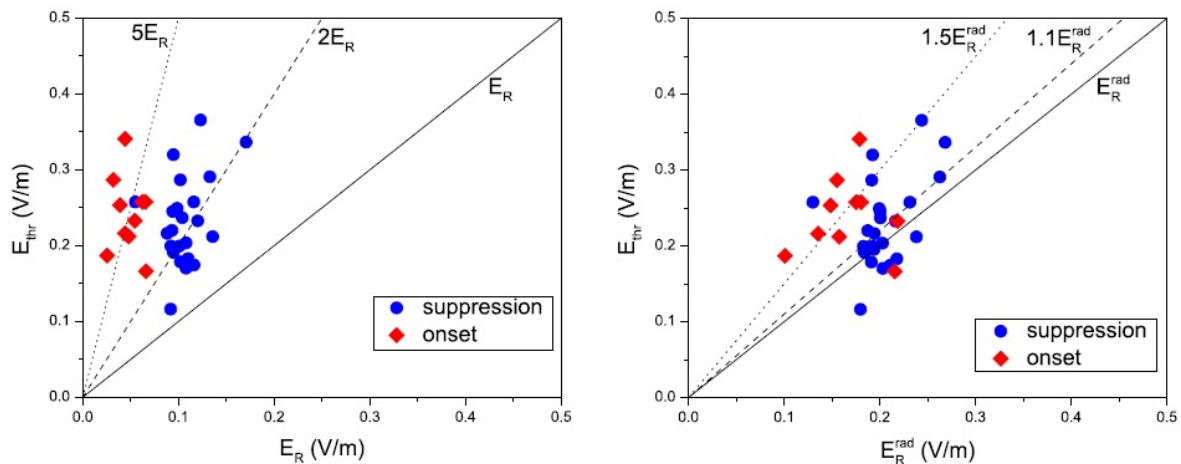

Figure 1.2 - Comparison of measured E_{thr} with relativistic collisional (left) and collisional+synchrotron radiation (right) theory predictions

The work is based on plasma experiments in the FTU facility and modelling. The highlights of 2015 are:

* the real-time (RT) upgrade of the FTU CO2 scanning interferometer and its integration in the FTU real-time plasma control system;
* the development of a linearized model of runaway current and horizontal position;

- experiments of RE generation during of Electron Cyclotron (EC) assisted breakdown showing the generation of RE even at moderate RF power injection. [see also paragraph on RE generation during EC Assisted plasma start-up];
- experiments of RE onset, suppression and control in ohmic discharges leading to the addition of new points (at 3.6 T and 4 T, 350 kA) to the existing database on the critical electric field for RE generation (E_{thr}). *Figure 1.2* confirms that the measured E_{thr} is ~2-5 times larger than predicted by the classical collisional theory [1.1] and consistent with the new threshold calculated including synchrotron radiation losses [1.2]. The local central density is used to calculate *ERrad* since RE are initially generated in the core of the plasma.

Runaway Electrons Control

In FTU a large database (650 pulses) of highly energetic post-disruption Runaway Electrons (RE) beam, produced spontaneously or with high-Z gas injection, have been analyzed in order to provide reliable and safe RE beam suppression strategies.
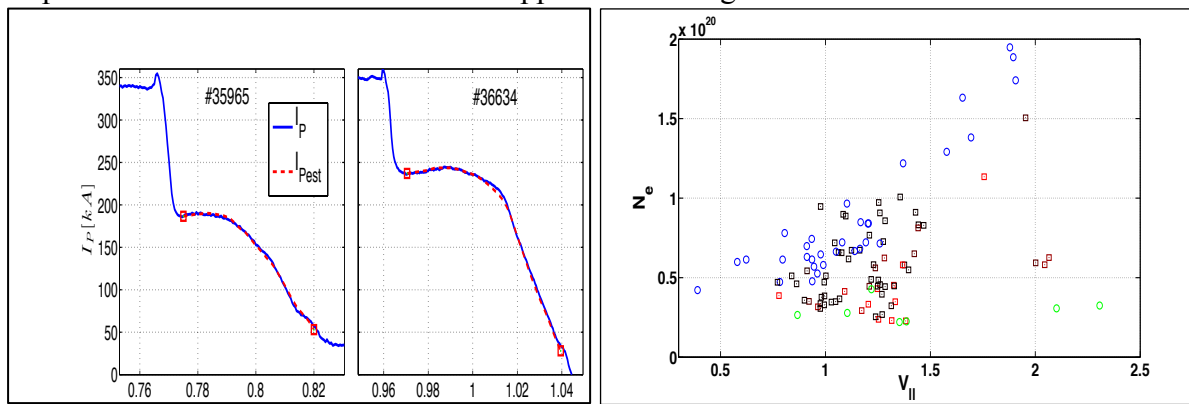

Figure 1.3 - (Left) Estimated model (red) and experimental (blue) RE beam current. (Right) hysteresis affecting the runaway dynamics: generation in green, suppression blue, steady state values are in squares with different values of RE from black (no RE) to red (high RE)

The study reveals that the decay rate during RE beam current ramp-down is a key parameter for runaway energy suppression. Small current rates are less demanding for the radial/vertical stabilization and are therefore profitable to fast RE current decay, which induce also strong magnetic forces on the mechanical structure. Also MHD instabilities have been found to play an important role. The analysis reveals that large toroidal electrical field, produced by the central solenoid steered by the plasma control system trying to sustain the RE beam current generally much below the standard current reference, seems to induce or increase harmful MHD activity, potentially destabilising the RE beam. Such MHD destabilizing effects have been observed in correspondence to these large electrical fields during post-disruptive RE beam. First experimental results quantitatively show that MHD amplitude is correlated with loop voltage during a RE plateau. Current studies are also devoted to investigate the optimal current dissipation rate compared to the measured loop voltage. Experimental findings suggest a post-disruption RE beam suppression strategy in order to obtain decay rate of about 1MA/s as provided also by other researchers on different tokamaks. The FTU team is now working to provide the control logic necessary to limit the electrical field in order to minimize the probability of triggering MHD activity during the controlled RE current ramp-down. New experiments have highlighted the vertical instability of the RE beams, that is assumed to be induced by the values of the two poloidal field coil currents (V and F as shown), that during the RE beam plateau reach values associated to highly elongated (standard) plasmas. Linear dynamical models have been identified showing a good approximation with experimental data, *Figure 1.3* left, and characterized by two unstable eigenvalues. These models are now

used to derive new current and position controllers for RE beam. The hysteretic behaviour of the runaway dynamics highlighted experimentally by the present study is shown in *Figure 1.3* right.

Runaways generation during EC Assisted plasma start-up

Studies on Runaway Electron (RE) formation in tokamak during EC assistance in plasma start-up have been performed under the *MST-9-1-1(FTU)* project *"Mitigation of runaways, validation of runaway generation models studies and related diagnostics in support of MST and JET activities"*.

Considering that in ITER the start-up phase of plasma current will be obtained with the assistance of strong RF wave additional power (up to 4 MW) it is necessary to extend the RE generation studies to the plasma ramp up phase in presence of EC waves. In experiments performed in FTU unexpected generation of REs has been observed at low toroidal electric field, in conditions of E_{tor} below the Dreicer threshold. An analysis of the part of the EC assisted breakdown FTU database, with different neutral filling pressure, EC polarization and E_{tor} has shown (see FIG.3) as the EC power acts on the threshold for RE formation, while the ohmic case is well described by the classic Dreicer theory. The presence of REs was revealed by a gamma ray diagnostic (NE213 detector) together with Cherenkov
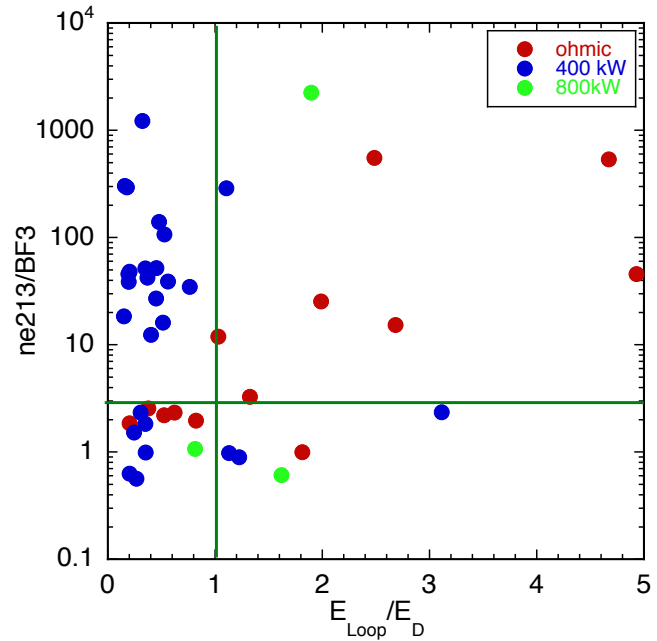

Figure 1.4 - RE presence (from the rate of gamma / neutron diagnostic) as a function of toroidal electric field normalized to the Dreicer threshold. Date for pure ohmic (red) and EC assisted (blue and green) are presented

probes. Even in presence of an E_{tor} 5 times lower than the Dreicer threshold, REs were detected during and after a 350 kW EC pulse. From the analysis of the RE timing there are evidences that EC wave acts as a seeding for fast electrons, further accelerated by E_{tor} increase. The formation of fast electron tails is likely related to EC absorbed power by increasing prefill pressure or by high enough initial electron density.

Neon impurity seeded FTU plasma

Seeding of Neon impurity in FTU ohmic plasmas causes a spontaneous increase of line averaged electron density up to a factor two (notwithstanding the absence of Deuterium gas puffing) associated with a significant increase of the peaking factor [1.3].

These effects, studied in the recent experimental campaigns have been further investigated in the 2015 experiments, in particular to set the scaling with current, but above all to obtain better spectroscopic data. A detailed particle transport and the microturbolence analysis were performed, because first results lead to relate the mechanism of density peaking to the ITG growth rate, as calculated by Gyro-Kinetic codes (GENE). In order to assess the role of the ITG growth rate during 2015, a detailed linear micro-stability analysis of Neon doped pulse has been carried out with the gyro-kinetic code GKW, and compared with a reference undoped pulse at the same line-average electron density and set plasma parameters. The doped discharge has higher ion and electron gradients after the Neon injection (consequently
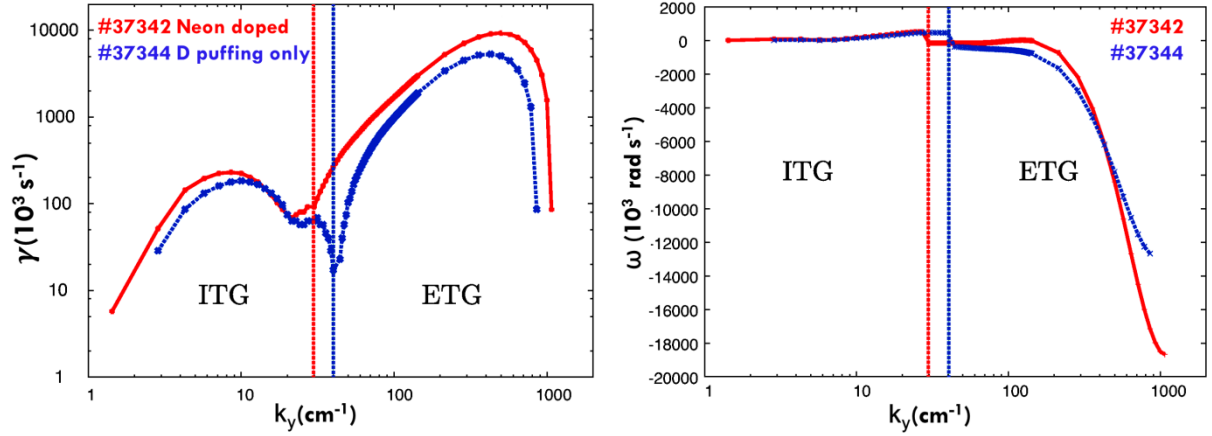
Figure 1.5 - Linear growth rates (left panel) and frequencies (right panel) for a doped (red trace) and an undoped (blue trace) discharge

higher ITG and ETG modes) than the undoped one taken at the same line averaged density (*Figure 1.5*). Positive and negative frequencies refer to modes drifting in the ion (ITG branch) and electron (ETG branch) diamagnetic direction).

More recent simulations take into account the impurity profiles as reconstructed by an impurity transport code [1.4]. The presence and the peaking of the Neon impurity reconstructed profile plays an important role on the presence of unstable modes.

ExB drift effects on MARFE.

The MARFE instability is present at various current and magnetic field values on FTU; in the case of a well developed MARFE, a peaking of density profiles is observed, this occurrence favors the exceeding of the Greenwald density limit [1.5, 1.6]. The MARFE oscillations cause continuous density fluctuations affecting the line-integrated density measurements The amplitude of density fluctuations decreases with edge safety factor and with electron density. During the experimental campaigns 2015, one dedicated experimental session was devoted performed to study the $\vec{E} \times \vec{B}$ drift effect on the MARFE instability on FTU, including some discharges with reversed toroidal magnetic field; the field sign has provoked the MARFE positioning in the upper midplane or lower, respectively.
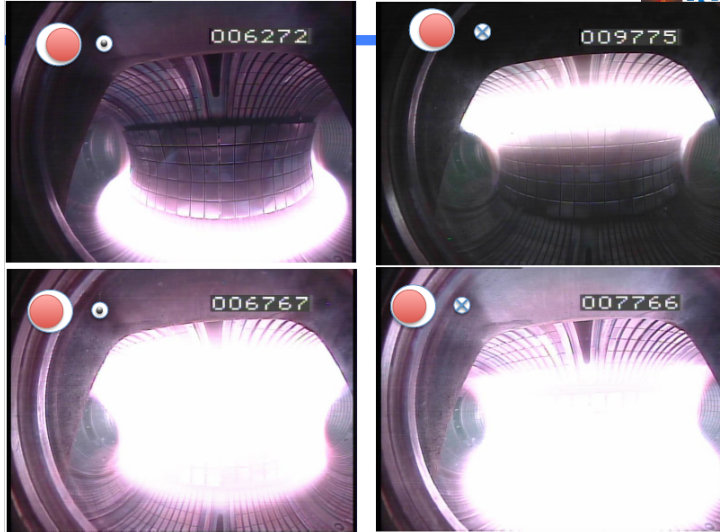

Figure 1.6 - Visible light shots of the four configurations, in the two circles the plasma position and electric field are pictured

Furthermore the plasma was moved on equatorial plane from high field side to low field side (*Figure 1.6*). In fact this experiment was focused to observe the MARFE localization in respect of the drift, due to the influence of the radial electric field Er on the stable and unstable positions [1.7].

Evidence of thermo-diffusive pinch in particle transport

Density evolution in a set of discharges performed in FTU, can be well described by assuming a particle pinch with dependence on temperature gradients (thermo-diffusion) given by $\Gamma_p = -n_e D_T \, \partial ln T_e / \partial T_e$. In these discharges a sensible density peaking is observed at high density, subsequent the formation of

a strong MARFE thermal instability [1.8] at plasma edge. While central density is increasing of about a factor 2, edge chords, within a large plasma shell, remains almost unchanged [1.9] generating a neat density peaking. As a consequence, strong density gradients arose between r/a = 0.6 and 0.8. The measurement of such density profile details has been possible owing to FTU scanning interferometer, which has 32 independent chords with spatial resolution of 1 cm. [1.5] This effect is more evident in presence of low Z impurities, as B and Li, used for wall conditioning. The presence of a strong MARFE seems to be key to get the density peaking in these discharges. The peaking of density profile is preceded by a drop of the edge temperature in a wide external region, caused by the thermal collapse at the edge, which led to the MARFE formation. The extension of such a region can be large up to ¼ of minor radius, and temperature inside MARFE can be as low as 1-2eV. At this temperature recombination dominates, and a huge numbers of neutral particles are present in the MARFE region. In order to estimate the contribution of neutrals to particle balance, a neutral diffusion code has been used to evaluate the evolution of the source term. The uncertainty on the plasma parameters inside the MARFE are, however, so large that only a rough estimation of neutral level can be done using D_α emission, and measured density inside the MARFE. According to these calculations, the source term remains negligible in large part of the radius (from plasma core to r/a=0.8) and in particular in the region where the changes of density gradient are observed. Neglecting the source term in diffusion equation, it is found experimentally that the increase of peaking can be explained only with a sensible increase of the total inward particle pinch between 0.5 < r/a < 0.8. Having observed a good correlation between density and temperature characteristic lengths, the thermo-diffusive term has been taken into account to verify to which extent it can reproduce the effect on density profile. The diffusion equation considered for the simulation has the following expression

$$\frac{\partial n_e}{\partial t} = \frac{1}{r}\frac{\partial}{\partial r}r\left(D\frac{\partial n_e}{\partial r} - D_T\frac{n_e}{T_e}\frac{\partial T_e}{\partial r}\right)$$

Diffusion coefficients D and D_T are flat in the region of the simulation and have been assumed to be constant in time. The simulated density evolution at different radii (solid line) is shown together with experimental values (dots) in *Figure 1.7*.
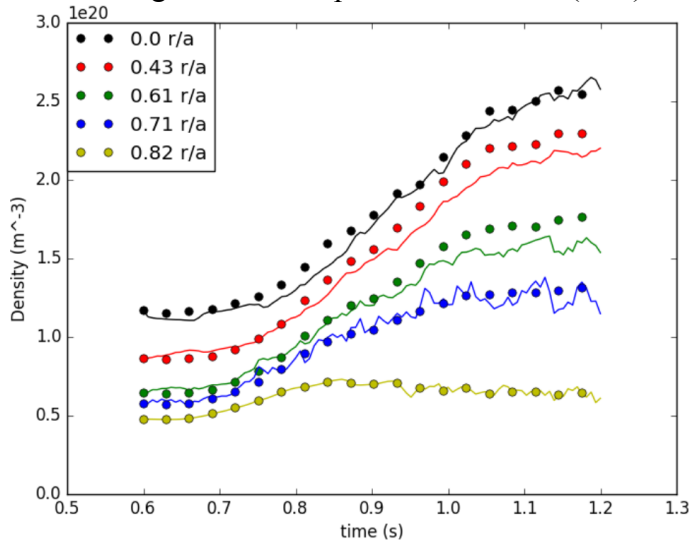

Figure 1.7 - Simulation of density evolution at different plasma normalized plasma radius. Calculated density (lines) are well in agreement with experimental data (dots)

The density evolution at r/a = 0.82, has been taken as boundary condition for the diffusion code, while experimental density profile at t=0.6 s has been used as initial condition. The diffusion coefficient's amplitude has been taken to keep initial condition profile stationary, for constant boundary condition and constant temperature profile. The evolution of density is mainly associated to the change of temperature profile and partially to the slight increase of the boundary density. The steepening of density gradient between r/a = 0.71 and r/a = 0.82, is well described by the simulation, hence the whole variation of inward particle flux can be described considering the change in temperature

characteristics length. The simulation has been successfully applied to other discharges with similar phenomenology.

TM onset near the density limit

Due to the dependence of fusion power on plasma density, the tokamak density limit has been the subject of intense study over several decades.

Density limit disruptions are usually ascribed to a thermal instability occurring when the radiation loss near the edge region overcomes the heat flux from the core. The ensuing contraction of the temperature profile leads to a shrinkage of the current profile driving unstable a global MHD mode, such as the tearing, leading to disruption if the density continues to grow (*Figure 1.8*). Dedicated density limit experiments were performed on FTU in a wide range of plasma current and toroidal magnetic field values. The analysis of the linear stability of the tearing mode on FTU, performed by means of a modified cylindrical code and also by means of a complete linear resistive MHD code, has confirmed a destabilization of the tearing mode during the density ramp-up as a consequence of the increasing peaking of the current density profile.
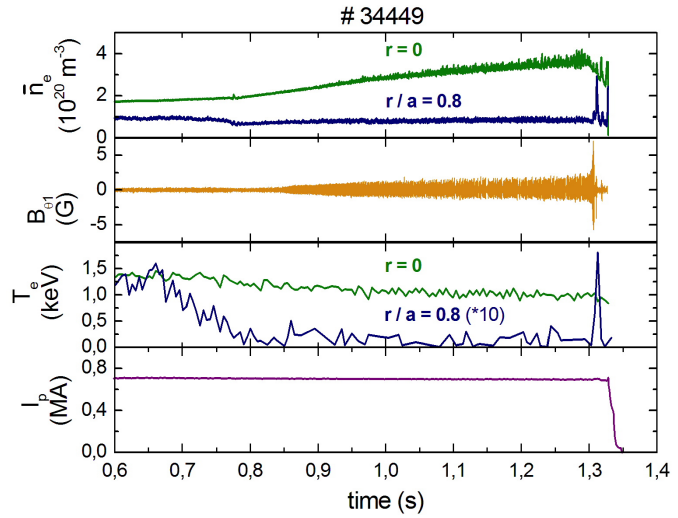
Figure 1.8 - Time traces of some relevant quantities for MHD activity on FTU (from top to bottom): central and peripheral line-averaged density, poloidal magnetic perturbation, central and peripheral electron temperature, plasma current

MHD limit cycles

The development of large-amplitude tearing modes during the pre-programmed plasma density ramp-up in proximity of the density limit or after injection of sufficient amounts of Ne gas on FTU shows a complex behaviour that can be outlined in three stages (*Figure 1.9*).

First stage: the magnetic island grows smoothly at constant rotation frequency. Second stage: amplitude and frequency feature large cycles of oscillations, with peak amplitude increasing progressively across cycles. Third stage: the island grows quickly to large amplitude and locks; this stage generally ends in a disruption. The amplitude and frequency oscillations show a well defined phase portrait, determining a so-called "limit cycle" on the Amplitude/Frequency plane (*Figure 1.10*). Dedicated experiments were performed on FTU, in a wide range of plasma current and toroidal magnetic field values, to understand the origin of
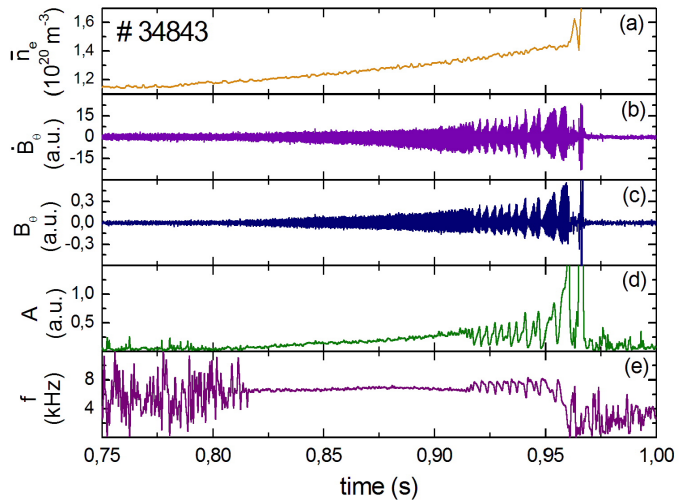
Figure 1.9 - Time traces of some relevant quantities for the MHD activity for a specific pulse on FTU: (a) central line-averaged density, (b) output from the pick-up coil, (c) poloidal magnetic perturbation, (d) mode amplitude, (e) mode frequency

amplitude and frequency modulations of the tearing mode and to obtain the scaling for transitions between different regimes (saturation, limit cycles, locking) in terms of plasma parameters and mode amplitude.

The existence of a stage with large amplitude and frequency modulations could be caused by interaction between modes of different helicity, also if in our pulses the $(m, n) = (2, 1)$ tearing mode seems to be the only large amplitude mode. In particular, the presence of the q=3 rational surface in the plasma seems to be necessary for the occurrence of deep and regular limit cycles for the (2, 1) tearing mode, so that the q = 3 rational surface could play an important role. On the other hands, the amplitude modulations could be caused also by island self-healing phenomena, with a recursive island fragmentation mechanism; in fact the island distortion increases before amplitude drops. We are currently working to understand the effective cause of this interesting behaviour.
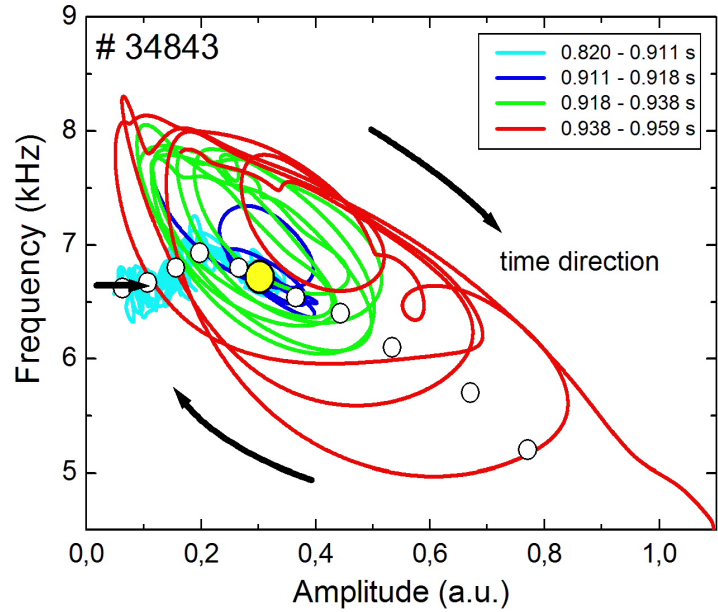

Figure 1.10 - *Tearing mode time evolution on the plane Amplitude/Frequency (see legend for colour meaning). The evolution of the amplitude and frequency envelopes is also reported as open circles. The yellow's corresponds to the critical mode amplitude for transition from smooth to cyclic behaviour*

Density limit at low B_T and I_P

A study concerning the density limit at high field and current (4 - 8 T, 500 -900 kA) on FTU pointed out that the dependence of the density peaking on the edge safety factor, in presence of a MARFE, is crucial in the determination of a density limit scaling law for the central line averaged density. This study has been completed exploiting an experimental campaign devoted to explore high density regime for low field and current (2.5 - 4 T, 250 - 500 kA). For each I_p and B_T configuration, the discharge was performed with a continuous gas flow injected into the plasma in order to produce an increasing density up to the disruption for the density limit, occurring because of the rapid increase in the amplitude of MHD activity. All discharges considered here had gas puffing and ohmic heating only and the selection criterion was the density limit to be reached during the I_p flat-top. At high-density operation, an increase in the density beyond a certain value usually produces the MARFE phenomenon: all the considered discharges present a density level around the threshold for the appearance of the MARFE. For this reason it is present, but it does not develop completely. It has been observed that the density peaking is not growing in time during the discharges and the MARFE does not seem to have any impact on the evolution of the density limit and peaking of the discharge. As expected, none of the considered discharges overcome the Greenwald limit. The observed dependence of the density limit on the magnetic field for the central line averaged density is compatible with the scaling law determined at higher magnetic field and plasma current where it was found $n = 0.19 \cdot B_T^{1.5}$. This density has also been evaluated at the onset of the MHD activity leading to disruption: in this case too a dependence of the density on the magnetic field is visible through the relation $n = 0.24 \cdot B_T^{1.2}$, very similar to the one

obtain for higher current and field ($n = 0.19 \cdot B_T^{1.3}$).

Central Density Limit: FTU Data Interpretation

In [1.10], a theoretical study was performed on the possible intrinsic nature of the central density limit in Tokamak configurations, with particular reference to the interpretation of FTU data.
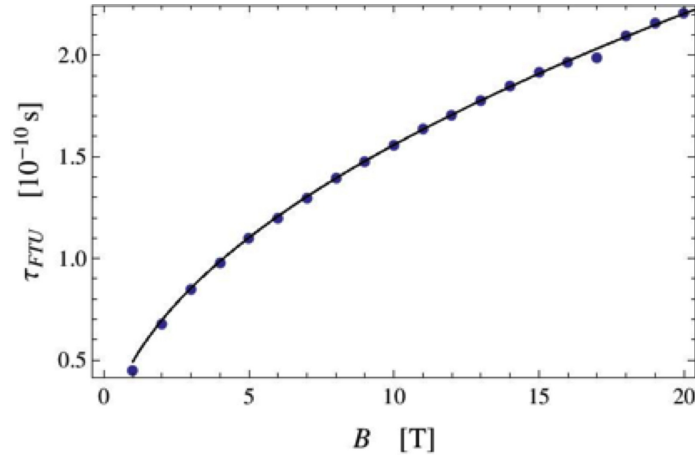

Figure 1.11 - Time scale τ (in seconds) as a function of the magnetic field B (in Tesla). The dots are the data sampled according to the model equations, while the line represent the function that best fits the data.

The conceptual framework, originally proposed in [1.11], is based on the idea that the electron Larmor orbit is destabilized by electrostatic turbulence and this effect is maximized when such orbit lives outside the Debye sphere, *i.e.* when the plasma frequency exceeds the gyro-frequency. It was investigated the spatial distribution of magnetically confined electron in the presence of a Gaussian random transverse electric field, whose variance contains a phenomenological parameter, namely, the time scale of the electric fluctuations.

The main merit of this study is to show that, if the FTU data are fitted and the free parameter is fixed (*Figure 1.11*), we see that the corresponding spatial scale of the electric turbulence corresponds to the microphysics scale of the Tokamak, *i.e.* of order of few millimetres.

Liquid Metal Limiters on FTU

Research on liquid metals, as a viable solution to solve the power exhaust problem, is progressing in Europe. The experiments on FTU aim at testing a cooled liquid lithium limiter (CLL) (2014&2015) and subsequently a cooled liquid tin limiter (TLL) (2016) under reactor relevant thermal loads of up to 10 MW/m^2 in stationary conditions.
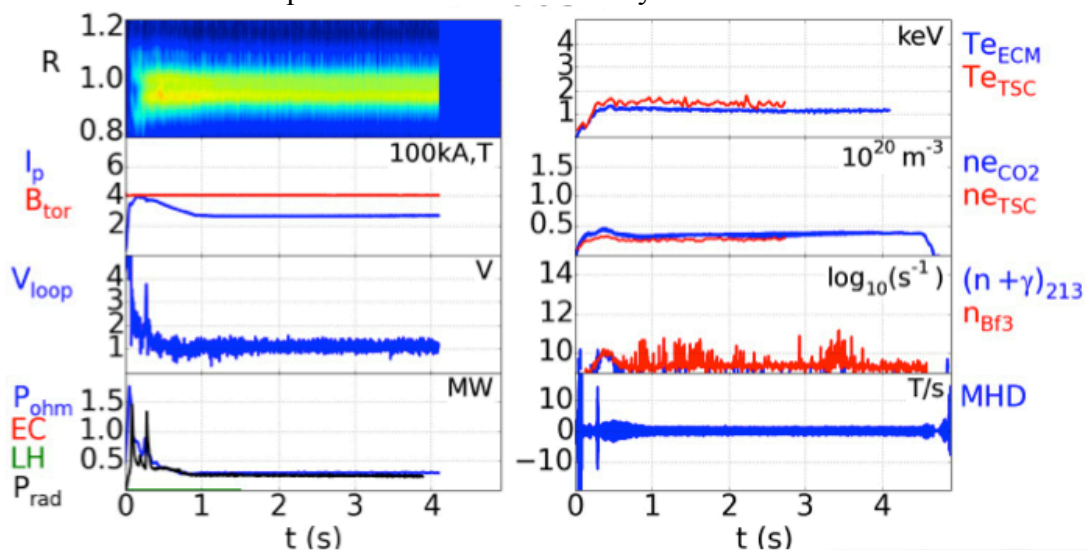

Figure 1.12 - Stationary heat flux controlled by plasma position (shot n. 40052)

In preparation of this program, improvements of the FTU facility started in 2014 and continued during 2015 with the extension of FTU pulses to 4.5 s and $B_T = 2.5 - 4$ T. A plasma

stationary phase of 3.5s at Ip =0.25 MA and B_T= 4 T was obtained (see *Figure 1.12* shot n.40052) with a current variation in the transformer from + 24 to -24 KA and with a margin of 1KA from the upper and lower limits of ±25 KA [1.12]. To maximise and control heat load on limiters, elongated configurations (k ~ 1.2) have been also obtained for 3.5 s on FTU, with the X-point just outside the plasma chamber [1.13]. To realize this improvement, a dedicated work on the FTU control and data acquisition systems was required as well as on the sequence of the programmed discharges. Unfortunately, CLL experiments on FTU with heat loads higher than 2.3 MW/m^2 and time duration grater than 1.5 s were prevented by the onset of hot spots on the joint points of the strips of the capillary porous system (CPS) structure and by the poor control of the Li temperature that displayed large oscillations. To solve these problems, during 2015 a new active CLL refrigeration head in Red Star Labs has been realized with a larger curvature radius and the CLL control system has been successfully implemented in ENEA in order to optimize the temperature monitoring and the control of the circulating water. Nevertheless, no FTU experiments with the new CLL version were possible. Indeed, during the temperature conditioning inside the CLL volume, a small water leak occurred on the CLL head, at the welded connection of the CPS Mo tube with the SS tube. An accurate revision of the project was required and a third CLL head was designed and then constructed. It is planned to be in ENEA in April 2016. The contractual phases for the construction of the new Cooled Liquid Sn Limiter, employing an intermittent injection of Ar-water spray for cooling and a resistor for heating the Tin CPS were carried on. Red Star completed the experimental tests on wetting, corrosion and those relevant for the calorimetric measurements with the supervision of ENEA experts. The manufacturing and the delivery of TLL are foreseen in the first semester of 2016. In the European framework of coordinated actions, a cooled sample of Sn CPS type envisaged for the TLL in FTU has been tested on Pilot-PSI linear device. A power handling of 26 MW/m^2 has been demonstrated under stationary conditions and without apparent damage of Sn sample, giving early indications the TLL will be effective. Finally, a radiative model has been developed to clarify the mechanisms of the FTU radiation shield as observed with the previous liquid lithium limiter (LLL). This model accounts for the dissipation terms of the power flux reaching the liquid lithium surface such as: the Li radiation losses, the Li evaporation and the replenishment of liquid lithium on the CPS surface.

Erosion and retention studies on FTU
In the frame of EUROfusion Work Package Plasma Facing "Component" (WP-PFC) the FTU Sample Introduction System has been used for exposing in the scrape-off plasma samples with the purpose of checking the effectiveness of preferential sputtering in the tungsten enrichment of the very surface layer of first wall material, like EUROFER steel. The latter could represent a valuable alternative to a solid tungsten or tungsten coated first wall, with obvious saving of money and decrease of weight.
Two rectangular samples have been exposed to the plasma flux, the first consisting of a Ti substrate coated with a thin (300 nm) mixed layer of W and Fe, with the W concentration very low (about 1%) and the second of P92 steel with similar W concentration. To avoid sample contamination by a close source of Fe, the sample holder was made of Ti. The W/Fe and the P92 samples were exposed to 14 and 26 discharges, respectively, with the former suffering also some disruptions, resulting in melting of the edge closest to the plasma boundary. The edge temperature, as measured by Langmuir probes in the plasma tube connected to the samples, was about 20 eV, with a rather long e-folding length, a value ruling out W sputtering while allowing a moderate, but not negligible, Fe erosion. On the other hand the fluence was *rather low, the FTU shots lasting 1-1.5 s,* and therefore the effect of preferential sputtering is to be expected not very evident.

Table 1.2 - Fe and W conc. in the W/Fe reference sample and in the sample exposed in FTU

Sample	RBS Fe conc. (%)	RBS W conc. (%)	TOF ERDA Fe conc.(%)	TOF ERDA W conc.(%)
W/Fe not exposed	94.9 ± 4.0	1.5 ± 0.2	90.7 ± 4.0	1.0 ± 0.3
W/Fe exposed	14.6 ± 1.0	0.3 ± 0.1	15.7 ± 0.3	0.2 ± 0.1

After exposure the samples were analyzed with SEM, EDX, XRF, RBS and TOF ERDA, in collaboration with the National Institute for Laser, Plasma and Radiation Physics of Romania and the Ruđer Bošković Institute of Croatia. Data analysis is still in progress. From the analyses carried out so far, the comparison with non-exposed sample shows an overall decrease of Fe and W concentration in the exposed sample with large Ti concentration in the probed thickness as a result of W/Fe coating erosion or re-deposited Ti from the sample holder. The ratio between the concentration of Fe and W is decreased, as shown in the *Table 1.2*, although the error in the estimate of W concentration is rather large, because of its very low content.

Dust Studies on FTU

Following an investigation on the characteristics of dust collected in FTU at the end of 2013, an unexpected presence of ferromagnetic dust has been observed. Neutron and X-rays diffraction analyses on crystalline structures of that dust have thrown new light on the mechanism of formation of ferromagnetic dust in tokamaks. The origin of ferromagnetic dust is related to the molten drops ejected by austenitic stainless steel (non-magnetic) plasma facing components, such as first walls, diagnostics, antennas, etc., where the crystalline phase of iron changes from non-magnetic γ to magnetic α/δ phase. Two mechanisms are believed to be responsible for this change of phase; the first is the presence of a strong magnetic field environment during the re-solidification of molten grains that induces the transition from γ to α phase. The second mechanism, being FTU a cryogenic device, is the stabilization of δ-ferrite phase during the re-solidification of molten stainless steel grains due to the strong temperature quenching as soon as the molten grains get in contact with the cryogenic walls.

The presence of ferromagnetic particles in tokamaks could pose new problems due to their interaction with the magnetic field used for plasma confinement, in fact magnetic grains can be lifted up during the ramping up phase of the toroidal magnetic field due to ∇B force, and interfere with the start-up phase of plasma discharge [1.14].

WP15-MST2 -15 "REIS" Imaging of runaway electron beams

The WP15-MST2-15 activities have focused on the design, development and construction of the prototype of a portable Runaway Electron Imaging Spectroscopy (REIS) system for use in medium size tokamaks, namely AUG.

The system aims at the detection of the visible and near-infrared synchrotron radiation spectra from runaway electrons. It is based on a wide-angle visible camera and an
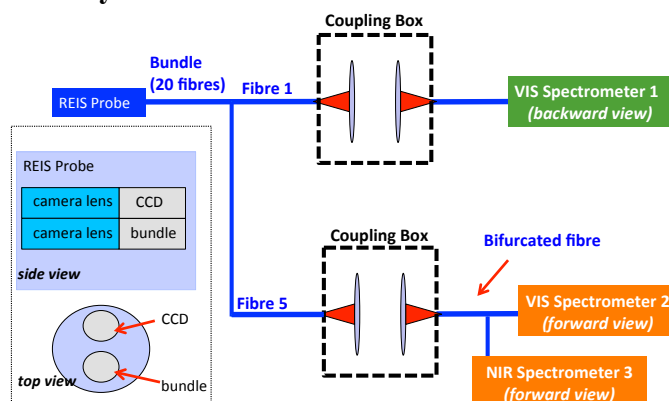

Figure 1.13 - *Scheme of REIS designed for installation at AUG.*

incoherent bundle of 20 optical fibres coupled to 2 visible spectrometers and 1 near-infrared spectrometer (see details in Figure 1.**13**). The prototype was tested in FTU during the 2015 experimental campaign: the data from the visible camera and the spectrometers were collected (not simultaneously) in several runaway discharges at 4T and 5T, Figure 1.14.

Visible Spectrometer (*backward*)

Visible Spectrometer (*forward*)

Visible Camera

Infrared Spectrometer (*forward*)
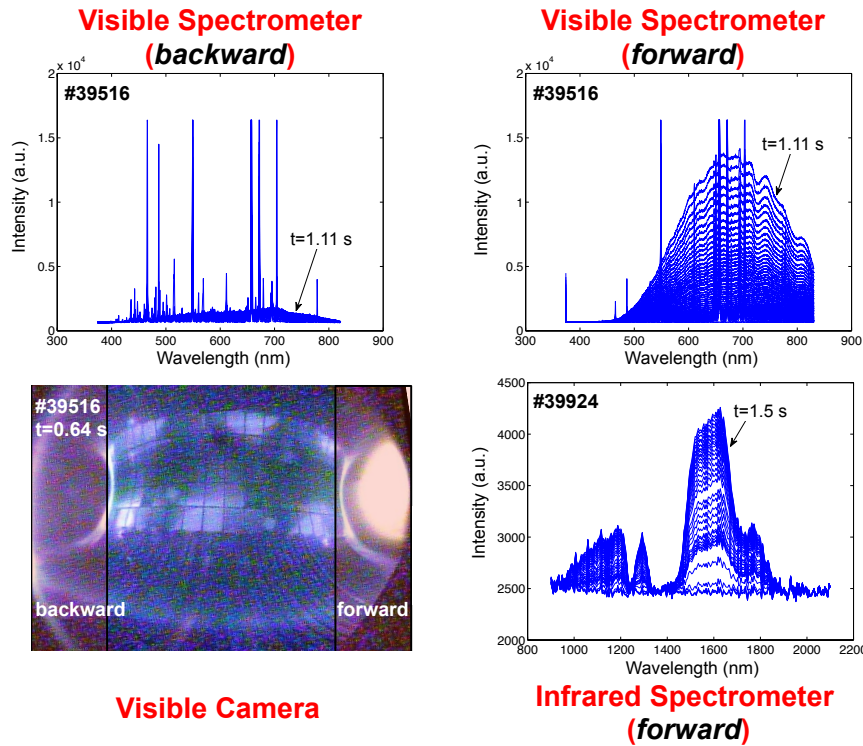
The results obtained are promising [1.15]: spectra in the visible 350 – 850 nm and infrared 900 – 2100 nm were acquired. Forward and backward RE synchrotron emission was measured and a clear distinction was observed between the two cases. The calibration of the data as well as the set up of the system for its installation in AUG is on going.

Figure 1.14 - *RE visible camera image and synchrotron spectra (raw data) in FTU*

CTS and PDI

The investigation on possible excitation of Parametric Decay Instabilities (PDI) by Electron Cyclotron (EC) beams in presence of magnetic islands using the Collective Thomson Scattering (CTS) diagnostic on FTU has been performed under Enabling Research project AWP15-ENR-01/ENEA-06.

Experiments were performed with a gyroton probe (140 GHz, 400 kW) launched in symmetric and asymmetric configurations with respect to the equatorial plane, in different conditions of plasma density and magnetic field (with or without the EC resonance in the plasma), and with magnetic islands generated by Neon injection. The CTS diagnostic was renewed [1.16] with the acquisition of a fast digitizer, which allowed the observation of spectral features with very high time and frequency resolution. In the experiments performed at 4.7 T, with the resonance on the high field side of the plasma column, or at 3.6 T, in this last case with the plasma between the first and the second EC harmonics, different spectral features were observed [1.17]. Two of them are presently under deeper investigation: the first is a rapid asynchronous sequence of bursts detected at frequency multiples of the (deuterium) ion cyclotron frequency above and below the gyrotron frequency, occurring in connection with a particularly complex MHD activity leading to plasma disruption (*Figure 1.***15** and *Figure 1.***16**). The second is a periodic emission at a frequency around 15 MHz from the probe frequency, with high repetition rate. The correlation of the observed peaks with the transit of the island O-point inferred from magnetic probes signals has been investigated, to characterize the observations and exclude parasitic effects, as well as breakdown phenomena in front of the antennas.
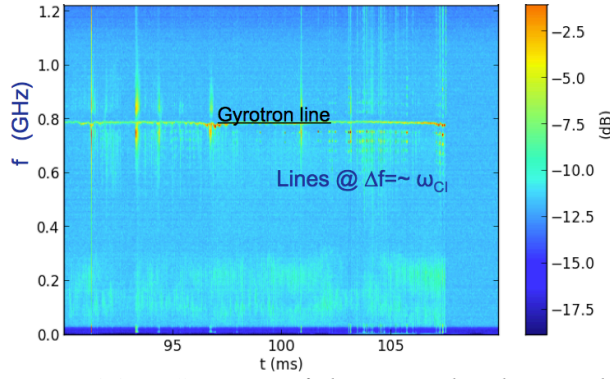
Figure 1.15 - Spectrum of the received radiation: the gyrotron line (highly attenuated) is visible at 800 MHz from the local oscillator frequency, at 139.48 GHz
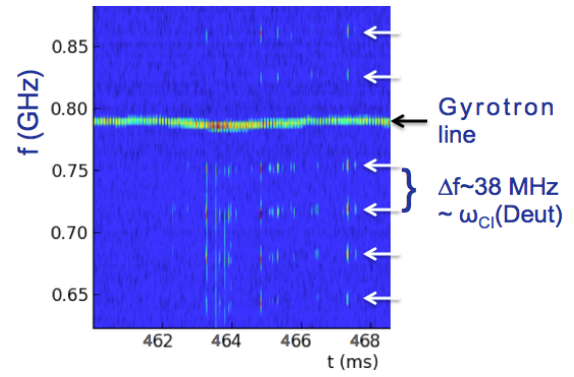

Figure 1.16 - Asynchronous sequence of bursts emitted at frequency multiple of the deuteron ion cyclotron frequency above and below the gyrotron line

The variation in the stray radiation distribution in the vessel has been studied with the aid of a diffusive model, to characterize variations on the probe beam absorption associated to the observed phenomena. Further improvements of the diagnostic both in frequency band (up to ±4.2 GHz from the probe) and with the addition of a second radiometer, will allow a clearer interpretation of the emissions.

Cherenkov probe and BAEs

Post-disruption events can be dramatic and represent a major concern for the safety of large tokamaks because uncontrolled rapid loss of runaway current may irreparably damage plasma-facing components The possibility to predict and control plasma disruptions and runaway electron (RE) beams in tokamaks is a key target for fusion research. REs can be detected when they are in flight in the tokamak vessel or when they escape the plasma. In the first case soft/hard X-ray profile monitors and synchrotron radiation detectors are generally used, while in the second case neutron and gamma ray detectors are employed.
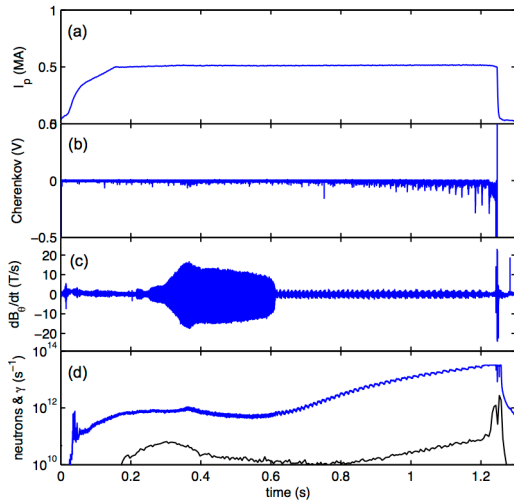

Figure 1.17 - Scenario involving island quasi-locking and BAEs at low plasma density (FTU #37655 B = 6 T, I = 0.5 MA): (a) plasma current, (b) Cherenkov signal, (c) Mirnov coils (channel 26), (d) NE213 and BF3 (black line) signals

Recently an optical diagnostic system based on the Cherenkov effect was successfully installed and tested in FTU in collaboration with the Polish National Centre for Nuclear Research (NCBJ), to detect REs escaping the plasma. Similar probes have been installed on other tokamaks by the NCBJ group, demonstrating the possibility of detecting the presence of high-energy RE beams by correlation with Hard X-ray emission. In FTU, Cherenkov signals were correlated with MHD activity to extend the work done by NCBJ, thus enabling a detailed study of RE dynamics to identify key mechanisms of the interaction of REs with magnetic perturbations. The Cherenkov probe was tested in various plasma scenarios in FTU, including experiments aimed at estimating the threshold electric field for RE generation, where the plasma density is intentionally reduced until REs are observed. Long-lived tearing modes and magnetic islands, often accompanied by beta-induced Alfvén eigenmodes (BAEs), are also typically observed in such low-density discharges.

In a typical discharge with BAE activity in FTU (magnetic field from 5.2 to 7.6 T, line-average density from 2.7×10^{19} to 1.5×10^{20} m^{-3}), *Figure 1.17*, in the initial phase, the Cherenkov signal modulation (3.2 kHz) is due to a tearing mode instability involving a rotating island developed in connection with the diminishing density. Cherenkov signal maxima occur when the island O-point faces the probe, demonstrating that RE losses are in sync with the island rotation, i.e., REs are expelled in the interaction with the magnetic perturbation due to the island. On the other hand, in the quasi-locking stage, when the island rotates at about 55 Hz and the magnetic signal is dominated by the high-frequency BAE component, the Cherenkov signal presents a bursty emission modulated by the island rotation frequency at 55 Hz. The high frequency components of the Cherenkov signal can be observed in *Figure 1.18*, where the power spectral density of Cherenkov and Mirnov signals are presented, respectively. This observation indicates that the amplitude fluctuations of the island represent a further RE expulsion mechanism.
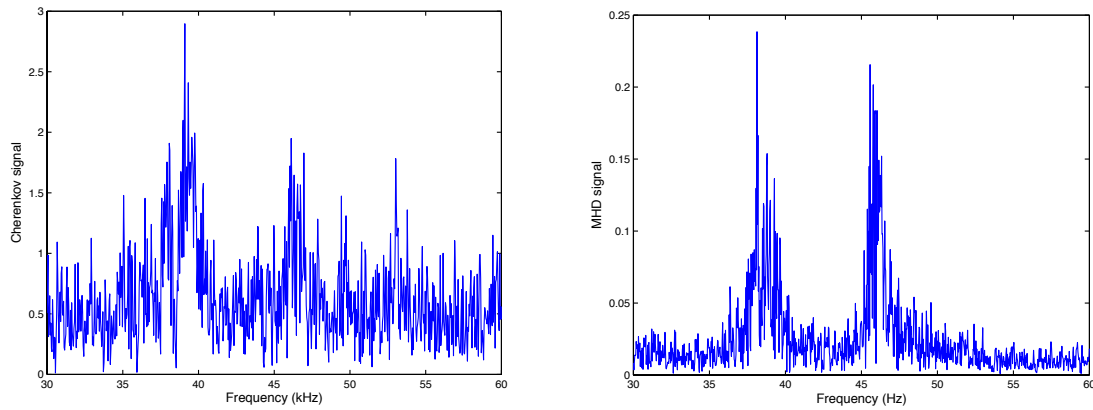

Figure 1.18 - Scenario involving BAE excitation (FTU #37655): power spectral density in the high frequency range (30-60) kHz of (Left) Mirnov and (Right) Cherenkov signals

In conclusion, in the presence of BAEs, the Cherenkov signal presents a bursty emission modulated by the slow, nearly locked island rotation frequency, demonstrating that RE expulsion is due to both the magnetic perturbation of the island and its amplitude fluctuations. This is the first time BAEs have been detected using a non-magnetic plasma diagnostics.

1.1.3 – Diagnostics Development

Cherenkov Upgrade

Post-disruption events represent a major concern for the safety of large tokamaks because uncontrolled rapid loss of runaway current may irreparably damage plasma-facing components. Significant research efforts are necessary to study and understand how to control Runaway Electrons (REs) and to implement adequate control schemes to prevent disruptions. Fast electrons within the plasma are typically monitored and detected using infrared, gamma-ray cameras and hard X-ray diagnostics. However, recently an optical diagnostics based on the Cherenkov effect was demonstrated to be effective in monitoring fast electron losses in FTU, particularly in scenarios involving plasma instabilities that can lead to disruption. The installation and test of the Cerenkov probe in FTU was done in collaboration with the Polish National Centre for Nuclear Research (NCBJ). Data interpretation and correlation with several other diagnostics operating in FTU, brought out the high level of detail provided by the Cerenkov probe in detecting RE losses driven by magnetic islands. The main limitation of the present single-channel Cherenkov diagnostic system is that it provides an integral signal from one location within the vessel, providing no information on the spatial and energy

distribution of incoming electrons. A Cherenkov probe upgrade that will enable energy and spatially resolved analysis of RE losses in FTU is planned for the next experimental campaign. The planned upgrade of the diagnostic system will permit RE energy-discrimination and simultaneous detection at two toroidal/poloidal positions to evaluate the potential of this diagnostic system for implementation in next-generation fusion reactors. The energy ranges of the three channels were chosen to permit a meaningful correlation with existing diagnostics, such as the Fast Electron Bremsstrahlung camera. Hardware components have been ordered and the sensor head has been assembled by NCBJ in Nov 2015. The head was shipped to ENEA and mounted on a suitably designed arm to permit rotation and translation of the head to control the orientation of the diamond window with respect to the equatorial plane of the tokamak, and the depth at which REs will be collected. After vacuum testing, it was installed in FTU ready for the next experimental campaign.

Triple-GEM Detector

The research on nuclear fusion requires the development of X-ray diagnostic with high temporal resolution (in the scale of microseconds) for the study of plasma physical fast processes (magneto-hydrodynamic instability, turbulence and heating) and imaging detectors for monitoring the plasma and the reconstruction of its magnetic topology.

NIXT X-ray laboratory, born of a decennial experience in detectors for fast two-dimensional soft-X imaging on nuclear fusion, is involved in developing, implementing and charactering these new diagnostic techniques that have a broad application, also beyond MCF field.

This X-ray laboratory has been built in ENEA Frascati and it is formed by a wide bunker, fully shielded to operate up to 120 keV, with all the devices remotely controlled from outside, it offers great flexibility in realizing customized optical configurations as required. The devices used in the laboratory (sources, detectors, optics, filters) are absolutely calibrated and characterized as a function of the X-ray energy (5-80 keV).

Actually micro-pattern gas detectors based triple-GEM (Gas Electron Multiplier [1.18]) reached a high level of performances together with a high degree of compactness [1.19]. They found important applications in soft-X ray diagnostic for Tokamak [1.20] and Laser Produced plasmas (LPPs).

Recently our work focalized on two kinds of triple-GEM detectors: we refer to them as GEM and GEMpix detectors. Both are head-on detectors with an aluminate mylar window, a 3 mm drift gap (the active volume of the detector) and three GEM foils separated by 1 and 2 mm gaps. Usually gas mixture is $ArCO_2$ (70/30) or $ArCO_2CF_4$ (45/15/40). The GEM detector covers an area of 10x10 cm^2, and is equipped with a Front-End-Electronics (FEE) based on CARIOCA chip cards and an FPGA (Field Programmable Gate Array) motherboard. Actually FEE can manage a maximum of 128 channels and the anode is realized by 120 pads, each one with an area of 8x8 mm^2.
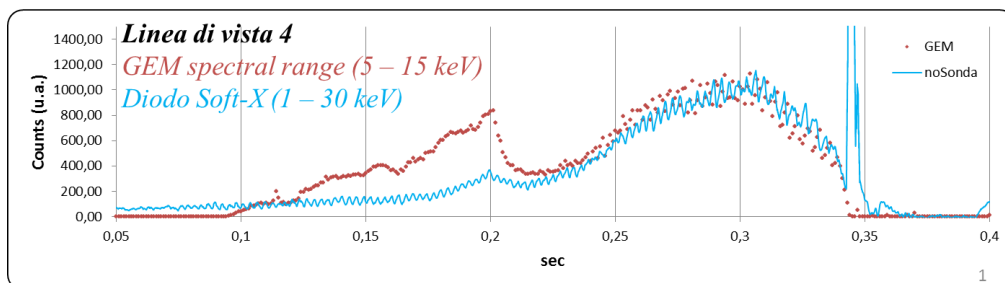

Figure 1.19 - Comparison between GEM detector signal and diode signal along a central line of view for an FTU Tokamak shot

GEM detector works in counting mode: charge released in the drift gap moves towards the GEM foils where it is proportionally amplified with a gain which can go up to 10^4, then a

current pulse is induced on pads and this is counted as one when a threshold level is exceeded. Threshold level is one of the parameter can be modified through the FPGA motherboard. FEE allows also the acquisition of a sequence of 60000 frames at a rate of 1 kHz. This is particularly useful for Tokamaks for which it is necessary to follow the evolution of plasmas during the shot. This kind of detector has been installed on the FTU Tokamak (ENEA). *Figure 1.19* shows the temporal trace as acquired by the GEM detector compared to a standard diode of the tomography system.

GEMpix detector, instead, has an area of 28 x 28 mm^2, while FEE is realized with four medipix chips hold together. Now there are 512 x 512 pixels, each one with an area of 55 x 55 μm^2. In this case spatial resolution is higher than GEM detector. In addition FEE con work not only in counting mode but also Time over Threshold (ToT) mode: it works like a Wilkinson ADC in which an internal clock gives a number of digits until the induced current signal on the pixel exceed a given threshold. GEMpix detector has been used successfully for soft-X rays diagnostic on LPPs. A first preliminary test was performed on the ABC laser ICF facility (ENEA, Frascati) [1.21]. In this case, we measured the X-rays produced when the ABC laser pulse, of 50 J and with 3 ns time width, hits an aluminium plane target. A pinhole system allows realizing soft X-ray image of the plasma (*Figure 1.20*). The results are encouraging regarding the capability of this imaging detector to work in experiments where soft X-ray emissivity varies over many orders of magnitude. Based on the successful results on ABC [1.22], we proposed some experimental tests on the ECLIPSE facility (CELIA, Bordeaux, France) [1.23] in order to study the capability of GEMpix to detect X-ray radiation emitted from various targets (Cu, Fe, Ti, Ni, Ag, and plastic), emitting characteristic k-alpha radiation at different energies and fluence. In order to analyse these measurements, a preliminary study of the detector response in regime of single photon was realized at the NIXT lab to estimate the number of photons per unit area for the different X-ray energies. This was performed using X-ray fluorescence coming from sample materials like those used on the ECLIPSE laser. Obtained results shows the potentialities of GEMpix as soft-X ray diagnostic devices for LPP: its response appears as blobs whose volume and area is proportional to the released charge Q, depending on the number of photons and their energy. Results show also that for a given target, the gain (V_{gem}) can be fixed in order to have all the collected charge over threshold and avoid the saturation of the blob volume. V_{gem} affects also the spatial resolution, and it depends on the energy of the single photon. An estimation of photon fluence has been obtained for the different kind of targets. *Figure 1.20* shows a map of the photon fluence estimated for Iron and Copper target [1.24].
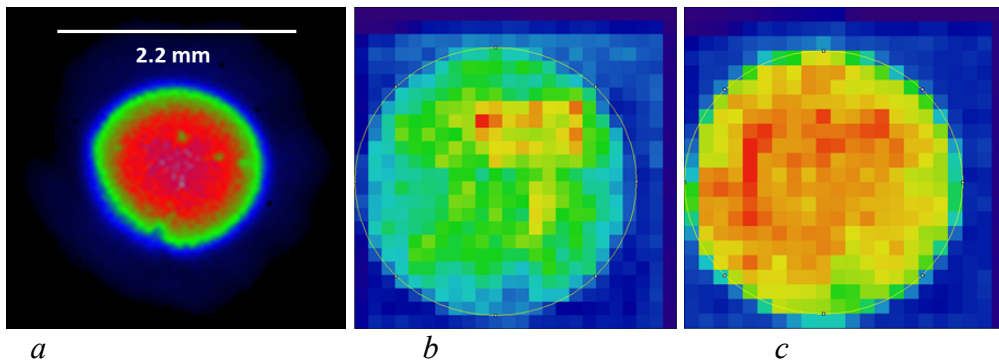

| *a* | *b* | *c* |

Figure 1.20 - Soft-X ray image obtained at the ABC facility with an aluminium target (a) and photon fluence distribution for Fe (b) and Cu (c) target at the ECLIPSE laser facility.

For copper the maximum number of photons ranges between 20 and 25, while for iron between 15 and 20, and 2-3 photons at the edge.

THz Development

The THz-TDS plasma diagnostic project received the EUROfusion Enabling Research award in 2014. On this basis the setup of the laboratory facilities has been accelerated and completed in all areas. In 2015 we tested several versions of the Free Air THz-TS setup, based on a 800 nm MIRA laser driving an Auston switch-type broadband THz emitter (100 GHz-5 THz). The optical designed has been optimised, signal processing, data acquisition and Power Supply systems realized and tested with several type of emitters, receivers, lenses and configuration modes. Typical signals are in the range 0.030-0.3 nA, with an IR laser input power of 0.5 mW, 170 fs pulse duration and 150V bias voltage.

The system is now ready for further improvements, like the use of Off-Axis Paraboloid elements to increase bandwidth and luminosity and for final testing of the Emitter and Receiver optical heads, which will use Silicon THz lenses for increased efficiency.

In parallel the design of the Group Velocity delay compensation section (GVD) has been completed, and it will be assembled and tested in the coming months

At the beginning of the year were taken a series of measurements with an industrial spectrometer TAS7500TS. The optical properties of different materials and components, apt to be used in fusion experiment have been studied. A Python Fourier Transform analysis code has been developed and tested with the aim of releasing a tailored, custom made tool to provide a full understanding of the data. Successful tests have been carried out with data from Clarendon Laboratory in Oxford and Advantest spectrometer.

The implementation of a THz diagnostic has been studied using FTU plasma conditions as benchmark for numerical simulations, comparing the known proprieties of THz radiation with the various diagnostic methods in order to devise the best measurements approach. Interferometry, Reflectometry and Polarimetry will be the first candidate for the application.

Fast Infrared Camera

The relevance of the thermal load measurements during disruptions in a limiter machine relies on the evidence that in a divertor tokamak the plasma configuration degrades to L-mode before the thermal quench.

In FTU plasma column usually leans to the inboard toroidal limiter and during the current quench it is pushed further inboard: therefore the largest heat load are expected to occur on the toroidal limiter. FTU being a cryogenic machine, with all inner surfaces at very low temperature at the onset of a discharge, disruptions represent almost the only possibility of carrying out heat load measurements by thermography.

In year 2015, the optical system, developed some years ago in collaboration with the Italian "Istituto Nazionale di Ottica" (INO), has been refurbished and newly installed in an equatorial port. It consists of 14 Germanium lenses, anti-

Figure 1.21 - Infrared image of the toroidal limiter sector during machine baking

reflection coated in the range 4.0÷5.5 m, and allows transferring the image of one, out of the 12 toroidal limiter sectors, through the port to the thermo camera. The latter is a FLIR model SC7500 capable of an image acquisition frequency of 380 Hz for full frame up to 40 kHz with windowing.

Emissivity calibration for temperature up to about 100 °C was carried out during inner vessel baking by comparison with the temperature measured by thermocouples embedded in the tiles of another toroidal limiter sector (see Fig.1)
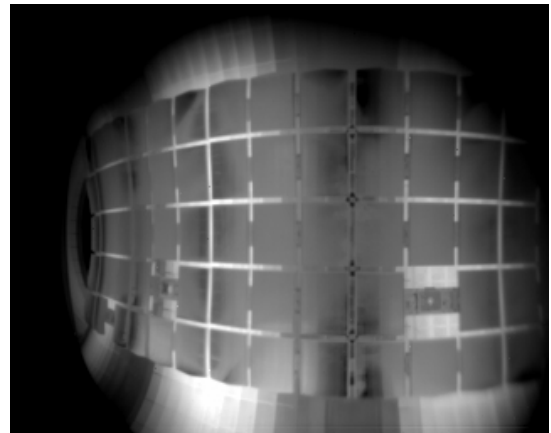
The toroidal limiter temperature was monitored in several disruptions by varying the image acquisition frequency. Quantitative analysis of the data is in progress. One of the drawbacks with thermo graphic measurements, in all-metal machines like FTU, is the reflection of IR light coming from not monitored surfaces. It will be taken into account by using the PFCFLUX code to locate possible sources of reflected light at the moment of the thermal quench onset.

Complementary to the measurement of thermal load on the toroidal limiter is also the detection of frequent and massive presence, during disruption, of eroded or mobilized dust. Its survival in the vacuum chamber for long time after the disruption confirms the indirect detection carried out in the past with Thompson scattering diagnostic [1.25]

1.1.4 – Plasma Theory

Introduction

Investigations of nonlinear behaviours in burning plasmas of fusion interest by formal analytical work and numerical simulations are the subjects of most significant recent progress of theoretical activities. These are accompanied by studies of radio-frequency wave propagation and absorption as well as of space and astrophysical plasmas. Most activities on nonlinear burning plasmas have been carried out within the framework of the "Enabling Research" project AWP15-ENR-01/ENEA-03 on *Theory and simulation of energetic particle dynamics and ensuing collective behaviors in fusion plasmas*" (shortly NLED, *NonLinear Energetic particle Dynamics*): in this section the activities developed primarily in ENEA-Frascati will be presented in an extended form. The complete report of the full NLED project, which includes research activities jointly pursued in collaboration with CEA Cadarache and IPP Garching and Greifswald, with the support of the Consortium EUROfusion, is presented in a separate Section (**Enabling Research**). Other important theoretical activities have been devoted to Integrated Tokamak Modeling, and are also reported in a dedicated Section (**WP - Code Development**).

Hereafter, the first section addresses basic fusion plasma physics issues. In particular, it gives updates on the probabilistic derivation of a parametric equilibrium distribution function; and addresses the general problem of n cold beams self-consistently evolving in the presence of m (greater or equal to n) Langmuir modes at the plasma frequency, formulated in Hamiltonian form. It also provides a theoretical-analytical description of the spontaneous excitation of convective cells by kinetic Alfvén waves, and a reconsideration of the asymptotic approach to the m=1 resistive mode for tokamak plasma. Aspects involving nonlinear dynamics and complexity are addressed in the second section, while the third reports about recent results obtained for radio-frequency wave propagation and absorption, with particular emphasis on lower hybrid wave heating and current drive for ITER and DEMO. Energetic particle physics are discussed in the fourth section, which deals, in particular, with theory of beta-induced Alfvén modes excited by energetic ions, and fast excitation of geodesic acoustic modes by energetic particle beams; moreover, the structure of wave-particle resonances and the relation to Alfvén mode saturation is addressed in detail using Hamiltonian mapping techniques; and the linear and nonlinear dynamics of electron fishbones is studied using the hybrid MHD-gyrokinetic code HMGC. The last section, meanwhile, addresses morphological aspects of the transport processes characterizing stellar accretion disks, in analogy to the phenomenology of the Tokamak devices.

Many of these activities are being pursued in the framework of international collaborations with University of California at Irvine (UCI), the Institute for Fusion Theory and Simulation

(IFTS), Zhejiang University, as well with the Sapienza - University of Rome and the Physics Department, Technical University of Denmark.

Basic fusion plasma physics

Updates on parametric equilibrium distribution function. A class of parametric distribution functions has been proposed in [1.26] as equilibrium distribution functions (EDFs) for charged particles in fusion plasmas, representing supra-thermal particles in anisotropic equilibria for Neutral Beam Injection, Ion Cyclotron Heating scenarios. Moreover, the EDFs can also represent nearly isotropic equilibria for Slowing-Down alpha particles and thermal plasma populations. These EDFs depend on constants of motion (COMs). Assuming an axisymmetric system with no equilibrium electric field, the EDF depends on the toroidal canonical momentum P_ϕ, kinetic energy w and the magnetic moment μ.

In [1.27] it has been proposed a method of probabilistic nature, for expressing the particle distribution function in an analytical form starting from reasonable simple assumptions. Once obtained the EDF depending only on COMs, it is also found, for consistency, a collisional operator that can allow the distribution of particles to relax towards the proposed EDF. Thus, it has been described what can be the minimum changes for the Landau collision operator to allow the proposed EDF to be the relaxed distribution function for a thermal plasma population.

In such probabilistic approach for obtaining the EDF functional form, the maxwellian distribution function is considered as the prior probability distribution function (pdf) in the Bayes's theorem. At the same time, the joint distribution function to find a particle with given P_ϕ, w and $\lambda = \mu/w$ is considered the final EDF expressed as the product of the conditional probability, to have such P_ϕ and λ once the energy of the particle is known, multiplied for the prior pdf.

Four EDFs have been explicitly obtained depending on if (i) the mean magnetic moment is almost constant for particles with different energies, or (ii) it scales in magnitude with the particle energy, and if (iii) a Maxwellian or (iv) a Slowing Down is considered as prior pdf. These EDFs can be used in the following scenarios: burning plasmas with fusion products and plasmas in thermal equilibrium or when external heating sources, i.e. Ion Cyclotron Resonance Heating or Neutral Beam Injection, are employed.

The relevance of the present derivation resides in its generality since it only requires the (non perturbative [1.28]) Guiding Center transformation of phase space coordinates and an axisymmetric equilibrium magnetic field. Moreover, such derivation doesn't depend on the detailed form of the axisymmetric magnetic field. This means that the derived functional form of the EDF is machine independent for axisymmetric tokamak.

Nonlinear Physics of Energetic Particle and Transport Features of the Beam-Plasma instability. The transport features of a one-dimensional (1D) beam-plasma system were studied in the presence of multiple resonances. The relevance of the beam-plasma instability problem [1.29] stands in the paradigmatic description it can provide for energetic particle (EP) transport due to Alfvén eigenmodes (AEs). In particular, a correspondence can be determined between velocity space transport due to beam heating and EP radial transport in the presence of resonantly exited AEs (as far as the nonlinear particle displacement is small compared to the perpendicular fluctuation scale).

The investigation of the 1D bump-on-tail problem was proposed [1.30] in terms of n cold beams injected in a cold background plasma behaving as a linear dielectric medium, and m≥n self-consistently coupled nonlinear oscillators. Such a scheme properly represents the features of a warm fast particle distribution interacting with a spectrum of linear stable (absence of particle drive) and unstable Langmuir waves at the plasma frequency. This approach can

properly describe the case of isolated resonances as well as the quasi-linear diffusion regime typical of a broad fluctuation spectrum.

The model was specialized for the case of two supra-thermal beams, and a threshold for the initial beam velocity ratio was determined, in correspondence to which the two instabilities, rather than remaining isolated resonances, mutually interact transferring energy from the mode associated with the faster beam to the slower one. In this case, significant phase-space mixing takes place between the two beam populations. Furthermore, it was shown how sideband modes might saturate at almost the same level reached by the most unstable waves, pointing out that the long time-scale evolution would be significantly affected by nonlinear sideband generation.

The mixing process was studied to quantitatively define the transport barriers of the system by means of the so-called Lagrangian Coherent Structures (LCSs). These structures are 1D curves (in our system) and are defined maximizing the Finite Time Lyapunov Exponent (FTLE) fields [1.31]. Phase-space mixing was found (see *Figure 1.22*) to be enhanced at the intersections between LCSs belonging to different beam populations.

The threshold for transport onset and the resulting critical value for the beam initial velocity ratio was found to be ~ 0.96 (for the present simulation parameters). It is consistent with previous estimations for a supra-thermal warm beam and it fulfils the Chirikov criterion.
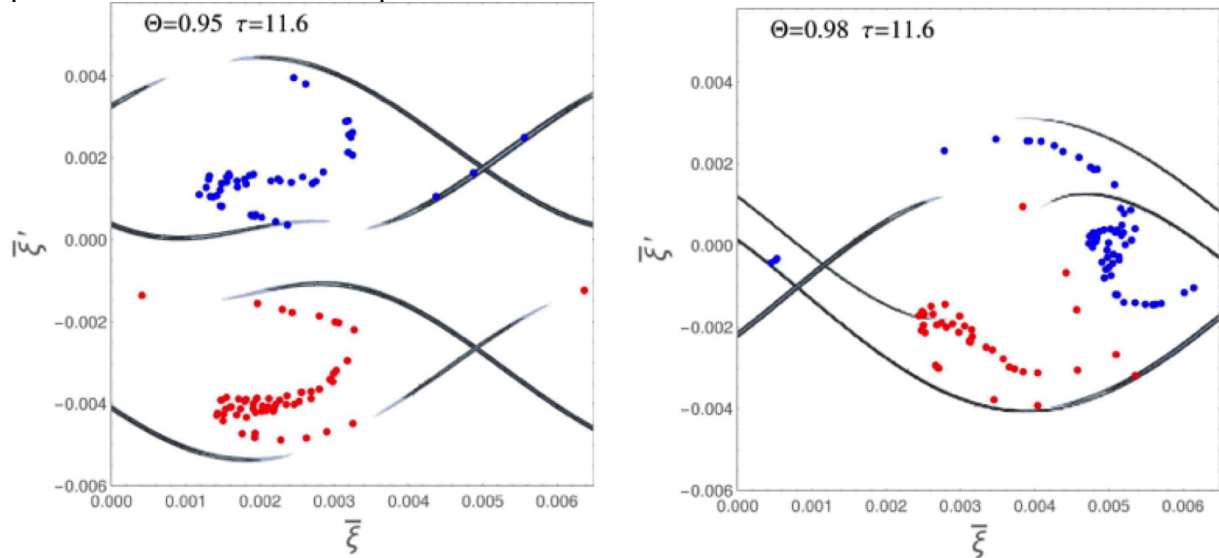

Figure 1.22 - Overlay of the phase-space snapshots (blue and red points for the fastest and slowest beam, respectively) and the LCSs (thick lines) defined trough the contour plot peaks of the FTLE. The beams have equal densities, the considered time is set as τ = 11.6. The different values of the beam initial velocity ratio Θ are indicated in the plots

Spontaneous excitation of convective cells by kinetic Alfvén waves. Kinetic Alfvén waves [1.32] (KAW) and convective cells (CC) are prevalent and fundamental electro-magnetic waves and structures in magnetized plasmas. Spontaneous excitation of CC by KAW has been of interest for many years [1.33] due to its important implications to transport across the confining magnetic field, and to the dynamics of the upper auroral ionosphere. In recent years, it has received renewed interest since zonal flow and zonal current/field or, generally, zonal structures [1.34, 1.35], which could regulate plasma turbulence and, thereby, the associated transport, have direct correspondence, respectively, with electrostatic CC (ESCC) and magnetostatic CC (MSCC). Thus, CC excitation by KAW can be considered as a paradigmatic example of zonal structure generation by turbulence in magnetized plasmas, and of structure formation effect on fluctuation-induced cross-field transport. Spontaneous excitation of CCs by KAW in uniform plasma is investigated analytically employing the nonlinear gyrokinetic equations. Self-consistent theoretical analysis demonstrates the novel

results that excitation via modulational instability can only occur when the finite ion Larmor radius effects are properly included, and, furthermore, both the ESCC and MSCC are excited simultaneously. Theoreti-cal predictions are verified with direct numerical simulations; showing excellent agreement in the modulational growth rate and field structures. Significant implications of the present results to the cross-field transport in space and fusion plasmas are also briefly discussed [1.36].

Analysis of MHD instabilities by asymptotic methods.

The m=1 resistive mode for a tokamak plasma with large aspect ratio [1.37] is reconsidered employing a different analytical approach [1.38, 1.39]. The dynamic equations in a resistive layer are solved by means of an asymptotic expansion for values of the growth rate in a suitable range. The eigenvalues characterizing the perturbation are found by means of a series expansion. It is shown that the main contribution to the expression of the eigenvalues is given by the first and the second order term of this expansion. We find stable and unstable solutions at the first and second order.
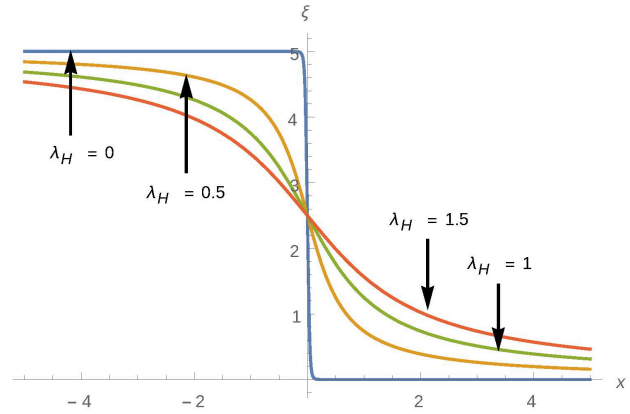

Figure 1.23 - Profiles of the radial displacement eigenfunction for different values of the ideal instability parameter as defined in [1.32]

Eigenfunctions found for different values of the ideal instability parameter are shown in *Figure 1.23*.

Nonlinear dynamics and complexity

Studies of complexity in extended dissipative systems, in nature and in laboratory, require multiple approaches and the framework of self-organized criticality (SOC) has been used extensively in the modelling of such non-equilibrium systems. SOC is a paradigmatic concept of statistical mechanics that describes an attractor state of a driven, open system in which an instability threshold is present, and that exhibits scale-free, divergent dynamics up to the cutoff imposed by finite-size effects. In magnetically confined fusion plasma, SOC has been proposed as an alternative to the turbulence theoretical framework to explain and control the large levels of transport and heat across the magnetic field lines, known as anomalous transport, and the associated intermittent character of the energy release that is often found to occur in bursts with a waiting time distribution. The role of SOC in advancing our understanding of space and laboratory plasmas as non-equilibrium complex systems has been reviewed in [1.40, 1.41]. The main emphasis is on how SOC and related approaches have provided new insights and models of non-equilibrium plasma phenomena. In [1.42] a new kind of complexity process is proposed, which brings together the theoretical concept of SOC and that of two-dimensional fluid (or fluid-like, such as the electrostatic drift-wave) turbulence, unifying them in one description. This work is built around the idea that some systems do not develop a pure critical state associable with SOC, since their dynamical evolution involves as a competing key factor an inverse cascade of the energy in reciprocal space. Then relaxation of slowly increasing stresses will give rise to intermittent bursts of transport in coordinate space and outstanding transport events beyond the range of applicability of the "conventional" SOC. Also the work in [1.42] is concerned with causes and origins of so-called non-local transport in magnetized plasma, for which there are no simple flux-gradient relations, nor familiar coefficients such as the usual diffusivities and conductivities, and which constitutes one outstanding "hot" topic in contemporary fusion

research. It is argued using the idea of SOC-turbulence coupling that non-local transport occurs through amplification (and amplification of amplification) of unstable fronts in the presence of absorbing boundary at the plasma edge. More so, it is proposed based on the familiar Hasegawa-Wakatani model of the drift-wave turbulence that the phenomena of SOC-turbulence coupling occupy the so far largely unexplored regime of strong nonlinearity and time scale separation when the Rhines time in the system is small compared with the instability growth time. The idea that self-consistent strong turbulence may amplify SOC via coupling to the inverse cascade is theoretically very general and is not restricted to (although greatly motivated by) the realm of fusion research. In fact it may be used as a proxy to understand the events of anomalously large size spanning phenomena as diverse as magnetospheric storms, climate disruptions, huge solar flares and outstanding coronal mass ejections [1.40]. Research over these issues is under way for comparison with the analytical predictions.

Radio-Frequency wave propagation and absorption
Quasi-linear modeling of Lower Hybrid current drive in ITER and DEMO: numerical and analytical studies. The active control of the radial current density profile is one of the major issues of thermonuclear fusion energy research based on magnetic confinement. Lower hybrid (LH) waves at several GHz could in principle be efficiently used, but the fact that electron temperature at reactor pedestal is too high for allowing efficient penetration of the coupled RF power due to the strong linear Landau damping, could prevent the current profile control over the desirable radial domain. On the other hand, the high density of thermonuclear plasma requires the grill to launch LH waves with parallel wavenumber greater then the critical one, in order to satisfy the accessibility condition. Analytical and numerical results, based on the quasilinear theory, demonstrating that lower hybrid waves at several GHz can efficiently drive current in the outer radial half of a reactor plasma by using suitable power spectra, have been performed. This analysis has been carried out by means of the code "Raystar", a numerical tool that includes and integrates several modules: i) "LHPI", for parametric decay instability analysis at the plasma edge, ii) "Grill3D" for establishing the coupled spectrum, iii) "RayLH", to account for the evolution of wave trajectory and the calculation of the quasilinear diffusion coefficient, iv) "FokPla" to determine the 2D (in velocity space) equilibrium electron distribution function in presence of the LH waves, including electron trapping. The results of this analysis, performed for the expected plasma parameters of ITER (Scenario 2 and 4) and DEMO (Pulsed and Steady State), demonstrate the key role of the $n_\parallel$ antenna spectrum as well as the antenna location (e.g., in the high field side) in determining the LH power penetration to the core of thermonuclear plasmas. An antenna spectrum with sufficiently narrow principal peak at the minimum accessible $n_\parallel$ moderates the strong absorption expected in a high temperature plasma (which however remains single-pass), and allows the wave to reach inner layers. PAM (passive-active multi-junction) antennas realistically designed for ITER and DEMO have been considered; the peak of the power spectrum and the spectral width can consistently be obtained by suitably feeding and phasing the waveguide of the PAM antenna in order to get a fine control of the radial deposition profile. Wave propagation and quasilinear damping of LH waves have also been studied analytically, supporting the above numerical approach. The combined analytical solution of ray tracing, amplitude transport equations and time dependent 1D Fokker Planck equation, in fact, illuminates and explains features of the quasilinear approach and the key role of the wave spectrum for the LH power deposition profiles [1.43, 1.44].
High Frequency waves in plasmas: an asymptotic approach. The equations describing the propagation of an electromagnetic wave in tokamak plasma are more manageable when the frequencies of the electric field are much higher than the electron cyclotron frequency in the

plasma. In this framework an application of asymptotic methods is quite appealing if we consider the formulation as given in the Babich's textbook, (Babich and Buldyrev, Asymptotic methods in short-wavelength diffraction theory, Alfa Science, Oxford, 2009). Applying these methods we find the Hamilton-Jacobi equation and the transport equation. The Hamilton-Jacobi equation can be easily solved while the transport equation can be solved iteratively. So we find the amplitude of the electric field at any order of the expansion. This analysis is particular useful in order to predict the behaviour of the broadband terahertz (THz) pulse in a non-uniform and dispersive plasma. It is mainly oriented to a new plasma diagnostic system based on THz time-domain spectroscopy that simultaneously provides high time resolution and THz bandwidth coverage, allowing an analysis of wide ranges of plasma density variations without incurring opacity [1.45].

Complex Maslov germs and high frequency Gausian beams in a cold plasma in a toroidal region. We consider a system of PDE describing cold plasma in a toroidal region in three-dimensional space. This system simulates the passage of a laser beam through the TOKAMAK, it consists of 9 equations for the electric field and velocities of electrons and ions in a given magnetic field. Asymptotic solutions describing high-frequency Gaussian beams are constructed using the theory of Maslov's complex germs in a fairly effective form. The solutions of the system are localized in the neighbourhood of the beam passing through the toroidal domain (the camera). The equations for the ray take into account the density of particles in the camera and don't "feel" the presence of the magnetic field because of the high frequency of the Gaussian beam; the dependence on the magnetic field is contained in the amplitude of the electric field. Before entering in the TOKAMAK camera the amplitude of the Guassian beam is the same as in the free space, but after the camera the amplitude vector rotates under the influence of the magnetic field and the formula for the angle of rotation is given explicitly. An analytical-numerical algorithm based on the asymptotic solutions is used to analyse the parameters of the magnetic field in the TOKAMAK[1.46,1.47].

Hamiltonian approach in ray tracing LH wave propagation in tokamak plasmas

In our recent work "Analysis of the chaotic behavior of the Lower Hybrid Wave propagation in magnetised plasma by Hamiltonian theory", submitted to the journal Entropy, we have investigated the Hamiltonian character of the ray tracing equations describing the propagation of the Lower Hybrid Wave in tokamak in order to study the evolution of the parallel wave number $n_{\parallel}$ along the propagation path. The chaotic diffusion of the "time averaged" parallel wavenumber at higher values (with respect to that launched by the antenna at the plasma edge) has been evaluated, in order to find an explanation of the filling of the spectral gap by "Hamiltonian chaos" in the Lower Hybrid Current Drive (LHCD) experiments. We have shown in our work that the increase in $n_{\parallel}$ due to the toroidal effects, in the case of the typical plasma parameters of the FTU experiment, is insufficient to explain the filling of the spectral gap and the consequent Current Drive and another mechanism must come into play to justify the wave absorption by Landau damping. In fact, although previous works by several authors have tried to solve the problem of the spectral gap by the Hamiltonian theory, a complete agreement on the results is still missing. Here we focused on the multi-pass regime, in which a LH wave injected from the edge of the plasma experiences a large number of radial reflections. In this situation, the nonlinear effects, which come from the non-linear ray equations (Hamilton equations), can play a role in the chaotic evolution of the dynamical system. This chaotic evolution of the trajectory can be associated with a chaotic diffusion of $n_{\parallel}$. We have studied the effect of toroidal geometry on the wave propagation as a small perturbation to cylindrical geometry through the small inverse aspect ratio and we have applied the canonical perturbation theory to the LH Hamiltonian/dispersion relation to investigate the presence of resonances between the frequencies of the system. The result of our analysis performed on the integrable, cylindrical case, perturbed to first order in the small

inverse aspect ratio by toroidal effects, is that the perturbation doesn't give rise to resonances. On this theoretical bases, we could exclude the possibility of chaos in the ray propagation. Analytical calculations have been supplemented by a numerical algorithm based on the symplectic integration of the ray equations implemented in a ray tracing code, in order to preserve exactly the symplectic character of a Hamiltonian flow. The results of the simulations show that, in the range of parameters typical of LHCD experiments performed on FTU, the dynamics of the system remains regular, and the increase in, due to toroidal effects, is insufficient to justify the wave absorption by Landau damping. Only in the unrealistic high density case [ne>10^{14}cm^{-3}], the system reveals a chaotic behaviour, and has a large increase.

Collisions influence on parametric instabilities induced by LH waves in tokamaks

The injection of lower hybrid wave power, in addition to the bootstrap current, can provide a fully active control of the current density profiles [1.48]. However, in high density plasmas, relevant for fusion reactors, parametric instabilities (PI) at the plasma edge can prevent the wave power penetration unless the electron temperature and the density gradient are sufficiently high [1.49].

In modelling the parametric instabilities produced in LHCD experiments, the presence of collisions has been neglected so far. In 2015, a specific collisional parametric dispersion relation has been developed for the first time, based on a kinetic equation for the particle distribution functions with particle conserving collision operator [1.50]. Numerical solutions show that in cold plasma regions the collisions prevent the

Figure 1.24 - Contour plot of the ratio of collisional and collisionless PI growth rates of LH sidebands at parallel refractive index N//=10 in ITER (coupled LH wave parameters fo =5 GHz, P = 3.3 kW/cm2, N//,o=1.85)

onset of the parametric instabilities. In present day experiments, the collisional suppression of PI can explain why the LHCD efficiency is not reduced when gas injection near the antenna mouth is performed to improve the coupling of the LH waves, despite the local drop of the electron temperature. In fusion reactors, relative low electron temperature with flat profiles and relative low density gradient are expected to occur in the far SOL. For ITER scenarios, electron temperature as low as Te = 11.7eV is predicted along a distance of 12 cm from the wall, and the e-folding length for the density profile is expected in the range 4-5 cm. In such conditions, the PI prevent the LH power penetration, following the collisionless model. The collisions determine PI suppression, as shown in *Figure 1.24*.
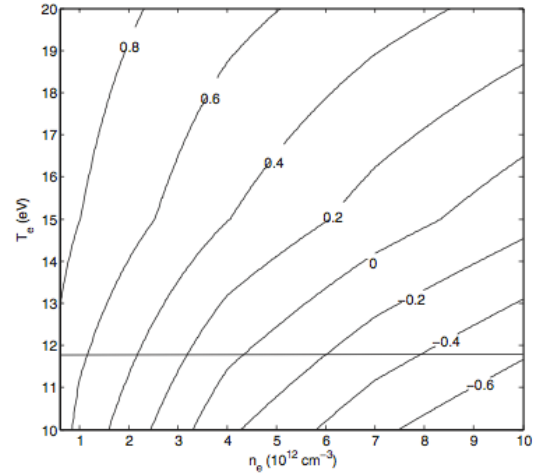
Energetic particle physics

Global theory of beta-induced Alfvén eigenmodes excited by energetic ions. The two-dimensional global stability and mode structures of high-n beta-induced Alfvén eigenmodes excited by energetic ions in tokamaks are examined both analytically and numerically, employing the WKB-ballooning mode representation along with the general fishbone like dispersion relation [1.51, 1.52]. Here n»1 is the toroidal mode number. Theoretical results indicate that (i) the lowest radial bound state corresponds to the most unstable eigenmode, and (ii) the anti-Hermitian contributions due to wave-energetic particle resonance give rise to the twisting radial mode structures [53[3]. More precisely, analytical and numerical analyses demonstrate that, when the non-perturbative EP wave-particle resonant effect is considered, the BAE is radially localized by the EP-pressure-gradient drive and the lowest bound state is most unstable. Furthermore, the BAE exhibits the typical twisting radial mode structure in

contrast to the ideal MHD limit with up-down symmetry. The present results offer specific theoretical explanations for the experimental and numerical simulation observations of the BAE asymmetric mode structures in the poloidal plane, and more generally of other Alfvén eigenmodes, when the EP drive is sufficiently strong.

Fast excitation of geodesic acoustic mode by energetic particle beams. A new mechanism for geodesic acoustic mode (GAM) excitation by a not fully slowed down energetic particle (EP) beam is analyzed to explain experimental observations in the Large Helical Device (LHD). It is shown that the positive velocity space gradient near the lower-energy end of the EP distribution function can strongly drive the GAM unstable. The new features of this EP-induced GAM (EGAM) are: (1) no instability threshold in the pitch angle; (2) the EGAM frequency can be higher than the local GAM frequency; and (3) the instability growth rate is much larger than that driven by a fully slowed down EP beam [1.54]. A recent paper by Ido et al. [1.55] presented experimental evidence in LHD, where EGAM is observed during tangential neutral beam injection, and some peculiarities ap-pear in the comparison with theoretical predictions. The EGAM is excited before the injected NBI is fully slowed down, and the EP birth energy (~170 KeV) is much larger than that predicted for wave-particle resonance; thus, earlier theories based on a fully slowed down NBI cannot be directly applied here [1.56, 1.57]. Here, theory explains why EGAM is excited by a not fully slowed down EP beam, with the EP distribution function being a function of time. The instability drive comes from the positive veloci-ty space gradient in the low-energy end of the EP distribution function, similar to that of a bump-on-tail distribution. The EGAM excited by such an EP beam can be applied to explain the experimental observations in LHD [1.55]. For the sake of clarity, only the local dispersion relation of EGAM is consid-ered while neglecting system nonuniformity and higher order effects, such as finite Larmor radius. Modulation of EP distribution function due to the excitation of EGAM is not taken into account either; thus, this work presents the linear theory of EGAM excitation by EP distribution function peculiar to the LHD scenarios. For the sake of simplicity, the helicity of the device is ignored and large aspect ratio is assumed, consistent with the experiment observation in the center of the device using heavy ion beam probe.

Structure of wave-particle resonances and Alfvén mode saturation. Understanding the properties of energetic particle (EP) confinement strongly rely on the comprehension of nonlinear Alfvén mode dynamics (which saturation level is expected for the mode amplitude and which effects on EP confinement). We have focused our analysis on nonlinear wave-particle interactions. Two extreme limits concerning nonlinear wave-particle dynamics have been already widely investigated: weakly driven Alfvén Eigenmodes (e.g. Toroidal Alfvén eigenmodes) close to marginal stability, for which mode saturation is due to phase mixing of resonant particles trapped in the potential well of the wave and the radial excursion of EPs is very limited so that the system is treated uniformly, this fact may result in the formation of phase-space holes and clumps and adiabatic frequency chirping due to resonant frequencies following hole and clump propagation; strongly driven Energetic Particle Modes (EPMs), for which saturation reaches because of macroscopic distortion of the EP pressure profile. The analysis of the intermediate situation (moderately unstable modes) has not yet been the object of adequate efforts. In our work, nonlinear dynamics in such intermediate regime has been investigated by means of the nonlinear hybrid magnetohydrodynamics gyrokinetic code (XHMGC) [1.58, 1.59].

Gap modes. A detailed analysis of resonant interactions between the mode and particles has been performed by using a state-of-the-art phase space numerical diagnostic method based on the Hamiltonian mapping [1.60]. Saturation mechanism, due to resonance detuning and/or radial decoupling, have been identified. It has been shown that saturation field level exhibits a

quadratic scaling with the growth rate, in the former case, a linear scaling, in the latter case (*Figure 1.25*).
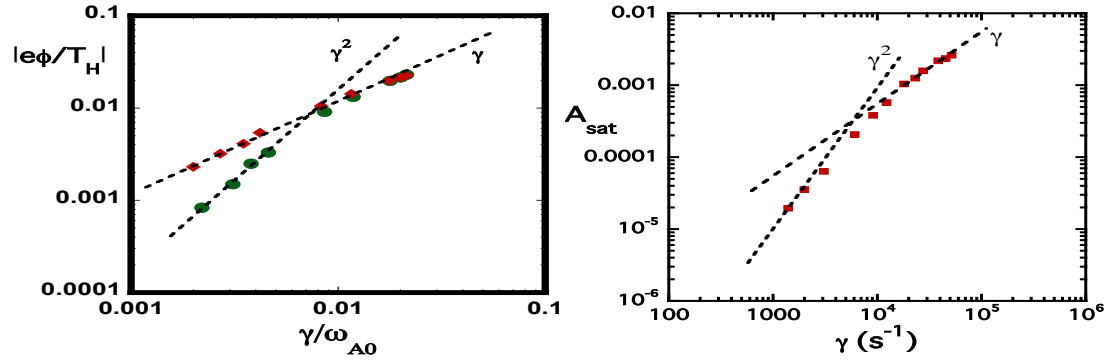

Figure 1.25 - Left: scaling of saturation amplitude of scalar potential versus mode growth rate for a reference Beta induced Alfvén Eigenmode driven by co-passing (diamonds) or counter-passing (circles) energetic ions [1.61]. The two cases are characterised by similar mode structures, but very different radial dependence of the resonance frequency; saturation occurs for radial decoupling in the former case, while a transition from resonance detuning to radial decoupling is observed in the latter case. Right: an analogous transition observed by HAGIS-LIGKA [1.62, 1.63] TAE simulation

The dominance of one or the other mechanism depends on the linear properties of the mode (in particular, the growth rate, the spatial structure and the radial dependence of the resonance frequency).

Energetic particle modes. Frequency chirping related to EPM's saturation has been observed both in experiments and simulations (e.g. chirping electron-fishbone by XHMGC simulation [1.64]). Phase locking has been proposed, within "fishbone" paradigm, to describe such chirping: the resonance condition with linearly resonant particles is maintained, while particles are radially displaced, through a continuous modification of the mode frequency. We have shown that an additional scenario is possible: mode radial localization and frequency appear to be locked to the shear Alfvén continuum; once the linear resonance population has exhausted its driving capability (because of local flattening of the phase-space distribution function), the mode looks for non-exhausted (non-zero gradient) regions of the phase space. The effect is a succession of resonant contributions from different phase-space regions (each characterized by a different flattening time), rather than mode adjustment to the evolution of the linearly-resonant particles.

Linear and nonlinear dynamics of electron fishbones. The fishbones modes are internal kink (m,n)=(1,1) instabilities induced by fast particles. Ion fishbones (internal kink induced by fast ions) were first observed in the PDX machine with a density profile of the energetic particles peaked on axis. More recently, electron fishbones (internal kink induced by fast electrons) were observed with both a density profile of the energetic electrons peaked on axis and peaked off axis. In both cases, the observed mode frequency was found to be consistent with the precession frequency of deeply trapped energetic particles for on axis density profile and the reversed precession frequency of barely trapped/circulating energetic particles for off-axis density profile. The numerical approach has been applied to study electron fishbones with a density profile of the energetic electrons peaked on axis [1.64] and with a density profile of the energetic electrons peaked off axis [1.65, 1.66]. The study has been carried on with the XHMGC code [1.58]: the possibility of inducing the electron fishbones is demonstrated in both cases and thanks to the numerical approach, the saturation process is analyzed in detail. Concerning the linear dynamics studies, the different fraction of energetic particles involved for the on axis density profile and off axis density profile was confirmed: particles involved are trapped particles in the former profile and barely trapped/circulating particles for the latter one. To fulfill the instability condition [1.67], the mode propagates poloidally parallel to the

bulk electron diamagnetic direction for the peaked on axis profile and parallel to the bulk ion diamagnetic direction for the peaked off axis profile. About the non-linear dynamics, it has been studied using the test particle Hamiltonian mapping technique [1.60]; the test particle coordinates are evolved in the fields computed in a previous self-consistent simulation allowing a detailed study of the dynamics properties. In fact, the energetic particles driving the mode, can be represented in a (Pφ,Θ) Poincare phase space, where Pφ is the toroidal canonical momentum and Θ the wave phase seen by the particle.
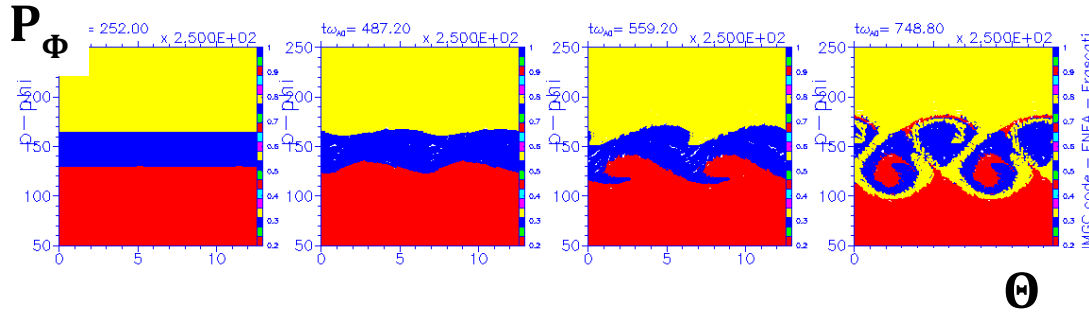
Figure 1.26 - Energetic particles, driving the electron fishbone, are represented with different colors in the (P$_\varphi$,Θ) Poincare phase space. The colors depend on the position of the particles with respect to the resonance radial position. In this case, there are two resonances. As the saturation condition is reached, particles exchanges position, showing penetrating structures and wave particle trapping

In *Figure 1.26*, for example, the non-linear dynamics is represented for an off-axis density profile. As the saturation process keeps on, it is readily apparent the formation of mutually penetrating structures that give rise to flattening of the density profile of the energetic particles. Density flattening, reducing the free energy source, contributes to the mode saturation.

Space and astrophysical plasmas. This line of research is devoted to understand the cross-fertilization features between the behaviour of laboratory and astrophysical magnetized plasmas, especially in view of their axial symmetry. In particular, we analyze morphological aspects of the transport processes characterizing stellar accretion disks, in analogy to the phenomenology of the Tokamak devices.

In [1.68], the behaviour of the magneto-rotational instability in axial symmetry for a non-thin structure is addressed, in order to characterize the role played by the co-rotation theorem in fixing the parameter and space regions where the instability emerges. The study is performed using the magnetic flux function as the basic dynamical variable, and restricting the perturbation structure in order to select the Alfvén nature of the Magneto-Rotational Instability, i.e., we require that the plasma be incompressible and that the perturbations propagate along the background magnetic field. The main result coming from this analysis is that the instability condition retains the same form as in the case of a thin configuration (thin disks are commonly observed in astrophysical systems), i.e., the axial dependence of the background enters only parametrically and does not intrinsically affect the stability properties.

In [1.69], the behaviour of the gravostatic equilibrium for a perfect fluid on a Kerr space-time is investigated in detail. The aim of this approach is to determine the density profile and the stable and unstable configurations around a rotating back hole or very compact object. The important merit of this paper is to demonstrate the existence of ring-like matter distribution, compatible with the morphology of accretion scenarios (here characterized via the link existing with between the steady configuration and the horizon surface). This result provides a very significant hint on the observed formation of ring-like structures in accreting systems, such as nebulae around a Neutron Star. The generalization of this result in the presence of a sufficiently strong magnetic field call attention to understand if the corresponding confinement can play a relevant role in fixing the plasma distribution scenario.

WP - Code Development. The activities carried on under this Work Package mainly continue the ones developed in the Frascati Laboratories last year. They belong to the following subprojects: ACT1. Equilibrium and Stability chain, and Free boundary equilibrium code CLISTE, ACT6. Benchmark non-linear codes for fast-ion MHD interaction, ACT7: Adaptation of core-edge and edge codes.

Equilibrium and Stability chain. The development of a linear MHD stability chain toolset in the WPCD platform was aimed at providing a unique valuable instrument for the MHD stability analysis of equilibria from present EU devices and also future machine such as ITER, JT60-SA and DEMO. The toolset was developed in Kepler and the resulting workflow can be used in equilibria with/without separatrix offering interchangeability of some of the equilibrium and MHD stability codes.

In the EQSTABIL Kepler workflow, a custom "actor" extracts, from full domain equilibrium with a separatrix, a nested closed flux surface equilibrium with plasma boundary flux at selected fraction of the separatrix flux. The workflow includes HELENA, CHEASE and CAXE equilibrium codes and ILSA, MARS, MARS-F and KINX linear MHD stability codes. The modular approach allows interchangeability of the codes for compatible equilibrium metrics e.g. ILSA/MARS/MARS-F, compatible with CHEASE/HELENA. KINX, capable of addressing plasmas with separatrix, is limited to using a custom made quasi-polar quadrangular grid adapted to nested magnetic surfaces provided by CAXE. The whole package was assembled during 2015 for usage with the 4.10a3 schemas and UAL dataversion. The workflow went through a thorough verification and benchmarking of its MHD codes for AUG and JET shots (in collaboration with JET1, MST1), addressing code convergence with poloidal harmonics, grid resolution and growth rate dependence on radial location of a conformal conducting wall [1.70].

The specific activity in Frascati has been related to implementing and maintaining the linear MHD solver MARS [1.71] in the above mentioned EQSTABIL workflow, and providing specific benchmarks and documentation.

Free boundary equilibrium code CLISTE. As a first aim this year, we wanted to make CLISTE work with data plus signal identifier in arbitrary order. The beneficial part of the found solution is that it will be possible to have a single version of CLISTE instead of two, one compiled on the Gateway, and the other on AUG computers. This was possible because the main difference between the two versions was in the part that was reading the data and the signal identifier. A decision was made to develop a couple of Fortran modules with the same interface, basically composed of routines with same name and same arguments (except some initialization routines). Basically one module will read data from WPCD CPOs, while the other will read data provided by the AUG machine as it is working now. As a first step a module was written which is able to read magnetic data provided by AUG, while an adaptation is under way to make the existing module that accesses Gateway data to have the same interface as the previous one. Conditional compilation can be employed to compile CLISTE on the Gateway or on AUG.

A second aim was to change the way CLISTE read the code parameters, and for this purpose a module that read them from an XML file has been also prepared. Both aims have to be continued in the following years.

Linear benchmarks between the hybrid codes HYMAGYC and HMGC. The verification of the non-linear code HYMAGYC, the new Hybrid MHD-Gyrokinetic code for fast-ion and MHD interaction, was pursued in 2015 [1.72] on the so-called TAE n=6 ITPA Energetic Particle (EP) Group test case [1.73] for linear benchmark. The code HYMAGYC is suitable to study EP driven Alfvénic modes in general high-β axisymmetric equilibria, with perturbed electromagnetic fields fully accounted for.
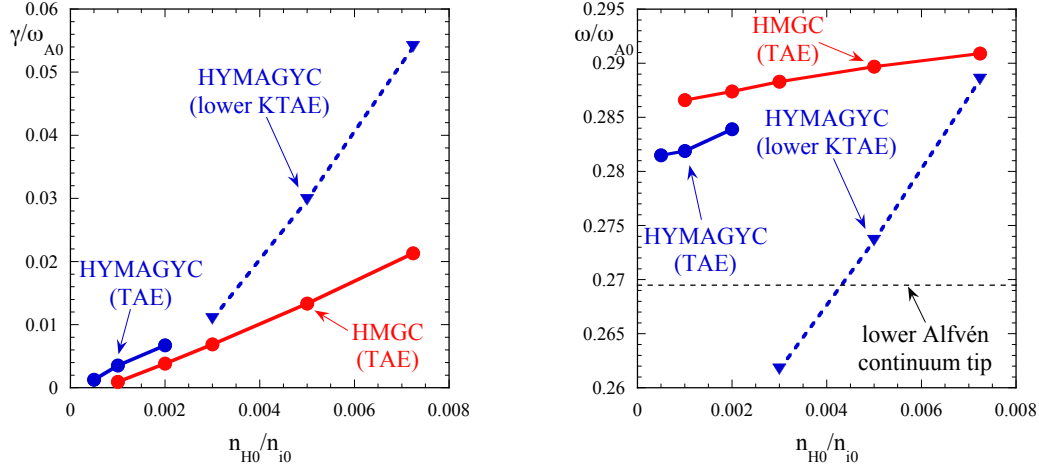
Figure 1.27 - Normalized growth rates (left) and frequencies (right) as a function of n_{H0}/n_{i0}.

An extensive benchmark against the code HMGC [1.58], which solves the reduced MHD equations for the bulk plasma and drift-kinetic equations for the EP species, was pursued: to this purpose, the gyrokinetic equations solved by HYMAGYC have been reduced in order to satisfy the same limits of validity of the HMGC ones. After a characterization of the MHD spectrum, the results of the EP drive have been considered, varying first EP density n_{H0}.

In order to ensure numerical stability in HMGC, a value of resistivity corresponding to the inverse Lundquist number $S^{-1} = 10^{-6}$ has been assumed for both codes. At low values of n_{H0}/n_{i0} (w.r.t. the reference ITPA benchmark case value $n_{H0}/n_{i0} = 7.20655 \times 10^{-3}$, n_{i0} being the on-axis bulk ion density), frequencies and growth-rates are very similar (see *Figure 1.27* right and left respectively, circle symbols) corresponding to a mode localized in the toroidal gap,
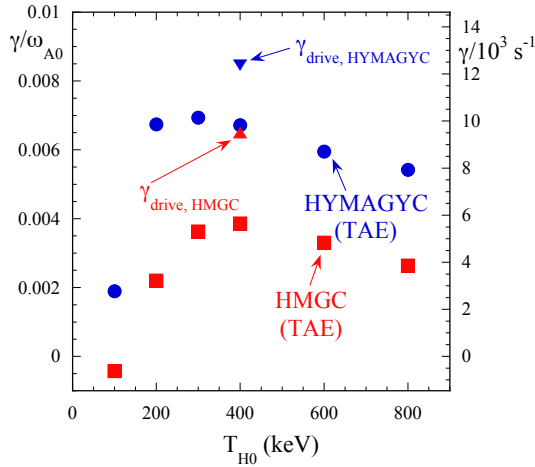

Figure 1.28 - *Normalized growth rates (left axis) versus TH0 at $n_{H0}/n_{i0} = 2.\times10^{-3}$; right axis reports the growth rates in $10^{-3}s^{-1}$. Results for HMGC (red square symbols) and HYMAGYC (blue circle symbols) simulations are shown; the triangles at $T_{H0}=400$ keV are the EP γ_{drive}*

i.e., a TAE. For higher values of n_{H0}/n_{i0}, the most unstable mode obtained by HYMAGYC is clearly a mode emerging from the lower Alfvén continuum, i.e., a lower KTAE (see *Figure 1.27* right, triangle symbols) exhibiting a higher growth rate compared to the most unstable mode observed by HMGC (*Figure 1.27*, left), which is still a TAE.

In the spirit of the ITPA benchmark, a scan on the EP temperature TH has been performed at the value $n_{H0}/n_{i0}=2\times10^{-3}$ (lower than the reference ITPA benchmark case value), in order to compare the two codes in a regime where both observe the same TAE as the most unstable mode. Qualitative agreement is obtained considering the dependence of the growth-rate on TH, while significant quantitative differences are observed, which reduce when comparing the contribution of the EP drive to the growth rates (see Figure 1.**28**). The main discrepancies observed can be traced back to the different response of the MHD solvers, e.g., with respect to the continuum damping and discretization schemes.

Adaptation of core-edge and edge code. The two transport codes, TECXY and COREDIV, have been ported to the Gateway. Stable versions have been uploaded to the svn Gforge repository and released for the general use. In addition, post-processing based on the CERNLIB graphical library has been added and is working.

In case of the COREDIV code, a routine has been prepared to generate input CPO for ETS based on the COREDIV results. The calculated CPO is written to both, local ASCII file and UAL. CPO is generated by the **routine prepare_input_cpo_cd.F90**. In addition, work has been started to prepare the SCENARIO CPO.

In case of the TECXY code, works on the development of simplified mesh generator for TECXY have been continued. The new mesh, in addition to the SOL part of the mesh, contains also the core and private regions (see *Figure 1.29*). TECXY has been adapted to work on the full mesh. This new features still requires some testing before public release of this new version of the TECXY code.

Works to generate edge CPO from TECXY data has been started. A new routine **prepare_tecxy_edgecpo.f90** working on gateway has been prepared which reads the TECXY data and

Figure 1.29 - TECXY mesh for the DEMO Super –X divertor configuration

produces a template EDGECPO. However, It is necessary to define what kind of EDGECPO is required. Works on the development of the multi-species version of the TECXY has been initiated and first test performed.

Both codes, COREDIV and TEXCY are working on gateway. Works on the model and codes enhancements are to be continued.
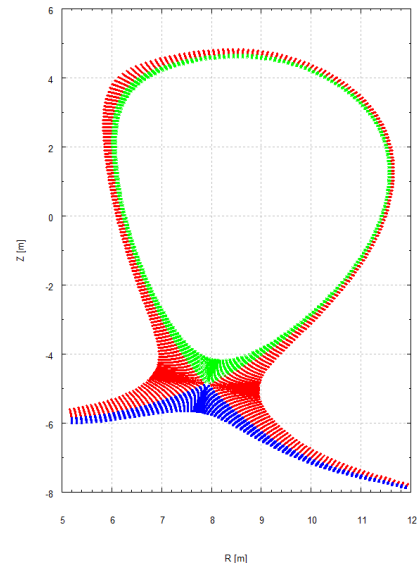
1.1.5 WP – MST1

AUG15-1.1-1 ITER baseline confinement and development of alternative scenarios
The main goals of the experiment are the following:

ITER baseline scenario at q~ 3.6, (i.e. here Bt=-2.0T & Ip=1.0MA)

- Started from reference #31148
- Study ELM-mitigation with B-coils
- Study ELM-mitigation with N-seeding
- Study confinement improvement with N-seeding

For this experiment is required the pedestal stability analysis by using the analysis tools of the JET and comparing the outcomes with the results obtained from the analysis tool of ASDEX.

The Peeling-Ballooning stability boundary is evaluated, at JET, using an ideal MHD eigenvalue solver, MISHKA-1 or ELITE.

First, a plasma equilibrium characteristic of a specified Jped and p′ped is calculated by HELENA, a fixed boundary equilibrium solver. Then MISHKA-1 (or ELITE) evaluates the growth rate
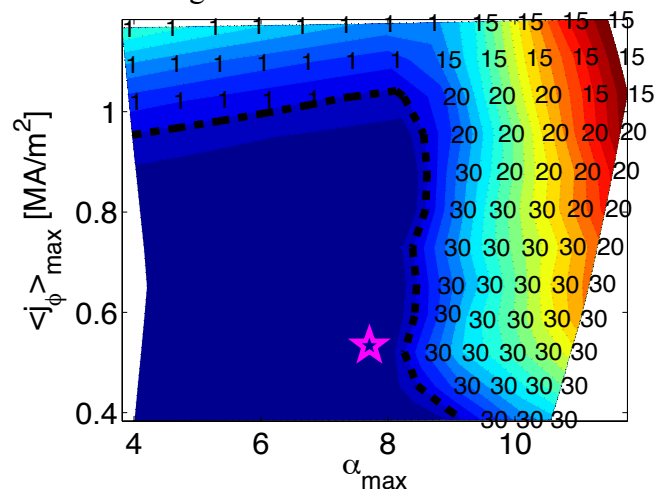

Figure 1.30 - s Stability analysis for the AUG #31148 pulse. Analysis performed by MISHKA-1, using fits to HRTS Te and ne profiles as an input

(eigenvalue) and mode structure (eigenfunction) for a given toroidal mode number and equilibrium.

The version of HELENA used at ASDEX, uses quite different input file format than the JET version of HELENA. To feed the ASDEX HELENA's input file to the JET version of HELENA some transformation were necessary and some tools to do the transfer from one version to the other have been developed. *Figure 1.30* shows the stability analysis for the reference for the experiment, the #31148, performed by MISHKA-1. The stability diagram presented here uses the dimensionless maximum pressure gradient (α_{max}) instead of the p'_{ped}. The star is the operational point representing the plasma state in a specific time of the discharge. The change in colour from blue to red corresponds to an increase in the growth rate of the most unstable mode. A contour of constant growth rate is used to define the stability boundary. The proximity of the point to the stability boundary indicates the stability of the plasma edge at time corresponding to the input profile. The location of the stability boundary depends on the pedestal width.

TCV15-1.3-6 Decorrelation of runaway electrons by magnetic perturbations and role of 3D plasma response

Experiments were performed in 2015 to obtain and control a runaway electron (RE) beam during the post-disruption phases of TCV plasmas (25 shots).

RE beams (*Figure 1.31*) have been produced after disruptions induced by small injections of high-Z impurities (Ar and Ne) in low-density (n_e=1÷5x10^{18} m^{-3}) discharges in limiter configurations with circular plasmas and B_T=1.4 T. A dedicated controller for RE suppression has been implemented on the SCD (Système Distribué de Contrôle), the plasma control system of TCV. Promising results on runaway beam current ramp-down have been

Figure 1.31 - *Runaway electron plateaus in TCV*

obtained using ohmic coils. A new algorithm that detects the runaway plateau onset and replace the standard current reference with a suitable one (ramp-down) has been implemented. Further tools (double integrator) to improve the current decay have been partially tested.
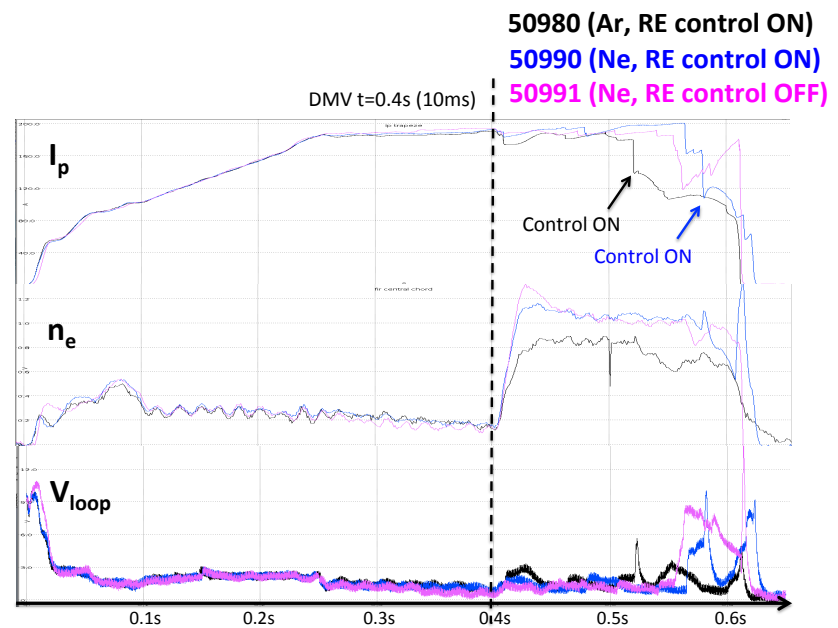
AUG15-1.3-3 Disruption avoidance using ECCD in high beta conditions

Two new disruption target scenarios for avoidance with EC power have been prepared in 2015 AUG disruption avoidance experiments: H-mode Density Limit (HDL, 6 shots, 0.8 MA, -2.2T) and Impurity Injection (2 shots, 1MA, -2.5T). Both scenarios suffered from reaching the EC cutoff density at the application of the EC. The analysis of the results of the preparatory discharges indicates that: a) a lower I_p target must be chosen (0.6 MA, -2.2 T) in order not to reach the EC cut off preventing EC absorption; b) the MARFE activity is starting

before any MHD onset (this is common with the L-mode Density Limit (LDL) cases) but the MHD phase is shorter in HDL. As a consequence of point b) the EC injection should be started as soon as possible, if necessary using a pre-programmed trigger instead of a RT one. The preparation of additional RT trigger signals for EC (in addition to the existing Loop Voltage and Locked Mode) based on Mirnov coils and on a bolometry MARFE detector is being pursued. Moreover, the RT implementation of the SVD analysis, providing information on the mode m and n numbers, is on going and shall be used in future experiments. Four shots relevant for the high β_N scenario were also successfully performed in 2015: ECCD application (using 2 upper gyrotron mirrors RT-controlled on the q=2 before the EC trigger) lead to disruption avoidance, with the discharge surviving for over 1 s.

AUG15-1.7-2 Active control of Alfvén Eigenmodes using ECRH/ECCD, ICRH and RMPs

The activity has been focused on the analysis of the experimental data of the reference shots as well as on the first shots of the experimental program, performed in October 2015. In particular, the SN32315 has been studied, in which AEs were driven by ICRH during L-Mode phase and associated fast-ion transport was observed. The data interpretation has required the development of specific modelling. The experimental scenarios have been analysed utilizing the code TORIC [1.74] to evaluate the power deposition and the distribution functions of the ions accelerated by the additional ICRF power. The rf power spectrum coupled to the plasma has been calculated for both types of antenna in AUG utilizing the code TOPICA [1.75] assessing the sensitivity to the ion temperature and to the tilt angle of the magnetic field. The distribution functions provided by such analysis represent an average performed on a magnetic surface, thus the poloidal dependence is lost. Therefore, they allow only a rough evaluation of the ICRF power effects on the AEs. A numerical code has been developed to express the equilibrium distribution functions in the presence of ICRF heating by the parametric form proposed in Ref. [1.26] and [1.27] in terms of the toroidal canonical momentum, the kinetic energy and the magnetic moment, and consistently with the results of the TORIC code. Once completed the testing and debugging phase of such code, the calculated distribution functions will be used to perform the stability analysis of the AEs and to evaluate their frequency spectra utilizing the HMGC code [1.58], [1.59], for a direct comparison with the experimental results.

TCV15-1.4-4 Advanced NTM physics

TCV experiments for the understanding of the EC effect on the low plasma rotation and on the NTM onset have been performed injecting central EC power in L-mode scenario. Main plasma parameters are characterized by I_p=-110 kA, B_0=-1.41 T, averaged $n_e \sim 1.1 \times 10^{19} m^{-3}$,

Figure 1.32 - Toroidal plasma velocity

triangularity ~0.24 and elongation 1.45, as in previous similar TCV experiments [1.76].
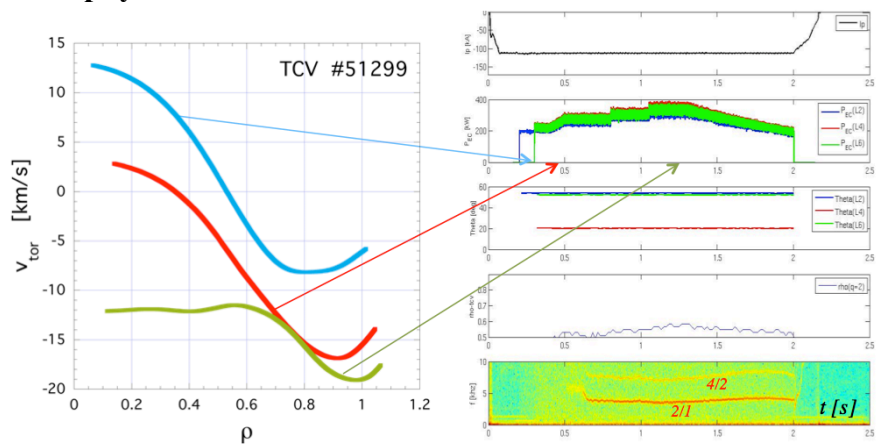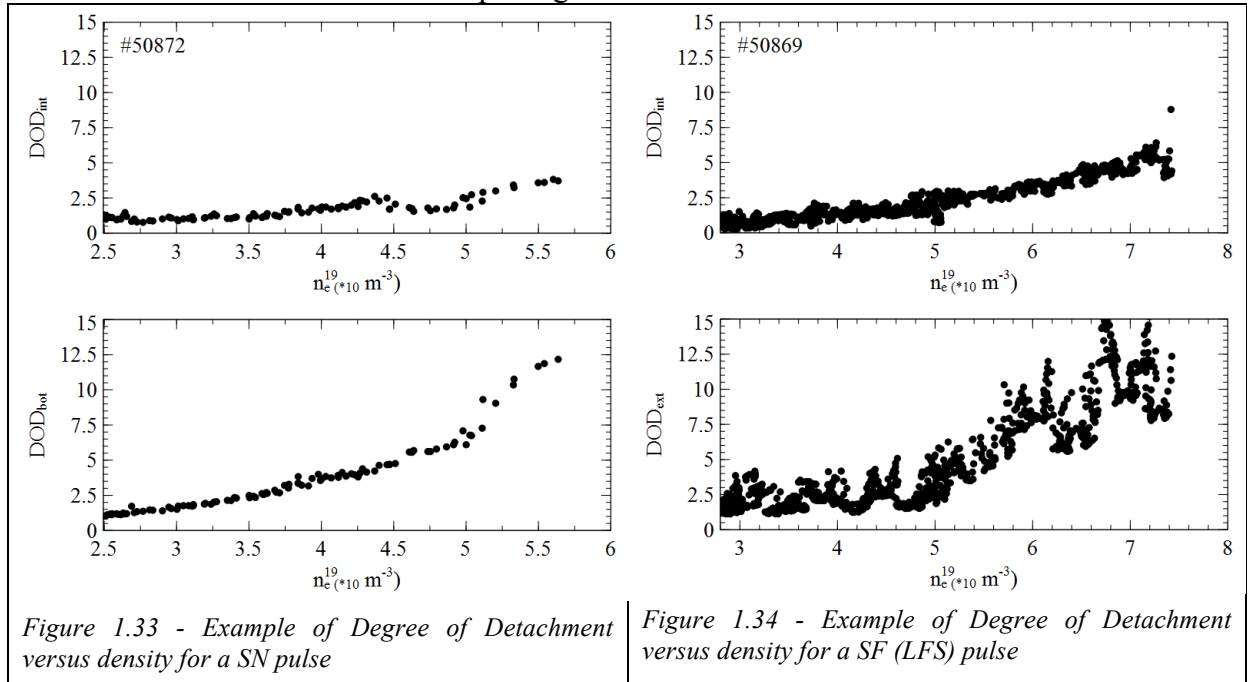
Rotation changes from counter (positive values) to co (negative values) plasma current direction and NTM destabilization have been investigated with co-ECCD and different EC power ramps up to a maximum level of about 1 MW. The toroidal plasma velocity is observed to decrease promptly, as shown in *Figure 1.32*. The 2/1 mode is triggered during the ramp up phase when the EC power is ~0.8 MW and it lasts for 1.4 s also in the ramp down EC phase until the end of the discharge. In figure on the right the main experimental traces are plotted, as the plasma current, the power level of the 3 used gyrotrons and the 2/1 mode frequency. The harmonic 4/2 is also observed. The theoretical interpretation of this kind of plasma response to the EC injection is in progress and different physical mechanisms are taken into account as turbulent effects, pump-out phenomena at the edge and a non vanishing torque driving the toroidal rotation by a displacement current.

TCV15-2.4-1 Detachment optimisation in snowflake configuration
The so called 'snowflake' (SF) configuration, in which two close x-points and four strike points are magnetically produced, has been proposed as a method to reduce the density of the power load to the divertor. In principle the SF configuration can also provide the advantage of achieving plasma detachment from divertor at a lower density than in the standard single null (SN) configuration. This could allow the operation in the detached regime of reduced divertor power load far from density limit disruption, which is mandatory for the foreseen future DEMO device. To verify experimentally this last SF feature some experiments in various SF configuration (SF+, SF- HFS/LFS) without and with Nitrogen seeding have been executed in TCV and compared with matched experiments performed in SN configuration, in the contest of the EUROFUSION MST1 work package.

Figure 1.33 - Example of Degree of Detachment versus density for a SN pulse

Figure 1.34 - Example of Degree of Detachment versus density for a SF (LFS) pulse

In these experiments a similar degree of detachment has been obtained in all tested magnetic configurations (see two examples in *Figure 1.33*, *Figure 1.34*), while some differences have been observed in terms of core/edge radiation distribution. ENEA – Consorzio RFX activity has been mainly focused on pulse optimization, Langmuir probe data analysis, detachment data-analysis and edge modelling. Langmuir probe data analysis codes has been analysed and improved in term of speed to allow and easier inter-shot data analysis. To understand the experimental results edge modelling of discharges has been started using the SOLEDGE2D-EIRENE code. Further experiments have been foreseen in 2016 to extend the range of

explored density and Nitrogen seeding with the aid of NBI heating and ECRH for mode suppression.

TCV15-2.4-3 Characterisation of advanced divertor configurations

Double Decker (DD) configuration [1.77] has been proposed as a novel divertor concept to investigate alternative power exaust solutions for DEMO: the inboard leg of a single null poloidal field divertor is pulled around the interior of the vacuum vessel to allow it to be
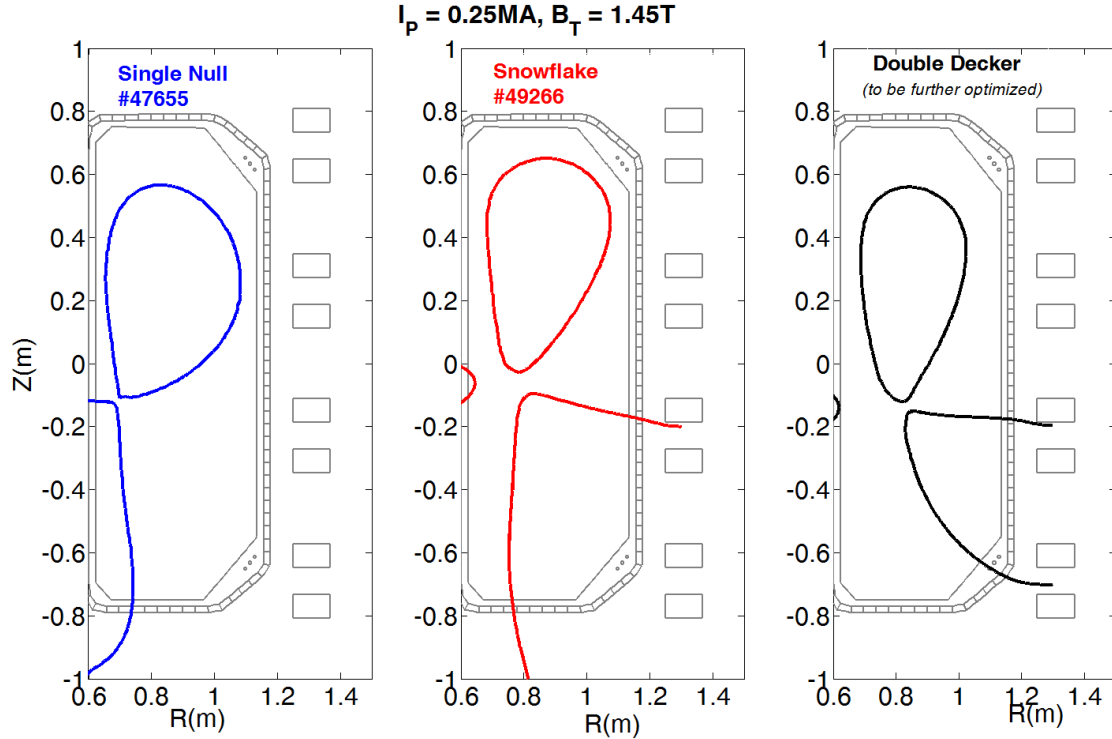

Figure 1.35 - Single Null (blue solid line), Snowflake (red solid line) and Double Decker like configuration (black solid line) equilibria for TCV tokamak. DD configuration been preliminary studied by CREATE-NL tools code starting from SF discharge #49266 at t=0.8s

treated as an outboard leg. This topology reduces the inboard leg parallel heat flux by increasing the target radius, moving the plasma wall interaction to an area of lower magnetic field. Both divertor legs are pulled outwards in major radius to form a horizontal double deck. The potential benefits of a DD configuration will be investigated and compared to snowflake (SF) and standard single null (SN) for TCV tokamka (*Figure 1.35*) in the contest of the EUROFUSION MST1. Experiments have been foreseen to be executed in 2016.

1.1.6 WP – MST2

Reflectometry on AUG ICRH antennas

A multichannel reflectometer has been developed and installed on AUG, in collaboration with IST (Lisbon) and IPP (Garching), with the purpose of measuring the anisotropy of density in front of the antenna. Waveguides of 10 access points have been integrated within the structure of the new ICRF antenna for AUG, to provide as many as possible view lines of the plasma in front of the ICRF antenna. The in-vessel components, previously tested on AUG octant have been installed during last AUG shut-down and completed in spring 2015. External waveguides from vacuum windows to the rack of electronics were tailored and mounted (*Figure 1.36*), for only three channels out of seven available (at top-right and bottom-left corners and middle of the antenna). Electrical insulation is ensured by 0.2 mm thick foil

of kapton inside a waveguide junction. Final assembling of the whole system with 3 instrumented channels was achieved at the end of 2015, so that some data on AUG plasma have been obtained before the end of the year. Commissioning of the instruments will continue on 2016.
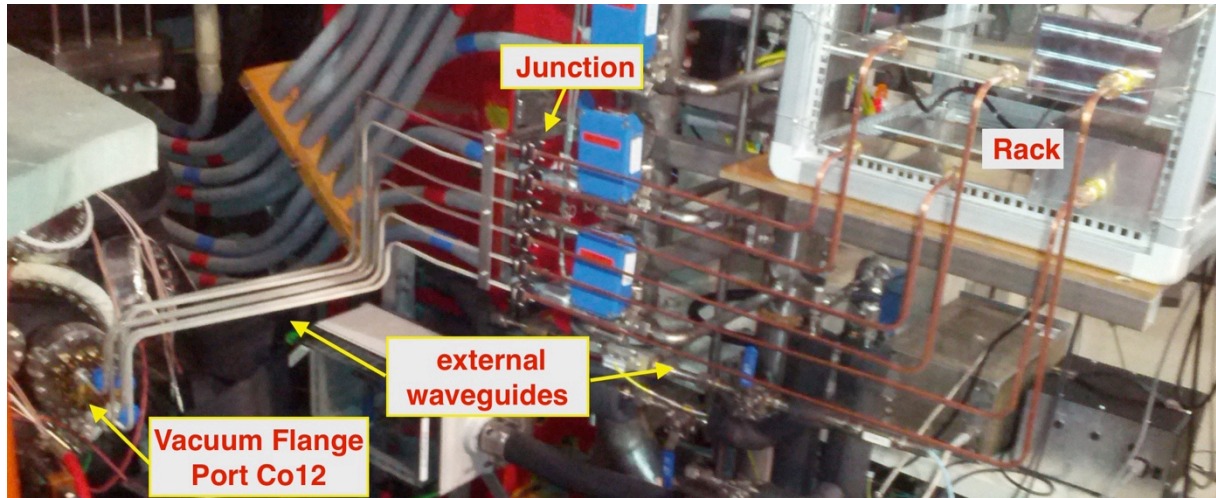

Figure 1.36 - Layout of the external waveguide from vacuum window at port Co12 to the rack of electronics

A calibration of the 3 channels, with complete final layout of waveguides, was performed before closing AUG vacuum. The calibration measures the total time delay of waveguides, which is necessary for balance the delay in reference signal, and to provide a zero position for each launched frequency. A flat mirror has been put at a known position in front of the antenna inside vacuum vessel, and the time delay is measured during the frequency scan. As the final system was not available for the calibration, a temporary layout has been assembled in homodyne detection, using part of the reflectometer electronics and part of components available at IPP.

The measured calibration signal in one of the three channels, together with its spectrogram is shown in *Figure 1.37*. It can be observed that the signal-to-noise ration is quite good. The observed modulation is the beating frequency due to the time delay between the two beams at the mixer that is seen by the mixer as frequency shift for the fast change of frequency. It's worth to note that the beating frequency slightly decreases with scanning frequency, for the waveguide dispersion relation that caused
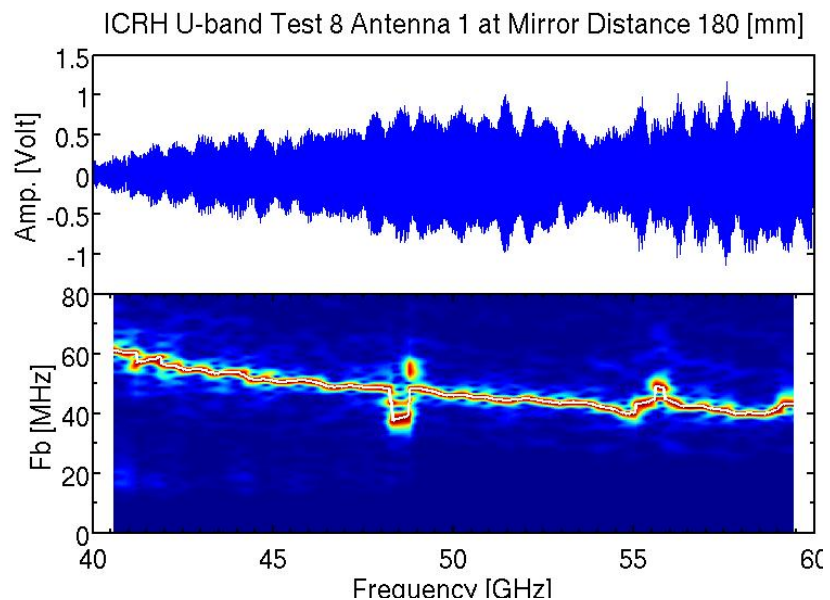

Figure 1.37 - Amplitude and spectrogram of the signal measured on ch 8, with a mirror placed 180 mm from the horns. The x-axis is the frequency of RF launched. The slow change of the beating frequency (y-axis) is due to the dispersion relation of waveguide. Jumps at certain frequencies are caused by multi-reflection, between the mirror and the ICRF antenna structure

different delay for different frequency, so that from the total change of the beating frequency the length of waveguide can be inferred. The jumps of beating frequency observed at about 48

GHz and 56 GHz, were produced by multi-reflections between mirror and antenna structure, that form a resonating cavity for certain frequencies.

RF components of the reflectometers (front-end) must be located as close as possible to the vacuum windows in order to reduce the waveguide losses. To avoid interference of part of electronics with stray field of the tokamak, IF components has been assembled in separated boxes and connected with front-end by low-loss coaxial cables, so that the can be displaced if required. Fortunately, this was not the case, even though a magnetic shield for the power supplies was installed to avoid failures.

Together with the reflectometer an acquisition system based on ATCA standard, have been put into operation. A Linux processor controls the ATCA crate with an 8 channels ADC having 250 Mb on board and 200 MS/s sampling frequency. The acquisition system have been installed and interfaced with ASDEX database.
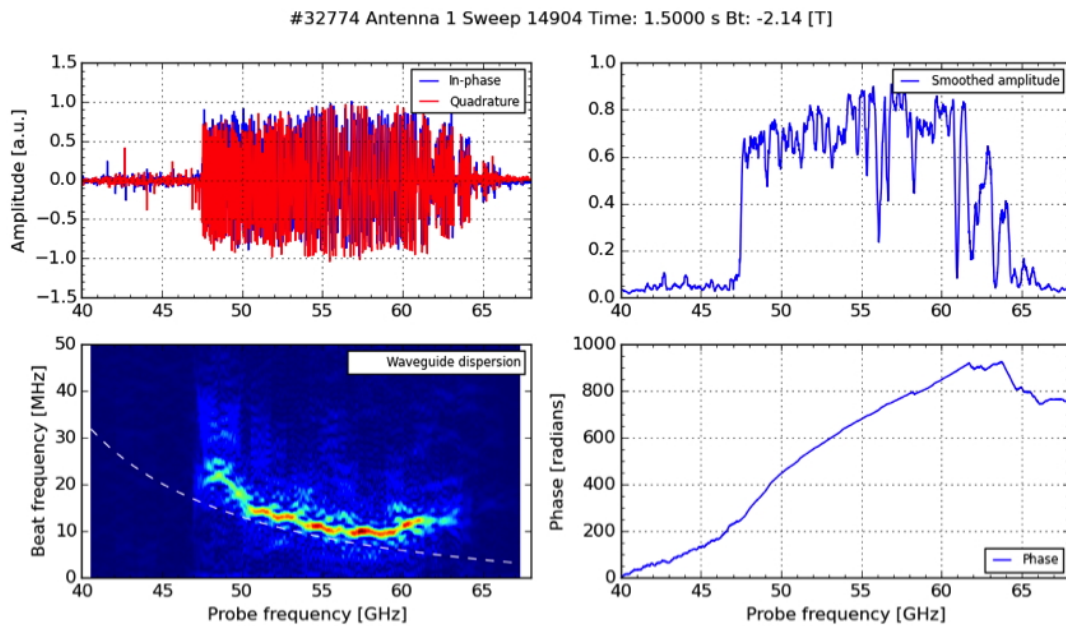

Figure 1.38 - Reflectometer data from antenna 1 for shot #32774. Left-top) I and Q signals plotted versus the scanning frequency; right-top) signal amplitude; right-bottom) signal phase; left-bottom) spectrogram of the phase derivative (beating frequency)

The diagnostics is now installed and running on AUG tokamak. One of the first signal acquired is reported in *Figure 1.38*. The elaboration program for the calculation of the has been

1.1.7 – International Collaboration

IPP ICRH antennas

Two new antennas have been constructed and assembled in collaboration with IPP (Garching) and ASIPP (Hefei, China) in order to optimize electric field of the antenna minimizing the spurious component. A set of waveguides of a multichannel reflectometer has been embedded in one of the two ICRF antennas, in order to measures the density in front of the antenna.

The construction has been completed in autumn 2014 and during the mounted inside AUG during the long shut-down in spring 2015. No major issues arose during the installation, owing to the detailed design made of all components on CATIA model. Only small issues occurred for the presence of small components present on vessel that where not present

neither on 3D model nor on octant mock-up, that interfere especially with embedded reflectometry components. Issues have rapidly been solved with small modifications of some mechanical support of the reflectometry waveguide, without introducing any delay in scheduled activities.

The new antennas have taken the place of two of the four old antennas. In *Figure 1.39*, the new (left) and old (right) antennas are shown together. Parts of three straps of the new antenna are slightly visible through the Faraday shield.

First results on plasma are very promising. In fact, as a result of the optimized electric field, the new antennas produce a reduced influx of impurity also in presence of tungsten wall, where an increase of impurity is observed in same condition and power level.
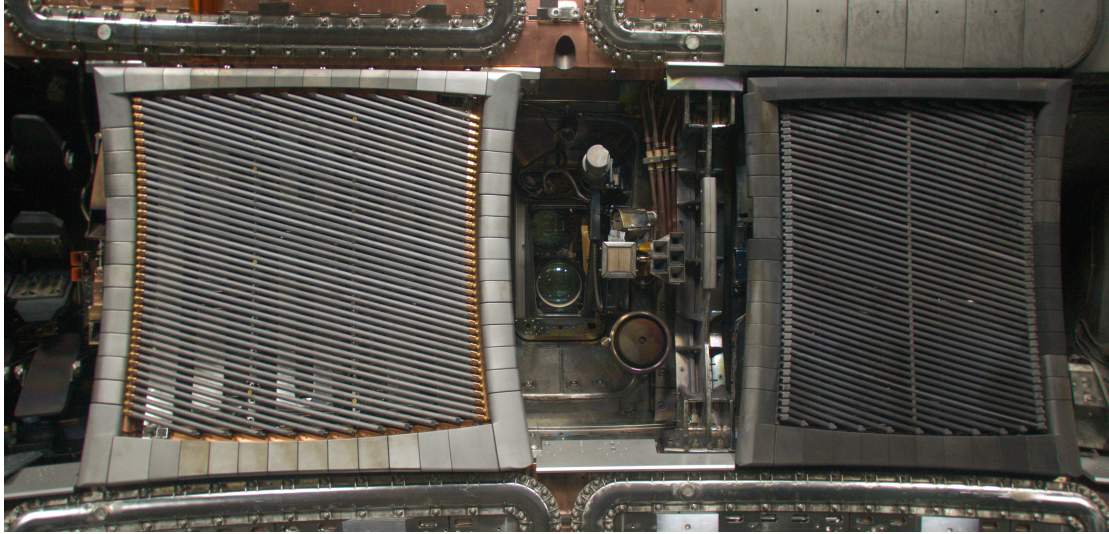

Figure 1.39 - The new (left) and old (right) antennas

GEM Imaging and Tomography W7X e KSTAR

Activity of soft-X ray diagnostic on Tokamak plasmas with triple-GEM (Gas Electron Multiplier [1.78]) detectors [1.79] continues to have a growing interest [1.80]. Recently more results have been achieved during the experimental campaign of the KSTAR Tokamak (KAIST, Daejeon - South Corea).
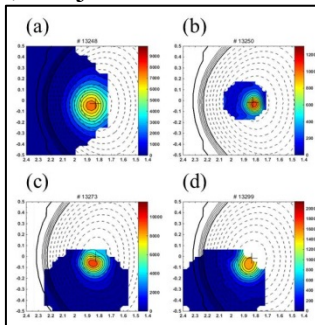

Figure 1.40 - The reconstruction images overlapped to the Magnetic flux surfaces obtained from rtEFIT
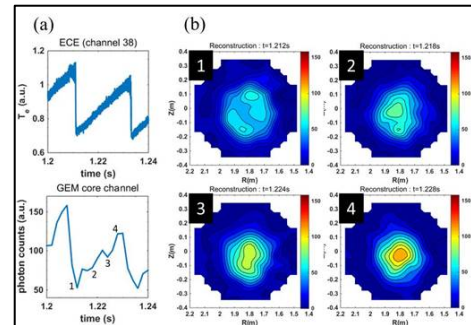
Figure 1.41 - (a) a sawtooth oscillation from the ECE signal and the GEM signal for one KSTAR shot. (b) Reconstructed magnetic islands at the end of a crash and during the build-up phase

The GEM detector has an active area of 10 x 10 cm^2 with 120 pixels, each one having an area of 8 x 8 mm^2. Front-End-Electronics is based on a set of 8 CARIOCA chip cards and an FPGA (Field Programmable Gate Array) mother board. A pin-hole camera has been realized using this GEM detector on a tangential port of the KSTAR Tokamak. Pin-hole is realized with a beryllium window 150 μm thick and 2 cm in diameter. GEM detector can move back and forth and then the spatial resolution on the magnetic axes can range from 3.3 to 9.6 cm. In

addition it can move up/down and left/right in order to observe different areas of the Tokamak camera (*Figure 1.40*).
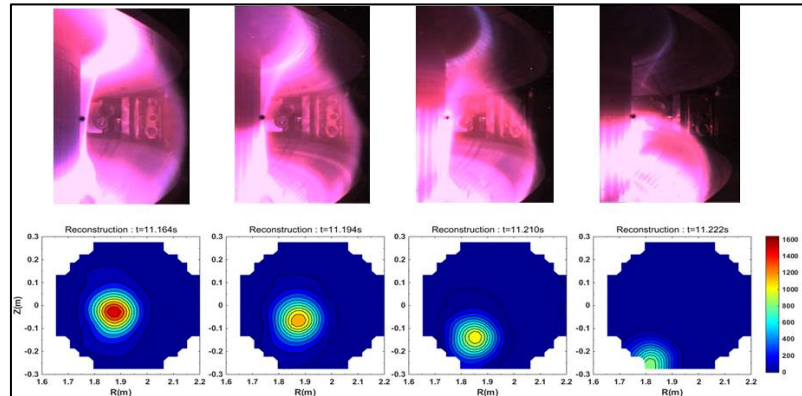

Figure 1.42 - Reconstructed images from the visible camera (top) and the GEM X-ray camera (bottom) when a vertical displace event happens

The aim was the study of high temperature plasmas that emit X-ray photons in the energy band of 4÷15 keV. Front-endelectronics allows the acquisition of a maximum of 60,000 frames at a maximum frequency of 1 kHz. For the next experimental campaign, FPGA will be reprogrammed in order to increase the frame rate up to 1 MHz. Poloidal cross-sectional images were reconstructed through the Philips-Tikhonov algorithm applied to the original data acquired by the GEM detector. Phantom tests with synthetic D-shaped plasma images and a comparison with the magnetic equilibrium flux surfaces from the real-time EFIT code were performed obtaining a good agreement between each other. The KSTAR experiments show the main advantages of using a tangential camera system: compactness, high efficiency, energy discrimination in bands, selectivity of the photon energy range and so on. 2-D X-ray images of the KSTAR plasma were acquired during some typical plasma phenomena: sawtooth crash, electron cyclotron heating, vertical displacement event, emissivity from the injected trace Ar impurity and so on. In all cases the observed phenomena are correctly described in accordance to the other standard diagnostic systems [1.81]. *Figure 1.41* and *Figure 1.42* show the plasma mapping obtained during a sawtooth crash and a plasma shutdown phase.

For the year 2016, the installation of a similar GEM camera is scheduled for the Wendelstein Stellarator (W7X, IPP Max-Planck-Institut fur Plasmaphysik - Greifswald). This new German machine produced its first plasma on December 2015.

Snow Flake configuration

The SF configuration is characterized by a second-order null in the poloidal magnetic field (B_P), where both B_P itself and its spatial derivatives vanish. As it was realized in the first assessment of the SF [1,82], an exact SF configuration is topologically unstable: any imbalance of the Poloidal Field (PF) coil currents, splits the second-order null in two first-order nulls, leading to a variety of the topologically-stable SF-like configurations [1.83].

A divertor configuration with two nearby nulls has been modelled and created for EAT tokamak. In the two nearby nulls configuration, or so-called quasi-snowflake (QSF), the secondary null could be moved around to change its distance from the first null and to form a magnetic configuration that features either contracting or flaring geometry near the plate [1.84]. QSF equilibria (400kA/1.8T, vertical target configuration), with the secondary x-point "close" or "far" from the vessel structures [1.85], have been designed and optimized by means of CREATE-NL equilibrium code [1.86] for EAST tokamak (see *Figure 1.43* and *Figure 1.44*).

The experiments have been devoted to study the linear dependence of the gradient of magnetic field B_P in the primary null on the distance between the two nulls, that characterizes the interdependence of the field structures of both nulls. Indeed, the flaring of the magnetic flux (characterized by the magnetic field gradient) in the primary null is affected by the presence of the secondary null as discussed in [1.85]. This flaring could be then directly translated to the increased wetted surface area and reduced heat flux [1.83]. A self-explanatory way to show the aforementioned dependence is to plot the iso-contours of $|R \cdot B_p|/|R \cdot B_p|_{midplane}$ = const around the nulls, with const = 0.01 - 0.1 [1.85] for QSF EAST configurations modelled by CREATE-NL equilibrium code.

Figure 1.43 - Iso-contours $|R \cdot B_p|/|R \cdot B_p|_{midplane}$ = const for "far nulls" QSF configuration in EAST tokamak   *Figure 1.44 - Iso-contours $|R \cdot B_p|/|R \cdot B_p|_{midplane}$ = const for "far nulls" QSF configuration in EAST tokamak*

A direct manifestation of the conversation between the nulls is that the flux flaring (characterized by the magnetic field gradient) in the main null is affected by the presence of the second null. Indeed, as it may judged from the *Figure 1.43* and *Figure 1.44*, the gradient of $|B_P|$ is proportional to the distance between the nulls.

Experimentally, first L-mode [1.85] and recent long pulse and H-mode discharges [1.87] at EAST have shown heat flux reduction once the shape moves from SN to a two nearby nulls divertor configuration with a contracting geometry near the target plates and a significant distance between the two nulls. In coming 2016 EAST experiments, the upgrade of ISOFLUX control system will allow to control the exact position of secondary x-point. This will permit to increase the additional heating power and to easily vary some of the features of the topological configuration in H-mode discharges at low and high plasma current, i.e. moving from contracting to flaring geometry near the target plates with the second null located on the vessel.

LH on EAST

LH Systems. The 4.6 GHz antenna on EAST underwent damages during the experimental campaign in Summer 2015 owing to electrical discharges at the launcher mouth. Support from ENEA-Frascati helped in identifying the causes of the damages through the analyses of experimental data as well as full-wave simulations of the electric fields. In addition to optical arc detectors looking at the radiofrequency windows, the use of detection systems, suitable for plasma facing arcing events, was proposed. Coupling performance and launched power spectra in realistic EAST plasmas were calculated for the 2.45 and 4.6 GHz antennas using different numerical tools available at the Frascati research center, namely GRILL3D, TOPLHA and Comsol Multiphysics. Good agreement between the predictions of the coupling codes were obtained. The full antenna designs were carefully checked finding out the presence of poloidal phase compensation and studying the effect of periodically spaced holes, conceived to produce vacuum in the waveguides. Power spectra sensitivity owith respect to the angle between the equilibrium magnetic field and the equatorial plane was assessed.

LH wave physics of plasma edge. Assessing wave physics in the plasma edge is important for LH penetration and consequent current drive effect in tokamak main plasmas, especially at reactor-graded, high plasma densities, as important FTU results demonstrated [1.88].

Modelling of Parametric Instability (PI) has been performed using the LHPI ENEA-Frascati code, considering the parameters of two EAST reference discharges, respectively with weak and strong lithisation. Frequencies and growth rates of coupled modes have been identified, considering several radial layers located near the antenna, more internally in the scrape-off layer (SOL), and also in the periphery of the main plasma, where the PI growth rate results to be still not negligible.

The performed modelling work focused on interpreting the sideband, present in the RF probe spectra, which is separated from the operating line frequency by amount in the range of the ion-cyclotron (IC) resonant frequency close to the edge. However, in the two compared operating conditions, it is problematic inferring the location of the radial layer where the sideband should be originated, namely, in the low- or in the high-field side.

The behaviour of such sideband has been successfully interpreted, indeed, by modelling results showing that an LH wave can actually propagate at a frequency downshifted from the pump ranging from about 10 MHz to 15 MHz, depending on the operating conditions of experiment. This frequency corresponds to condition of maximum PI growth rate, which is however originated in a layer located near the plasma edge, in the low-field, roughly at normalized minor radius $0.9 \leq r/a \leq 1.02$, ($r/a=1$ corresponds to the last closed magnetic field surface).

Consequently, the origin of the observed sideband has been indeed inferred as, in both the considered operating conditions, the relevant sideband is reasonably originated in the scrape-off layer, in the low-field side.

1.2 – JET

1.2.1 – JET1

Introduction

After the shut down, started in October 2014 with the main aim of removing tile samples, re-instate the ITER Like Wall antenna (ILA) and optimizing the pellet injection track, JET restarted in June 2015 achieving the first plasma on 26 July 2015 (#88088). After standard commissioning procedures, Campaign C-35 then started on 10 November 2015 and ended on 18 December 2015.

During the year 2015, before the experimental campaign, ENEA scientists were engaged in proposing and preparing experiments for both C-35 and C-36. At the same time they brought forward the analysis of previously collected data and prepared papers for the coming conferences.

Since the beginning, JET operation was affected by a limited availability of additional heating power thus causing the objective of developing high performance plasmas for future Deuterium-Tritium (DT) experiments to be only partially addressed. Especially the main plasma scenarios, the so called Baseline and Hybrid scenarios, proposed for future DT operation could not be taken to the highest performance which require, at the same time, high current and normalized pressure (β_N). In spite of this, many investigations were carried out to progress physics understanding and prepare for full power operation.

In regard to the regarding JET campaigns work program (JET1-WP) ENEA scientists and associated partners were involved in the following topics:

1. Development of the Hybrid Scenario
2. Analysis of MHD instabilities in the Hybrid scenario
3. Safety factor profile determination using MHD markers and mode localization
4. Radiation fraction studies in quasi-snow-flake magnetic configuration
5. Flux expansion EDGE2D-EIRENE simulations
6. Pedestal stability analysis
7. Ion Cyclotron Resonant Heating (ICRH): modelling with TORIC
8. In collaboration with CREATE
    a. Development of advanced tools for plasma shape control
9. In collaboration with Tor Vergata
    a. Equilibrium reconstruction code: JEC2020 benchmark and constraints
    b. Confinement scaling laws
    c. Assessment of pellet pacing efficiency
10. In collaboration with Politecnico di Torino
    a. ICRF Antennas Analysis with TOPICA
11. In collaboration with Università di Cagliari
    a. Plasma Instability studies

In addition to contributing to JET1-WP, there was a substantial contribution to the work program 'Technological Exploitation of JET DT Operations" (JET3-WP) lead by an ENEA scientist. Here is a list of the main topics of interest:

1. Neutron detector calibration at 14-MeV neutron energy - NC14
2. Validation of neutronics and activation codes - NEXP
3. Tests of neutron and tritium detectors for Test Blanket Modules (TBMs) - TBMD
4. Data validation for the activation predictions of ITER materials - ACT
5. Collection of operational experience on occupational dose – NSAF
6. Measurements of tritium retention and outgassing, and of airborne tritium – TRI
7. Characterisation of neutron field, activation and dose rates - NCAL

Under the coordination of ENEA researchers there were also two projects of the work program "Enhancement" on the following topics (JET4-WP) dealing with the following topics:

1. Neutron Camera Upgrade (NCU)
2. Vertical Neutron Spectrometer (VSN)

Development of the Hybrid scenario for DT

The so-called "Hybrid" scenario operates in an intermediate (hybrid) parameter range between the inductive or "Baseline H-mode" and the "Steady State" scenarios [1.89]. The Hybrid aims at a low central shear safety factor profile, no or moderate sawtooth, medium density (Greenwald fraction ~0.6), edge q_{95}~4, normalized pressure β_N>2.5 and confinement factor H_{98y2} > 1.2, where H_{98y2} is the confinement time divided by the prediction of the ITER-98y2 scaling [1.90]. The Hybrid is considered to be one of the best candidates for DT operation especially in relation to its ability of maximizing the fusion performance expressed in terms of neutron yield.

In the first half of 2015 the analysis of the data produced in the previous campaigns was completed and results were presented at the Lisbon European Physics Society conference (EPS) held in June 2015 [1.91]. A new ILW neutron yield record had been achieved corresponding to 2.3×10^{16} n/s at normalized pressure β_N= 2.1 and confinement H_{98y2}= 1.1.
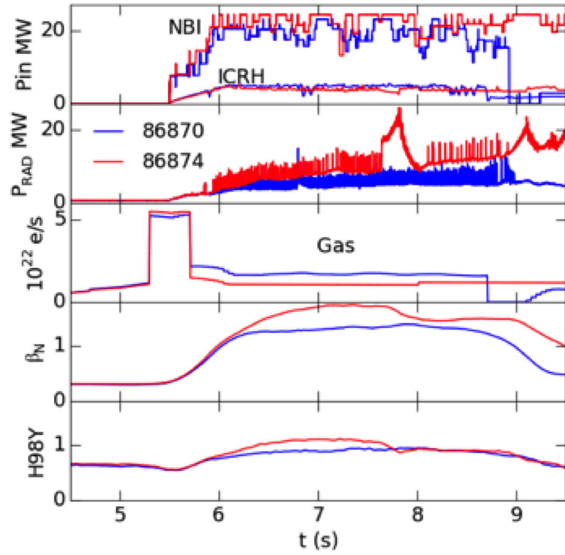
Figure 1.45 - Gas scan at 2.5 MA, 2.9 T, low triangularity, tile 6. From top: NBI (solid) and ICRH (dashed) power, total radiation, gas rate, normalized beta and normalized confinement. Shot 88874 (blue) with 40% less gas exhibits a better performance at the cost of more radiation, lower ELM frequency and poorer stability

In spite of the limited amount of available power, it was possible to achieve a good peak performance, while the required duration (5 s) remains to be achieved yet. The performance duration was limited by impurity accumulation and MHD instabilities leading either to performance deterioration or a disruptive termination of the discharge. A gas scan performed at 2.5 MA, 2.9 T and 23-26 MW of additional power, revealed a strong sensitivity of edge instabilities (ELM) to small changes of gas rate not seen at lower current and power: this made it difficult to find a good compromise between impurity control, eased by frequent ELMs, and performance degradation. *Figure 1.45* shows the two extremes of a five shot scan in which the gas rate was gradually increased: a 40% gas reduction is seen to cause a dramatic effect on performance and impurity behaviour. Previous power scans, performed at constant engineering parameters i.e. plasma current, toroidal field and density, had already shown a weaker power degradation of the confinement than expected from ITER scaling.

An extension of this analysis to a wider database, including plasmas with different engineering parameters, indicated that the thermal pressure, normalized to magnetic pressure and current (β_N), was more relevant for high confinement than the input power per se, though disentangling the role of these two parameters remains not trivial.

A dependence, $H_{98y2} \propto \beta_N^{0.63}$, was found to best fit data for I_p > 1.8 MA and 1.1 < β_N < 2.4 (*Figure 1.46*). The indication that best performance is obtained at high beta (and/or power) is also theoretically justified and reproduced in modeling activity as a virtuous core-edge feedback that reduces micro-turbulence and MHD effects [1.92]. In *Figure 1.46*, in order to eliminate the possible effect of
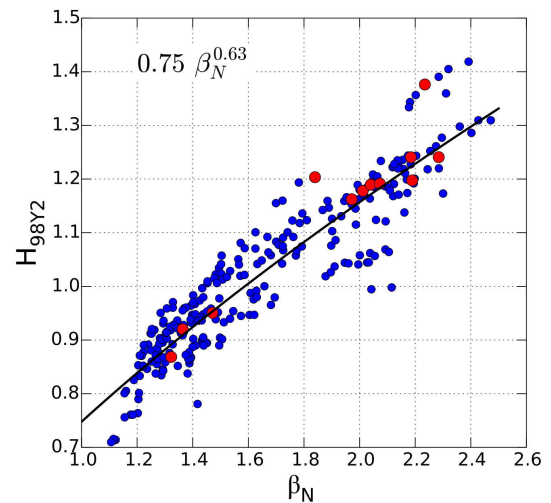
Figure 1.46 - H98y2 versus β_N for Hybrid with I_p> 1.8 MA. Red symbols refer to plasmas with constant ρ^* (5.0-5.1 x10^{-3})

changes of the ion Larmor radius, normalized to the plasma minor radius (ρ*), some points at fixed ρ* have been highlighted in red. These points are well aligned with the scaling confirming the β_N dependence [1.91].

In November 2015 with the start of the new Campaign C36, the Hybrid development continued with the main aim of addressing the capability of the divertor to withstand the elevated power flux expected at high performance. Two routes have been investigated. The so-called "unseeded route", based on strike point sweeping techniques meant to spread the load on a larger divertor area, gave encouraging results. The "seeded route", tested so far only with Neon injection, though capable to significantly reduce the peak tile temperature while maintain a good average performance, shows a significant reduction of the fusion performance (neutron yield) due to profile effects and core plasma cooling. This effect, if confirmed, would make this technique unsuitable for a successful DT operation. It must be noted that, due to the limited availability of power, these results need to be extrapolated to the high power case and any conclusion will need to be confirmed at full performance.

Analysis of MHD instabilities in the Hybrid scenario

The achievable performance in terms of beta and duration of hybrid scenarios is often limited by the onset of Magneto-hydro-dynamic modes (MHD) that degrade confinement or even induce disruptions. The analysis of MHD modes in terms of toroidal periodicity number (n), amplitude and radial localisation has been completed for all ILW Hybrid and Advanced scenarios. A set of Baseline scenario pulses has been analysed as well. Results are available in PPF channels as described in the T13-11 wiki page at:

http://users.jet.efda.org/tfwiki/images/4/4c/Description_of_MHD_PPF_channels.pdf.

A commented list of the pulses included in the database is available at

http://users.euro-fusion.org/tfwiki/images/b/b5/T13-11_lists.xls.

A statistical survey of MHD instabilities in JET hybrid discharges has been performed for hybrid scenario pulses [1.93], with particular attention to onset conditions and saturated amplitude in terms of the normalised beta (β_N). The database includes about 260 pulses for JET-ILW and 180 selected pulses for the previous carbon wall (JET-C).
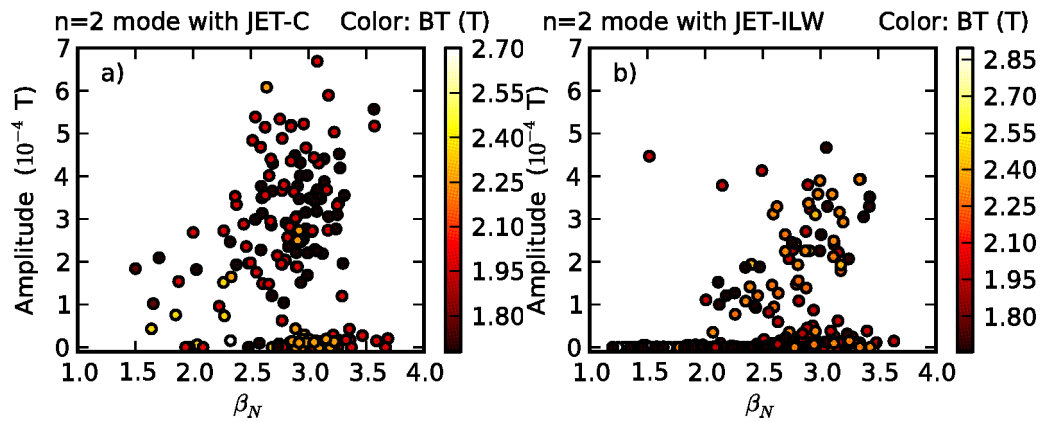
Figure 1.47 - Maximum amplitude of the n = 2 mode (with poloidal number m = 3, corresponding to q = 1.5) during each pulse as a function of normalised beta a) with the C-wall and b) with the ILW. The toroidal field is shown by color code. Outliers above $3 \cdot 10^{-4}$ T at $b_N < 2.5$ in b) are from pulses with early NBI at $q_{95} = 3$

The maximum amplitude reached by the $n = 2$ mode during each pulse is shown in *Figure 1.47* for JET-C and JET-ILW datasets separately. A similar trend to increase mode amplitude with normalised beta can be observed in both cases, with about 30% larger values for JET-C. Data clustered near zero amplitude correspond to weak (1-2 cm island width) and generally transient modes that are not relevant to the present analysis. In the statistical survey these modes were discarded by imposing a threshold of $3 \cdot 10^{-6}$ T s on the time-integrated amplitude.
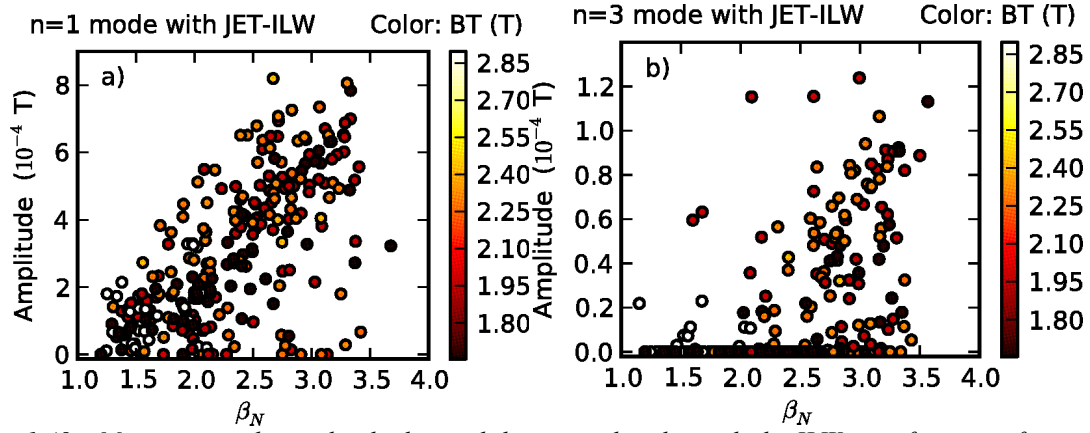
Figure 1.48 - Maximum mode amplitude detected during each pulse with the ILW as a function of normalised beta a) for m = l, n = l and b) for m = 4 (or 5), n = 3. The toroidal field is shown by color code

Maximum amplitudes of $n = 1$ and $n = 3$ modes with the ILW are shown in *Figure 1.48*. The $n = 1$ activity is in the core ($q \gg 1$) region; modes with poloidal number $m = 2$ (at the $q = 2$ surface) are not shown in *Figure 1.48*. Generally the $n = 3$ activity is at the $q = 4/3$ surface, but in some pulses it is at the $q = 5/3$ surface. Threshold values of 10^{-5} T s for $n = 1$ and 10^{-6} T s for $n = 3$ have been used to select relevant modes.

The main addressed question was how long the high performance phase of hybrid pulses lasts before the onset of MHD activities. From *Figure 1.49* it can be seen that presently achieved durations from NBI start to mode onset time with JET-ILW can only exceed 3 s at $\beta_N < 2.5$, while longer durations were obtained with the JET-C at any β_N.

The effect of MHD modes on confinement and tungsten impurity accumulation has been analysed in the framework of T13-13 task (Understanding the interplay of MHD stability and W peaking); results of this analysis have been submitted for publication to Nucl. Fusion.
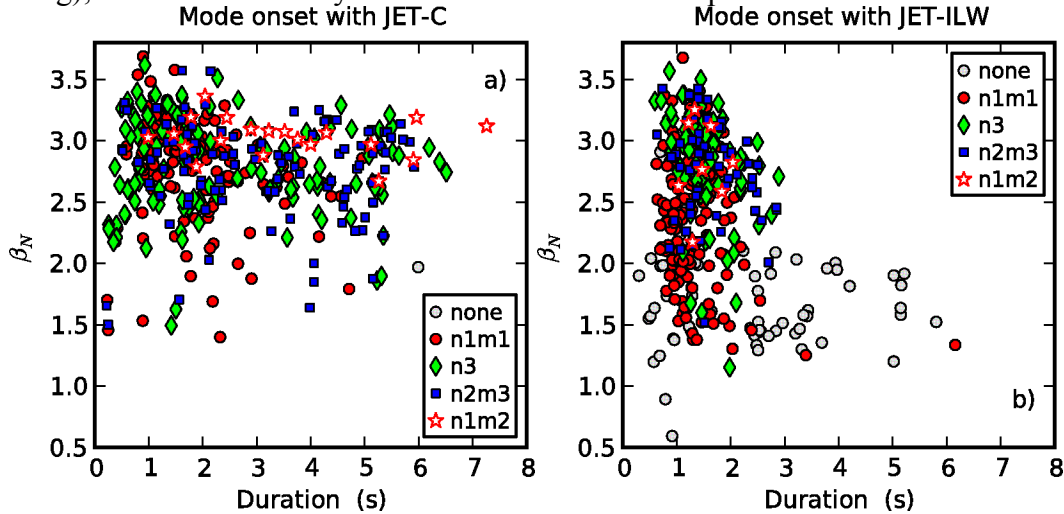
Figure 1.49 - Normalised beta at mode onset as a function of duration from NBI start to mode onset time as defined by threshold crossing For modes with n = l, m = l (red dots), n = l, m = 2 (red stars), n = 2, m = 3 (blue squares), n = 3, m = 4 or 5 (green diamonds). Duration before radiation exceeds 70% of input power is used for pulses without any MHD above threshold (grey dots)

Safety factor profile determination using MHD markers and mode localization

Measurements of the propagation frequency of magnetic islands in JET have been compared with diamagnetic drift frequencies, in view of the determination of markers for the safety factor profile. Statistical analysis was performed for a database including many well-diagnosed plasma discharges. Propagation in the plasma frame, i.e. with subtracted E×B Doppler shift, resulted to be in the ion diamagnetic drift direction, as shown in *Figure 1.50*. Rational-q locations obtained under the assumption of propagation at the ion diamagnetic

frequency (as described in *Figure 1.51*) were compared with the ones measured by equilibrium reconstruction including motional Stark effect measurements (MSE) as constraints.
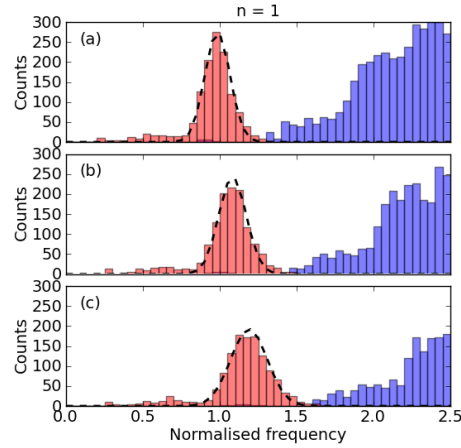
Figure 1.50 - Histograms of ratio between propagation frequency of modes with n = 1 toroidal periodicity and: (a) ion diamagnetic frequency, (b) E´B drift frequency, (c) electron diamagnetic frequency, all calculated at the q = 2 radius from active charge exchange spectroscopy data. Bars in red correspond to (2, 1) modes; bars in blue correspond to (1, 1) modes (not relevant for the comparison). Overlaid curves show scaled normal distributions. Best agreement is obtained with the ion diamagnetic frequency, for which the normal fit gives an average ratio of 0.985 and a standard deviation of 8%

Systematic shifts and standard deviations were determined for islands with (poloidal, toroidal) periodicity indexes of (2, 1), (3, 2), (4, 3) and (5, 3), see *Table 1.3*. The results of this analysis have been submitted for publication to Nucl. Fusion. Previous work was reported in references [1.94] and [1.95].
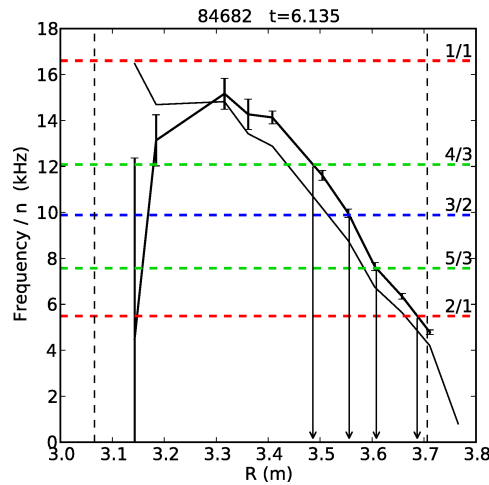
Figure 1.51 - Frequency-matching diagram. The thick solid line with error bars shows the ion diamagnetic frequency and the thin line shows the toroidal angular frequency profile. Horizontal dashed lines show mode frequencies divided by the respective toroidal number n. Red, blue and green indicate n = 1, 2 and 3 respectively. The identified (m, n) pairs are annotated. The outer (inner) vertical dashed line shows the q = 2 radius (the plasma axis) from equilibrium reconstruction. Rational-q locations as obtained from crossing between island frequencies and the diamagnetic frequency profile are indicated by vertical arrows

Table 1.3 - Statistics of the shift between rational-q location from mode frequency and MSE

mode	mean	standard deviation
(2, 1)	1.5 cm	3.9 cm
(3, 2)	-1.6 cm	3.8 cm
(4, 3)	-2.8 cm	5.6 cm
(5, 3)	0.5 cm	4.3cm

Radiation fraction maximization in quasi-snow-flake magnetic configuration

The so called Snow Flake configuration (SF) is characterized by a second-order null in the poloidal magnetic field (B_P), where both B_P itself and its spatial derivatives vanish. As it was realized in the first assessment of the SF [1.82], an exact SF configuration is topologically unstable: any imbalance of the Poloidal Field (PF) coil currents, splits the second-order null in two first-order nulls, leading to a variety of the topologically-stable SF-like configurations [1.83,1.84]. A divertor configuration with two nearby nulls [1.85] has been modelled for JET tokamak: the secondary null could be moved around to change its distance from the first null (primary x-point) and to form a magnetic configuration that features either contracting or flaring geometry near the plate. Two 2.5MA/2.7T semi-horizontal target configurations (V5D and VD5-HFE), with the secondary x-point "close" or "far" from the vessel structures, have been designed and optimized by means of CREATE-NL code (non linear plasma evolution code) [1.86], for JET tokamak, see *Figure 1.52* and *Figure 1.53*. The closed configuration V5D-HFE shows an increase of flux expansion on outer target of a factor ~1.6. Nitrogen seeded H-mode experiments are foreseen to be executed at JET in 2016, addressing the physics of the dependence of radiative volume and total radiated power on the distance between the two nulls. The impact of main magnetic divertor geometry parameters (flux expansion, connection length, etc.) on the radiation pattern disentangled by the change of recycling happening at the same time, will be investigated, focusing on bolometer and Langmuir probe measurements analysis supported by edge modelling.
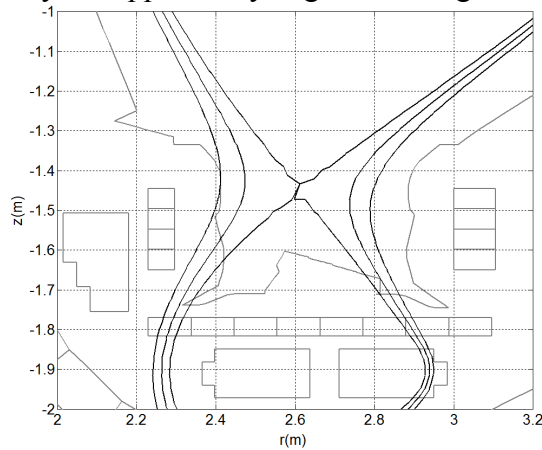
Figure 1.52 - V5D configuration modelled by CREATE-NL equilibrium code
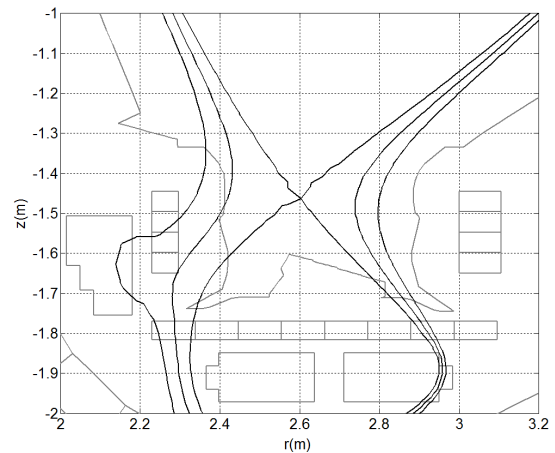
Figure 1.53 - V5D-HFE configuration modelled by CREATE-NL equilibrium code

Flux expansion EDGE2D-EIRENE simulations at JET

Nitrogen seeded H-mode experiments are foreseen to be executed at JET in 2016, addressing the physics of the dependence of radiative volume and total radiated power on the distance between the two-nulls.

The addressed physics is the impact of main magnetic divertor geometry parameters (flux expansion, connection length, etc.) on the radiation pattern trying to disentangle it from the change of recycling happening at the same time at the inner target. Typical semi-horizontal configurations have been modified only on the divertor zone by keeping the plasma boundary unchanged. The modified magnetic configurations, with inner strike point located on inner vertical target and outer one on full W horizontal target, have been designed to increase similarly flux expansion by **40%** on both inner and outer target.

Modeling activity with the fluid-code EDGE2D coupled to EIRENE supports the experiment preparation: predictive simulations have already shown that the divertor heat fluxes can be

reduced with N₂-injection, qualitatively consistent with experimental observations, by adjusting the impurity injection rate to reproduce the measured divertor radiation [1.96].
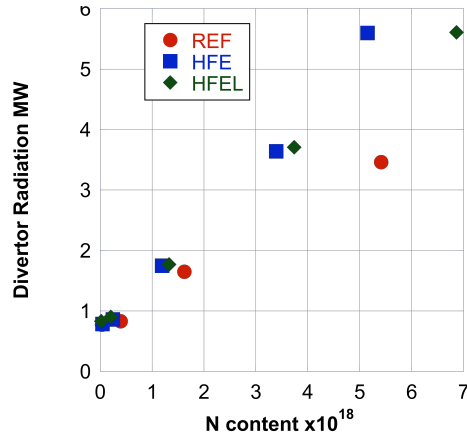

Figure 1.54 - Divertor Radiation versus N content in three modelled cases. REF is a slighly modified experimental plasma. HFE is the high flux expansion case and HFEL is a variant, which minimises the interaction with the innermost tile 1. The plot shows that, according to simulations, the HFE configurations need less N to achieve the same high divertor radiation

In order to distinguish the effects on the divertor radiation due to a possible higher recycling contribution from the interaction with the inner wall, the inner target to X-point distance are different. Predictive simulation using density scans and radiation scans have been done keeping unchanged simulation parameters like, albedo and transport. The simulations have shown so far an increase of radiation on the outer divertor region for both the modified equilibria. Radiation losses are enhanced at mid/high densities ($> 4.5 \times 10^{19} \text{m}^{-3}$): modified equilibria radiate 30% more using a lover N content, *Figure 1.54*. The modified equilibria are also better at confining neutrals: for a given $n_{e,sep,LFS-mp}$ edge2d predicts lower neutral currents crossing the separatrix and subsequently lower CX losses in the core.

Future works aims at simulating a more experimental oriented range of parameters. More details will be given in the paper accepted for the next PSI 2016 conference.

Pedestal Stability Analysis

Understanding the physics that rules the edge transport barrier region (called also 'pedestal') in high performance tokamak plasmas (H-mode) is of critical importance for future burning scenarios. This is because the core confinement strongly depends on the pressure at the top of the pedestal ('pedestal height') as observed in experiments as well as predicted by a range of transport models.
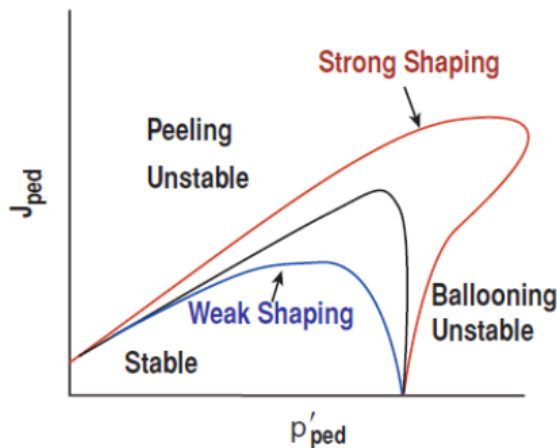
Figure 1.55 - *Schematic of stability boundaries for Peeling-Ballooning limit as a function of pedestal pressure gradient p'ped) and edge current (Jped). Three limits are shown; blue represents a more weakly shaped plasma relative to the black line. The red line represents a strongly shaped plasma*

In the vicinity of the pedestal, edge localized modes (ELMs) take place transporting in quasi-regular bursts, energy and particles to the material surfaces of the divertor. Many theoretical studies of ELMs have focused on MHD instabilities. In the peeling–ballooning model, a key element is that the coupled peeling–ballooning (PB) modes provide an effective limit on the pedestal height (at a given pedestal width) and also drive the ELMs. The two drivers of PB instability are the edge current (Jped) and the pressure gradient (p'ped). Given than, the PB stability boundary can be represented on a plot of Jped versus p'ped as illustrated in Figure 1.**55**. Below the boundary, the plasma edge is stable. Above the boundary, at high Jped, the

plasma edge is peeling unstable. Similarly, at high p′ped the plasma edge is ballooning unstable. The region between peeling and ballooning limited plasmas at high Jped and p′ped is referred to as the PB corner or nose. The stability boundary corresponds to a specific pedestal width. As also illustrated in Figure 1.**55**, the plasma shape, can modify the PB stability boundary: weak and strong refer to deviation from circularity in terms of triangularity (δ) and elongation (κ). A larger pressure gradient and current density can be maintained with high shaping as this favorably moves the PB stability boundary [1.97]. The PB stability boundary is evaluated using an ideal MHD eigenvalue solver, MISHKA-1 or ELITE. First, a plasma equilibrium characteristic of a specified Jped and p′ped is calculated by HELENA, a fixed boundary equilibrium solver. Then MISHKA-1 (or ELITE) evaluates the growth rate (eigenvalue) and mode structure (eigenfunction) for a given toroidal mode number and equilibrium. This is repeated over a range of toroidal mode numbers to find the eigenfunction that minimises the change in potential energy. If, over all n values, the change in stored energy is positive ($\delta W>0$), then the plasma equilibrium is stable and the growth rate is zero. Conversely, if, for any n value, the change in stored energy is negative ($\delta W<0$), then the plasma equilibrium is unstable and the growth rate is non-zero. The eigenfunction corresponding to the highest growth rate defines the most unstable/limiting toroidal mode number. The eigenfunction defines the nature of the limiting mode (i.e. peeling or ballooning). This process is repeated for different values of Jped and p′ped over a 2D grid to define the stable and unstable regions. Typically, the peeling mode is unstable to low n (<5) modes, whereas the ballooning mode is unstable to high n (>20) modes. The PB mode is unstable to intermediate n values (5-20). The PB mode is usually the limiting instability in the pedestal that results in an ELM crash.

An operational point, representing the edge stability of experimental plasma, can be compared to the calculated PB stability boundary. To calculate the experimental equilibrium, the pressure gradient is determined from radial temperature and density profile measurements. The edge current is assumed to be dominated by the bootstrap current and can be calculated using the Sauter's analytical formula. The proximity of the operation point to the PB stability boundary indicates if the plasma edge is stable or unstable. Furthermore, the position of the operation point relative to the PB corner indicates if the plasma edge is peeling or ballooning limited. It is important to note that the PB stability calculation provides the maximum achievable pedestal height for a given pedestal width [1.98, 1.99].

Under the framework described above, a wide activity of stability analysis was carried out during the year 2015. The analysis of Hybrid plasmas for the experiment M13-10 "develop hybrid scenario at low q95" and M13-33 "JET high performance hybrid scenario", useful for planning the experiment M15-02 of the C35 campaign. The purpose of the analysis was to:

(1) determine if the hybrid plasmas with high fusion performance from M13-33 are consistent with marginal peeling-ballooning stability at the pedestal. If this is the case it will increase our confidence in using the peeling-ballooning paradigm in our extrapolations to DT

(2) determine how the pedestal stability varies with q95 from the 3-point scan in M13-10. This would help us to understand what to expect from the pedestal as we optimise q_{95} to maximise fusion performance.

For that analysis, the many plasma discharges have been taken into account for hybrid plasmas and for q-95 scan plasmas. Some results have been discussed in the joint JET/MST1 pedestal-modelling meeting of the 02/03/2015. The discussion focused on the problem of how to obtain reliable pedestal stability analysis for high beta hybrid plasmas.

The Pedestal Stability Analysis is required also in the C35-36 experimental campaign, especially in the following experiments:

- M15-02 Hybrid scenario for DT;
- M15-05 Dimensionless beta scan in low delta baseline;
- M15-12 Pedestal optimization in high shaped plasmas;
- M15-15 Avoiding the ballooning boundary.

The activity related to the experimental campaign is ongoing also during the 2016.

Another important activity is related to the task force T15-02 on pedestal analysis and 51odelling for which is required the use of the CASTOR, that is a non-ideal resistive MHD code. The purpose of the activity is to compare analysis results from ideal (MISHKA, ELITE) and non-ideal (CASTOR) MHD codes.

Figure 1.56 shows the result of the PB stability analysis performed by MISHKA-1, as previously describe. The stability diagrams presented in this section use the dimensionless maximum pressure gradient (α_{max}) instead of the p'_{ped}. The star is the operational point representing the state of a plasma in a specific time of the discharge. The change in colour from blue through to red corresponds to an increase in the growth rate of the most unstable mode. A contour of constant growth rate is used to define the stability boundary. The proximity of the point to the stability boundary indicates the stability of the plasma edge at the time corresponding to the input profile. The location of the stability boundary depends on the pedestal width.
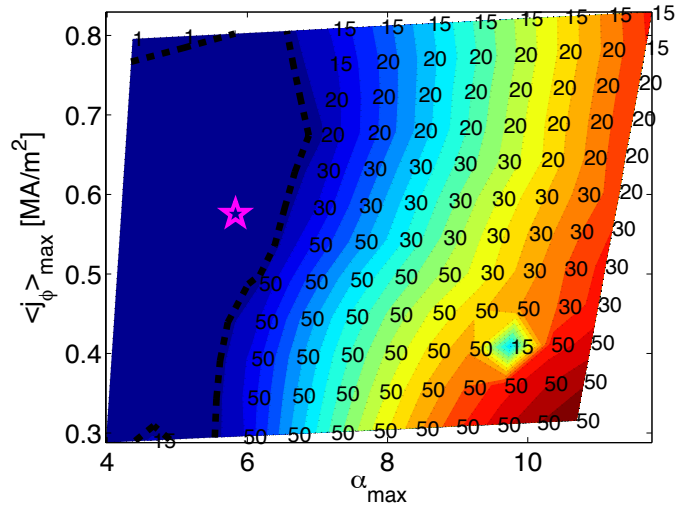
Figure 1.56 - Stability analysis for JET #86533 pulse. Analysis performed by MISHKA-1, using fits to HRTS Te and ne profiles as an input

ICRH modelling for DT plasma and experiment M15-27

A preliminary analysis of the results of the M15-27 experiment about ICRH for DT plasmas has been performed by using TORIC-5 numerical code. In particular looking at the best shots (in terms of the coupled power and collected data) obtained last November.

The coupled power was about 5MW on a plasma target characterized by B_0=3.4T, I_p=2MA with different fraction of minority species: Hydrogen and Helium 3 in a Deuterium plasma. The behaviour of the plasma parameters for the shots number 89192 and 89193 (electron and ion temperatures and density) vs the major radius on the equatorial plane are shown in *Figure 1.57*. Note that the plots of *Figure 1.57* are obtained by data analysis of the related diagnostics and in the simulation we have used an interpolation function.

The results (concerning only the hydrogen minority species) are summarized in *Figure 1.58* where the total absorbed power per channel (ion majority, ion minority, electron Landau damping, IB electron heating) has been reported vs the hydrogen minority concentration. The best transfer of the wave energy on the minority species (at the first harmonic) is obtained for a minority concentration of about 5%. At lower concentration <1% the majority heating at the second harmonic of the deuterium prevails.
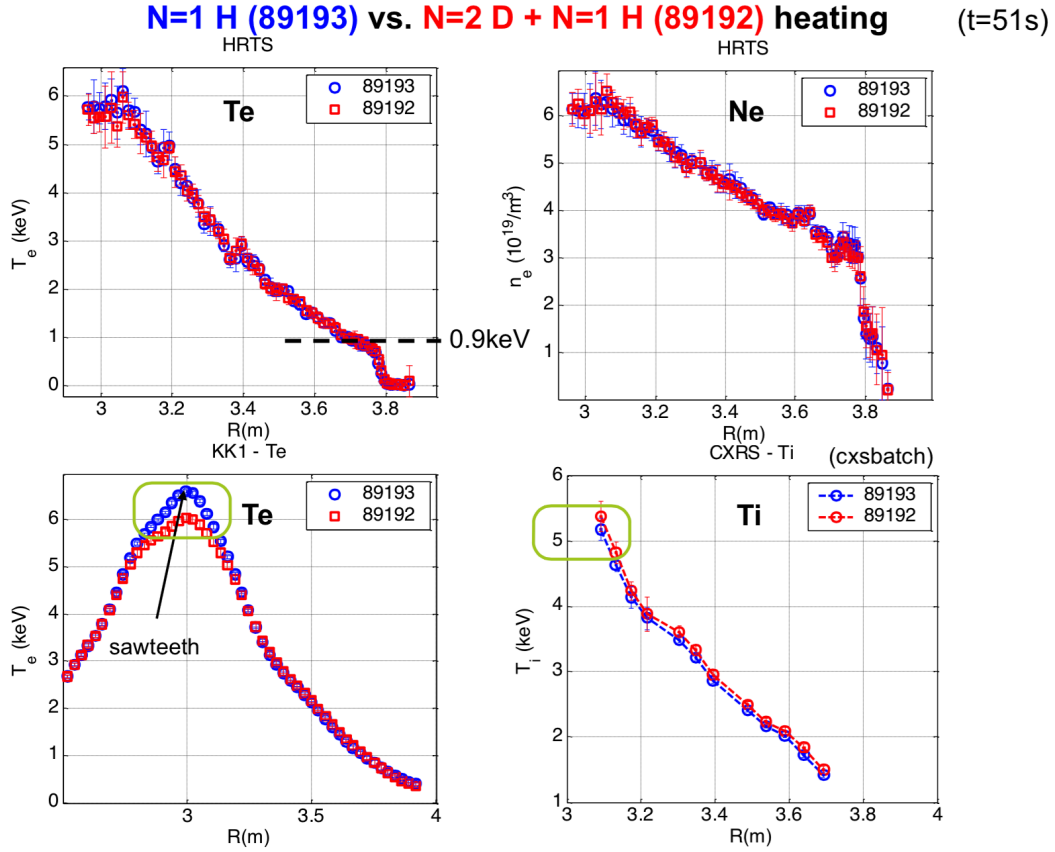
Figure 1.57 - Behavior of the plasma parameters electron (a) & (c), ion (d) temperatures and density (b)) as function of the major radius on the equatorial plane, for the shot number 89192 and 89193 (characterized by $B_0=3.4T$, $I_p=2MA$) of the experiment M15-27. The electron temperature profile has been deduced by means of two diagnostics, HRTS (which includes also the SOL) and KK1 (Interferometer))
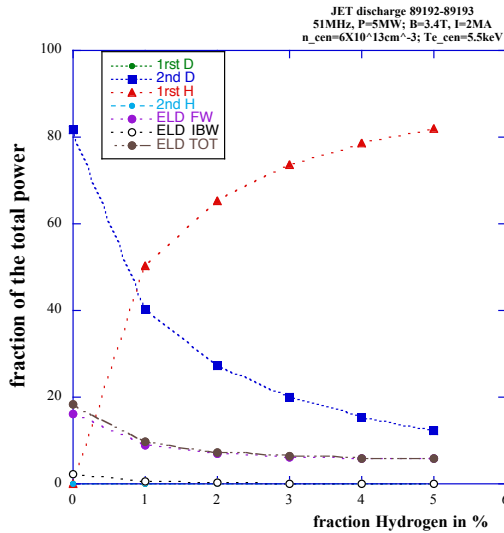

The electron is lower then 20% for all the concentration with a very poor contribution of the IB heating. These results at the end of the campaign must be supplied with a quasilinear analysis by the code SSQLFP in order to study the redistribution of the energy by collisions on the bulk plasma. A more complete analysis including also the ^{3}He minority (instead of the Hydrogen, and combined wit the Hydrogen) is under consideration.

Figure 1.58 - Results of the simulation with TORIC-5 by using the plasma parameters of Fig. 1, for the shot number 89192 and 89193 (characterized by $B_0=3.4T$, $I_p=2MA$) of the experiment M15-27. The plot shows the fractional distribution of the power vs the minority concentration, on the various species, electron, ion majority (Deuterium and ion minority (hydrogen), and also on the various heating channels: fundamental resonance absorption, first harmonic, ELD and IBW mode converted wave.

Development of advanced tools for plasma shape control

The 2015 activities mainly included the development of scenarios for the eXtreme Shape Controller and the Current Limit Avoidance Systems for the plasma configuration named V5D-HFEL. The use of this XSC/CLA setup is envisaged for the experiment M15-20 "Seeding to maximum f_{rad} towards high P_{sep}/R" to control plasma shapes with higher flux expansion in the divertor region.

The commissioning and use of these scenarios is planned in the first quarter of 2016.

Equilibrium reconstruction code: JEC2020 benchmark and constraints

As it is well known, in Tokamaks the configuration of the magnetic fields remains the key element to improve performance and to maximise the scientific exploitation of the devices. On the other hand, the quality of the reconstructed fields depends crucially on the available measurements. In 2015 the team of Tor Vergata University has continued the benchmarking and validation of the new equilibrium code of JET, called JEC2020, using both internal and edge constraints. In particular the work has focused on the improvement of reliability of the polarimeter constraint and on the development of a new iron model to overcome the issues encountered with the previous one.

For the offline analysis, a set of interesting discharges for the analysis of the equilibrium in the core and pedestal, for which the main diagnostics are validated (pressure, polarimeter, MSE etc), has been identified in consultation with the old Task Forces. For the core a list of about 40 shots has been selected: they include baseline and hybrid scenarios.

For the list and for details refer to the wikipage: Task Force Meeting – 5 February 2015, M. Gelfusa "Status of the T13-19 task: Exploitation and validation of JEC2020" and for Task T13-19: review meeting 29th January 2015. [1.100]

Scaling Laws

Scaling laws of the confinement time are essential both to design future devices and to understand the physics of confinement. In the Tokomak community, all the proposed scaling laws are in power law form. The University of Tor Vergata has developed a method, based on Symbolic regression and genetic computing, to derive scaling laws without any constraints on their mathematical form. The technique has provided interesting results on the expectations for ITER using both dimensional and dimensionless quantities. Moreover, an extension of the method has allowed to test whether the traditional dimensionless variables are adequate to interpret the available data. [1.101]

Assessment of pellet pacing efficiency

The Group has also applied a new method to assess the efficiency of ELM Pacing with pellets. The technique is based on an information theoretic criterion and has shown how JET pellets are significantly more effective in triggering ELMs than previously believed. [1.102]

Plasma instabilities studies

The work carried out by the researchers of the University of Cagliari has been done within the Work Programs JET1 and MST1. In particular, the work has been focused on the headlines H-1.2 *Operation with reduced or suppressed ELMs* and H-1.3 *Avoidance and mitigation of disruptions and runaway electrons*.

Disruptions studies. The activities performed during 2015 in the field of disruption classification and prediction have been focused on different issues:

− a support activity for maintenance and update of the disruption database for ILW campaigns has been done by developing an interactive tool for check and automatic calculation of relevant parameters (thermal quench, current quench rate, etc.). In *Figure*

1.59, one of the implemented panel available for the analyses is shown. The tool has been proposed and tested on the discharges of recent campaigns in both JET and ASDEX-Upgrade (AUG) [1.103] and it can support the operators in a very time consuming activity, reducing significantly the possibility of human errors. The underlying algorithm performs its choice on the base of shared and defined criteria discussed with the Plasma and Control Operation Groups of the considered devices. Moreover, being the algorithm fully parameterized, it can be easily customized to other tokamaks and/or it can be used for statistical purposes, according to criteria adopted in the framework of each device.
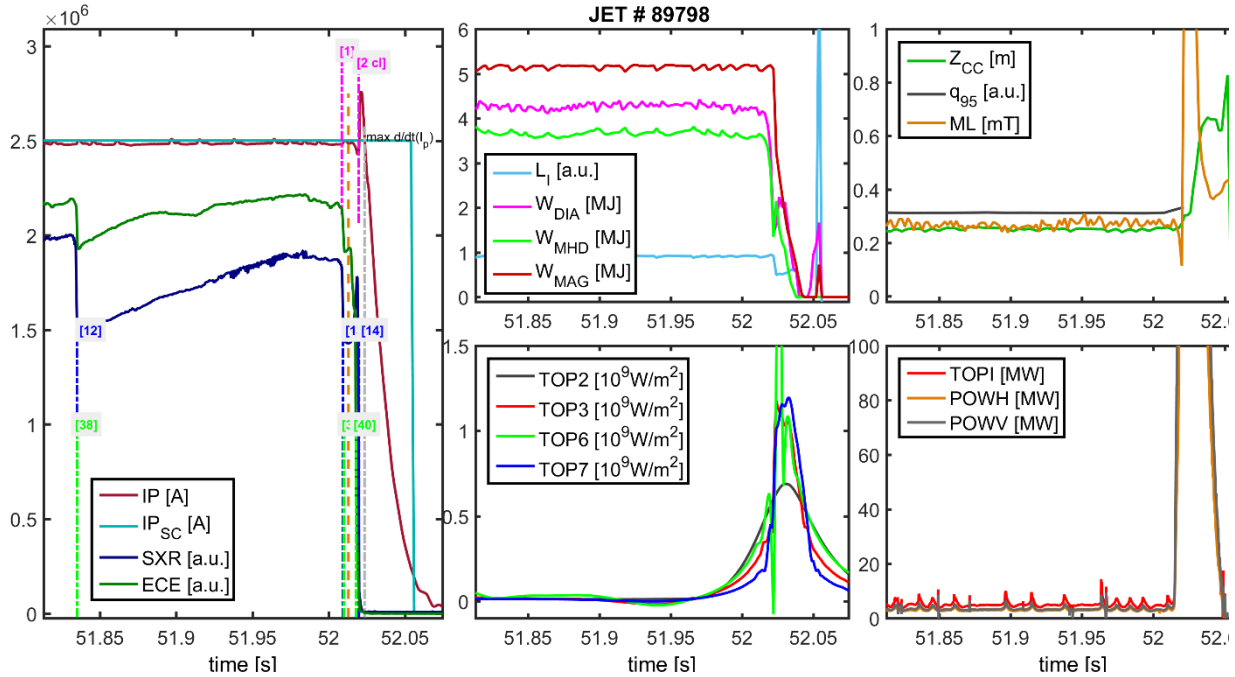
Figure 1.59 - Tool interface for main disruption analyses. Example: discharge No. 89798 - experiment M15-17 on "Optimization of disruption mitigation at high Ip". Left side: Plasma current (IP), current requested by the Shape Controller (IP$_{SC}$), elaborated ECE averaged central channels (ECE) and SXR central LOS time evolution for thermal quenches estimation (respectively vertical dashed lines in green and blue); vertical dashed lines in magenta are indicative of current spikes correlated with thermal quenches detected both by ECE and SXR elaborations. Central column top: Internal Inductance (L$_i$) and Plasma Stored Energies (Diamagnetic (W$_{DIA}$), MHD (W$_{MHD}$) and Magnetic (W$_{MAG}$)). Central column bottom: KB1 bolometer signals in the four octants (2,3,6,7). Right side top: Plasma Current Vertical Centroid position (Z$_{CC}$), Safety Factor at 95% of the poloidal flux (q$_{95}$) and Locked Mode signal (ML). Right side bottom: Total Radiated Power evaluated by KB5 bolometer (estimation by both cameras (TOPI), and estimation through horizontal (H) and vertical (V) cameras (POWH and POWV respectively)

- In [1.104] an automatic disruption classification for JET with carbon wall (CW) was developed using the nonlinear generative topographic map (GTM) manifold learning technique. It was tested using an extensive database of JET discharges selected from JET-CW campaigns from 2005 up to 2009. The success rate of the classification was extremely high, reaching for some classes even 100%. However, the new full-metal ITER-like wall (ILW) at JET was found to have a deep impact on the physics of disruptions at JET. Hence, the disruption classes in the JET-ILW have been deeply analyzed and compared with those in the JET-C and a new GTM map has been trained for JET-ILW [3]. In order to assess the performances of the classifier, its potential real-time application has been tested in conjunction with the prediction system APODIS, for the non-intentional disruptions belonging to the classes described in [1.105], selected from JET-ILW

campaigns from 2011 up to 2013. In Figure 1.60, an example of GTM classification is reported. The obtained results assessed the suitability of the GTM based classifier for real time applications with good performance: the prediction success rate was quite high (87%) according to the manual classification. The good results motivate the deployment of this tool in the real time digital network (ATM) of JET.
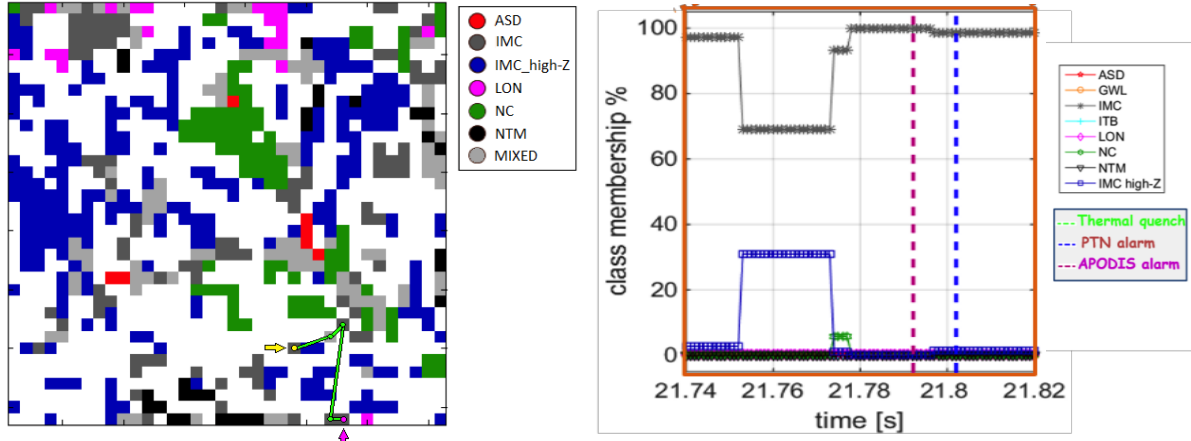

Figure 1.60 - Left side: projection of the discharge No. 82569 (which has been manually classified as an IMC IMpurity Control problem disruption) on the GTM map of the disruption operational space of JET-ILW. The map nodes are represented with different colors as indicated in the legend, empty nodes are white; the green line represents the discharge trajectory, it starts from the yellow dot and terminates in the magenta dot; Right side: class-membership functions of the same disruption. The vertical green dashed line identifies the thermal quench, the vertical blue dashed line the PTN alarm, and the vertical pink dashed line the APODIS alarm (for each sample and each class, the class membership is defined as the percentage of samples of the considered class in the node of the GTM to which the sample is associated, with respect to the total number of disruptive samples in the node itself). The class membership of IMC is the highest, then the GTM correctly classifies the discharge as IMC.

– Extensive studies on automatic data-based disruption prediction has been performed by the research group. Among them, the mapping of the n-dimensional plasma parameter space of a tokamak has been successfully used to develop a disruption predictor for AUG [1.106]. Various criteria have been studied to associate the risk of disruption of each cluster in the map to a disruption alarm threshold. Recently, an alternative statistical disruption predictor based on a logit model for AUG has been proposed [1.107]. The novelty of the approach consists in a criterion, based on the Mahalanobis distance, to assess a specific disruptive phase for each disruptive discharge. The global success rate is very good, higher than 91%. The obtained results confirm that enhancements on the achieved performances on the logit model predictor are possible by defining a specific disruptive phase for each disruption.

– Both the developed disruption prediction and classification tools behave quite good in the considered machine. However, in order to extrapolate results from existing devices to the next step ones, it is crucial to interpret the multi-machine plasma confined experiments data with a firm physical basis. The definition of common basis and criteria for cross-machine analysis would facilitate the development of portable systems for disruption prediction and classification, which is becoming of increasingly importance for the real-time plasma control and operation. To this purpose, two data bases have been built containing flat-top disruptions occurred at JET with ILW from 2011 to 2012 and occurred at AUG from 2011 to 2014. Their analysis highlights that several physics instabilities in AUG are also usual disruption precursors in JET. Then, the considered AUG discharges

have been clustered in different classes following, where possible, the criteria proposed for JET in [1.108]. It has been found that the distribution of the same classes of disruptions is not directly comparable due to technical differences in the two machines, as different heating schemes, and is strongly influenced by the scientific program and/or by the number of sessions devoted to a given program [1.109]. The availability of common disruption classes for the two machines allowed us to perform an analysis aiming to identify a robust set of dimensionless parameters, with particular reference to basic quantities available in real-time in different machines. The raw signals have been processed in the time and frequency domains in order to synthesize non-dimensional indicators fitting both the considered devices. In particular, the validity of the integration of the developed data-based predictors and classifiers with such physics-based indicators has been assessed by using the locked mode (LM) signal as disruption predictor. The performance of the LM indicator has been compared with that of the LM raw signal, which is commonly used both at AUG and JET to trigger the mitigation system, showing a significant improvement of at least 10% of the successful predictions.

ELM studies. The studies on Type-I ELM aim at identification of statistical properties of ELM intervals, dynamical characterization, and advances in the physics understanding.
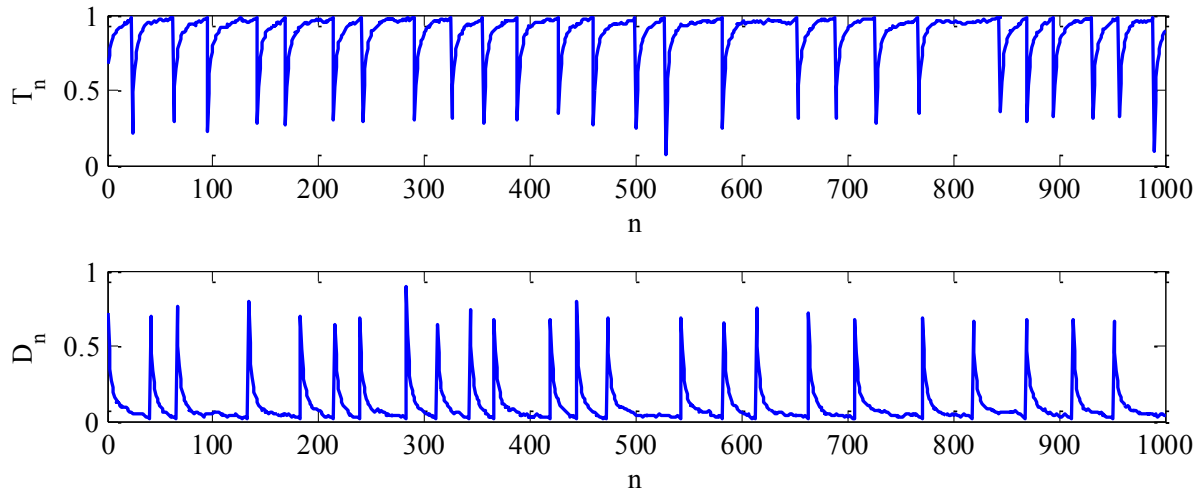
Figure 1.61 - Temperature and D_α nearly periodic oscillating time series obtained through the proposed qualitative model. Both the series are in agreement with experimental behaviours: temperature time series exhibits slow growth towards an equilibrium value and fast decay; D_α shows a fast growth interrupted by a slow crash that can be related to the critical pressure gradient, consistently with the peeling-ballooning model

In particular, the dynamic characteristics of Type-I ELM time-series from the JET tokamak with the CW and the ILW have been investigated [1.110, 1.111, 1.112]. The dynamic analysis has been focused on the detection of nonlinear structure in line integrated electron density, total outer divertor Beryllium, D_α photon flux, and top pedestal electron temperature time series. The method of surrogate data has been applied to evaluate the statistical significance of the null hypothesis of static nonlinear distortion of an underlying Gaussian linear process. Several nonlinear statistics have been evaluated, such us the time delayed mutual information, the correlation dimension and the maximal Lyapunov exponent. The obtained results give evidence of underlying nonlinear dynamics. Moreover, no evidence of low-dimensional chaos has been found; indeed, the analyzed time series are better characterized by the power law sensitivity to initial conditions (PSIC), which can suggest noise contaminated quasi-periodic motion at the "edge of chaos", i.e. at the border between chaotic and non-chaotic dynamics.

Interpreting ELM time series from the standpoint of PSIC is a fundamental information to approach at the choice of a proper dynamical model, which is the subject of present investigations [1.111]. In particular, recurrence plots have been applied to investigate the characteristics of Type-I ELM time-series of JET with CW [1.112]. Recurrence plots of temperature time series show patterns similar to those characteristic of signals exhibiting type II intermittency, in particular, a characteristic kite-like shape. Starting from this similarity, a qualitative model of temperature and D_α time series has been derived starting from a type II intermittency model (see *Figure 1.61*)

ICRF Antennas Analysis with TOPICA. All the results related to the Ion Cyclotron A2 antenna analysis and performance prediction were obtained with the help of TOPICA code, a numerical tool developed by the Plasma Facing Antennas (PFA) group at Politecnico Torino, DET, Italy.
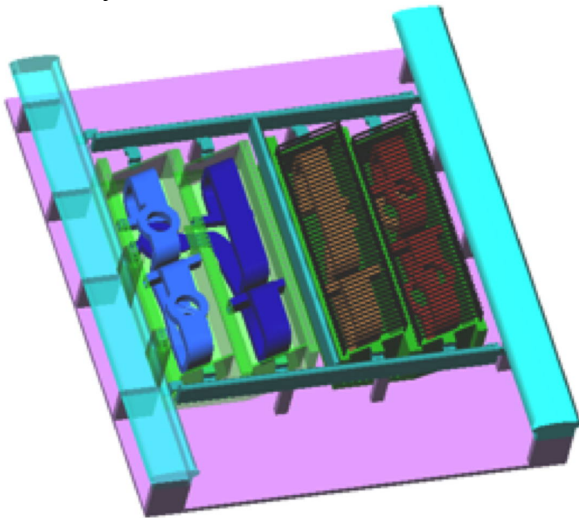
Figure 1.62 - The 3D flat antenna model
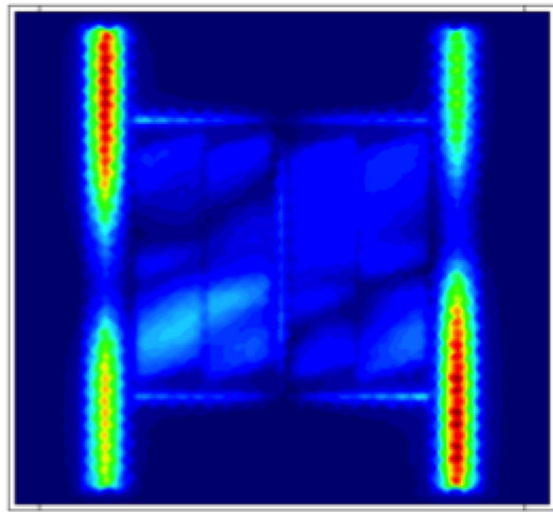
Figure 1.63 - Antenna electric field pattern for $0\pi 0\pi$ phasing

The main activities pursued with TOPICA code on the JET A2 antenna were related to the evaluation of the input parameters, the electric field distribution (in front of the IC antenna) and, above all, the current flowing on specific geometrical elements such as the side limiters.

The 3D flat antenna model reported in `Figure 1.62` was adopted, together with few measured plasma profiles, both L and H modes. In order to account for measurement imprecision, an average procedure was included to provide more realistic plasma profiles; in addition, radial shifts of ±1cm were applied to estimate the effect on the antenna performances due to the distance between the launcher and the plasma cut-off.

A clear dependence of the electric field and currents to the input phasing of the antenna was enlighten, as shown on `Figure 1.63` for $0\pi 0\pi$ phasing. Several input configurations were tested (phasing and power division) in order to optimize the antenna operative behavior. Good agreement was eventually observed between code predictions and experimental evidences.

The very same analysis was performed at 33MHz and 42.5MHz.

1.2.2 – WP JET3 Technological Exploitation of JET DT Operations

The objective of *WP JET3 - Technological Exploitation of JET DT Operations* is to take advantage of JET operations with tritium and of significant 14 MeV neutron production to improve our knowledge and validate current assumptions on ITER relevant issues, and thus reduce the risks and uncertainties in ITER plant operation & management.

This will be pursued by providing a consistent and complete analysis of JET tokamak "nuclear case", including the accurate measurement of the neutron source and radiation field in the device and in the surrounding areas, the neutron induced activity and dose rates in

components and materials, the radiation damage in ITER relevant materials, tritium retention in plasma facing materials, the waste production and characterization, and the occupational dose. The collected data are used to validate codes, nuclear data and assumptions used in the preparation of ITER operation and plant management, and relevant also to DEMO design.

To this purpose the following objectives and the related specific Sub-Projects have been identified:

- *Neutron detector calibration at 14-MeV neutron energy* - NC14
- *Validation of neutronics and activation codes* - NEXP
- *Tests of neutron and tritium detectors for Test Blanket Modules (TBMs)* - TBMD
- *Data validation for the activation predictions of ITER materials* - ACT
- *Studies of irradiation damage on functional materials* - RADA
- *Measurements of tritium retention and outgassing, and of airborne tritium* - TRI
- *Collection of operational experience on occupational dose* - NSAF
- *Studies on waste production and characterization* - WPC
- *DEMO-relevant studies: Fuel Cycle* – DFC
- *Characterisation of neutron field, activation and dose rates* – NCAL

WP JET3 Management

ENEA has the leadership of the whole Work Package, as well as of Sub-Projects NC14, NEXP, TBMD, and a participation in all Sub-Projects except RADA, WPC, DFC and NCAL. The WP JET3 activity started in January 2014, and the final Project Management Plan (PMP, version 1.1) was approved by the Project Board during its first meeting on 14th of April 2014. The kick-off meeting and the first Project Team meeting were held in Culham on June 10-11, 2014. The first General Monitoring Meeting was held in Culham on December 2-4, 2014 followed by a Project Team Meeting, during which the revised PMP (version 1.2) was released.

In the following, the activities carried out and results achieved in WP JET3 in 2015 are summarized. In general, a very significant progress in the activities has been obtained in all cases in 2015 [1.113], and the required design reviews have been completed or is close to completion for most of new installations. The 2nd General Monitoring Meeting was held in Culham on December 8-10, 2015. A Project Team Meeting was held on the 11th of December 2015 to elaborate the revised PMP (version 2). The previous JET3 PMP versions 1.1 (April 2014) and 1.2 (Jan 2015) had been based on the JET S1-2018 schedule leading to 100% tritium and DT operation in 2017. A new JET 2020 schedule (S2-2020), which would lead to JET operation until 2020, with a tritium campaign in 2018 and DT campaign in 2019, has been recently proposed. As it is now clear that S1-2018 will be not be adopted, the revised version of the PMP (PMP vers.2) has been prepared to align the Project activities in 2016-2020 to the new S2-2020 schedule though it has not been formally approved yet. The Project objectives have not been modified, the scope is substantially unchanged, whereas the time plan has been revised accordingly for the 2016 – 2020 period, including the related resources.

NC14: 14 MeV neutron calibration

An accurate calibration of JET neutron detectors - ^{235}U fission chambers (KN1) and the in-vessel activation system (KN2) - at 14-MeV neutron energy is needed to allow accurate measurements of the fusion power and of plasma ion parameters during DTE2. It is also needed in order to fully exploit the nominal neutron budget available, and to obtain a full scientific return for the investment in DTE2 [1.114, 115]. The 14-MeV neutron calibration will take advantage of the experience gained with the 2013 calibration of JET neutron detectors with 2.5 MeV neutrons [1.116, 117], and will also benchmark the calibration

procedure envisaged in ITER where neutron detectors have to provide, with an accuracy better than 10%, not only the fusion power but also the amount of tritium burnt for tritium accountancy. (Institutes involved: CCFE, ENEA, ENEA-CNR, IPPLM, KIT, VR, MESCS).

In 2014 the following milestone were achieved:

- A neutron generator (NG), suitable for the purpose and compliant with the requirements of the use of RH in JET torus hall, was selected in collaboration with the JET Operator. The procurement contract was signed in Dec. 2014, with delivery date in Sept. 2015. Two neutron generator units were purchased to mitigate the risks associated to a failure during the in-vessel calibration.

- The neutron laboratory was selected for the calibration and characterization of NG (The National Physics Laboratory (NPL, Teddington, UK) and the contract signed at the beginning of 2015.

- The selected neutron source "monitoring" detectors include: a CVD single crystal diamond spectrometer by ENEA; a Si-diode by JOC; activation foils by IPPLM. The neutron source "calibration/characterization" detectors include: two long counters and activation foils by NPL; a single-crystal diamond detector by CNR; a NE-213 organic liquid scintillator by KIT.

Figure 1.64 - The two NG units VNIIA ING-17 (left) and the power supply and control unit (right)

- The two NG units and the power supply/control unit were delivered and the acceptance tests were completed in October 2015 (*Figure 1.64*). The neutron emission rate was $\sim 2\cdot10^8$ n/s for both units.
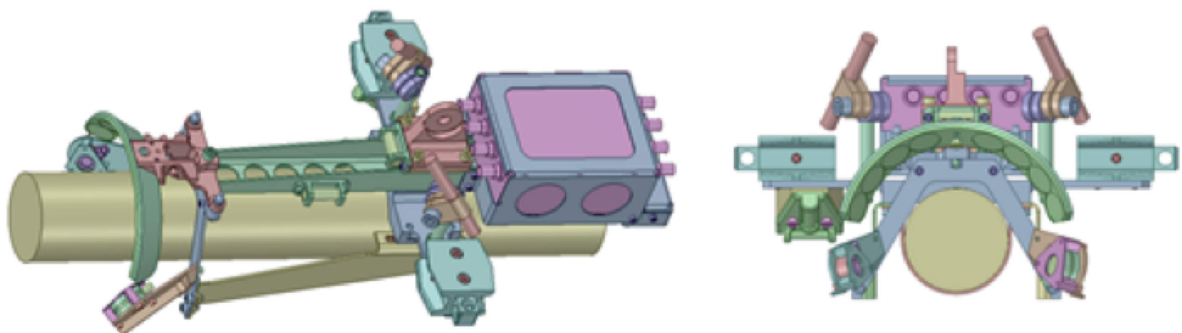
Figure 1.65 - The Neutron Generator with the mechanical tools designed for MASCOT handling, and to support the monitoring detectors (diamond detector and Si-diode on the lateral wings, activation foils on the "horse-hoe"), the pre-amplifier, and two lasers for NG positioning under KN2

- The mechanical support needed to handle the NG and for hosting the monitoring detectors has been designed, and manufactured by the JET Operator. It consists of a light aluminium structure to host a diamond detector and Si-diode on the lateral wings, the activation foils on a "horse-hoe" support, a pre-amplifier, and two lasers for NG positioning under KN2 (*Figure 1.65*).

- *Preliminary Remote Handling Case* and *Safety Case* have been produced by the JET Operator.
- *Monitoring and characterization detectors were characterized at home laboratories.* The response of the ENEA single crystal diamond (SCD) detectors (monitoring) and a compact MCA digitized, used with a single channel charge preamplifier, has been characterized in terms of absolute efficiency, time stability and resolution at the 14-MeV Frascati Neutron Generator (FNG) [1.118]. In order to study the response of the monitor to different energies the diamond detector was
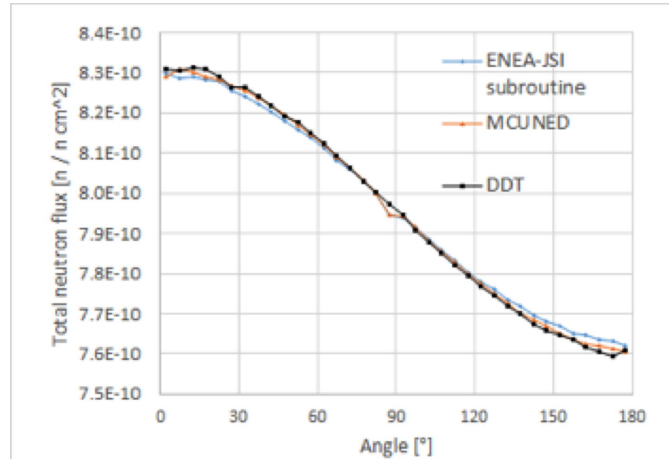
Figure 1.66 - Dependence of the NG neutron emission on the emission angle (D+ beam energy E= 100 keV)

positioned at 22 different angles from -90° to 120° in front of FNG neutron target using a step motor. The absolute efficiency of the SCD was obtained calculating the predicted flux at the SCD positions, using MCNP-5 code with a source subroutine containing a detailed description the energy-angle distribution of the neutrons produced for the acceleration energy and target data used at FNG. The total counts in the $^{12}C(n,\alpha)^{9}Be$ peaks were used to calculate the detector efficiency and compare it with the measured one, using the number of ^{12}C atoms in the detector volume and the value of the $^{12}C(n,\alpha)^{9}Be$ reaction cross section. Agreement was found within the total experimental uncertainties (≤4.5%).
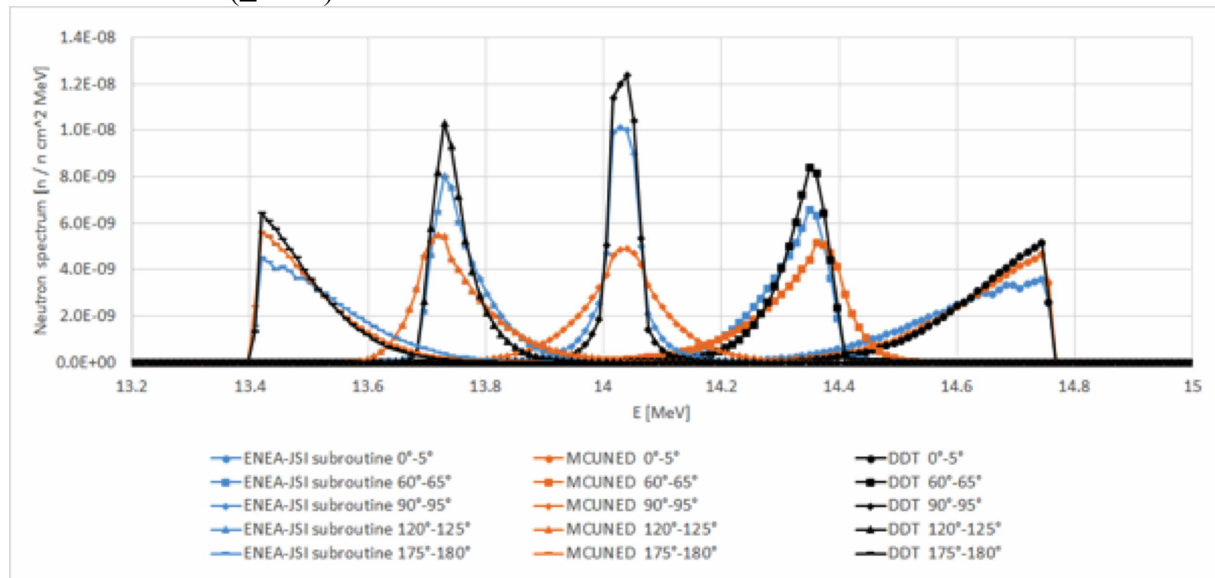
Figure 1.67 - Neutron spectrum for different neutron emission directions (D+ beam energy E= 100 keV)

- *Neutronics modelling of NG, activation and dose rates calculations.* The in-vessel calibration will rely on extensive neutronics analyses to derive the calibration factors related to the plasma neutron source from those measured by deploying the NG inside the vessel. For these reasons, a detailed and validated MCNP model of the NG and source routine are needed.

Simulations of the source of neutrons in the DT neutron generator were performed using three different codes which simulate the slowing down of deuteron ions in a Ti target, and

the DT reaction kinematics: the ENEA-JSI subroutine used at FNG, MCUNED and DDT. The dependence of the total neutron flux on the angle and the neutron energy spectra at different angles are shown in *Figure 1.66*, *Figure 1.67* as calculated by the 3 codes for a deuteron beam energy E= 100 keV. An MCNP model of the neutron generator has been developed according to the information on the configuration and material composition provided by the supplier. This model with the ENEA-JSI source routine has been used to predict the neutron energy spectra and the anisotropy profiles expected from the NG.

The *Detailed plan of calibration/characterization measurements* was elaborated in June based on the detector characteristics (efficiency, counting time) and on the assumption that the NG would operate in continuous mode for 20 minutes, followed by 20 minutes of cooling time. In the plan, the number of measurements of the NG emission rate and energy spectra at given angles were defined in details for both the NG tubes, including contingency. The NG characterization campaign at NPL actually took place from 9th to

Figure 1.68 - Neutron generator with the mechanical tool hosting the monitoring detector, in the configuration characterized/calibrated at NPL

20th November 2015 according to the prepared plan (*Figure 1.68*, *Figure 1.69*), with the participation of CCFE, ENEA, ENEA-CNR, IPPLM and KIT.
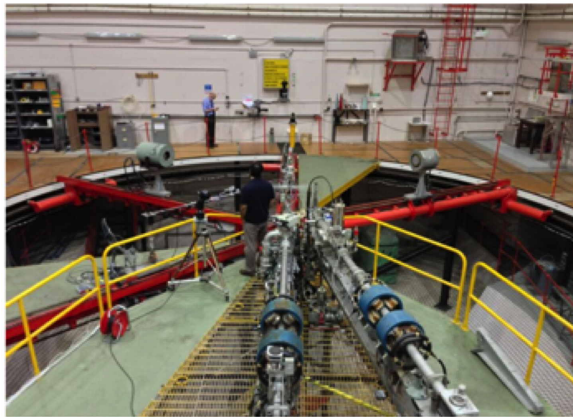
Figure 1.69 - Left: The NG in the centre of the low-scattering hall at NPL where it has been calibrated/characterized. The NG was located in the centre of the circular rotating platform. Right: The JET3 NC14 team participating in the NPL campaign

The characterization plan was completed, in particular: NG#1 and to a sufficient extent NG#2 were tested, the emission rates at many different angles were measured and the anisotropy profiles, from which the total yield in 4π will be derived, was obtained, the neutron tube cylindrical simmetry was checked, the neutron spectra at several different angles were measured - they show interesting features from which information about the D/T mixtures in the beam and in the target can be derived, the stability the monitoring detectors attached to the neutron generators were tested and their calibration factor obtained. The analysis of all measurements will be completed in March 201.

NEXP: Validation of fusion neutronics and activation codes

The validation of neutronics codes is addressed with *ad hoc* experiments in JET in fusion relevant conditions, with the appropriate neutron source and environmental complexities to validate the codes used in ITER design to predict quantities such as the neutron flux along streaming paths, the activation of materials, as well as the resulting shutdown dose rates.

In the Neutron Streaming Experiment, neutron fluence and dose measurements are performed by thermoluminescent dosimeter (TLDs). In this campaign, also activation foils placed in several positions inside and outside the Torus Hall (TH) to provide cross-calibration with the TLDs [1.119, 1.120, 1.121].

In 2015 TLDs and activation foils assemblies were produced by IPPLM and HELL on the basis of previous experience and pre-analyses. The TLDs and activation foils were installed at JET in 22 positions in November 2015. The TLDs positions are the same as in 2013 experiment, plus six new positions in South East Basement, in J1F Bunker, in J1E and in Baking chimney at the basement level. Activation foils were located in six positions inside the TH, close to TLDs.

Pre-analyses of the streaming experiment were performed by CCFE, MESC and HELL. CCFE carried out neutron streaming calculations for the JET TH and surrounding areas. To decrease the computational time required for the neutron streaming calculations, the ADVANTG code has been used to generate weight windows. ADVANTG took approximately 4 hours on 16 processors to generate the weight window and the MCNP was run for 10000 CPU minutes. The previous MCNP calculation lasted about a week to generate the weight window and ~3 days on 64 cores to generate the results. The results of this pre-analysis are shown in *Figure 1.70*.
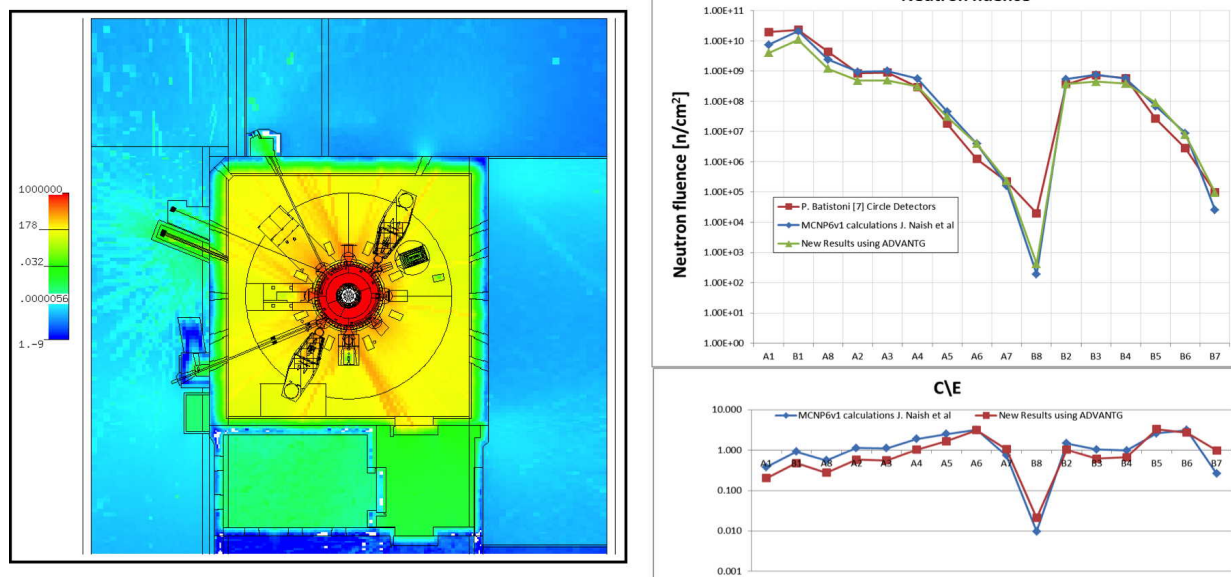

Figure 1.70 - Left) Neutron fmesh tally map calculated with MCNP5 using weight windows created by ADVANTG; Right) Comparison of the calculated neutron fluence with MCNP6v1, MCNP5 accelerated by ADVANTG and the TLD measurements of 2013 DD campaign

Several activities were also performed for the preparation of the *Shutdown dose rate experiment* [1.122]. The design of the detectors assembly was completed as well as the review and approval of the measurements to be carried-out during DD shutdown. Three spherical air-vented ionization chambers (IC) were procured by ENEA and KIT for ex-vessel decay gamma dose measurements during JET shutdown. Activation foils assembly were also provided by HELL to perform neutron fluence measurements close to ICs. The two ENEA ICs and one activation foil holder will be located at the side port of Octant 1. The IC of KIT together with the second activation foil holder will be located on the top of ITER like Antenna (ILA) in Octant 2. Low noise special cables 100 m long have been installed to connect the ICs to the electrometers located in J1D and the high voltage and acquisition of the chambers will be

remotely controlled. Aproper software has been developed by ENEA for the on-time acquisition during off-operational periods.
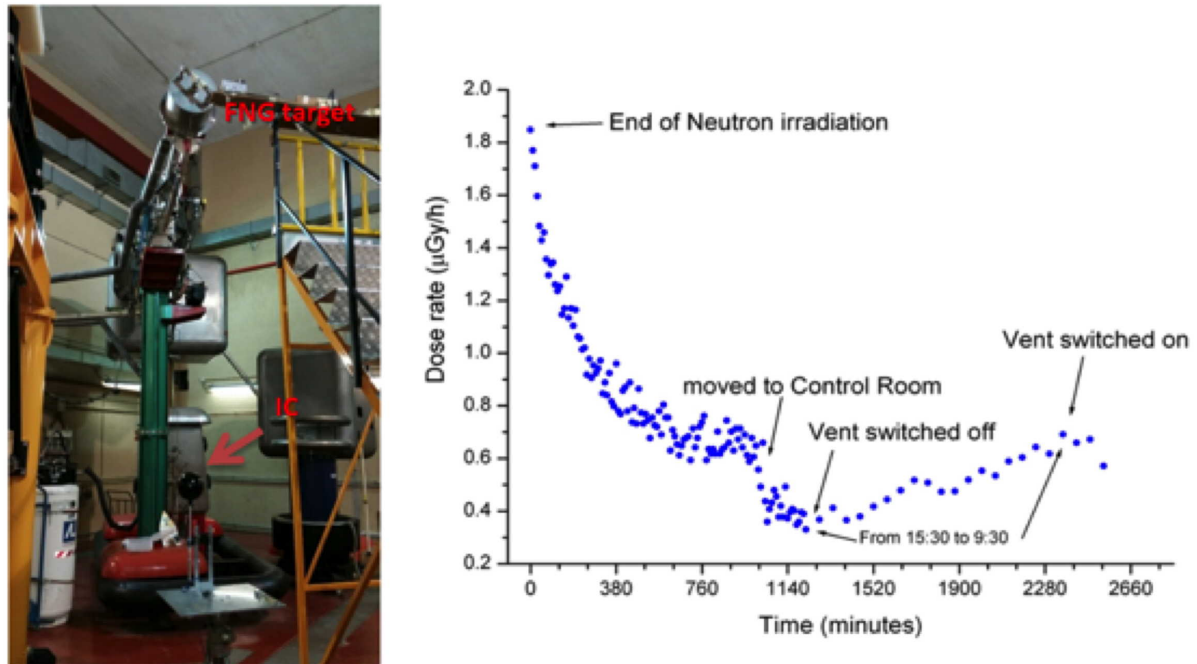

Figure 1.71 - Left) Installation of the ionization chamber in the FNG bunker; Right) dose rate versus time after 14 MeV neutron irradiation

The ENEA ICs were calibrated at ENEA-INMRI (Istituto Nazionale di Metrologia delle Radazioni Ionizzanti) from 30 keV to 1.3 MeV. KIT IC was cross-calibrated with ENEA IC at the gamma calibration laboratory of ENEA-INMRI under ^{137}Cs gamma sources. A very low systematic difference in the measurement of the collected charge of about 0.5 % was observed, with an average charge ratio KIT/ ENEA of 1.005.

Natural background dose measurements were performed in Frascati to confirm the stability. Tests were also performed at FNG under 14 MeV neutron irradiation (*Figure 1.71*) to verify the capability of the system to perform on-line decay gamma dose rate measurements and to check for neutron-induced self-activation of the detectors.
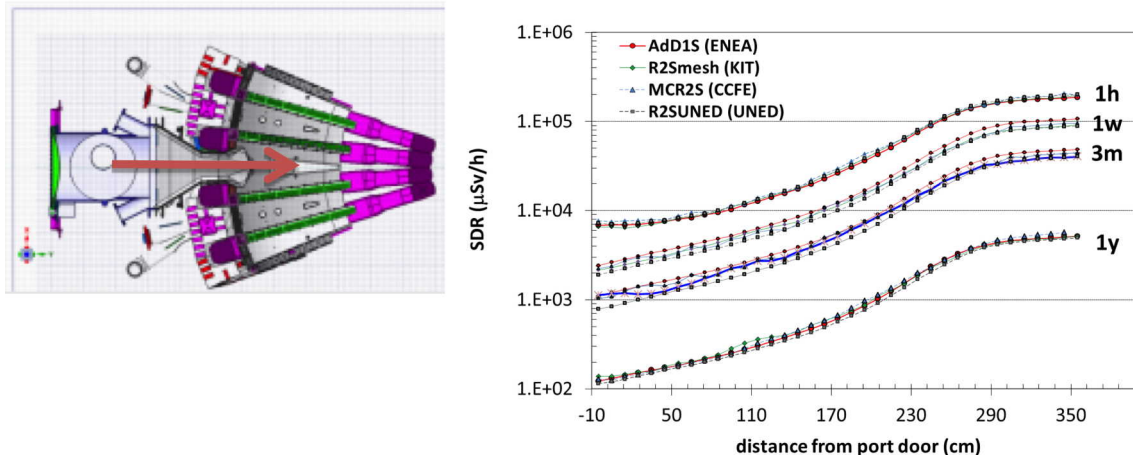
Figure 1.72 - Shutdown dose rate results of the 2015 simulations versus distance from port door calculated with Advanced D1S, R2Smesh, MCR2S and R2S-UNED at various time after DTE-2 shutdown

The tests were successful and confirmed the high stability of the systems to measure background level and to follow gamma dose decay at the end of irradiation as well as insignificant activation of the detectors. The ICs and electronics were shipped to JET in December 2015 and these will be installed in Octant 1 and 2 in January 2016.

Regarding the calculation part, many efforts were devoted to understand the discrepancy among the Advances D1S (ENEA), MCR2S (CCFE), R2SUNED (UNED) and R2Smesh (KIT) codes observed in 2014 calculations. In particular the calculations at 1 week and 1 year after DTE2 shutdown done in 2014 were repeated using the same neutron/gamma mesh in R2S codes, same nuclear data and tallies. On the basis of the ACAB files provided by UNED it was verified that Advanced-D1S included the dominant activation reactions except for the production of Co-57 that can provides a contribution at 1 year after shutdown. New calculation including Co-57 was performed by ENEA.

The new simulations resulted in a sensible reduction of the differences observed in 2014 study with a general agreement within ±20% over the whole temporal range for mid-port calculations in Octant 1 (*Figure 1.72*). At 1 year from shutdown the MCR2S (CCFE) results are generally higher and R2SUNED (UNED) are generally lower than the other codes. R2SUNED shows the same trend as Advanced D1S. Advanced D1S, R2Smesh and R2SUNED codes agree also very well in the ex-vessel position, whereas MCR2S results are generally higher. R2SUNED and MCR2S code provide the same results when the decay gamma source is exchanged. Hence the observed differences between R2S codes can be due to the different method used to evaluate the neutron flux (cell-under-voxel in R2SUNED and voxel-averaged in MCR2S).

TBMD: Tests of neutron and tritium detectors for Test Blanket Modules (TBMs)
The development and testing of nuclear instrumentation for on-line measurement of neutron/gamma fluxes and tritium production in ITER TBMs is required as such instrumentation will have to withstand the harsh working conditions expected in the TBMs. Several detectors are currently under development by F4E for this purpose. It is planned to test these detectors in JET during DTE2 in the frame of JET3-TBMD in the relevant fusion environment, high temperature (up to 300 °C), magnetic field (up to 3 T), and high level of radiation fluxes ($>10^{12}$ n/(cm^{2}s), $>10^{12}$ γ/(cm^{2}s)).

CCFE has proposed foil activation neutron spectrometry using the internal activation system available at JET (KN2). HAS proposes the Secondary Charged Particle Activation (SCPA) method to measure the tritium production, which consists in the measurement of the activity induced in a suitable material (indicator) by the triton generated in the ^{6}Li(n, t) reaction. A Neutron Activation System is planned in the TBMs although preliminary information are available about it. Based on the preliminary design information it was concluded that the SCPA method can be applied in this system.
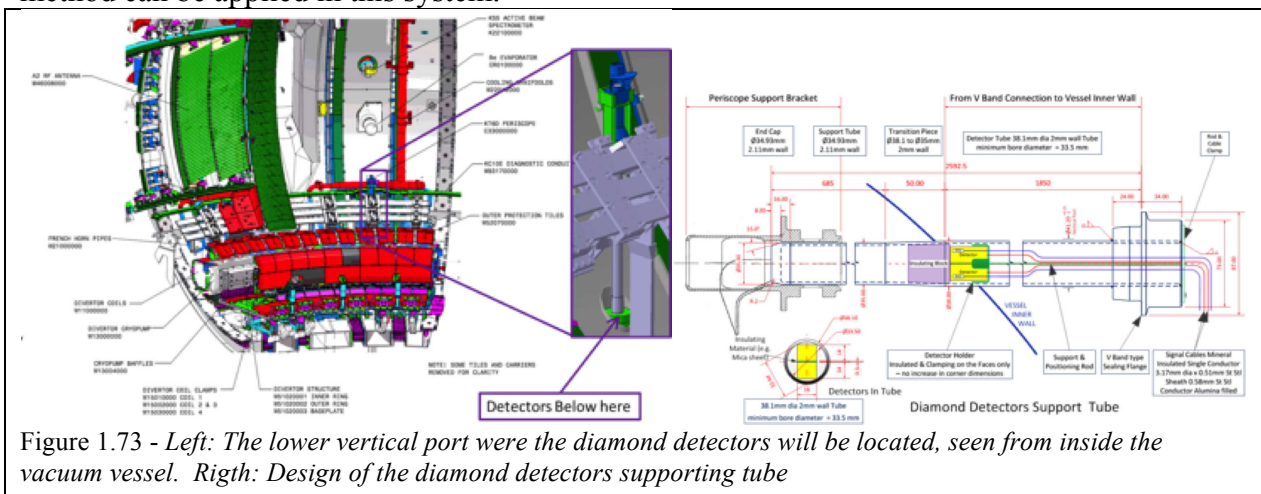

Figure 1.73 - *Left: The lower vertical port were the diamond detectors will be located, seen from inside the vacuum vessel. Rigth: Design of the diamond detectors supporting tube*

ENEA will install three diamond detectors in total. Of these, two diamond detectors, one covered with LiF and the other without LiF, will be located inside the Octant 3 vertical port close to the plasma. The two diamond detectors will be installed in the vacuum vessel using a long tube inserted in the port where a KT6D Periscope was previously located (Figure 1.**73**).

They will be equipped with a thermocouple in order to monitor the temperature. The third diamond detector, also covered with LiF, will be installed inside a TBM mock-up located in front of Octant 8 main horizontal port (*Figure 1.74*). The goal of this experiment is to measure Tritium production rate during DT operations and to compare it with calculations.

In 2015 the TBMD activities focussed on the following:

Calculation of neutron flux and tritium production rate inside the TBM mock-up.

The study of the effect on KN1 fission chambers response of the presence of a TBM mock-up in front of JET Octant 8 horizontal port has been analysed in the case of DT operations. It has been

Figure 1.74 - HCBP TBM mock up in front of Oct.8 main horizontal port of JET

found that the effect on the calibration factor of this detector is within an acceptable level, i.e. <3%. The contributions of the neutrons scattered by the torus hall walls and by structure surrounding the Octant 8 port have been evaluated and amount to less than 10%. Also, the tritium production rate (TPR) inside the TBM mock-up has been calculated and it serves as a basis for designing the tritium detectors to be used to measure the TPR during the DT campaign. The calculations have shown a production of about 4×10^{-9} T/(cm^{3}s)/(n/s) inside the sample volumes of the TBM mock up. With a JET D-T neutron emission rate of 10^{18} n/s we will have a diamond detector count rate of 114000 C/s. This could be very demanding but it is an interesting test to be done. The amount of ^{6}Li atoms in one detector could be reduced of a factor 10, thus also the count rate will be reduced of the same amount.

Completion of feasibility study and optimization of measurements techniques.

A critical point of diamond detectors operated at high temperature is the metal contact deposited on top of the diamond faces and the metal/diamond interface.
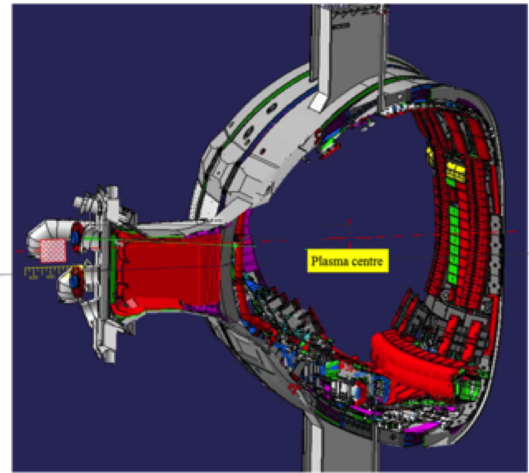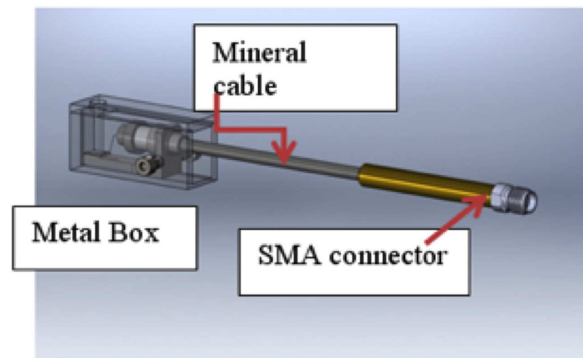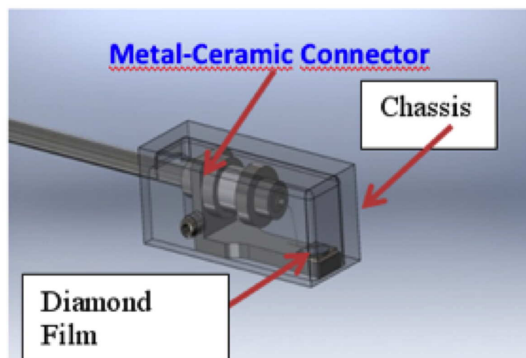

Figure 1.75 - Diamond detector prototype made of mineral cable and metal-ceramic connector

The metal/diamond interface is forming a depletion zone characterized by the presence of a small electrical potential known as Schottky barrier, which changes with temperature but this is depending upon the metal. Just as an example, for Ag the barrier is stable even for T > 800 °C but for Ti it is stable up to about 400 °C. The behaviour of the metal-diamond interface was studied by using two different approaches. In the first the contact was deposited (by sputtering technique) and the detector was studied vs. temperature. In a second round, the metal contact, once deposited was annealed in void at 600°C for one hour and tested vs. temperature too. The annealing modifies the structure at the metal-diamond interface by forming the so called carbon-like region which is expected to improve the performances of the contact. In our tests first a double layered Ti/Pt metal contact was used and then Ag contacts were deposited on a

second diamond plate. In the case of double layered metal contact, Titanium is deposited first (100 nm thick) so the Ti-diamond interface is the one of interest while Pt is deposited on top of Ti to avoid the formation of Ti-oxide. In parallel to the above activity, new prototype detectors were designed and realized in collaboration with THERMOCOAX company (France).

The design of the new detectors was based upon the already available experience on running diamond detectors at high temperature gained at ENEA in previous work. The new prototypes are made by mineral cable (of the proper type to support the very fast signal produced by the diamond, and able to work up to 800°C) and of special wire-detector connectors made of metal-ceramic type and able to withstand up to 400°C (*Figure 1.75*). Laser welding,

Figure 1.76 - Detail of the prototype diamond detector with the "mechanical" connection

whether necessary, was used too (*Figure 1.76*). A serious problem was represented by the solution to be used to connect the diamond film to the ground of the chassis and to connector. In this respect a number of different ideas and technical solutions were proposed and tested, the more effective resulted the one based on "mechanical" contacts between the diamond film and the chassis of the detector (*Figure 1.76*).
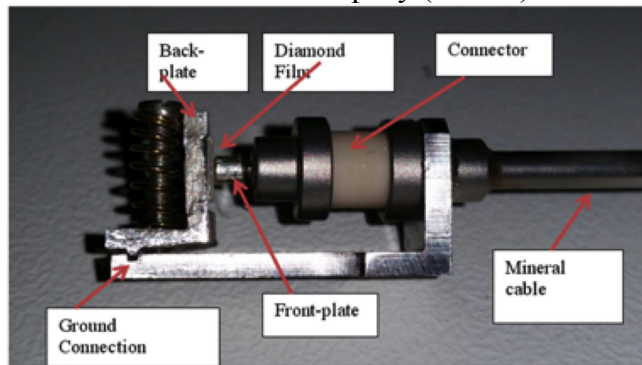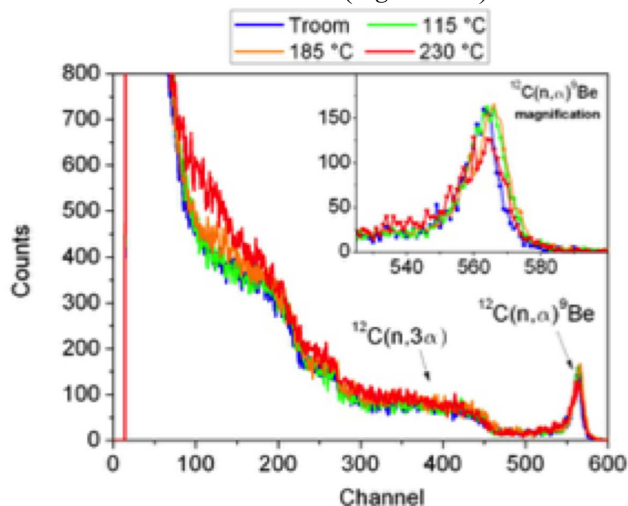

Figure 1.77 - PHS spectra as function of temperatures measured for the prototype diamond detector with mechanical contact equipped with a diamond films having post annealed (600 °C) Ag metal contacts. The inset shows the comparison of the main alpha-peak at various temperatures

Several tests were performed at FNG under 14 MeV irradiation to study the response and behaviour of the various prototypes above discussed. The diamond detector prototype realised with mechanical contacts and diamond film with annealed Ag contacts, resulted the one with the best performances in terms of time stability, signal to noise ratio and spectrometric properties (energy resolution around ±3% at FWHM). The tests were performed measuring the pulse height spectra (PHS) produced by 14 MeV neutrons at various temperatures, considering the response at room temperature (300°K) as the reference one. The detector showed a very stable behaviour and a very low signal/noise ratio (perfectly comparable to data at room temperature) up to about 235°C (Fig. 14).

At higher temperatures polarisation effects were observed and the detector did not longer work properly. Studies are still ongoing to understand the reason of this behaviour of the detector.

ACT: Activation of real ITER materials

This Sub-project aims to take advantage of the 14 MeV neutron flux/fluence produced during DTE2 to irradiate samples of real ITER materials, used in the manufacturing of the in-vessel components, and measure the neutron induced activities to validate the calculation predictions for ITER.
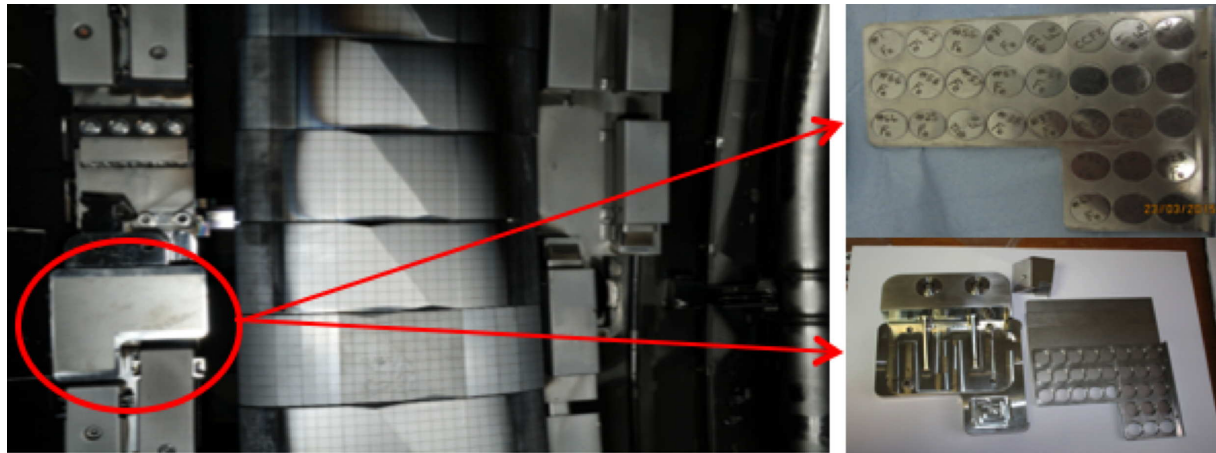
Figure 1.78 - Left: One of the 2 Internal Long Term Irradiation Stations (I-LTIS) installed inside JET at the outboard midplane, close to the Wide Poloidal Limiters. Right bottom: the LTIS open to show its components. Right top: the activation samples located inside the LTIS

The first part of 2015 for the ACT project was focused on the set up and installation of the two Long Term Irradiations Stations (LTIS) within the JET vessel for the 2015-2016 DD campaign. The LTIS were filled with over 200 dosimetry foils provided by the different institutions participating in ACT. Once the foils were delivered to CCFE they were engraved with a unique id number and the LTIS were assembled. The LTISs were installed in the JET Vessel (Octants 4 and 8) in April 2015; the LTIS in position is shown in *Figure 1.78*. The foils will be removed in June 2016 and then analysed to obtain the local neutron fluence and energy spectrum from 14 MeV down to thermal energy.

Table 1.4 - Specific activity (Bq/g) Results at 100 days after end of DT phase for different steels

Nuclide	Fe 59	Co 58	Mn 54	Sc 46	Nb 91m	Cr 51	Ta182	Zr 95	Co 57	Co 60	Nb 95	W 185	Nb 95m
Kind VV	224.9	17290	10250	0.7902	120.5	7100	1124	7.613	15890	808.6	31.93	-	-
316_fw an1	224.5	15980	10690	-	106.7	7043	-	6.742	14730	608.1	28.26	-	-
316_fw an2	225	15930	10600	-	108.9	7070	-	6.878	14670	606.7	28.85	-	-
316_fw l	225	15890	10410	0.1317	106.3	7000	702.8	6.713	14640	597.8	28.16	12.52	-
TFC_daido_ha	225.9	16000	8946	0.5267	122	6989	1405	7.707	14740	649.5	32.29	25.02	-
TFC_daido an1	225.8	15930	8930	0.2634	120.5	7004	1405	7.612	14680	628	31.91	25.03	-
TFC_daido an2	227	15970	8947	0.2639	123	7129	1407	7.766	14680	628	32.66	25.09	-
TFC_hy_ladle	222.6	14540	10060	0.2636	104.8	7485	140.6	6.618	13370	652	27.74	25.04	-
TFC_hy_an1	222.4	14480	10040	0.2635	104.7	7499	140.6	6.616	13320	640.8	27.74	30.05	-
TFC_hy_an2	222.1	14680	10060	0.3953	105.3	7512	140.6	6.649	13500	654.7	27.87	27.54	-
TFC_Kind ladle	224.6	16080	10470	0.1317	104.7	6890	323.3	6.614	14840	540.7	27.72	12.52	-
TFC_KIND product analysis 1	224.1	15950	10550	0.527	104.2	6933	702.8	6.583	14720	507.6	27.6	20.03	-
TFC_KIND product analysis 2	224.3	15880	10560	0.5269	103.7	6894	562.3	6.55	14650	506.3	27.45	25.03	-
TFC Plate Thyssen heat analysis	217.1	17360	9976	-	129.3	7328	-	8.165	16050	434.5	34.24	-	-
TFC Plate Thyssen product analysis	216.3	17590	10070	-	140	7488	-	8.844	16240	539.5	37.09	-	0.1012
VV Industeel product analysis	223.5	17630	9802	0.6588	124.2	7283	421.7	7.844	16220	742	32.91	-	-
VV Industeel ladle	223.7	17630	10050	0.6589	123.7	7184	421.8	7.813	16220	742	32.76	-	-
VV Outokumpo	224.3	17370	10030	-	122.1	7337	-	7.714	15990	736.3	32.36	-	-
VV Thyssen An1	219.6	17700	9855	0.2897	119.5	7223	435.6	7.546	16350	542.1	31.62	-	-
VV Thyssen Ladle	220.5	17450	9838	0.3425	117.5	7217	365.4	7.42	16120	537.2	31.11	-	-

The remainder of the year was focused on the pre analysis of ITER real materials, selected in 2014, for the DT campaign. The material composition information for the materials have been provided by F4E. In some cases the certificates include the specifications and the results of several sample analysis. In this case the real samples rather than the specifications were considered. In some cases there is no specific sample analysis and the data needs to be taken from available literature. The best literature source for ITER materials without supplier information is the Barabash report on ITER materials [ITER IDM:HTN8X3], this provides the specifications that the material must meet and hence should be a worst case for impurities.

The pre-analysis was performed using FISPACT-II code with EAF2010 and EAF2007 nuclear data. All of the above materials have been considered in LTIS and for short term irradiation in the KN2 system. The results of the analysis give the specific activity, the dose rate, the dominant nuclides and the pathway analysis for each material of interest (*Table 1.4*, *Table 1.5*) ferent detector response functions for the detectors available at each institution to determine the possible count rates for each material as a function of time.

Table 1.5 - Specific activity (Bq/g) Results 100 days after end of DT phase for TFC conductor

Nuclide	Te125m	Mn 54	Sn119m	Sn117m	Co 57	Sb125	Sn113	Nb 93m	Nb 94
TFC conductor	57.84	0.1614	2267	62	0.5965	296.1	915.6	407.8	3.272

Nuclide	Ta182	In113m	Sn123	Co 58	Te127m	Co 60	Ag109m	In114m	Sc 46
TFC conductor	840800	916.1	884.1	0.6443	0.1582	1560	2.611	1.072	17.57

In this pre-analysis only the DT phase is considered, the assumed total neutron yield in the campaign is 1.7×10^{21} neutrons in 4 months. The neutron spectra for both the LTIS and OLTIS irradiation positions had previously been calculated. The total neutron fluence in LTIS during DT is 1×10^{16} n/cm^2. The activity levels have been calculated from 1 day to 600 days after the end of the DT irradiation. As the measurability criterion, it has been assumed that any reaction giving a singlet gamma peak in the measurable energy range (10-3000 KeV) with a net area of more than 1000 in a 12 hour count is definitely measurable.

One of the key outputs of the pre-analysis has been that it has identified that it is vital to retrieve the foils early if some of the important reactions are to be successfully measured. This means that in the future experiments the outer LTIS will be key to the success of the project. The analysis showed that in steel samples the majority of the products produced are the 'usual suspects'. They dominate the activity levels with Co57, Co58 & Mn54 being 4 orders of magnitude higher than say Sc46m, Zr95 and Nb95. This will make it very difficult to measure those products against a Compton background cause by the dominant products. One of the interesting aspect of the experiments will be if the steels whose specifications did not include all the impurities actually produce any of the expected products i.e. W185. A second interesting aspect will be the comparison between different steel manufacturers. The pre-analysis shows that for some nuclides there is a similar level of activity regardless of manufacturer whilst others such as Ta182 vary by a factor of 3 or more. The TFC conductor is one of the more complex material samples as it is a mix of materials with many impurities that are not usually seen in steels samples. It appears to have a large number of more unusual products such as the Ag109m and a variety of Tin products. These are however typically several orders of magnitude less than the Ta182, which may be cause a large Compton background.

NSAF: Operational experience on occupational dose

ITER Occupational Radiation Exposure (ORE) assessment strategy is based on operating experience collected in the existing experimental fusion devices during maintenance activities, of most relevance is information from JET. However, data for specific maintenance activities is still missing or largely uncertain. The objective of NSAF is to collect additional data at JET in maintenance activities, during normal operation and during shutdowns, to reduce the uncertainties and lack of information, to improve the database for ITER ORE and provide its validation.

Following the agreement with IO on main tasks, systems, locations to be monitored, the strategy for the data collection (tritium concentration, dust concentration and traces, dose rates, work effort) was defined and initially four maintenance activities were selected for study in the 2014/5 shutdown.

During the planning of the 2014/15 shutdown one of the tasks selected was cancelled. The tasks finally chosen for monitoring were: 1) Repair IVIS view tube at Octant 4, 2) KT7D

SOXMOS spectrometer feedthrough replacement, 3) KS7 octant 4 lower periscope work. A detailed breakdown of each task was made available by the respective ROs. Each task was broken down into specific sub-tasks, which were monitored, as far as possible, individually. Though currently radiological contamination and external radiation levels on JET are very low and may not be relevant to ITER, this was a useful exercise for establishing the data collection process for future shutdowns and for information regarding task duration and worker proximity to the hazards.

A detailed monitoring report was created for each task. This described the activity, the time taken to perform it, how many persons were involved, the background dose-rates in the area and the individual personal electronic dosimeter (PED) results. The results allowed extrapolating the ITER case assuming that the same tasks were carried out outside the diagnostic equatorial port in the presence of a dose rate of 10 μSv/h. For example, in the case of Task 1, the dose rate

Figure 1.79 - Collective dose in the repair IVIS view tube: comparison between JET and ITER. The dose rate measured in JET during the task was 0.315 microSv/h, whereas the dose supposed for ITER is 10 μSv/h

measured in JET was 0.315 μSv/h, and for the whole task the JET collective dose is 17 μSv. In the hypothesis made for ITER (10 μSv/h) the collective dose for the same task reaches 567 μSv (*Figure 1.79*). The JET experience allows also validating the work effort, including all the actions required to complete a task and their duration.

TRI: Tritium retention, permeation, outgassing and airborne tritium
The activity in 2015 has been devoted to the finalisation of the designs of the Tritium Loading Facility (TLF) and the Tritium Permeation Facility (TPF), after having delivered the preliminary design of the latter at the beginning of the year.
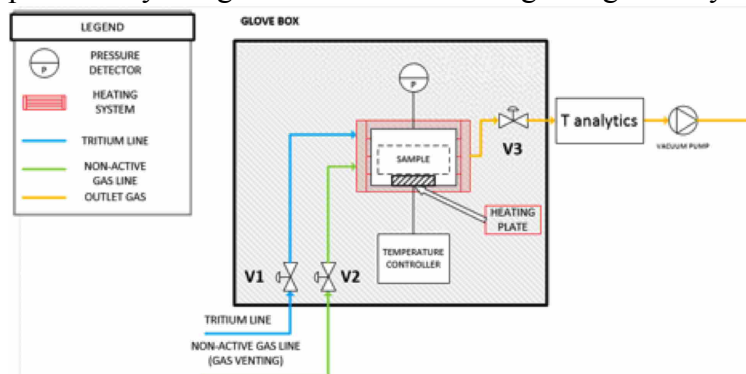

Figure 1.80 - Block diagram of the Tritium Soaking Facility (TSF

Originally, within the TPF part of the project, it was foreseen to construct 2 facilities, one to study the effect of tritium soaking (TSF) on samples and one to measure the diffusion coefficient of tritium through JET relevant materials (TPF). Unfortunately, the cutting of the samples with an acceptable thickness and diameter (a higher diameter would have allowed to minimise the measurement errors) has turned out to be impossible to achieve. In addition, the leak tightness has been found to be excessively difficult to realise due to the minimum achievable thickness (2.5 mm). It was decided to abandon the TPF and only design the TSF and the TLF.

The TSF will be consist of a chamber equipped with two heating systems (one for the sample and one for the chamber bake-out), a pressure sensor and three gas lines (one for tritium, one

for air or nitrogen and one that goes to the tritium analytics) (*Figure 1.80*). A precise measurement of the pressure is important not only for the control of the operating conditions but also because by measuring the pressure it is possible to have direct information about the amount of tritium adsorbed in and released from the samples. The total number of the switching valves is 3.

The design of the facilities has been delivered in December 2015. The TLF experiments will be carried out on Be only because it turned out to be impossible to design safely and within budget the TLF with a heating system able to reach the temperature of W during plasma operations (~1000°C) due to the maximum temperature the wobble stick (used to transfer the sample from the loading chamber to the tritium-free outgassing chamber) is able to cope with.

In parallel, the relevant samples have been choosen and booked. The choice has been made to focus on the centre part of inner wall guard limiters. Two samples have been booked (one pristine and one exposed to JET DD plasmas, the exposed has to be shared with JET2) and sent to MEdC in Romania for cutting in 2016. The final experimental plan has been delivered in September 2015.

Due to JET 2020 rescheduling, the commissioning of the TSF is now planned for September 2016 at the same time as the TLF. The experiments will start after the commissioning of the facilities, and will be complemented by SEM characterisation of sample surfaces, TDS analyses on small samples and modelling using the TMAP code. In parallel, theoretical studies have been conducted on Be and W literature data but also on TDS experiments done as part of the JET2 project, on samples from the JET ITER-Like Wall.

NCAL: Characterisation of neutron field, activation and dose rates
In 2014 the neutron flux spectra were calculated at all experimental positions, in the irradiation ends, in the inner LTIS and outer LTIS, and at other potential irradiation positions (vertical ports, outside the vacuum vessel), for DD and DT operations. In 2015, neutron flux spectra were calculated also inside the TBM mockup. In preparation of the TT campaign, the TT neutron source was modelled for use in MCNP code. The activation and dose rates in foils and functional material samples irradiated in the LTIS during DTE2 were calculated for several cooling times after irradiation [1.123, 1.124].

International Collaborations
A collaboration has been started between EURATOM - JET and US DOE on simulations of neutron streaming experiments and shutdown dose rate experiments carried out at JET in the frame of WP JET3 using advanced neutronics transport and activation codes such as the hybrid ADVANTG code and the DAG-MCNP code. A part of this scope will include providing the ADVANTG code to EURATOM-JET, along with expertise at applying the code. JET would provide experimental data of streaming experiment and of shutdown dose rate experiment performed in the frame of WP JET3, the existing MCNP input models of JET, the DD, DT neutron source and the operation histories. US DOE will provide the resources for the simulation of JET experiments using ADVANTG DAG-MCNP and results. In the frame of this collaboration, a course on ADVANTG was organized by ENEA and CCFE. The course was delivered by ORNL Neutron Group in the frame of the US DoE – EUROfusion JET collaboration on WP JET3 NEXP, Culham, 7 December 2015. About 20 neutronics analysts attended from all over Europe.

Invited and orals at ISFNT12 Conferences
P. Batistoni et al., Technological exploitation of Deuterium-Tritium operations at JET in support of ITER design, operation and safety / R. Villari at el., Neutronics Experiments and Analyses in Preparation of DT Operations at JET / M. Pillon et al., Characterization of a Diamond Detector to be used as Neutron Yield Monitor during the in-vessel Calibration of JET Neutron Detectors in preparation of the DT Experiment

1.2.3 – JET4

Neutron Camera Upgrade

The Neutron Camera (NC) is a JET diagnostic with the main function of measuring the neutron emissivity profile due to 2.5 MeV (DD) and 14 MeV (DT) neutrons over a poloidal plasma cross-section using line-integrated measurements along a set of 19 collimated channels (10 horizontal and 9 vertical channels). In view of the future JET DT campaigns an upgrade project (Neutron Camera Upgrade, NCU) was launched in 2014 with the objective of increasing the performances and reliability of the NC 14 MeV neutron measurements. Such objective is to be achieved by replacing the old analogic acquisition electronics of the NC plastic scintillator detectors (BC418) with a new digital acquisition system (DAS). A possible replacement of the digital acquisition electronics presently used by another set of NC detectors (NE213 liquid scintillators), to be decided after 14 MeV neutrons irradiations tests at the ENEA Frascati neutron generator facility (FNG) with a NC spare detector unit, is also foreseen.

During 2015 requirements were defined for the new DAS, also by means of experimental tests performed at JET on BC418/NE213 NC detectors. *Figure 1.81* shows, as an example, a set of ^{22}Na gamma pulse height spectra (PHS) acquired with the NC BC418 detectors and used to identify the optimal ADC input range for the new DAS.
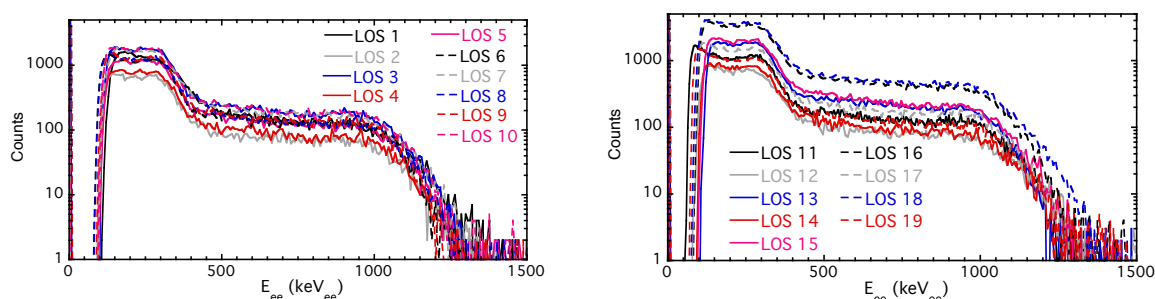
Figure 1.81 - Energy calibrated ^{22}Na PHS for the horizontal (left) and vertical (right) JET neutron camera BC418 detectors

Based on the identified requirements a market survey was carried out and the specific hardware to be procured was selected. The new DAS will be based on ten X6-400M acquisition boards produced by *Innovative Integration,* each having the following characteristics:
• Two A/D channels (400 Msps; 14 bits; 1V input range).
• PCIe x8 architecture (data transfer >1Gbyte/s).
• Xilinx Virtex 6 FPGA.
• 4 GB on-board memory.
The boards will be distributed on three rack mounted units housing 10 PCs with associated local mass storage devices and managed through a single KVM (Keyboard, Video and Mouse) switch.
Additional tests were finally carried out at JET using the NC spare detector unit coupled to an X6-400M acquisition board. Scope of the tests was to define the experimental set-up to be used for FNG irradiations (detectors high voltages, cable lengths, additional units to include in the acquisition chain) and in particular to find a working point for the spare unit detectors producing an output resembling as much as possible that of actual detectors installed on the camera, both in terms of pulse amplitude (i.e. filling of the ADCs input range) and pulse shape (i.e. pulse full width half maximum (FWHM)). *Figure 1.82* shows the comparison between a typical ^{22}Na PHS from BC418 NC detectors and the best matching PHS obtained using the spare detector unit.
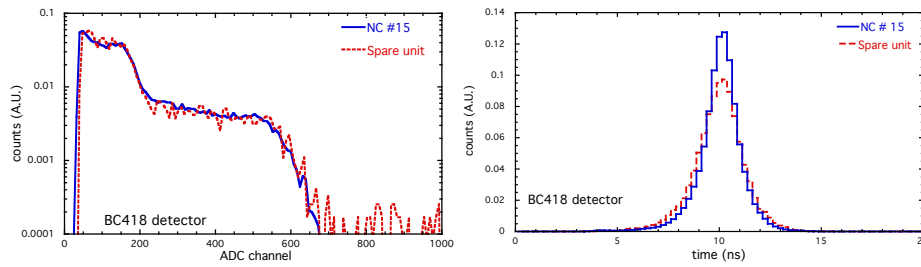
Figure 1.82 - Left: Comparison between the Na-22 PHS from a NC BC418 detector (channel # 15) and the best matching PHS obtained with the NC spare detector unit (high voltage= 860V, cable length= 40m, Ortec 771 amplifier (×2) included in the acquisition chain). Right: FWHM distributions for the same acquisitions

Compact Vertical Neutron Spectrometer

The VNS project is part of the JET component of the EFDA 2012 Work Programme which includes 4 enhancement projects, referred to as EDT (Enhancements for DT Operations) and it has the goal to install in the JET Roof Lab a compact neutron spectrometer similar to the previous JET-EP2 Project "Compact Neutron Spectrometer" (CNS, commissioned during 2012), presently located in the JET KM2 bunker in J1D, with a horizontal tangential line of sight to the tokamak toroidal field lines.
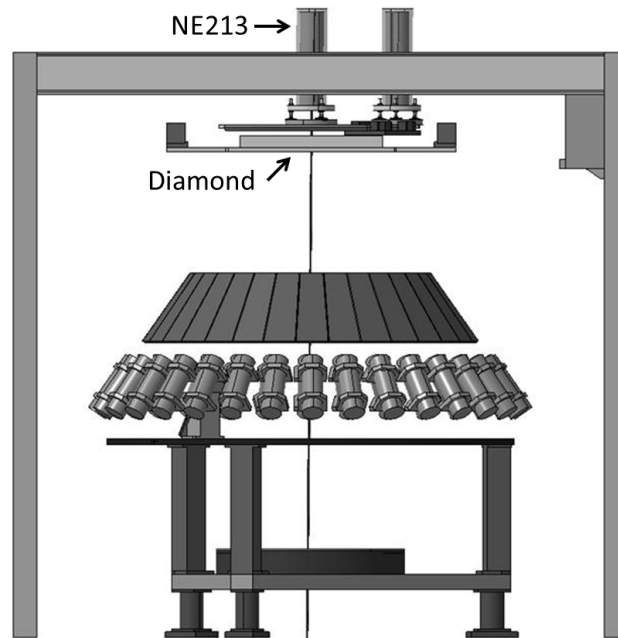
Figure 1.83 - Support design by HEPCO for the installation of the VNS diamond and scintillator detectors, along the TOFOR line of sight in the JET Roof Lab

CNS Project was led by ENEA who built a Digital Pulse Shape Discrimination (DPSD) board, coupled to a NE213 scintillator detector (diameter 2.5 cm x 2.5 cm thick) with LED for photomultiplier gain variation corrections, built and characterized by Physikalisch-Technische Bundesanstalt (PTB) [1.125]. The request for a similar spectrometer in the Roof Lab has been due to the fact that JET has not yet a 14 MeV compact neutron spectrometer, suitable for DT plasma Campaigns, on a vertical, radial line of sight.

Together with the NE213 scintillator detector, a diamond detector (provided by CNR-Milano) suitable for 14 MeV neutron measurements at very high count rates (> 1 MHz), will be installed in front of the NE213 detector and along the same line of view of TOFOR (Time-Of-Flight neutron spectrometer at Optimized Rate), as illustrated in *Figure 1.83*. In 2015 the final design (by HEPCO) of the VNS support, with a rotating arm for the NE213 detector (in *Figure 1.83* both its rest and operative positions are showed), has been approved: installation will be completed in the early 2016.

The main activities during 2015 have been the determination of the response functions for both diamond and scintillator detectors, along with the installation, optimization and preliminary tests of their digital acquisition electronics.

1.3 - Enabling Research

1.3.1 "NLED" Project ER15-ENEA-03 on "*Theory and simulation of energetic particle dynamics and ensuing collective behaviors in fusion plasmas*", PI: F. Zonca

The Research Team of the NLED project ENEA-03 has consolidated the general framework established for general theory and numerical simulation of energetic particle (EP) dynamics and ensuing collective behaviors in fusion plasmas introduced in 2014 [1.126]. In fact, with the aim not to provide a modeling support to experimental activities, but rather to adopt experimental "cases" to "extract" the underlying physics processes, mutual positive feedbacks have been achieved between general theory, numerical simulations and properly diagnosed experimental observations, as new element of the 2015 w.r.t. the 2014 NLED Project activities [1.126].

Based on the plasma conditions in the ASDEX Upgrade discharge 31213@0.84s, a set of equilbria and profiles were collected, parameterized and made available to the NLED project team [1.127]. In order to satisfy the limitations of some numerical codes, the equilibrium was chosen to be circular, which is a reasonable approximation for the core region in this discharge. Several stages and profiles for code-comparison purposes are defined. Linear local LIGKA results are given for reference. The most important feature of the equilibrium is its large ratio of $\beta_{EP}/\beta_{thermal} \approx 1$, which shows the onset of strongly non-linear Toroidal/Reversed-Shear Alfvén Eigenmodes (TAE/RSAE) dynamics in the presence of EP-driven Geodesic Acoustic Modes (EGAMs). The interest in these findings triggered further experiments at ASDEX Upgrade that confirmed previous findings and added new data. Theoretical predictions of mode onset conditions in these new experiments were confirmed. A key element of this NLED reference scenario is the model parametric distribution function for EPs in the space of constants of motion, based on probabilistic assumptions and capable of rendering realistic experimental conditions [1.27]. This is crucial for the V&V of various codes involved in the project. The reference scenario is kept up to date and routinely used by project participants. In the future, it will be made available to all researchers interested in V&V of EP physics.

The Beta-induced AE (BAE) dynamics excited by anisotropic EPs at low magnetic shear has been investigated by the XHMGC code. Linear dynamics in similar for co-passing and counter-passing EPs, while nonlinear behaviour is different in the two cases [1.128]. Nonlinear saturation amplitude is much larger for the co-passing than the counter-passing EP. Moreover, in the former case the scaling of saturation amplitude with growth rate is linear, different from the usual quadratic scaling observed in the low growth rate limit and for counter-passing ions. Linear scaling is obtained also for the counter-passing ions at sufficiently large growth rates. These differences are due to different radial structures of resonance frequencies, yielding distinct saturation mechanisms and confirming the crucial role predicted theoretically for *radial non-uniformity* and *equilibrium geometry* [1.129, 1.130, 1.131]. For co-passing ions case, saturation is reached when EP density-flattening region is limited by the mode width (*radial decoupling*). For counter-passing ions, saturation occurs when the flattening region is set by the resonance width (*resonance detuning*). These two different processes cause the observed differences in terms of saturation amplitude and its scaling with the mode growth rate [1.132]. Nonlinear dynamics of chirping EP Modes (EPMs) driven unstable by transit resonance has been also investigated. It has been shown

that it is due to the succession of resonant excitations from different phase-space regions [1.128, 1.133, 1.134].

The benchmark between HYMAGYC and HMGC codes has been performed for the ITPA-TAE test case [1.73]. At low values of the EP drive, the frequencies and growth-rates, obtained by the two codes, are very similar, and correspond to the same mode (TAE). For higher values of the EP drive, the differences observed between HYMAGYC and HMGC are mainly due to the different response of the MHD modules; in particular, to the smaller continuum damping observed in HYMAGYC w.r.t. HMGC. A scan with respect to EP temperature (T=200 - 800 keV) has been performed, with good agreement between HYMAGYC and HMGC computed EP drive, once the damping is subtracted [1.135, 1.72]. A newly developed scheme for computing shear Alfvén continuum damping in both tokamak and stellarator geometries has been proposed [1.136, 1.137].

A detailed linear analysis of Alfvén modes has been carried out with NEMORB [1.138]. Linear benchmarks with EUTERPE and HMGC on the ITPA-TAE case have been successfully completed finding good agreement. Radial mode structure ("boomerang shape") has been found to be due to the coupling effect of the EP drive and the radial variation of the continuous spectrum. Nonlinear investigations of the ITPA-TAE case (with wave-particle nonlinearities only) suggest nonlinear structure modification due to EPs [1.139], consistent with [1.140]. A comparison of the nonlinear saturation levels with EUTERPE has also started. Comparison between the wave-particle nonlinear dynamics predicted by CKA-EUTERPE, HAGIS/LIGKA and XHMGC has been further carried out with reference to the n=6 ITPA-TAE benchmark. It has been shown that both CKA-EUTERPE and HAGIS/LIGKA exhibit a quadratic scaling of the saturation amplitude with the growth rate of the mode in the weak-mode regime (saturation due to resonance detuning), along with a transition to a linear scaling for strongly driven modes (saturation due to radial decoupling) [1.141]. These results are consistent with those obtained by XHMGC for the same TAE case and in BAE studies [1.128, 1.132, 1.134]. They also fit with the predictions of a toy-model, developed for interpreting simulation results [1.132]. The fluid electron hybrid model FLU-EUTERPE code has been extended to work nonlinearly and has been applied to the ITPA-TAE benchmark case for a tokamak. With finite resistivity, a saturation of the mode amplitude close to that of CKA-EUTERPE and HMGC has been found. The scaling of saturated amplitude with changing linear growth is also comparable.

A Fourier representation in the toroidal direction has been introduced into the CKA code (reduced MHD) to speed up MHD calculation for stellarators. Convergence speed can be improved further, but CKA solver now works for large resolution. Furthermore, the gyrokinetic EUTERPE code has been improved and different models (e.g., fluid-hybrid, CKA-EUTERPE) have been merged [1.142]. This improvement provides flexibility and allows computing drift Alfvén wave (DAW) fluctuations in stellarators [1.142, 1.143, 1.144, 1.145, 1.146, 1.147]. In particular, DAW have been investigated in LHD, showing that a TAE-like mode with a frequency lying in the TAE gap could be destabilized by the gradients of the bulk plasma without EPs. Similar modes have also been found in W7-X. The newly developed "pull-back scheme" for the solution of the electromagnetic gyrokinetic Vlasov Poisson system has been used for these calculations [1.148, 1.149, 1.150, 1.151].

The nonlinear version of the CKA-EUTERPE code has been successfully applied to stellarators [1.152, 1.153]. To allow computations, phase factor extraction of the dominant Fourier harmonic has been retained. Saturation levels of an NBI-driven TAE mode in W7-X and a α-driven HAE mode in the HELIAS reactor have been calculated. The time step necessary to converge the results is found to be smaller by more than an order of magnitude compared with a tokamak case. The saturation levels found for relevant parameters are around $\delta B_{rad}/B_0 \approx 10^{-3}$. Proof of principle FLU-EUTERPE simulations within a limited range of

numerical parameters have been performed in W7-AS, LHD, and W7-X stellarator geometries. Global modes driven by EPs have been found in W7-X geometry. Work to expand the working parameter range to experimentally relevant values is in progress.

Nonlinear simulations of Alfvén modes with wave-particle and wave-wave nonlinearities have also been performed with NEMORB, in particular for the coupling with zonal structures [1.139]. With flat q-profile, wave-wave coupling has been found to dominate the saturation mechanism, preventing the Alfvén mode to reach the amplitudes necessary for appreciable EP radial redistribution. Linear simulations of GAMs with the realistic equilibrium of the NLED-AUG reference case have also been investigated. Nonlinear EGAMs have also been studied with wave-particle nonlinearities only, and with the EP distribution function suggested in [1.26] (see also [1.27]).

Numerical simulations of electrostatic turbulence have shown that instead of the expected moderating effect, EGAMs could on the contrary enhance ITG turbulence [1.154, 1.155]. An analytical, non-linear three-wave parametric interaction model has been developed to better understand the interaction between these instabilities observed in the simulations. A local dispersion relation shows that the non-linear excitation of two linearly stable ITG modes by an EGAM is only possible under stringent conditions, in line with expectations and the mitigating impact of GAMs on turbulence. Meanwhile, a three-wave interaction propagative model predicts that, if ITG modes are linearly unstable in the core region and linearly stable in the outer region, the EGAM can act as a pump to non-linearly destabilize ITG modes in the outer region.

The link between GAMs and EGAMs has been clarified by detailed analyses of the linear dispersion relation, as well as extensive gyrokinetic simulations [1.156, 1.157]. These findings may have impact on turbulence control. The validity of these results has been checked using the new 2-ion species version of the GYSELA code [1.158]. Good agreement of the EGAM frequency and linear growth rate was found. This motivates new simulations to be conducted, with a focus on identifying potentially different effects on ITG turbulence.

Nonlinear EP interaction with multiple TAEs has been studied for the ITER 15 MA baseline scenario (q_0= 0.986) using the HAGIS code [1.159, 1.160, 1.161, 1.162]. Similar to earlier studies of ASDEX Upgrade [1.163], it was found that global, nonlinear effects are crucial for the evolution of the multi mode scenario. Taking into account all weakly damped modes that can be identified linearly with the gyrokinetic, non-perturbative LIGKA solver, simulations with HAGIS demonstrated that the nonlinear excitation of linearly sub-dominant modes can be crucial to the relaxed EP profile. Whereas the most unstable, mid-radius localized TAEs lead only to a moderate EP redistribution that is rather close to quasi-linear estimates, in a certain parameter regime, the slowly growing low-n TAEs eventually lead to a substantial EP relaxation in the outer core region via domino-effect [1.164]. Similarity and differences of EP transport by multiple modes, and multi-beam interaction with plasma waves in 1D uniform system has been addressed. In particular, the general problem of n cold beams self-consistently evolving in the presence of m (greater or equal to n) Langmuir modes at the plasma frequency has been formulated in Hamiltonian form [1.165]. A theoretical analysis combined with numerical simulations has demonstrated non-diffusive behavior beyond the quasi-linear paradigm, as well as the necessity of accounting for modes of the linear stable spectrum for proper description of EP transport [1.166]. This is qualitatively consistent with EP transport by multi modes in fusion plasmas. A quantitative comparison is underway.

Linear and nonlinear studies of electron fishbone instability have been performed with the HMGC code. Standard (peaked on-axis) [1.64] and inverted (peaked off-axis) [1.65, 1.66] supra-thermal electron density profiles with moderately hollow q-profile have been studied. The linear analysis demonstrated that the two situations are different in terms of the characteristic resonance frequency of the mode, as well as the fraction of supra-thermal

particles involved in the destabilization of the mode, confirming theoretical expectations. The study of e-fishbone nonlinear saturation mechanisms adopted the test particle Hamiltonian method (TPHM) package [1.60] and it has been performed for both the on axis profile as well as for the off axis density profile. The two cases show a different behaviour of phase-space resonant structures, which yield mode saturation via reduction of the free energy source by energetic electron density flattening.

A minimal model was developed for the nonlinear analysis of precessional fishbones. In this framework, only deeply trapped particles are retained in order to deal with a single, and relatively simple, mode-particle resonance. The bulk of the plasma it is described in the cold plasma approximation by the Reduced-MHD equations in a cylindrical geometry. An hybrid numerical code, based on this approach, was developed adopting a semi-lagrangian scheme for the evolution of the particle distribution function and a semi-spectral scheme for the MHD part. At the same time the growth rate and the real frequency of the Fishbone instability have been determined using a standard analytic approach. The numerical code has been benchmarked with the analytical results and it is able to correctly recover them, during the linear phase of the instability [1.167]. The non-linear phase is under investigation. Other NLED activity is also published in [1.168]

1.3.2 Project AWP15-ENR-01/ENEA-08: Unexplored magnetic vortex regimes relevant for fusion applications of superconductors, PI: G. Celentano

It is widely recognized that in perspective of DEMO, High Temperature Superconductors (HTS) REBa$_2$Cu$_3$O$_{7-x}$ (RE = rare earths and Y, REBCO) could enable operation at larger fields (13 – 16 T) at the same temperature, or at higher temperature (20 K or higher) with the same field as ITER. However, in spite of this interest, up to now there is a lack of knowledge and experimental studies of the fundamental properties of superconducting materials in either intermediate temperature range (20 – 50 K) or extreme high field conditions at 4.2 K. The aim of this project is the acquisition of knowledge on current transport properties of REBCO films in those fusion relevant conditions. It is believed that the knowledge acquired during this 3 years long activity will constitute a background for the assessment of the potential in performance improvements of REBCO-based conductors, as a reference for the design of the HTS based magnet system for a fusion reactor.

Table 1.6 - Critical Temperature, T_C, for MOD YBCO films as a function of the BZO content, obtained by resistive measurements

	YBCO	YBCO-5% BZO	YBCO-7.5% BZO	YBCO-10% BZO
T_c (K)	91.0 ± 0.3	90.5 ± 0.8	90.0 ± 0.1	89.1 ± 0.8
ΔT_c (K)	0.5 ± 0.1	0.6 ± 0.2	0.9 ± 0.1	0.8 ± 0.4

The first year of the project was devoted to the optimization of the YBa$_2$Cu$_3$O$_{7-x}$ (YBCO) and BaZrO$_3$ (BZO)-YBCO nanocomposite film depositions. In agreement with the 1st year objective (film growth optimization, Deliverable 1, 12 month), the research activity was organized as follow: growth and characterization of superconducting films and the investigations of current transport properties by dc and microwave techniques.

YBCO and composite BZO-YBCO films were deposited with two different film deposition techniques: Pulsed laser deposition (PLD) and chemical Metal-Organic Decomposition (MOD) methods. For PLD sample deposition the composite targets have been prepared by mixing together YBCO and BZO compounds (obtained by solid state reaction) in the given molar % concentrations, pressing and finally sintering by high temperature thermal treatment (at 950 °C for 24 h in oxygen atmosphere). The following targets have been obtained: (1) YBCO+2.5 mol% BZO; (2) YBCO+5 mol% BZO; (3) YBCO+7 mol% BZO;
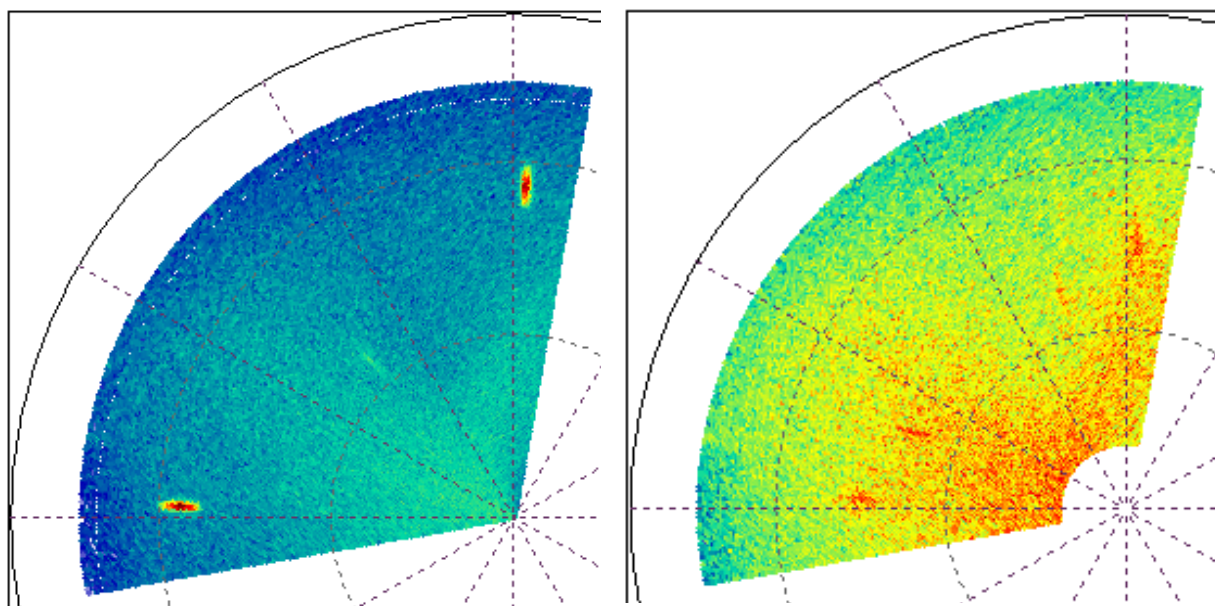
Figure 1.84 – (102) YBCO pole figure for YBCO-5%BZO film

Figure 1.85 – (101) BZO pole figure for a YBCO-5%BZO film

(4) YBCO+10 mol% BZO. MOD-YBCO films were deposited using low fluorine solution precursor prepared starting from yttrium acetate hydrate, barium trifluoroacetate hydrate and copper acetate corresponding to the 1:2:3 stoichiometry.
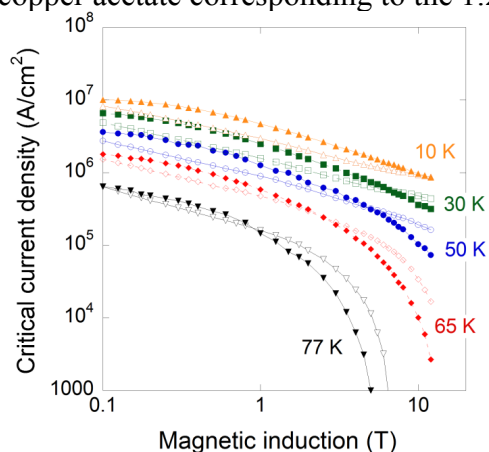

Figure 1.86 - Critical current density, Jc, dependences on magnetic flux density measured in temperature range 10 K- 77 K for YBCO (full symbols) and YBCO–5%BZO (empty symbols)
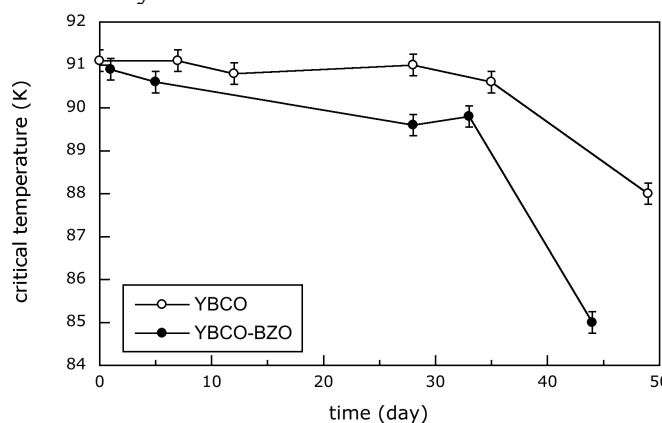
Figure 1.87 - Critical temperature of pure YBCO and YBCO-BZO films obtained from as-prepared and aged solutions. Time represents solutions age

The YBCO-BZO solution was prepared adding barium trifluoroacetate and zirconium acetylacetonate precursors, in stoichiometric proportion to reach 5, 7.5 and 10 mol.% of doping [1.169]. The critical temperature, T_c, measured by dc resistivity have shown that BZO introduction slightly affect the superconducting transition (see *Table 1*).

X-ray diffraction pole figures analyses reveal a clear epitaxial growth for the MOD YBCO films with or without BZO nano-inclusion. A weak sign of *a*-axis orientation can be detected. The phi-scan of the YBCO(102) reflections gives rise to a FWHM-value of about 1°, indicating a sharp in-plane orientation (see *Figure 1.84*). The BZO poles figure shows that BZO is randomly incorporated into the YBCO without preferred orientation (see *Figure 1.85*). The BZO addition on YBCO film effectively improves J_c (B) dependences as shown in *Figure 1.86* for a 5%BZO films.The aging of precursor solutions for YBCO and YBCO with addition of BZO pinning center films has been studied monitoring the time evolution of both

solutions and films deposited with aged solutions. The use of NMR spectroscopic techniques evidenced some differences in the two precursor solutions at zero time and time evolutions corresponding to different microstructural and superconducting properties of deposited samples. BZO addition seems to increase the reactivity and degradation of the precursor solution [1.169].

In spite of the poor solution time stability usually exhibited by low fluorine solutions, the developed YBCO and BZO-YBCO coating solutions have shown remarkable stability over an extended period of more than 2 months making them suitable for film deposition, see *Figure 1.87*. A study aimed at the comprehension of the underlying chemical mechanisms of aging (salts precipitation, oxidation, polymerization) and its effect on film properties has been carried out. The formation of new compounds has been revealed in both YBCO and YBCO-BZO aged solutions by using high resolution NMR spectroscopy techniques [1.169]. This study is currently in progress.

The introduction of BZO leads to a T_c depression only in PLD films ($T_c = 87$ K for 10 mol.% BZO YBCO), *Figure 1.88*
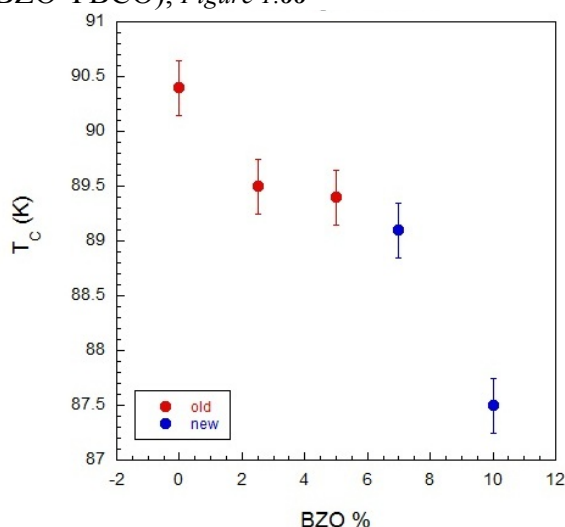
Figure 1.88 - T_c values for PLD films for different BZO content
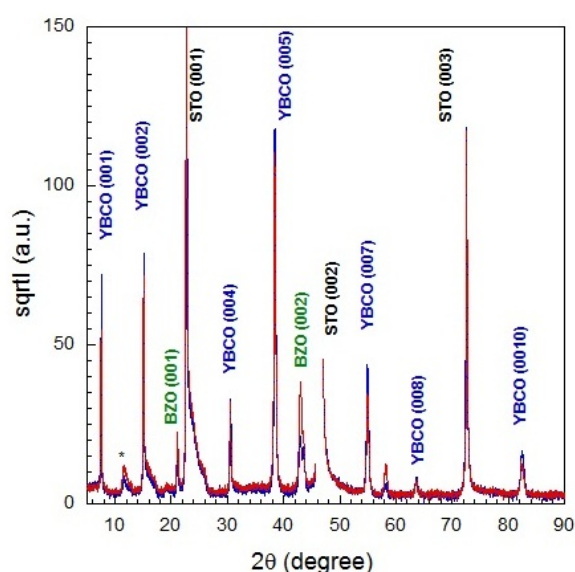
Figure 1.89 - XRD θ-2θ spectra for PLD YBCO films with different BZO content: 7% (blue curve) and 10% (red)

XRD investigations have shown that the presence of BZO can be detected by XRD analyses. In the θ-2θ spectra an increase of BZO peak intensity with target BZO content as been reported (*Figure 1.89*). Polar figures revealed that in PLD YBCO film BZO inclusions develop the (100)BZO//(100)YBCO and <011>BZO//<011> YBCO crystallographic orientation relationship.

However, improved J_c values and magnetic field behaviour is observed in both MOD and PLD composite YBCO films [1.170]. Angle dependent J_c curves revealed different nature of pinning mechanisms in PLD and MOD films. Form microwave measurements in some PLD- and MOD-YBCO and YBCO/BZO films, the vortex parameters (pinning coefficient r, depinning frequency ν_p, pinning constant k_p, maximum creep factor χ_M) and their field-dependence have been obtained and compared to dc, J_c measurements [1.170, 1.171]. Typical results for r and k_p obtained on MOD samples are plotted in *Figure 1.90*. Results, the validation of the models and of the technique were presented to international Conferences and submitted for publication to international journals [1.170, 1.171].

In agreement with the project plan activity, a second approach for the introduction of artificial pinning centers in YBCO films based on surface decoration has been faced. MgO(100) substrates have been successfully decorated by a homogenous size and shape distribution of
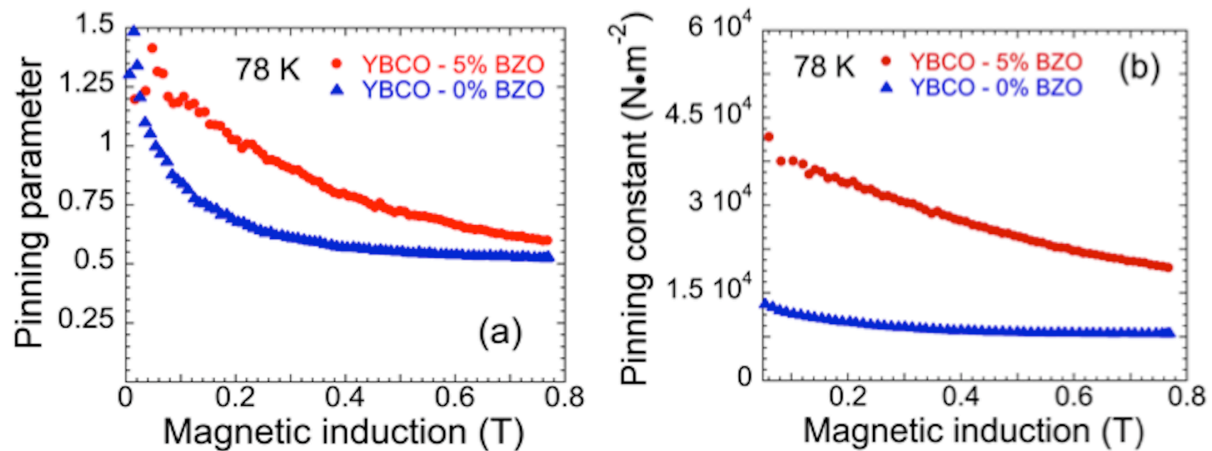

Figure 1.90 - Pinning parameter r (a) and Pinning constant k_p (b) for pure (blue triangles) and YBCO/BZO (red circles) samples by MOD: higher r value obtained in YBCO/BZO means stronger pinning, decreasing of $k_p(B)$ in YBCO/BZO indicates essentially unchanged the pinning mechanism

the LSMO nanoislands (density $\approx 500 \ \mu m^{-2}$) using very dilute solutions. A quantitative study has been performed, indicating that the equivalent islands diameter is $D = 27 \pm 11$ nm, while the average height is $h \approx 6$ nm. Part of results has been reported on a manuscript submitted for publication to an international journal [1.172].

In addition, an extensive characterization campaign has been organized for a comprehension of the microstructural nature of the films and effect of secondary phase addition on the YBCO films. A part from dc, microwave, X-ray diffraction and photoemission spectroscopy characterizations, some selected samples have been subjected to deeper analysis by SIMS-ToF technique, TEM and temperature dependent SAXS/GI-SAXS investigations carried out at Electra Syncrotron Radiation facility and (previously mentioned) high resolution NMR spectroscopy. A proposal for EXAFS measurements at ESFR Synchrotron Radiation has been submitted. Some of these measurements are still in progress. The results of this set of advanced investigations will be described in the next period report.

1.3.2 "TOIFE" Project AWP15-ENR-01/ENEA-08

Scientific research related to fusion inertial confinement in ENEA is performed by the ABC group in Frascati in the framework of the Enabling Research Eurofusion program ER-WP15_CEA-02 (TOIFE) in collaboration with Italian Universities and European institutions. In 2015 studies on the possibility of inducing proton boron reactions by laser, have performed in ABC on cavity targets and in ECLIPSE (CELIA, Bordeaux) by proton acceleration on solid Boron. The homogenization and heat transmission of porous materials has been investigated on free standing Agar Agar samples. Diagnostics of the electromagnetic pulses (emp) has been performed by means of metallic antennas and diamagnetic probes based on the Pockel's cell effect. Calibration of Imaging Plates to X radiation has been performed in ABC and in ECLIPSE.

Aneutronic fusion.

LICPA (Laser-Induced Cavity Pressure Acceleration) cavity targets have been tested in ABC as a means of producing fast protons and attain p-B^{11} fusion reactions. The experiments have been performed in collaboration with IPPLM in Warsaw who developed the targets and

demonstrated the capability of efficiently accelerating fast ions out of a plastic membrane on the cavity output. In a previous ABC campaign with a single beam, proton energies up to 200keV have been measured. However in these experiment,
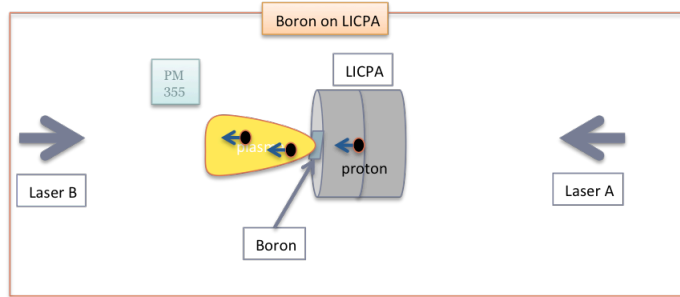

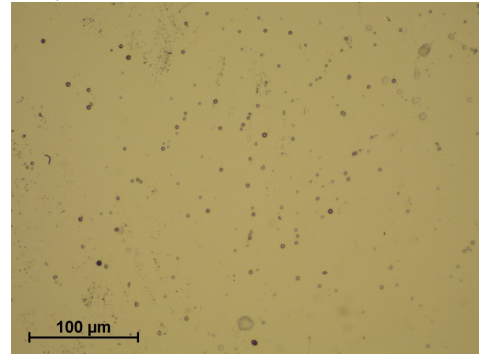**Figure 1.91 - Schematics of the LICPA p-B experiment**

Figure 1.92 - Tracks on a PM355 detector placed at 4.2 cm from the target and 6.0 µm Al filter. The tracks can be assumed to be due to α particles with energy > 1.8 MeV, consistent with a p-B fusion origin

when the proton beam hit a boron solid target, there was no production of alpha particles, as expected in p-^{11}B fusion reactions. In the present campaign two laser beams have been shot on opposite sides of the targets (see *Figure 1.91*), the first (A) to produce the fast protons and the second (B) to simultaneously produce a Boron plasma. In these conditions the tracks observed in the PM355 detector were compatible with the alpha particle originating from proton Boron, *Figure 1.92*. A second set of experiments on the femtosecond laser ECLIPSE in Bordeaux, was performed in collaboration with the CELIA team. In this experiments the fast protons were produced by TNSA (Tare Normal Sheath Acceleration) and hit a solid Boron target in proximity of CR39 track detector. The results are under study.

Light absorption by foams.

The study of porous materials, or foams, has been continued from the past year in collaboration with the Lebedev Institut of Moscow.
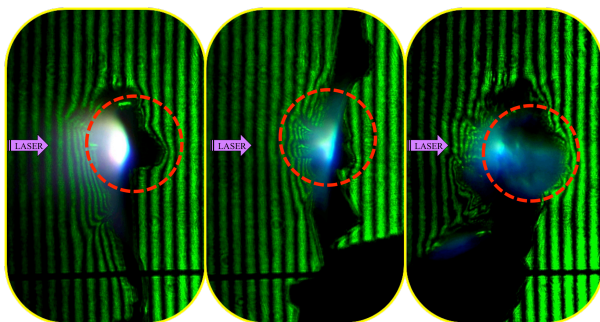

Figure 1.93 - Effect of sharp laser profile variations on different targets: Al (no mask); Al with mask; foam (with mask)
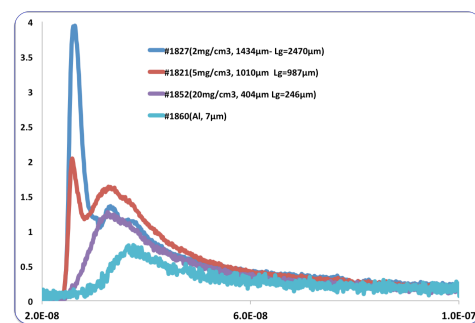

Figure 1.94 - X ray emission from front side target illustrating different propagation time

These materials are characterized by an internal structure constituted by randomly alternating membranes or filaments, and voids. Due to the irregular density distribution of the plasma produced by laser irradiation inside a foam target, the laser energy is absorbed in a volume, rather than in a thin layer as it happens for ordinary homogeneous materials [1.173, 1.174, 1.175]. For this reason, porous materials can smooth out laser inhomogeneity and enhance the pressure in the laser-produced plasma [1.176]. New experimental results have been obtained by using suitable masks along the laser path before the experimental chamber, producing a known perturbation in the laser transverse spatial profile.

The targets were constituted by aluminium foils and free standing layers of porous material. By observing the shadowgraphy of the side of the target opposite to the irradiated one it has been possible to see that in the case of the aluminium foils the transverse shape of the incident laser pulse was quite replicated by the shock wave front reaching the back face of the target; on the other hand, the freestanding porous material layer showed a regular front on the rear side *Figure 1.93*. This can be interpreted as a smoothing effect of the foam on the laser light absorption in the plasma. Moreover, the propagation of the heat wave in these materials has been studied by irradiating foam targets with a metallic deposition on their backside. These experiments showed that at the beginning of irradiation part of the laser light can pass thru the foam target and heat the rear side, where the metallic deposition produced X-rays which have been revealed. When the randomly distributed plasma produced inside the foam becomes homogeneous, the emission of X-rays from the rear side is attenuated, due to the formation of a layer of critical density in the plasma, which completely stops the laser light *Figure 1.94*.
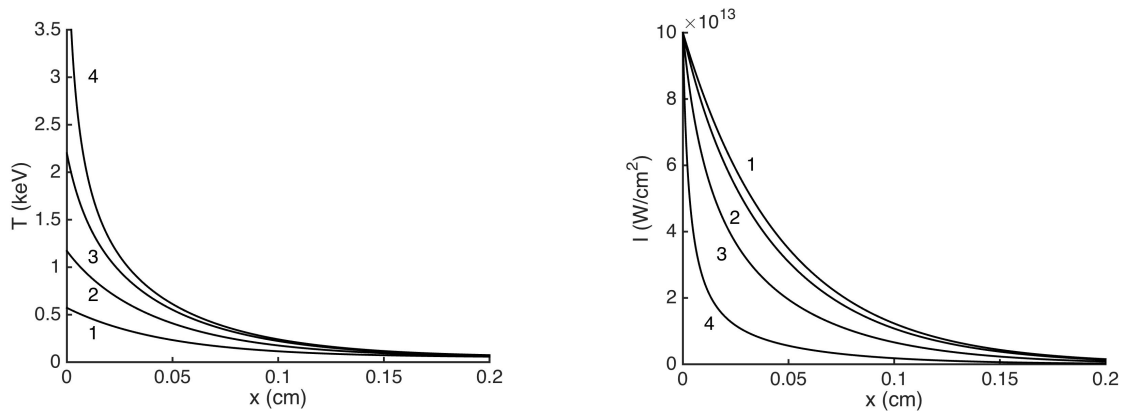

Figure 1.95 - he spatial profiles of temperature (left) and laser intensity (right) in a simulation of a porous medium of density $\rho_p = 10$ mg/cm^3 irradiated by a laser pulse of an intensity $I = 10^{14}$ W/cm^2. The curves are taken at the simulation times (1) 0.25 ns, (2) 0.5 ns, (3) 0.75 ns, (4) 0.95 ns

Another related line of research is constituted by the theoretical study of the laser light absorption in the porous materials. Hydrodynamic simulations regarding these materials are lacking of information about their internal structure, which should be accounted properly to reliably reproduce their features. In order to better model the absorption of laser light, an existing theoretical model has been further developed and has been used to calculate a spatially and temporally dependent absorption coefficient. A simple numerical model has been developed to test the features of absorption [1.177]. The pictures in *Figure 1.95* show examples from177 of the temperature and the laser intensity pro.les along the laser propagation direction at different times of a simulation of a foam with an average initial density larger than the critical density for the laser wavelength of 1054 nm. The laser intensity on the target was of 10^{14} W/cm^2 and the foam average density was of 10 mg/cm^3. The plasma in the foam became overdense after around 1 ns, according with estimations from an analytical calculation.

Study on Electomagnetic Pulses (EMPs).
Measurements of Electomagnetic Pulses (EMPs) have been performed with ABC Laser. A thick solid Al target interacted with two laser beams, for ~25-40 J energies and ~0.5 PW/cm2 intensities, respectively, on two opposite and parallel surfaces the target [1.1781]. Lasers have 3 ns FWHM (Full Width Half Maximum) and fundamental wavelength $\lambda_0 = 1054$ nm. The shots were diagnosed by two antenna types. The first is a commercial monopolar antenna used for multiband wireless communications and optimized in the range (0.8-2.5) GHz [1.179]. A prototype was inside the experimental vacuum chamber (Antenna 1), and one just outside, close to one of its quartz windows (Antenna 3). The second type of antenna (Antenna

2) is also placed inside the chamber, and it is a custom microstrip SuperWideBand antenna (SWB) [1.180], optimized in the range (0.8-18) GHz and with an almost omnidirectional radiation pattern, changing with frequency. The complex nature of the detected signals required their multi-domain study, with related measurements shown in *Figure 1.96*. Classical time-domain analysis was accompanied with representation of signal Amplitude Envelope. For a real signal x(t) the Amplitude Envelope (AE) is defined as [1.181, 1.182] $AE[x(t)] \equiv \left| x(t) + i/\pi \, p.v. \int_{-\infty}^{+\infty} x(\tau)/(t-\tau)d\tau \right|$, where the second addendum represents the Hilbert Transform of x(t) and "p.v." stands for the Cauchy principal value of the integral.
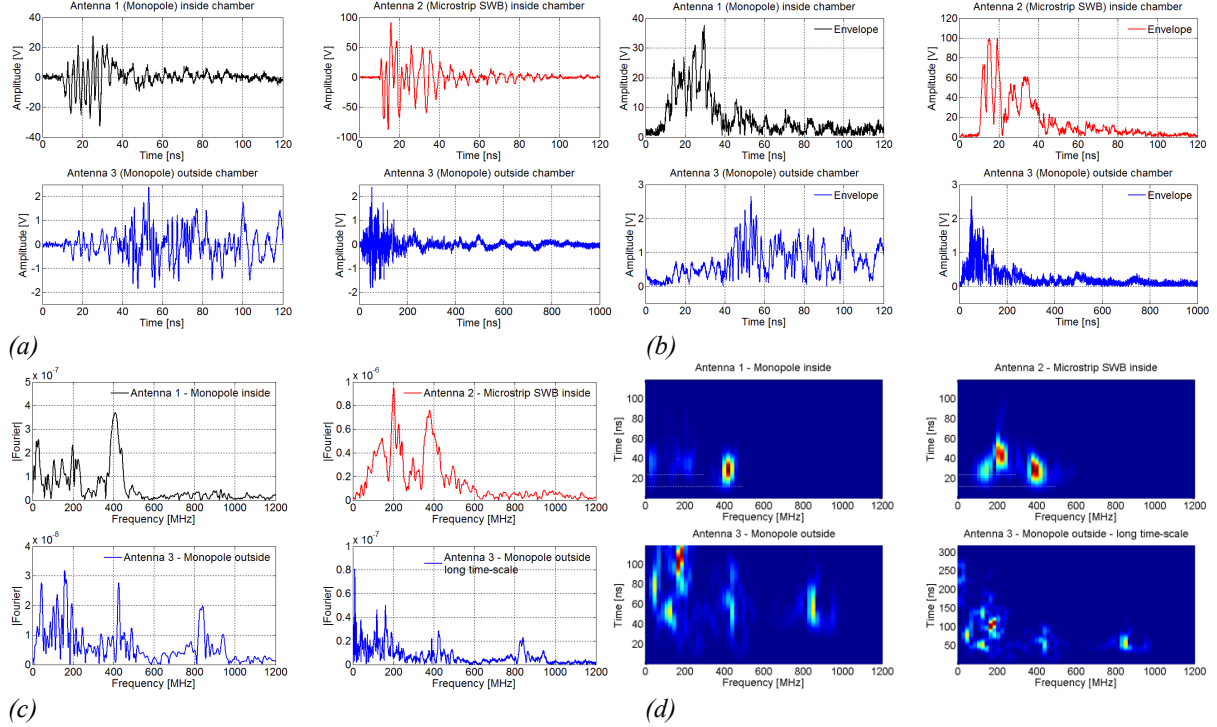
Figure 1.96 - Time domain measurements (a), related Amplitude Envelopes (b), Fourier Transforms (c) and Short-Time Fourier Transforms (d), of results for shot #1525 with the three antennas. For Antenna 3 two different time scales have been used

Classical frequency-domain approach by Fast Fourier Transform (FFT) gives information on the spectral content of a signal on the whole analyzed time interval, but in the shown measurements indeed signal period changes with time. For this reason we applied to the measured signal a time-frequency analysis by means of the Short-Time Fourier Transform (STFT), defined as [1.182] $F_s^w(t,f) \equiv \int_{-\infty}^{+\infty} s(\tau)w(\tau-t)e^{-i2\pi f\tau}d\tau$ where s(t) is the time domain signal, and w(t) is the Hamming window function being zero outside a specific time set. The associated Spectrogram is defined as: $S_s^w(t,f) \equiv |F_s^w(t,f)|^2$. With FFT, because of Nyquist-Shannon's theorem, the sampling rate puts a limit to the maximum frequency of the signal that can be analyzed. On the other hand, the frequency resolution is dependent on the number of acquired samples. This applies also for the STFT [1.182]. In practice, in this case a Fourier Transform is performed in consecutive time intervals, which overlap with the following ones for a fixed time duration. In this way, time and frequency content are correlated, but higher time resolution means lower frequency resolution and vice-versa. We showed that measured electromagnetic fields inside the experimental chamber have time duration up to ~100 ns, and spectral content changing with time. This multicomponent nature of the signals might be due to the superimposition of modal fields localized within the experimental chamber. Signals observed outside it appear to be constituted by two components. One with low time duration, which may be related to fields inside the chamber and the other, existent for longer intervals and with low frequency content. Routs of main

coupling of fields inside the chamber to the outside are quartz windows and cables attached to vacuum RF feedthroughs, whose external conductor is galvanically isolated from the chamber. We see that for all the antennas there is correspondence of the main spectral components at ~ 140 MHz, ~ 200 MHz and ~ 400 MHz. Contributions at low frequencies (up to 50 MHz) are visible for Antenna 1 and 3 only. The main part of the spectrum is limited to approximately the first 600 MHz for antennas inside the chamber, whereas the spectrum for Antenna 3 is more composite. The application of STFT showed that for both Antenna 1 and 2 the ~ 200 MHz and ~ 400 MHz components are respectively synchronous, that the one at ~ 200 MHz lasts for longer time and it is slightly time-shifted with respect to the other. For Antenna 3 we observed a similar shift of the ~200 MHz component with respect to the ~400 MHz one, but they have intrinsically longer time duration. The ~140 MHz contribution is observed for all the antennas (although less definite for Antenna 1) and it is synchronized with the onset of the ~400 MHz component. The multi-domain analysis is a powerful instruments for the understanding of EMP onset due to laser-plasma interaction. More experiments are required to have deeper insight on the effect of laser parameters and of target structure and material on the generated electromagnetic pulse.

Imaging Plate

Calibrations Imaging Plate detectors are largely used as x- ray and particle detectors and imagers, both in medical applications and research laboratories. The program for the calibration of Imaging Plates started in 2014 in collaboration with the laboratory for X-Ray in the ENEA magnetic fusion laboratory and with CELIA laboratories was continued.

Data from the 2014 experiments performed both in Frascati and in Bordeaux were analyzed, and the analysis allowed us to refine the calibrations already available. Since the two sets of calibrations were performed with different scanners, a Dürr CR35 Bio scanner in ABC laboratory in Frascati and a Fujifilm FLA 7000 scanner in CELIA laboratories in Bordeaux, and the Dürr scanner lacks a conversion algorithm to express its data in the widely used Photostimulated Luminescence (PSL) counts; an experiment for the cross-calibrations of these two
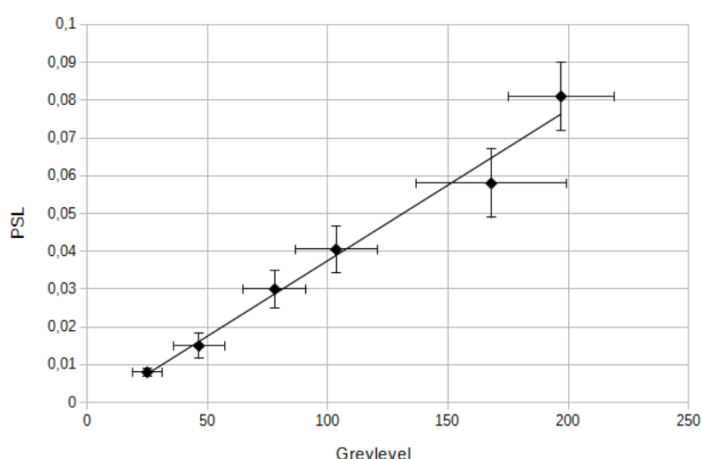

Figure 1.97 - The relationship between GL from Dürr CR35 Bio and PSL from Fujifilm FLA7000. Experimental data (dots with error bars) and fit (solid line)

scanners was performed, in CELIA laboratories. Using pieces of IP from the same batch, we produced pairs of identical samples irradiating them with a 55Fe β source. These identical samples were scanned with both scanners and we got an equation that allows us to compare data from the two laboratories (*Figure 1.97*). This calibration also discloses for the Dürr scanner the use of calibration found in literature and expressed in PSL counts unit. This program brought to the publication of three articles.

1.3.4 Project AWP15-CNR-01/ENEA-06: "Experimental investigation of PDIs and wave excitation by non-resonant mm-wave beams and their effect on localized Electron Cyclotron and Ion heating using an improved CTS diagnostic"

The recently renewed 140GHz Collective Thomson Scattering (CTS) system at FTU is being

used for the experimental investigation of Parametric Decay Instabilities (PDI) and wave excitation by non-resonant mm-wave, as well as for the study of their effect on localized Electron Cyclotron and Ion heating, in the Enabling Research project AWP15-CNR-01/ENEA-06. The main purposes of the project are

- Determine the EC launching and plasma condition in which PDI can be observed, in order to prevent their appearance in case they produce degradation of the EC deposition profiles for heating or current drive.
- Study the impact of the PDIs on the efficiency of EC to stabilize the magnetic island where they are localized
- Study the possibility to exploit PDIs to perform localized heating by means of the excited waves
- Verify the possibility that PDIs induce ion heating and estimate this effect on the ion temperature and distribution function
- Test the effect of the injection of two high power mm-wave beams such that their difference in frequency is a multiple of the ion gyro-frequency and estimate the effect on ion temperature and distribution function.

The specific experimental conditions on FTU are advantageous and make the purposed study of particular interest: FTU offers the possibility to work with plasma density condition and injection geometry similar to those envisaged for the CTS system in ITER. In the high field configuration ($B_T = 7.2$ T) the probe beam is non-resonant since the fundamental harmonic layer lies between the plasma edge and the vacuum vessel. The same condition could be obtained at $B_T = 3.6$ T where the first and the second EC harmonics are outside the plasma, surrounding it. The use of a fast digitizer allows the acquisition of the data over a wide frequency band (5 GHz) with an extremely high sampling rate of 12.5GS/s maximum. In order to optimize the quality of the acquired signal, a great effort has been performed to discriminate the radiation coming from the formation of undesired breakdown plasma near the injecting mirror. For this reason, three new sensors have been installed in the antenna port. Different configurations of signal injection and plasma condition have been explored during the last experimental campaign. Plasma discharges have been performed at 4.7 T (resonance inside the plasma) and 3.6 T (resonance outside the plasma). The two lines of sight of the new EC launcher of FTU are used to inject the high power beam (~400 kW) and to receive the scattered radiation, moving the receiving mirror during the discharge for a more precise localization of the source of the scattering phenomena. Details regarding the results of the experimental observations are reported in the FTU experimental activity section of this document.

1.4 Complementary Activity

1.4.1 CARM Source Development

Plasma heating systems based on the electron cyclotron resonance (ECRH) mechanism have been used effectively in different fusion devices exploiting the intrinsic potential features of this technique. Among these peculiarities it is worth to mention the local absorption of the RF power at the electron cyclotron resonance that may provide an increase of the plasma temperature, the damping of dangerous instabilities, the modification of the pressure and density profiles that can control electric current drive in the plasma itself.

The physical mechanisms underlying the plasma heating process and the damping of instabilities, like those of saw tooth type, using external electromagnetic sources, have been thoroughly investigated in plasma physics.

In the case of the international Tokamak experiment ITER, which operates at a magnetic field of 5.7 Tesla, Gyrotron sources are in an advanced phase of development and can provide a heating power of approximately 1 MW CW at a frequency of 170 GHz. The further step in fusion, DEMO, and any future fusion reactor, due to the high temperatures associated with the plasma, require higher ECRH frequencies to obtain a central Radio-Frequency (RF) power deposition, avoiding downshifted absorption on the distribution function tails. It will be therefore necessary to develop high-power sources ($\geq$ 1 MW) in the frequency range of 200-300 GHz.

The quest for the parallel development of different "heating tools" should therefore be considered. CARM sources have been viewed as promising devices since the 80's of the last century. The experimental effort put forward in the following decade was hampered by some technological issues, associated with the difficulties of getting a high quality intense electron beam, which did not allow the possibility of obtaining the required performances in terms of efficiency.

Major achievements in the design of emitters providing high quality e-beam, along with significant improvements in analytical and numerical modelling capability and the availability of unprecedented computational resources, are the key issues to overcome the quoted technological drawbacks. These reasons motivate the proposal of a new CARM sources dedicate to ECRH. A design study for such a source has been conducted at ENEA-Frascati, and a research programme is currently being carried out.

We have chosen the working frequency of the proposed CARM source taking into account the expected demands of reactor-relevant machines like DEMO
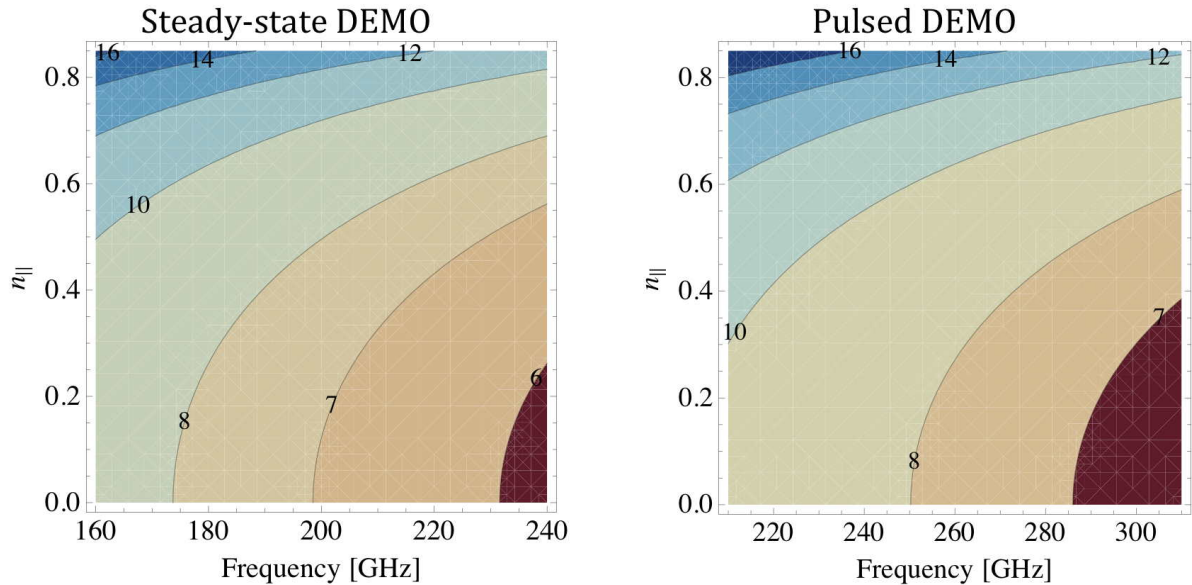

Figure 1.98 - Contour plots of parallel refraction index and frequency; different colors represent the radial position (in meters) at which the first harmonic absorption becomes possible.

A proper analysis of the plasma characteristics of DEMO 2014 design, and the relevant interaction with the electromagnetic waves lead to the result reported in *Figure 1.98* where the contour lines versus frequency and the parallel refractive index are plotted. Since the optimum current drive efficiency occurs at higher $n_{\parallel}$ (between 0.6and 0.8), and considering that absorption is more efficient close to the centre of the tours (the major radius R_0) we can conclude that the steady-state and pulsed DEMO operating modes are expected to require frequencies around 230 and 280 GHz, respectively, allowing the EC waves with larger $n_{\parallel}$ to reach the geometrical axis of the tokamak.

The availability of CARM sources operating at frequencies in the range 250 GHz, allows also its use on FTU to perform second-harmonic EC experiments.

The proposed device is a complex system that can be schematically described in term of single blocks that recall all the basic elements of the electron-based electromagnetic radiation sources like Free Electron Lasers and Gyrotrons. In *Figure 1.99* a schematic layout is reported.
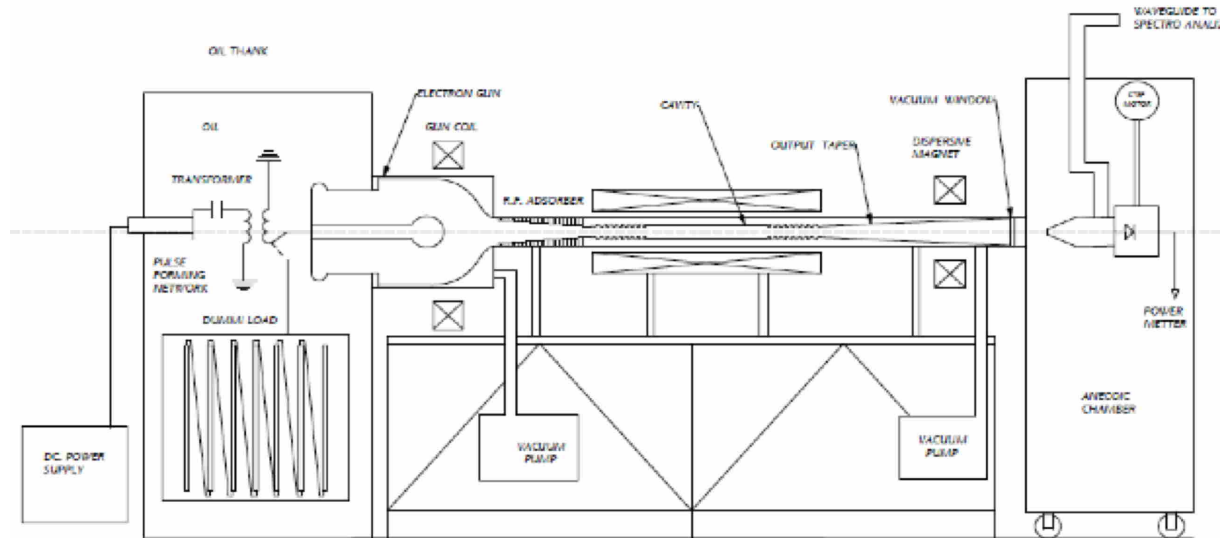

Figure 1.99 - ENEA CARM Layout

The *Modulator* is one of the most crucial, complex and expensive elements of the entire experiment. The relevant complexity comes from the noteworthy required stability of its electrical parameters, comparable with the modulators of High Power Klystrons, used to drive High-Gradient RF LINACs, albeit with a much longer pulse. The ENEA CARM project is to be developed in two steps. The first step considers a pulsed operation at low repetition rate and maximum pulse duration of 50 ms The second step is devoted to the development of a long pulse CARM prototype, requiring different type of modulator indeed equipped with a depressed collector, for beam energy recovery, and Vlasov-like mode converter to bring the RF power out of the CARM system. Due to the power losses into the RF circuit an intensive forced cooling is necessary. It is evident that both steps differs from each other for their respective pulse length but must have equal pulse time profile which applies different approach for designing the Modulator.

The *Electron-Gun* emits and accelerates the electron beam with the required parameters and it has a diode type geometry. The electron beam is and then transported through the vacuum vessel immersed in high magnetic field; most of the helical beam properties are strongly dependent on the Gun design. In general the electron beam is very sensitive to small changes of the electrode dimensions, emitter surface roughness and its chemical properties. The road map pursed, during the preliminary design of the electron gun, had as a goal the limitation of both the maximum surface electric field and the control of the initial electrons velocity spread. As a main target for the long pulse operation, the surface electric field at any point inside the gun has to be less than 10kV/mm. Moreover we have taken into account that, the geometrical shape of the electrodes, their surface roughness, the emitter temperature and its uniformity, rule the electron velocity spread over the whole emitter surface.

The RF Resonant Cavity is the element where the electron beam energy is partially transferred to the radiation electric field. The operating modes in CARM are usually TE_{mn} type. The conversion efficiency depends on the quality of the electron beam, which in turn demands for a high performance gun design. The possibility of achieving a suitable efficiency level depends also on the appropriate beam coupling to the operating mode. The mode

selection is an issue of crucial importance; the RF cavity must therefore guarantee an efficient beam interaction with a Doppler upshifted frequency and to suppress the down shifted (cutoff) counterpart. An oversized cavity will be used with cross section dimensions set by limits of the RF power dissipation on the cavity wall and by the electric breakdown in vacuum.

The *Magnetic Channel* provides the electron beam transport and appropriate shape before its injection into the cavity. It consists of a gun coil, a large cavity magnet and a kicker coil. Eventually an additional correcting coil positioned before the main magnet will be used to form the desired magnetic field topology along the z-axis. All elements must be aligned very accurately along the CARM axis in order to have an efficient beam transport and an optimal beam-RF coupling into the resonant cavity.

The last component of the magnet system is the *"Kicker Coil"* generating a field with a nominal value ranging 0.08-0.1 Tesla, perpendicular to the system axis. This coil is necessary to remove any stray remaining electron after the beam dump by forcing them into the beam pipe wall.

The *Beam Dump* is the region of the CARM in which the spent electron beam is terminated. The ENEA CARM generates high-energy electron beams (700 keV), hence as the beam terminates by impacting the walls of the beam pipe it produces a significant amount of x-ray radiation by bremsstrahlung. Thus the beam dump has to be carefully designed to absorb the x-ray flux. Usually a multi-layer lead surrounds this element to protect the nearby area from the produced radiation. The termination of the beam also produces heating due to both scattering and ohmic losses. Therefore, the beam dump is water cooled through channels in its exterior wall.

The *Vacuum System* is an important part of any high-power microwave tube. It is designed to maintain an extremely low pressure at high pumping rate. In general the vacuum is responsible for two extremely dangerous phenomena. The first one is a vacuum break-dawn due to a high electric field across the gaps. The second one is a surface field breakdown due to a high surface field. We have been very conscious when the decisions about the cavity size and the operating mode have been taken. Our experimental part under vacuum is about 2 meters long with a minimum cross-section of 15 mm. The device will operate at pulse duration between 1 and 50 µs, for the first step of the project, thus we will need a double side pumping to maintain the designed repetition rate of 10 Hz. Most of the components under vacuum can't be slotted apart for better pumping performance. The vacuum is mainly relevant for emitter due to poisoning possibility. A special chemical treatment of all the components, before the final assembling and installing, is considered in the project.

A Technical Design Report (TDR) has been prepared, and it will be soon submitted to an International Advisory Board composed of the most prestigious experts in this field.

1.5 Non Eurofusion Funded Activity

1.5.1 Proto-SPHERA
The first experimental phase of PROTO-SPHERA, with central column plasma only (dubbed as Multi-Pinch) had been running from the summer of 2014 up to February 2015.
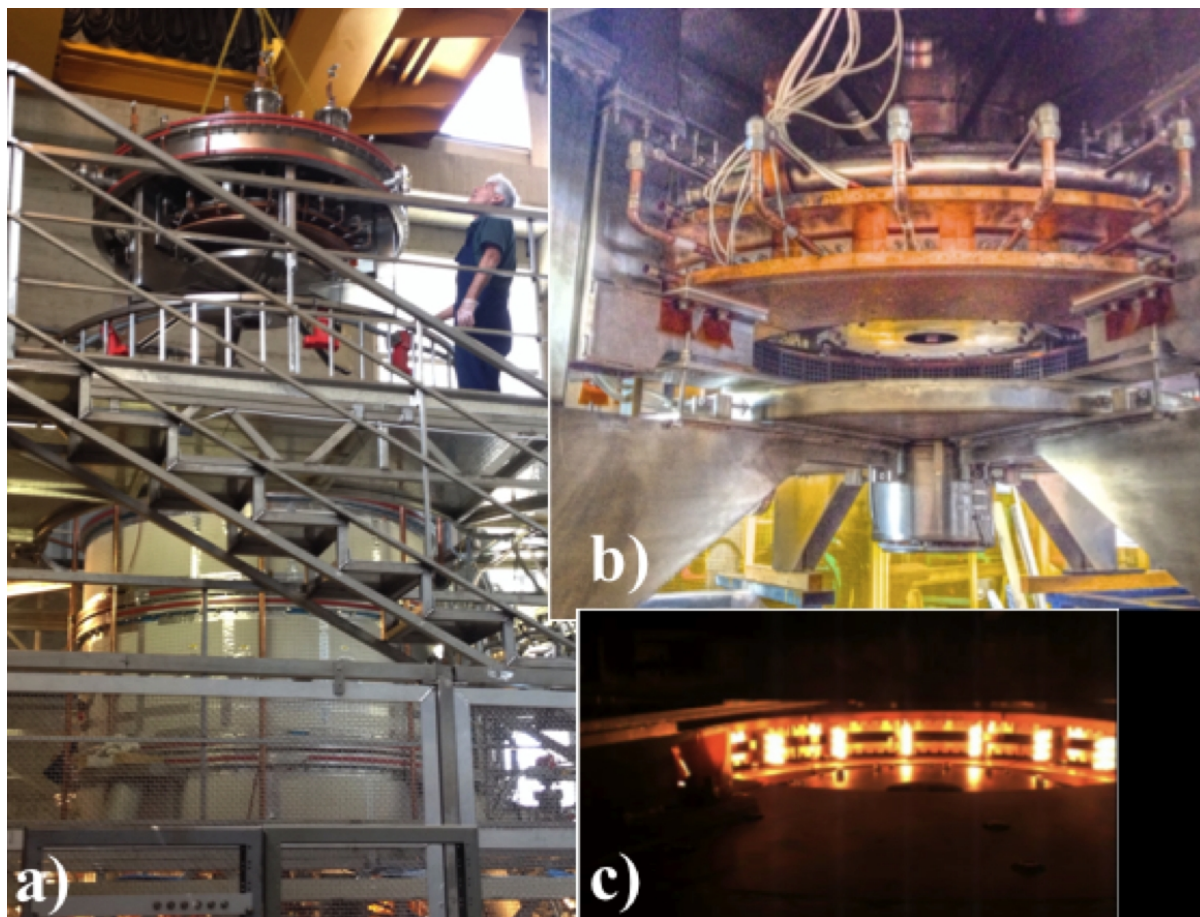
Figure 1.100 - The annular anode lowered on top of PROTO-SPHERA, b) The annular anode being assembled, c) The annular cathode being heated before the plasma discharge

In this first phase the plasma central column was obtained in presence of the annular cathode on the bottom of the machine, but with a simple provisional cylindrical anode on top of it.
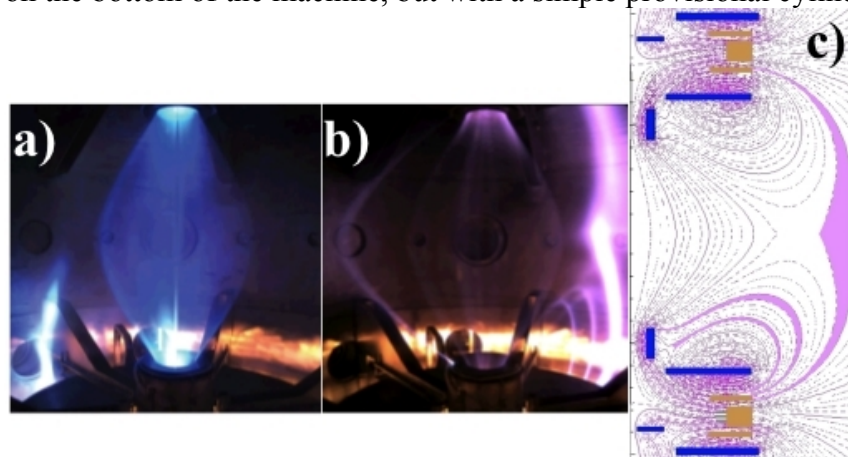

Figure 1.101 - a) Plasma Centerpost in Argon, b) in Hydrogen, 2c) Magnetic field map

In May 2015 the final annular anode was lowered on top of machine, see *Figure 1.100*. The new operation of PROTO-SPHERA phase 1 has been implemented during the year 2015 in presence the final annular anode in two main steps: the first in May 2015, which did not produce more than 2 kA of plasma centerpost current, see *Figure 1.101* a) and b). The reason was the presence of a regular X-point of the magnetic field on the outboard of the vacuum vessel: the plasma current could flow in secondary discharges. In order to remove this behavior 4 new (poloidal field) PF coils were wound in July around the vessel, in order to get rid of the ordinary X-point, see *Figure 1.102*.
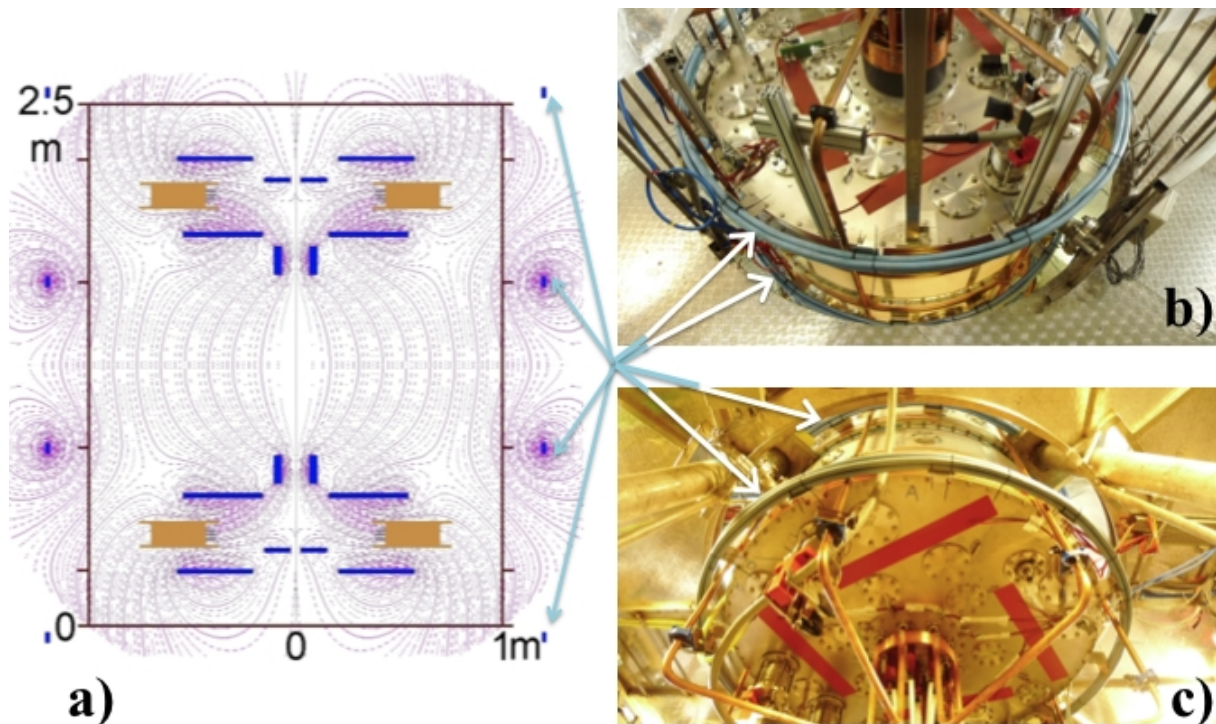
Figure 1.102 - The new magnetic field map of PROTO-SPHERA after the new PF coils (light blue) outside the vacuum vessel, shown from the top of the machine b) and the bottom of it c)

The result was quite encouraging: in the October 2015 plasma operation the secondary discharges vanished and the plasma centerpost current reached 3.4 kA (*Figure 1.103* a), with a duration of 0.3 s. Furthermore the plasma filamentation, due to the sparse cathode filaments (18 rows of 3 W coils), vanishes as the plasma approaches the anode, due to the electrostatic charging of the internal PF coils by the plasma itself (*Figure 1.103* b). This finding dispels any anode arc-anchoring effect, which was feared to occur in PROTO-SPHERA.
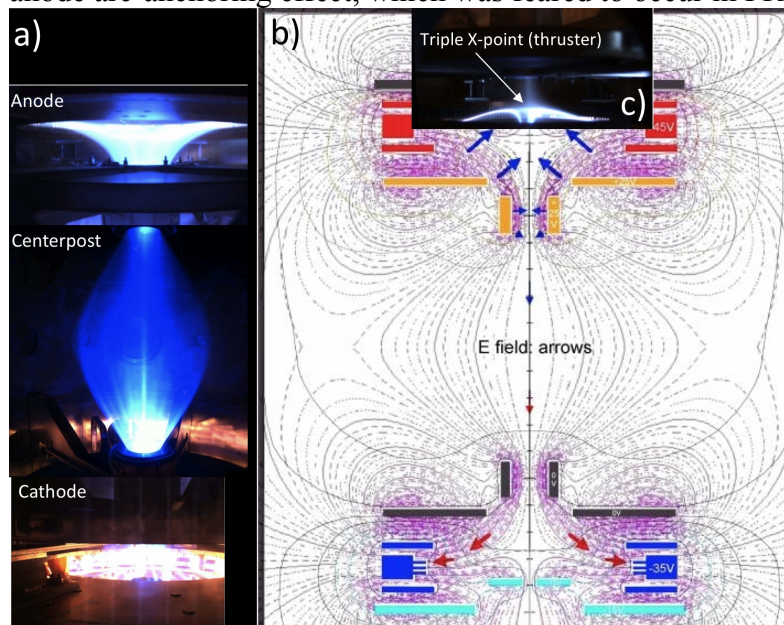
Figure 1.103 - PROTO-SPHERA plasma at 3.4 kA, b) Electrostatic fields (blue and red arrows) superposed to magnetic field (violet lines), c) Picture of triple X-point on top of anode

To reach the full plasma centerpost current of 8.5 kA, it is necessary to substitute the top and bottom Stainless Steel flanges, which host the busbars – feeding the plasma current to the anode and drawing it from the cathode – , with an insulating material, such as Polycarbonate, in order to avoid secondary discharges above the anode and below the cathode. This substitution is due to another magnetic X-point effect of the experiment, i.e. the triple X-point on top and bottom of the machine (*Figure 1.103* c). These X-points however are an asset of PROTO-SPHERA, which aims at exploring a fusion space thruster magnetic confinement configuration: one of the triple X-points will act as the nozzle of the thruster.

References

*[1.1] J. W. Connor and R. J. Hastie, Nucl. Fus., **15** (1975) 415*

*[1.2] J. R. Martin-Solis et al., Phys. Rev. Lett., **105** (2010) 185002*

*[1.3] C.Mazzotta et al. 2015 Nucl. Fusion **55** 073027*

[1.4] C.Mazzotta et al 2015. Neon transport simulation for highly peaked density FTU plasma. 42nd EPS Conf. on Plasma Physics, Lisbon, 22-26 June, 2015. Vol. 39E ISBN 2-914771-98-3. P4.114 http://ocs.ciemat.es/EPS2015PAP/pdf/P4.114.pdf

*[1.5] O.Tudisco et al, Fusion Eng. and Design **85** (2010) 902, doi:10.1016/j.fusengdes.2010.08.037*

*[1.6] G.Pucella et al. 2013 Nucl. Fusion **53** 083002*

*[1.7] A.V.Chankin. 2004 Physics of Plasmas **11** 1484*

[1.8] B. Lipschultz, J. Nucl. Mater. 145-147 (1987) 15

*[1.9] O.Tudisco et al, Fus Sci. Tech.**45** (2004), 402*

[1.10] R. Martorelli, G. Montani, N. Carlevaro, Mod. Phys. Lett. A 31(2), 1650005 (2016)

[1.11] A. Carati et al., Chaos 22, 033124 (2012)

[1.12] G. Pucella and FTU Team, "Overview of FTU Results"; G. Mazzitelli et al, to be presented to IAEA Fusion Energy Conference, Kyoto (2016)

[1.13] Holger R et al, Towards an Assessment of Alternative Divertor Solutions for DEMO, EPS 2015, Lisbon

[1.14] M. De Angeli, et al., Nuclear Fusion 55 (2015) 123005

[1.15] B. Esposito et al, Runaway electron experiments in FTU, Paper P4.113, 42nd EPS Conference on Plasma Physics 2015)

[1.16] W. Bin et al., Fusion Eng. Des. 96-97 (2015) 733-737

[1.17] A. Bruschi et al., to be presented to IAEA Fusion Energy Conference, Kyoto (2016)

[1.18] F. Sauli et al, Nucl. Instrum. And Meth. in Phys. Res. A. 386, 531 (1997)

[1.19] F. Murtas, Applications of triple GEM detectors beyond particle and nuclear physics, JINST 9 C01058 (2014)

[1.20] D. Pacella et al, 40th EPS Conference on Plasma Physics, P5.118 (2013)

[1.21] C. Strangio and A. Caruso, Study on the hydrodynamical behavior of thin foils irradiated by near-field ISI smoothed beams, Laser Part. Beams 16 (1998) 45

[1.22] D. Pacella, An hybrid detector GEM-ASIC for 2-D soft X-ray imaging for laser produced plasma and pulsed sources", in: 2016 JINST 11 C03022 (2016)

[1.23] D. Batani et al, Development of the PETAL Laser Facility and its Diagnostic Tools, Acta Polytechnica, 53(2):103109 (2013)

[1.24] G. Claps et al, The GEMpix detector as new soft X-rays diagnostic tool for Laser Produced Plasmas, in: RSI (submitted for publication)

[1.25] E. Giovannozzi et al., 33rd EPS Conference on Plasma Phys. Rome, ECA Vol.**30I**, P-2.093 (2006*)*

[1.26] C. Di Troia, Plasma Physics and Controlled Fusion, 54, (2012) 105017

[1.27] C. Di Troia, 55, Nucl. Fus., (2015) 123018

[1.28] C. Di Troia, Phys. of Plasmas, 22, (2015) 043502

*[1.29] T.M. O'Neil, J.H. Winfrey, J.H. Malmberg, Phys. Fluids **14**, 1204 (1971)*

*[1.30] N. Carlevaro, M.V. Falessi, G. Montani, F. Zonca, J. Plasma Phys. **81**, 495810515 (2015)*

*[1.31] T. Peacock, G. Haller, Phys. Today **66**, 41 (2013)*

[1.32] H. Hasegawa and L. Chen, Phys. Rev. Lett. 35, 370 (1975)

[1.33] R. Z. Sagdeev, V. D. Shapiro and V. I. Shevchenko, Zh. Eksp. Teor. Fiz. Pis'ma Red. 27, 361 (1978) [Sov. Phys. JETP 27, 340 (1978)]

[1.34] L. Chen and F. Zonca, Phys. Rev. Lett. 109, 145002 (2012)

[1.35] L. Chen and F. Zonca, Rev. Mod. Phys. 88, 015008 (2016)

[1.36] F. Zonca, Y. Lin and L. Chen, Europhys. Lett. 112, 65001 (2015)

[1.37] G. Ara et al. , Ann.Phys.,112, 443, (1978)

[1.38] Talk by Camillo Tassi at Sif 2015

[1.39] B. Tirozzi, C. Tassi, P. Buratti, to appear in Eur. Phys. J. D. (2016) DOI: 10.1140/epjd/e2016-60497-x

[1.40] Aschwanden, M. J., Crosby, N., Dimitropoulou, M., Georgoulis, M. K., Hergarten, S., McAteer, J., Milovanov, A.V., Mineshige, S., Morales, L., Nishizuka, N., Pruessner, G., Sanchez, R., Sharma, A. S., Strugarek, A., and Uritsky, V., to appear in 2016, 25 Years of self-organized criticality: Solar and astrophysics, Space Sci. Revs. 198, 47-166. Invited review: impact factor 5.874. Doi: 10.1007/s11214-014-0054-6

[1.41] Sharma, A. S., Aschwanden, M. J., Crosby, N., Klimas, A. J., Milovanov, A.V., Morales, L., Sanchez, R., and Uritsky, V., to appear in 2016, 25 Years of self-organized criticality: Geo-space and fusion plasmas, Space Sci. Revs. 198, 167-216. Invited review: impact factor 5.874. Doi: 10.1007/s11214-015-0225-0

[1.42] Milovanov, A.V. and Rasmussen, J. Juul. 2015, Self-organized criticality revisited: Non-local transport by turbulent amplification, J. Plasma Phys. 81, 495810606 (14pp). Doi: 10.1017/S0022377815001233

[1.43] A. Cardinali, L. Amicucci, C. Castaldo, S. Ceccuzzi, R. Cesario, F. Mirizzi, L. Panaccione, F. Santini, A.A. Tuccillo, Invited to the AIP Proceedings of the 21st RF Frequency Power in Plasmas, California, USA, 27-29 April 2015, Vol. 1689, p. 54

[1.44] A. Cardinali, L. Amicucci, C. Castaldo, S. Ceccuzzi, R. Cesario, F. Mirizzi, L. Panaccione, F. Santini, A.A. Tuccillo, Submitted to PRL 2015

[1.45] L. Guidi, A. Cardinali, B. Tirozzi, Accepted for publication to Journal of Plasma Physics

[1.46] A. Cardinali, S. Yu. Dobrokhotov, A. I. Klyovin, B. Tirozzi, Dokladi Akademii Nauk, Mathematical Physics Section, in press

[1.47] A. Cardinali, S. Yu. Dobrokhotov, A. I. Klyovin, B. Tirozzi, Talk by B. Tirozzi at the PPLA conference in Frascati, Sep. 2015 & Proceeding of the PPLA conference

[1.48] N.J. Fish, Rev. Mod. Phys 59 (1987) 175

[1.49] R. Cesario, et al Nat. Commun. 1 (2010) 55

[1.50] C. Castaldo, et al Nucl. Fusion 56 (2016) 016003

[1.51] F. Zonca and L. Chen, Physics of Plasmas 21, 072120 (2014)

[1.52] F. Zonca and L. Chen, Physics of Plasmas 21, 072121 (2014)

[1.53] R. Ma, F. Zonca and L. Chen, Physics of Plasmas 22, 092501 (2015)

[1.54] J. Cao, Z. Qiu and F. Zonca, Physics of Plasmas 22, 124505 (2015)

[1.55] T. Ido, M. Osakabe, A. Shimizu et al., Nucl. Fusion 55, 083024 (2015)

[1.56] G. Fu, Phys. Rev. Lett. 101, 185002 (2008)

[1.57] Z. Qiu, F. Zonca, and L. Chen, Plasma Phys. Control. Fusion 52, 095003 (2010)

[1.58] S. Briguglio et al., Phys. Plasmas 2, 3711-3723 (1995)

[1.59] X. Wang et al., Phys. Plasmas 18, 052504 (2011)

[1.60] S. Briguglio et al., Phy. Plasmas 21, 112301 (2014)

[1.61] X. Wang et al., (to be published) (2016)

[1.62] Ph. Lauber et al., J. Comp. Phys. 226, 447 (2007)

[1.63] S. Pinches et al., Comput. Phys. Commun. 111, 133 (1998)

[1.64] G. Vlad et al., Nucl. Fusion 53, 083008 (2013)

[1.65] V. Fusco et al., Analysis of the electron fishbone instability with the XHMGC code, 7th IAEA Technical Meeting on Plasma Instabilities, Frascati, Italy, March 4-6, 2015

[1.66] V. Fusco et al., Electron fishbone dynamics studies in tokamaks using the XHMGC code, 14th IAEA Technical Meeting on Energetic Particles in Magnetic Confinement Systems, Vienna 1-4 Sep. 2015

[1.67] Chen L., White R.B. and Rosenbluth M.N., et al. Phys. Rev. Lett., 52, (1984) 1122-5

[1.68] G. Montani, D. Pugliese, J. Plasma Phys. 81, 495810604 (2015)

[1.69] D. Pugliese, G. Montani, Phys. Rev. D 91, 083011 (2015)

[1.70] R. Coelho, A. Merle, G. Vlad, D. Yadikin, M. Owsiak, O. Sauter, I. Chapman, M. Dunne, P. Buratti, JET contributors, ASDEX Upgrade Team and the EU-IM Team, "Scientific workflows for MHD stability chain analysis of tokamak plasmas", 42nd EPS 2015, P4.178, ECA Vol. 39E ISBN 2-914771-98-3. http://ocs.ciemat.es/EPS2015PAP/pdf/P4.178.pdf

[1.71] A. Bondeson, G. Vlad and H. Lütjens, Proc. of the IAEA Technical Committee Meeting on Advances in Simulations and Modelling of Thermonuclear Plasmas (Montreal 1992), p. 306, IAEA–Vienna (1993)

[1.72] G. Fogaccia, G. Vlad, S. Briguglio, "Linear benchmarks between the hybrid codes HYMAGYC and HMGC to study energetic particle driven Alfvénic modes" 14th IAEA-TM on Energetic Particles 2015; submitted to Nuclear Fusion

[1.73] A. Könies et al. 2012 Proc. 24th Int. Conf. on Fusion Energy Vienna (San Diego, 2012). 437-ITR/P1-34. http://www-naweb.iaea.org/napc/physics/FEC/FEC2012/html/fec12.htm

*[1.74] M. Brambilla, R. Bilato, 2009 Nucl Fusion **49** 085004*

*[1.75] V. Lancellotti, et al., 2006 Nucl Fusion **46** S476*

[1.76] E. Lazzaro et al., Nucl. Fusion 55 (2015) 093031

[1.77] S. McIntosh et al., IAEA 2014, FIP/P8-9

[1.78] F. Sauli et al, Nucl. Instrum. And Meth. in Phys. Res. A. 386, 531 (1997)

[1.79] F. Murtas, Applications of triple GEM detectors beyond particle and nuclear physics, JINST 9 C01058 (2014)

[1.80] D. Pacella et al, 40th EPS Conference on Plasma Physics, P5.118 (2013)

[1.81] W. Choe et al, Tomographic 2-D X-ray imaging of toroidal high temperature plasma by a tangential pinhole camera with gas electron multiplier detector", in: PSST (IOP) (submitted for publication)

[1.82] D.D. Ryutov, Phys. Plasmas 14 (2007) 064502

[1.83] Ryutov, V.A. Soukhanovskii, Physics of Plasmas 22, 110901 (2015)

[1.84] G. Calabrò, et al., Nuclear Fusion 55 (8), 083005 (2015)

[1.85] G. Calabrò, to be presented at PSI 2016 conference

[1.86] R. Albanese, et al., Fusion Engineering and Design 96-97 (2015) 664-667

[1.87] B. Xiao, et al., 1st IAEA TM on Divertor Concept, Vienna (Austria), O.12 (2015)

[1.88] R. Cesario, et al., Nature Commun. (August 2010) http://dx.doi.org/10.1038/ncomms1052

[1.89] T. C. Luce et al 2003 Nucl. Fusion 43 321

[1.90] M. Shimada et al. Nucl. Fusion 47 (2007) S1–S17

[1.91] D. Frigione et al 42nd European Physical Society Conference on Plasma Physics, Lisbon 2015, Portugal, P2.116

[1.92] J. Garcia et al. , Nucl. Fusion 55 (2015) 053007

[1.93] P. Buratti et al 2015 "MHD in JET hybrid plasmas with the ITER Like Wall" 42nd EPS Conference on Plasma Physics Lisbon (European Physical Society 2015) paper P2.115

[1.94] P. Buratti et al 2014 Proc. 41st EPS Conf. on Plasma Physics (Berlin, Germany, 2014) P1.014 http://ocs.ciemat.es/EPS2014PAP/pdf/P1.014.pdf

[1.95] E.Giovannozzi et al 2014 Proc. 41st EPS Conf. on Plasma Physics (Berlin, Germany, 2014) P1.015 http://ocs.ciemat.es/EPS2014PAP/pdf/P1.015.pdf

[1.96] http://users.jet.efda.org/pages/tfiospti/TFmeetings/Lisbon2016/viola.pdf

[1.97] P. Snyder et al., 2004 Plasma Physics and Controlled Fusion 46 A131–A141 ISSN 0741-3335 URL

[1.98] Leyland J M "The pedestal structure in high performance JET plasmas" PhD Thesis

[1.99] Saarelma S, Alfier A, Beurskens M, Coelho R, Koslowski H, Liang Y and Nunes I 2009 Plasma Physics and Controlled Fusion 51 035001 ISSN 0741- 3335

[1.100] A. Murari, et al., (2015) Nuclear Fusion, 56 (2), art. no. 026006

[1.101] A. Murari, et al., (2015) Nuclear Fusion, 56 (2), art. no. 026005; A. Murari, et al. (2015) Nuclear Fusion, 55 (7), art. no. 073009; A. Murari, et al. (2015) Plasma Physics and Controlled Fusion, 57 (1), art. no. 014008; A. Murari, et al., (2015) Lecture Notes in Computer Science (including subseries Lecture Notes in Artificial Intelligence and Lecture Notes in Bioinformatics), 9047, pp. 347-355

[1.102] T. Craciunescu, et al., (2015) Fusion Engineering and Design, 96-97, pp. 765-768

[1.103] A. Pau, et al., "A method for the automatic construction of reliable disruption databases", to be submitted. Presently published in the EuroFusion pinboard

[1.104] B. Cannas, A. Fanni, A. Murari, A. Pau, G. Sias, and JET EFDA Contributors (2013), "Automatic Disruption Classification based on Manifold Learning for Real Time Applications on JET", Nucl. Fusion 53 093023

[1.105] B. Cannas, P. C. de Vries, A. Fanni, A. Murari, A. Pau, G. Sias and JET Contributors (2015) "Automatic disruption classification in JET with the ITER-like wall", Plasma Phys. Control. Fusion 57 125003 (15pp)

[1.106] R. Aledda R., B. Cannas, A. Fanni, G. Sias, G. Pautasso (2012), "Mapping of the ASDEX upgrade operational space for disruption prediction", IEEE Transactions on Plasma Science, Volume 40, Issue 3 PART 1, Article number 6099630, Pages 570-576

[1.107] R. Aledda , B. Cannas, A. Fanni, A. Pau, G. Sias (2015), "Improvements in disruption prediction at ASDEX Upgrade", Fusion Engineering and Design, Volume 96-97, Pages 698-702

[1.108] Nucl. Fusion 51 53018, 2011

[1.109] R. Aledda, B. Cannas, A. Fanni, A Murari, A. Pau, G. Sias, the ASDEX Upgrade Team, the JET Contributors and the EUROfusion MST1 Team (2015), "A comparative multivariate analysis of disruption classes between JET and AUG", 42nd European Physical Society Conference on Plasma Physics, Lisbon, Portugal, 22nd—26th June 2015

[1.110] A. Murari, F. Pisano, J. Vega, B. Cannas, A. Fanni, S. Gonzalez, M. Gelfusa, M. Grosso (2014), "Extensive statistical analysis of ELMs on JET with a carbon wall", Plasma Physics and Controlled Fusion, Volume 56, Issue 11, Article number 114007

[1.111] B. Cannas, A. Fanni, A. Murari, F. Pisano, and JET EFDA contributors "Nonlinear dynamic analysis of Da signals for type I Edge Localized Modes characterization on JET with a carbon wall", Pre-print published on IoPP website reference EFD-P(14)024 Dia ref CPS14.731

[1.112] B. Cannas, A. Fanni, A. Murari, F. Pisano, and JET Contributors, "Recurrence plots for dynamic analysis of type I ELMs at JET with a Carbon wall", to be submitted to IEEE Transactions on Plasma Science, presently published in the EuroFusion pinboard

[1.113] P. Batistoni, et al., Technological exploitation of Deuterium-Tritium operations at JET in support of ITER design, operation and safety, accepted for publication in Fus. Eng. Design (ISFNT12)

[1.114] L. Horton, et al., JET Experiments with Tritium and Deuterium-Tritium Mixtures, accepted for publication Fus. Eng. Design (ISFNT12)

[1.115] A. Murari, et al., Upgrades of Diagnostic Techniques and Technologies for JET next D-T Campaigns, accepted for publication IEEE Transactions on Plasma Sciences, April 2015

[1.116] L. Snoj, et al., Neutronic analysis of JET external neutron monitor response, accepted for publication Fus. Eng. Design (ISFNT12)

[1.117] G. Stankunas, et al., *Measurements of fusion neutron yields by neutron activation technique: Uncertainty due to the uncertainty on activation cross sections, Nuclear Instruments and Methods in Physics Research Section A: Accelerators, Spectrometers, Detectors and Associated Equipment*

[1.118] M. Pillon, et al., *Characterization of a Diamond Detector to be used as Neutron Yield Monitor during the in-vessel Calibration of JET Neutron Detectors in preparation of the DT Experiment, accepted for publication in Fus. Eng. Design (ISFNT12)*

[1.119] T. Vasilopoulou, et al., *Neutron streaming along ducts and labyrinths at the JET biological shielding: Effect of concrete composition, Radiation Physics and Chemistry, Volume 116, November 2015, Pages 359–364*

[1.120] I.E. Stamatelatos, T. Vasilopoulou, P. Batistoni, S. Conroy, B. Obryk, S. Popovichev, *Preanalysis of Neutron Activation Measurements in Shielding Penetrations at JET, presented at 24th Symposium of the Hellenic Nuclear Physics Society - HNPS 2015, University of Ioannina, Ioannina, Greece*

[1.121] P. Batistoni, S. Conroy, B. Obryk, S. Popovichev, I. Stamatelatos, B. Syme and T. Vasilopoulou, *Improved experiment on neutron streaming through JET Torus Hall ducts, Nuclear Fusion 55 (2015)*

[1.122] R. Villari, et al., *Neutronics Experiments and Analyses in Preparation of DT Operations at JET, accepted for publication in Fus. Eng. Design (ISFNT12)*

[1.123] Lengar, et al., A. Čufar *Characterization of JET neutron field for material activation and radiation damage studies, accepted for publication in Fus. Eng. Design (2015)*

[1.124] I. Lengar, et al., *Radiation Damage and nuclear heating studies in selected functional materials during JET DT campaign, accepted for publication in Fus. Eng. Design (ISFNT12)*

[1.125] F. Belli et al., *Conceptual Design, Development and Preliminary Tests of a Compact Neutron Spectrometer for the JET Experiment, IEEE Transactions on Nuclear Science, October 2012*

[1.126] ER15-ENEA-03, *Wiki Pages of NonLinear Energetic particle Dynamics (NLED) Project,* https://www2.euro-fusion.org/erwiki/index.php?title=ER15-ENEA-03

[1.127] Ph. Lauber et al., *NLED-AUG reference case,* http://www2.ipp.mpg.de/~pwl/NLED_AUG/data.html

[1.128] X. Wang et al. *Structure of wave-particle interactions in nonlinear beta induced Alfvén eigenmode dynamics. Invited talk at the 7th IAEA Technical Meeting on Plasma Instabilities, Frascati, Italy, March 4-6, 2015*

[1.129] F. Zonca et al., *Plasma Phys. Contr. Fusion* **57**, 014024 (2015)

[1.130] F. Zonca et al., *New. J. Phys.* **17**, 013052 (2015)

[1.131] L. Chen and F. Zonca, *Physics of Alfvén waves and energetic particles in burning plasmas, Rev. Mod. Phys.* **88**, 015008 (2016)

[1.132] X. Wang et al., *Structure of wave-particle resonances and Alfvén mode saturation. Submitted to Phys. Plasmas (2015)*

[1.133] S. Briguglio et al., *Nonlinear EPM dynamics: test case results, 15th Meeting of the ITPA Energetic Particle Topical Group, Sep. 7-9, 2015, Vienna*

[1.134] X. Wang et al., *Structure of wave-particle interactions in Nonlinear Alfvénic fluctuation dynamics, 14th IAEA Technical Meeting on Energetic Particles in Magnetic Confinement Systems, Vienna 1-4 Sep. 2015*

[1.135] G. Fogaccia et al., *Linear benchmark activity of HYMAGYC code, 7th IAEA Technical Meeting on Plasma Instabilities, Frascati, Italy, March 4-6, 2015*

[1.136] G. W. Bowden et al., *Calculation of continuum damping of Alfvén eigenmodes in tokamak and stellarator equilibria. Invited talk at the 20th International Stellarator-Heliotron Workshop, Greifswald, 2015*

[1.137] G. W. Bowden et al., *Calculation of continuum damping of Alfvén eigenmodes in tokamak and stellarator equilibria. Submitted to Phys. Plasmas (2015)*

[1.138] A. Biancalani et al., *Linear gyrokinetic particle-in-cell simulations of Alfvén instabilities in tokamaks. Submitted to Phys. Plasmas (2015)*

[1.139] A. Biancalani et al., *Non-perturbative nonlinear interplay of Alfvén modes and energetic ions, 14th IAEA Technical Meeting on Energetic Particles in Magnetic Confinement Systems, Vienna 1-4 Sep. 2015*

[1.140] R. Ma et al., *PoP* **22**, 092501 (2015)

[1.141] A. Könies et al., *The influence of FLR effects on tokamak saturation amplitude, 15th Meeting of the ITPA Energetic Particle Topical Group, Sep. 7-9, 2015, Vienna*

[1.142] M. D. J. Cole et al., *Plasma Phys. Contr. Fusion* **57**, 054013 (2015)

[1.143] A. Mishchenko et al., *Nucl. Fusion* **55**, 053006 (2015)

[1.144] R. Kleiber et al., *Gyrokinetic simulations for tokamaks and stellarators. Invited talk at the 7th IAEA Technical Meeting on Plasma Instabilities, Frascati, Italy, March 4-6, 2015*

[1.145] R. Kleiber et al., *Present status of the EUTERPE code. Oral talk at the IPP Theory Meeting, Plau am See, 2015*

[1.146] A. Mishchenko et al., *Gyrokinetic PIC simulations with GYGLES, EUTERPE and ORB5. Oral talk at the IPP Theory Meeting, Plau am See, 2015*

[1.147] M. D. J. Cole et al., Hybrid simulations of global modes in magnetic fusion devices. Oral talk at DPG Frühjahrstagung, Bochum, 2015

[1.148] C. Slaby, Energetic Particle Modes in Tokamaks and Stellarators. Master Thesis, Ernst-Moritz-Arndt-Universität Greifswald, 2015

[1.149] M. D. J. Cole et al., Progress in non-linear gyrokinetic simulations of global modes in tokamaks and stellarators. Invited talk at the 14th IAEA Technical Meeting on Energetic Particles in Magnetic Confinement Systems, Vienna 1-4 Sep. 2015

[1.150] M. D. J. Cole et al., Progress in non-linear gyrokinetic simulations of global modes in tokamaks and stellarators, 20th International Stellerator-Heliotron Workshop, Greifswald, 2015

[1.151] M. D. J. Cole et al., Progress in non-linear gyrokinetic simulations of global modes in tokamaks and stellarators, IPP Theory Meeting, Plau am See, 2015

[1.152] A. Könies et al., CKA-EUTERPE: A kinetic MHD model for nonlinear wave particle interaction, 20th International Stellerator-Heliotron Workshop, Greifswald, 2015

[1.153] A. Könies et al., Non-linear kinetic MHD with CKA-EUTERPE. Oral talk at the IPP Theory Meeting, Plau am See, 2015

[1.154] D. Zarzoso et al., PRL 110, 125002 (2013)

[1.155] R. J. Dumont et al. PPCF 55, 124012 (2013)

[1.156] J.-B. Girardo et al., PoP 21, 092507 (2014)

[1.157] D. Zarzoso et al., NF 54, 103006 (2014)

[1.158] D. Zarzoso, Verification of the 2-species version of GYSELA by means of energetic particle driven GAMs, NumKin Workshop 2015, Garching, Oct. 26-30, Germany

[1.159] M. Schneller et al., Plasma Phys. Contr. Fusion 58, 014019 (2015)

[1.160] M. Schneller et al., Nonlinear Energetic Particle Transport in the Presence of Multiple Alfvénic Waves in ITER. Invited talk at the 42nd European Physical Society Conf. on Plasma Physics (6/2015, Lisbon, Portugal)

[1.161] M. Schneller et al., Nonlinear Energetic Particle Transport in the Presence of Multiple Alfvénic Waves in ITER, 14th IAEA Technical Meeting on Energetic Particles in Magnetic Confinement Systems, Vienna 1-4 Sep. 2015

[1.162] M. Schneller et al., Nonlinear Energetic Particle Transport in the Presence of Multiple Alfvénic Waves in ASDEX Upgrade and ITER. Invited talk at the European Fusion Theory Conference 2015 (10/2015, Lisbon, Portugal)

[1.163] M. Schneller et al., NF 53, 123003 (2013)

[1.164] H. Berk et al., NF 35,1661 (1995)

[1.165] N. Carlevaro et al., J. Plasma Phys. 81, 495810515 (2015)

[1.166] N. Carlevaro et al., Mixed diffusive-convective relaxation of a broad beam of energetic particles in cold plasma. Submitted to Entropy (2015)

[1.167] M. Idouakass at al., Nonlinear simulations of the fishbone instability, 42nd European Physical Society Conf. on Plasma Physics (6/2015, Lisbon, Portugal)

[1.168] J. Cao, Z. Qiu and F. Zonca, Physics of Plasmas 22, 124505 (2015)

[1.169] Aging of Precursor Solutions Used For YBCO Films Chemical Solution Deposition: Study of Mechanisms and Effects on Film Properties, V. Pinto et al., accepted for publication on IEEE Trans. on Appl. Supercond.

[1.170] Analysis of Transport Properties of MOD YBCO Films with BaZrO3 as Artificial Vortex Pinning Centres. A. Frolova et al., accepted for publication on IEEE Trans. on Appl. Supercond.

[1.171] Measurement of Vortex Pinning in YBCO and YBCO/BZO coated conductors using a microwave technique, K. Torokhtii et al., accepted for publication on IEEE Trans. on Appl. Supercond.

[1.172] Epitaxial La0.7Sr0.3MnO3 nanostructures obtained by polymer assisted surface decoration (PASD) method, R.B. Mos, et al. Mater. Lett. (2015), submitted

[1.173] Gus'kov S Yu and Rozanov V B, Quantum Electron. 27, 696 (1997)

[1.174] Gus'kov S Yu, Caruso A, Rozanov V B and Strangio C, Quantum Electron. 30, 191 (2000)

[1.175] Caruso A, Strangio C, Gus'kov S Yu, and Rozanov VB, Laser Part. Beams 18, 25 (2000)

[1.176] De Angelis R, Consoli F, Gus'kov S Yu, Rupasov A A, Andreoli P, Cristofari G and Di Giorgio G, Phys. Plasmas 22, 072701 (2015)

[1.177] Gus'kov S Yu,et al., Plasma Phys. Control. Fusion 57, 125004 (2015)

[1.178] F. Consoli, et al., Proc. IEEE 15th Intern. Conf. Environ. Electr. Engin. (EEEIC), 2015, 10-13 June 2015, Rome, p. 182; ISBN: 978-1-4799-7992-9

[1.179] SPE-12-8-046/E/SS, Technical Report, Taoglas, 2009

[1.180] S. Barbarino and F. Consoli, IEEE Trans. Antennas Propag. 58 (2010) 4074.

[1.181] F. Consoli, et al., Physics Procedia 62 (2015) 11

[1.182] B. Boashash, Time Frequency Signal Analysis and Processing, Oxford: Elsevier, 2003

2. Extra Fusion Activities in FUSPHY

2.1 NIXT and X-Seta

In the framework of the NIXT Laboratory activity and on the base of the work carried out by the laboratory team in the course of past years, a new method to distinguish and separate different kind of black plastic wastes, for quality control and for recycling process, has been developed.

This technology, based on an innovative scheme using soft X-rays, is simple, compact, portable and suitable for a continuous flow processing and a patent has been granted during this year.

Near-infrared spectroscopy analysis cannot be used because black plastics are not reflecting and standard X-ray techniques are not effective because they are not sensitive to low-Z materials. Then there is a gap in recognition of dark plastic and this method may fill this need in the recognition of plastic.

The proposed technique includes also the X-ray fluorescence analysis.

The developed method allows also the recognition of the non-recyclable brominated plastics.

The innovative technique combines X-ray fluorescence spectra, generated by the sample, with its selective absorption of an optimized set of X-ray lines. There are two most important processes to be considered. SXR radiation is absorbed into the material through the photoelectric effect by the core electrons of the elements of the material and the Compton scattering at small angle: Compton scattering effect carries information about the polymeric structure.

The experimental apparatus requires only an X-ray tube of low power working in the energy range 2-25 kV and a commercial X-ray Silicon Drift Detector spectrometer.

The analysis of the acquired spectra, affected by the plastic sample, allows the recognition of the most common types of plastics. This specific analysis of the X-ray spectra allows removing a few degenerations, increasing the range of response and then the sensitivity of the method. It works for plastic materials with thickness between 1 and 6 mm.
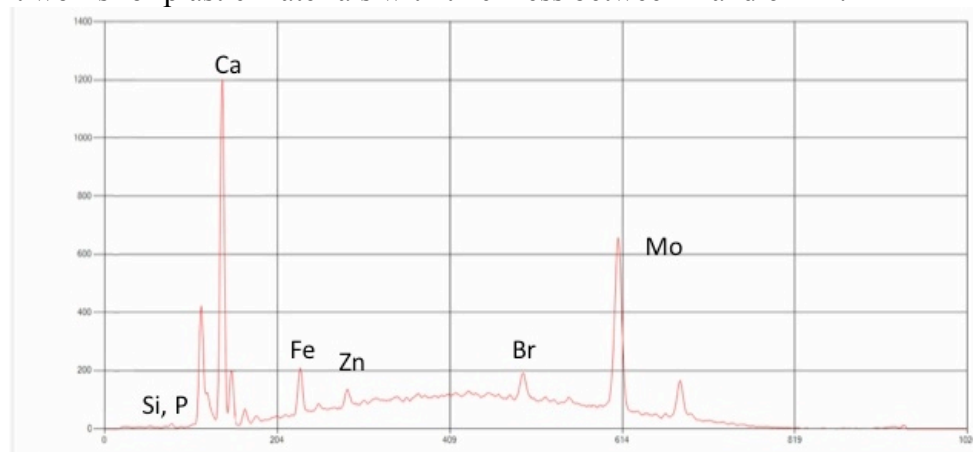

Figure 2.1 - Example of spectra of plastic sample: the fluorescence spectrum allows identifying the components of doping

This new technique permits also to reveal the presence of mineral charges or fillers (calcium carbonate, clay, fiber glass etc..), in general added to plastics to confer mechanical properties, flame retardants (as Bromine, Antimony or phosphates), pigments (as titanium or Iron oxides) or other additives (like Zinc as fluidizing) (*Figure 2.1*).

Nowadays a prototype has been realized and tested in collaboration with the BMCR S.r.l. (Civitella di Romagna, FC, Italy).

During this collaboration an extensive characterization of the method and subsequent realization of a prototype has been carried out. The characterization of the materials was made to include a range of products specified by the company BMCR, after a market study. This characterization has allowed the creation of a data file constituting the kit required for use of the instrument.

2.2   Short-wavelenght Sources and Applications

2.2.1   Discharge Produced Plasma source of EUV radiation

Extreme Ultraviolet (EUV) radiation can be used to modify both the chemical structure of many photoresists and some optical properties of various photonic materials. EUV sources are also exploited for testing EUV components: detectors, optics, masks etc.

The ENEA Discharge Produced Plasma (DPP) EUV source wasdeveloped in the framework of the collaboration between ENEA and the Physics Department of L'Aquila University (2003–2008) [2.1]. In April 2010 it has been transferred to the ENEA Frascati Research Centre, where it is operating since the end of the same year. In *Figure 2* a picture of the DPP is shown.
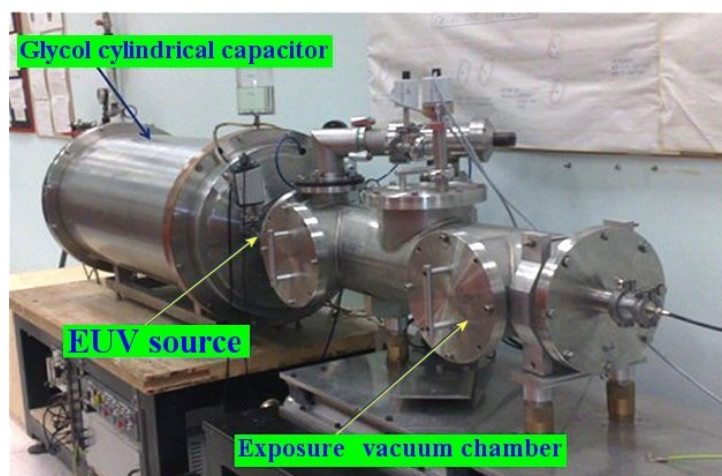
Figure 2.2 - The EUV DPP source operating at ENEA

Numerous and important modifications have been carried out on the apparatus, which greatly improved its performances [2. 2], making the apparatus suitable for applications in surface treatments, photonic materials processing, nanostructuring etc. Briefly, the DPP working principle can be described as follows: low pressure (0.5−1.0 mbar) Xe gas, filling an alumina tube, is pre–ionized (20−30 A, 10−20 μs); then, a low–inductance 50 nF glycol cylindrical capacitor, charged up to 20−25 kV, produces a discharge (11−12 kA peak current, 240 ns base duration) in the pre–ionized Xe gas; the resulting magnetic field (>1 T near the alumina tube inner wall) pinches the plasma towards the tube axis; the plasma resistance rises, thus the plasma temperature can increase up to 30−40 eV (3.5-4.5·10^5 K); the hot plasma emits radiation before relaxing and cooling.

Presently, the DPP emits more than 30 mJ/sr/shot in the λ=10−20 nm wavelength spectral range at 10 Hz repetition rate. The EUV pulses typical duration is about 100 ns FWHM, while the optical EUV source transverse size is less than 300 μm.

The implemented DPP diagnostics and the source reliable performances allow the controlled applications concerning direct EUV exposures of both photonic materials and innovative photoresists with a minor damage from plasma debris bombardment [2.3,2.4]. For example, the DPP has been utilized for the realization of the ENEA patented anti–counterfeiting tags. Another important application is the EUV direct exposure of innovative materials in the framework of a project funded by the CARIPLO Foundation (April 1st 2013, March 31st 2016), which involves ENEA and the Universities of Pavia and Padova. According to the

project plan, a large number of organic and inorganic photoresists, synthesized by the academic partners, have been exposed to EUV doses in the range 15−500 mJ/cm². These new materials, characterized by particular optical and mechanical properties, could be used as non-sacrificial layers in lithographic fabrications, and have been also added with various chemical innovative photoinitiators in order to improve their EUV sensitivity [2.5].
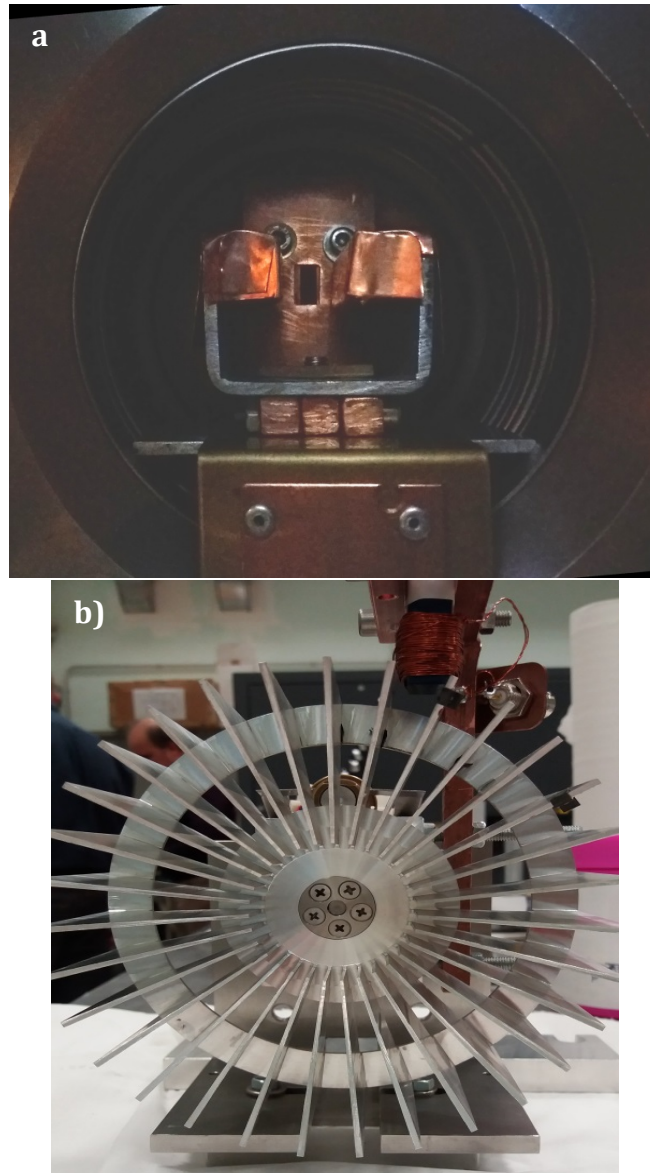

Figure 2.3 - The dipole magnet placed in front of the source, the rectangular slit is visible between the magnet poles; b) front view of the rotating structure, the pickup magnet is visible on the top

To test the sensitivity of all the cited materials, a huge number of DPP shots have been performed (about one million). During 2015, the DPP EUV energy per pulse emission has been increased by means of various modifications on the apparatus: the plasma column longitudinal length has been extended from ≃8 mm to ≃12 mm; the electric insulation of the alumina tube cooling system has been improved, making possible to charge the glycol cylindrical capacitor, that feeds the main discharge, up to 25 kV; to favour the onset of the discharge in the spark−gap that switches on the main discharge and to decrease its initial impedance, a small capacitor (Murata, 40kV,570pF) has been connected in parallel to the spark−gap. After the above mentioned modifications, the DPP EUV energy per pulse has increased by more than 30%, reaching the already declared 30−35 mJ/sr.

The forthcoming step within the aforementioned project is the patterns generation on the most sensitive photoresists at high spatial resolution. To this end, a contact EUV lithography technique has been developed to reach an effective sub–micrometric resolution patterning. In this technique, special EUV transmitting masks, made for us by CNR–IFN by depositing Au patterns on a 100 nm thick Si_3N_4 membranes, are placed by a particular holder at few μm from the samples to be patterned. The mask membrane, which transmits less than 30% of the incident EUV radiation, is so fragile and delicate that it must be protected from plasma debris bombardment. Thus, a debris mitigation system (DMS) has been set up, based on a twenty-years experience on a laser produced plasma source (EGERIA) installed in our Lab [2.6]. First of all, the DPP ground electrode has been re-made by using elkonite (Cu/W) to decrease the debris emission and the HV electrode has been constructed by tantalum since tungsten was not available. Further material tests are planned, including the insulating tube presently made by alumina.

The DMS installed on the DPP is composed by two main elements: a permanent magnet dipole placed at about 3 cm from the source to deflect ions; a 13cm in diameter rotating structure (RS) having 31 radial vanes, properly placed between the source and the sample to be patterned, to stop particulate debris. The radiation and the debris emitted by the plasma are properly bottom limited at the optical axis level and horizontally selected by a rectangular aperture (12 mm high and 5 mm wide). Both DMS elements are shown in *Figure 2.3*. The magnet, having an average field $\simeq 0.2$ T along a longitudinal ion path of 5 cm, can vertically deflect Xe ions with energies up to $10-20$ keV in such a way to avoid their impact on the small exposed samples ($< 1 \times 1$ mm^2). The RS, placed in front of the source at 11 cm from it, with its axis parallel to the optical one, is positioned in such a way that EUV radiation can reach the sample passing between two adjacent vanes thanks to a proper synchronisation between the RS phase and the DPP triggering.
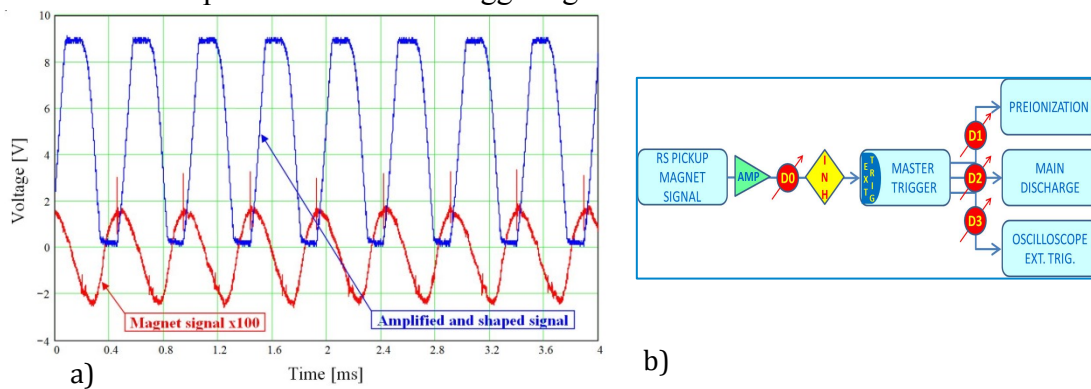

Figure 2.4 - a) RS pickup signal (red) and the corresponding trigger pulses (blue); b) DPP triggering block scheme, D0-D3 represent tunable delay units

The sample is placed at about 17 cm from the source and 1cm above the optical axis. The RS, already mentioned in an ENEA patent on DMSs, has a longitudinal length of 5 cm and rotates up to 100 Hz. Its geometry and angular velocity determine the velocity spectrum of the stopped debris. In order to get a signal from the RS capable to trigger the DPP, a specific magnetic pickup has been constructed and placed close to the external vane edge. The RS is made of a diamagnetic aluminium alloy, but the magnetic core of the pickup induces currents in the passing vanes and the resulting modulated magnetic field induces a voltage in the 144 turns coil of the pickup. This signal, properly amplified and shaped, has been utilized to trigger the DPP at the working repetition rate ($5-10$ Hz), selecting pulses by an inhibit unit. In *Figure 2.4* the pickup signal and its elaboration are reported (a), together with a block scheme of the DPP triggering (b). Before the DMS implementation, a patterning mask got completely broken just after few hundreds DPP shots, while more than 5000 shots are needed to perform

the planned patterning exposures. After the DMS started working, no more problem with broken masks have been experimented. Anyway, further DMS tests and upgrades are scheduled.
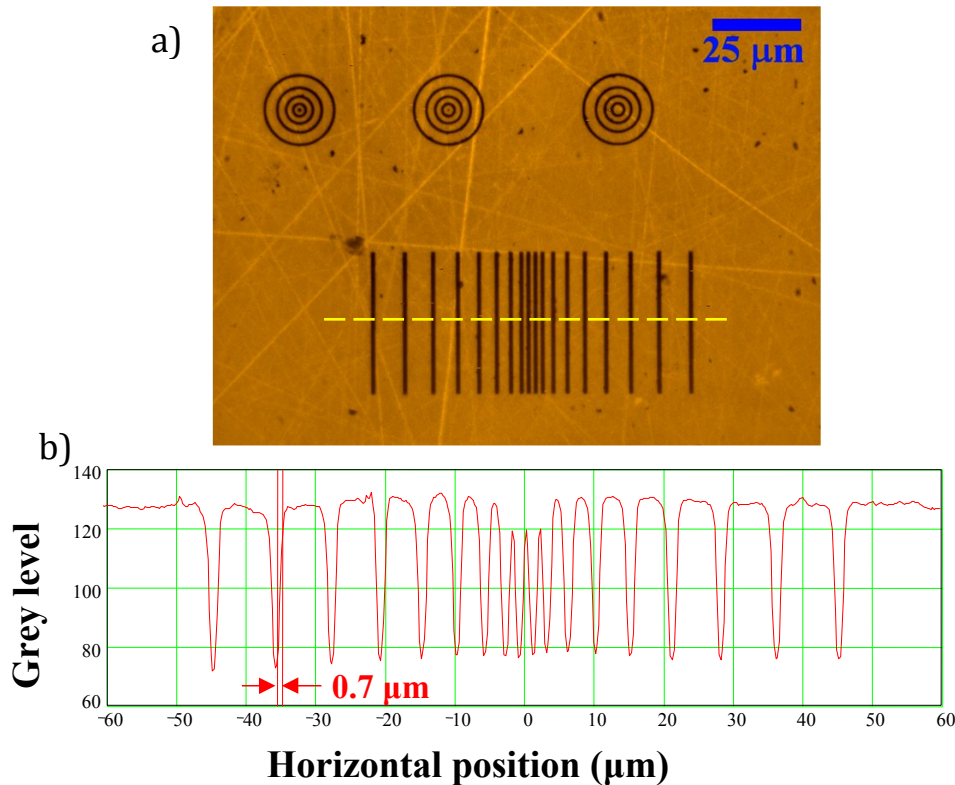

Figure 2.5 - a) Luminescent patterns on a LiF crystal observed by an optical microscope in fluorescence mode with a 100× objective; b) intensity profile along the yellow dashed line in a), the indicated spatial resolution is comparable with the microscope one

As a reliability proof for both the DMS and the patterning setup, the DPP EUV source has been successfully utilized for test patterns generation on a photonic material (lithium fluoride crystal), as reported in *Figure 2.5*, and on a commercial PMMA photoresist. In order to properly treat these samples, EUV doses up to $100\,mJ/cm^2$ have been delivered, obtaining the expected results: sub–micrometric resolution has been demonstrated and the DPP reliable performances are confirmed.

In the first months of 2016 contact EUV lithography exposures will be performed on the selected photoresists developed during the activities of the previously mentioned project founded by Cariplo Foundation.

2.2.2   Optical systems for solar technologies

During the last years, our group has been involved in the field of solar technologies, in particular in connection with Sun tracking and alignment of Concentrated Solar Power plants. We developed both a simple but robust solar position algorithm and a compact, low-cost, high-accuracy solar compass patented in 2012 [2.7, 2.8, 2.9, 2.10, 2.11] and shown in *Figure 2.6*.

In 2015, the activity in this field has been dedicated to the development of three solar compass prototypes within the scientific cooperation with D.D. Costruzioni Meccaniche s.r.l. The electronics of the compass has been developed inside ENEA and the technical drawing of the compass box, designed by ENEA and shown in *Figure 2.7*, has been delivered to D.D. by November 13th 2015. D.D. firm will construct the box within spring 2016.

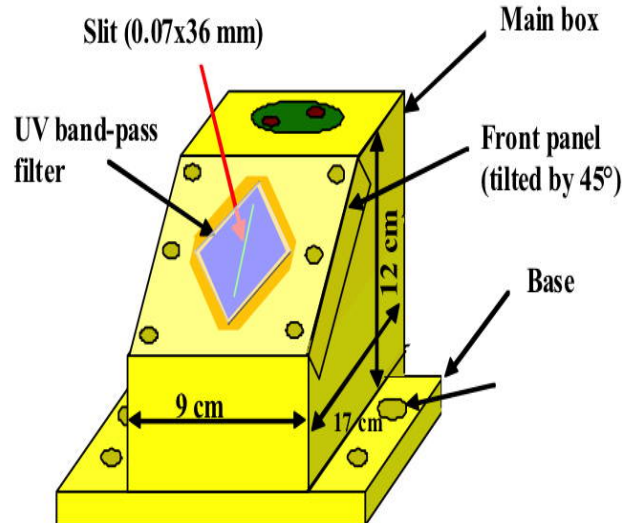*Figure 2.6 - The ENEA solar compass mounted on a theodolite*

Figure 2.7 - Layout of the compass box

With respect to the previous prototypes, this version of the compass is stand-alone (sun sensor and electronics are in a single box). It will be equipped with a three-axes digital inclinometer and will work both as compass and as sun tracker for guiding the mirrors of thermodynamic solar plants. The compass will be installed in the ENEA Casaccia parabolic trough by spring 2016 together with the new motion system made by D.D. s.r.l. (presently under assembling).
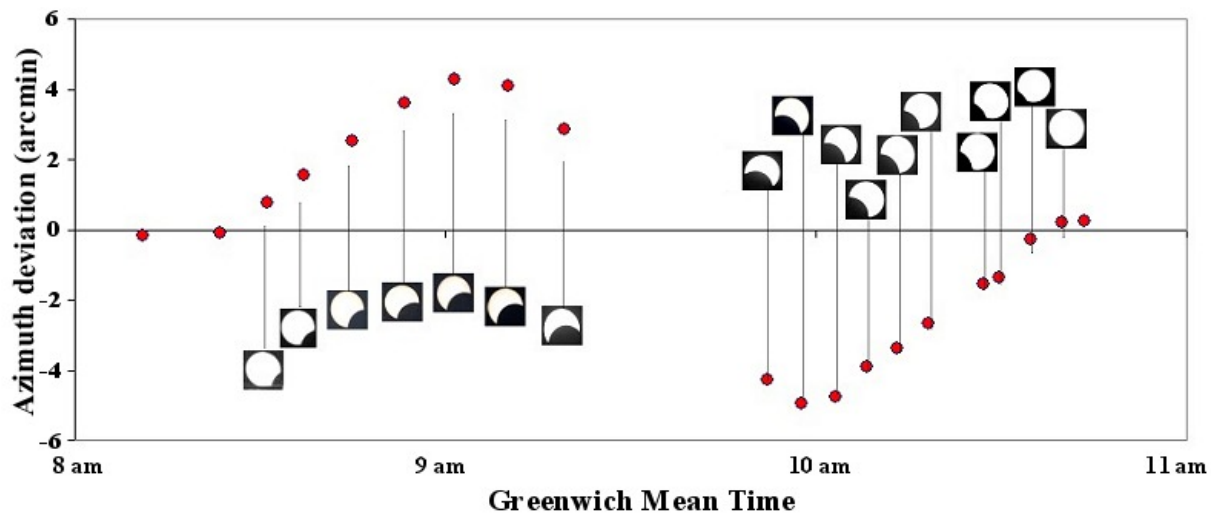
Figure 2.8 - Temporal evolution of the azimuth variation during various phases of the March 2015 eclipse. Red circles: experimental deviation of the azimuth. Black and white images: photos of the Sun taken during the eclipse

In 2015 we also tested the performance of the ENEA solar compass during the Sun eclipse occurred on March 20th [2.12]. In such occasion, we could carefully control the obscuration of the Sun due to the passage of the Moon and hence we could check the influence of the Sun partial coverage on the compass measurement accuracy. During the eclipse, with the compass pointing always towards the same direction, we measured the deviation of the azimuth from the right value (obtained with a full Sun). *Figure 2.8* shows the time evolution of the azimuth variation during various phases of the eclipse. The absolute error was less than 6 arc minutes, i.e. less than 0,1 degrees, in spite of a Sun obscuration up to 46%. This measurement demonstrated that the accuracy of the ENEA solar compass holds better than other magnetic or electronic compasses even when the Sun is partially covered, for example by a cloud.

The activity regarding the sun compass has been also dedicated to preliminary studies for a prototype suitable for boats or other transportation means and for a prototype suitable for solar power plants based on dish mirrors like that recently under study at the ENEA Casaccia in the frame of the OMSOP European project.

Figure 2.9 - Photograph taken during the measurement of the orientation of the MAD solar parabolic trough, done with the ENEA solar compass

These prototypes will be equipped with an integrated IMU (Inertial Measurement Unit) that will allow operations even when the compass is subject to oscillations (like, e.g., in a boat). Two new high precision IMUs have been acquired and will be tested in 2016.

In September 2015 the company MAD s.r.l. of Roccasecca (Frosinone) asked our group to verify the orientation of the parabolic trough by using the ENEA solar compass, since the power delivered by the system was significantly lower than expected. The measurement revealed an error of almost 0.5° on the nominal South-North orientation. The MAD plant, during the azimuth measurements, is shown in *Figure 2.9*.

2.3 Terahertz and mm-wave sources and applications

ENEA has a long term expertise in the construction of powerful short-pulse mm-wave and Terahertz free electron sources. Various electron-wave interaction schemes were successfully tested in the past, ranging from Cerenkov to Smith-Purcell radiators and to undulator devices. A variety of applications of millimetre waves and THz radiation have been covered through the years and have been carried continued through 2015.

2.3.1 Cultural Heritage applications: the THz-ARTE project

In the frame of the collaboration with the National Institute for Information and Communications Technology (NICT-Tokyo) and CNR-IFAC (Florence), a three-year bilateral Italy-Japan joint research project on cultural heritage conservation was selected and funded by the Ministry of Foreign Affairs in July 2013.

Figure 2.10 - 3D THz imaging scanner used on a real artwork

The project THz-ARTE ("Terahertz Advanced Research TEchniques for non-invasive analysis in art conservation") is devoted to the application of THz spectroscopy and reflective THz imaging as new non-invasive analytical methodologies applied to the investigation of artworks and other objects relevant in art conservation. One of the main objectives of the project is the construction of a 3D mm-wave/THz scanner to perform phase sensitive imaging measurements [2.13, 2.14] on paintings, to obtain simultaneously topologic and spectroscopic information and to detect sub-superficial damages.

Due to the capability of the THz radiation of penetrating dielectric materials, a typical application is related to the search for hidden paintings [2.13, 2.14] or drawings covered by a superimposed layer and to the detection of damages (detachments) under the frescoes surface. After the successful test of the first 3D scanning system in 2014 [2.15, 2.16], a new device, specifically designed to perform measurements on mural paintings, has been realized (*Figure 2.10*). The high speed motors used for the device allow the scanning of the whole 500x300 mm^2 surface with 1 mm resolution in about 40 minutes.

The radiation source is a 97 GHz IMPATT diode, able to provide up to 70 mW output power. Radiation is delivered toward the sample with a WR10 standard waveguide. A directional coupler is used to collect the reflected radiation injected back into the waveguide. A Shottky diode with 200 V/W responsivity is then used to detect the reflected signal.

Changing the distance from the sample, by means of one of the remotely controlled motors, allows measuring the amplitude and the phase of the reflected signal. A laser triangulation system is mounted on the same head, to measure the real distance of the probe head from the sample, in order to evaluate the phase component associated with the topology of the sample surface. With such a correction it is possible to measure the phase variation associated with the reflection from the sample that can provide information about the optical properties of the materials.

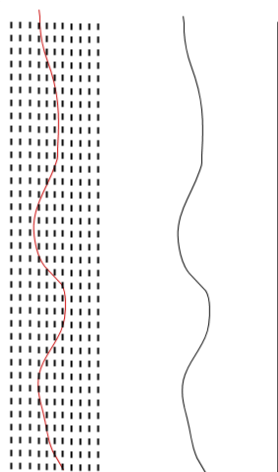*Figure 2.11 - 3D THz imaging scanner used on a real artwork*

Figure 2.12 - Scheme for the measurement: the red curve is obtained interpolating the experimental data with the theoretical model based on a simple diffraction model

A second source (YIG) is available to be mounted on the scanning device, with the ability of tuning the frequency from 18 to 40 GHz. Such an electronic tuning can be used to avoid the mechanical scans to get the information phase from the measurement.

After laboratory tests the device was used for a measurement on a real artwork: a mural painting on "tavella", depicting St. John Baptist, by Alessandro Gherardini, a fine art Florentine painter of the beginning of 1700 (*Figure 2.11*). The Museum of San Marco, in Florence, kindly provided the painting; the measurements took place at the Uffizi Museum Laboratories, in Florence (Ufficio e Laboratorio Restauri della ex Soprintendenza Speciale per il Patrimonio Storico, Artistico ed Etnoantropologico e per il Polo Museale della città di Firenze).

Due to the value of the artwork and the measurement technique, that requires the probe head to move very close to the sample, a specific measurement procedure has been established, in order to avoid any contact between the probe and the painting. To fulfil this requirement a new method of measurement and data analysis was developed, avoiding to "follow" the surface shape moving the probe head in real time during the measurement. Data on different planes, separated by a distance of 100 mm, were acquired and combined to build a "data cube".

The shape of the surface was recorded by means of the laser triangulation system. Combining the data from this data cube with the surface shape and interpolating using a simple diffraction-based model, that describes outcome from the reflection measurements, it is possible obtaining a certain number of "virtual surfaces", with a shape that reproduces the shape of the sample, thus eliminating the phase error coming from a non-planar artwork

surface (*Figure 2.12*). Such a system allows obtaining these virtual surfaces also for distances where there are no experimental point, very close to the sample surface.
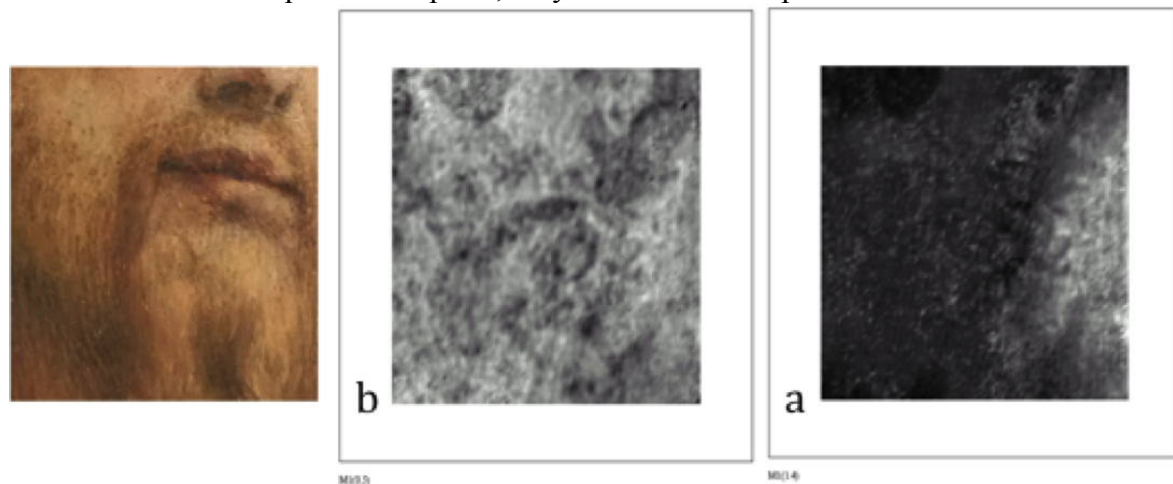

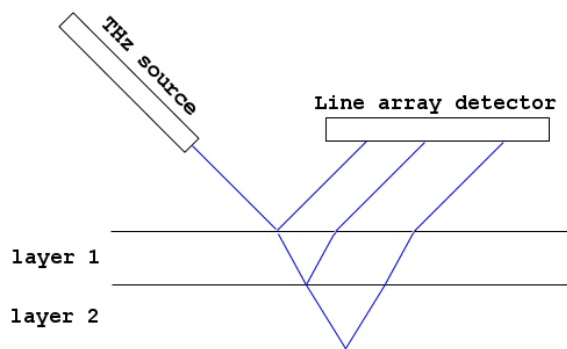*Figure 2.13 - Visible image and THz image for d=0.5 mm (a) and d=1.4 mm (b)*

Figure 2.14 - Layout of a measurement geometry to measure the position of defects inside a sample

Data analysis (*Figure 2.13*) revealed that there are structures hidden under the sample surface. Having a look at the amplitude of the signal oscillation while changing the distance from the sample it is possible to have a qualitative indication about how deep these structures are inside the sample, but the exact value of the depth cannot be derived, since it is not possible to perform a phase correction similar to the one performed on the surface shape, using the laser triangulation system.

In order to measure the exact depth of the refraction index discontinuity inside the sample it is necessary to use a THz-TDS system, or to change the measurement geometry.

Impinging on the sample with angles smaller than 90° and collecting the reflected radiation by means of a line array of THz detector, allows to convert the position of the defect inside the sample into a position on the array, as depicted in *Figure 2.14*. A quick calculation confirms that, choosing a setup that limits the beam waist to $w_0=3*l$, it is possible to determine the depth position of the discontinuity with a resolution of about 5 mm, comparable with the wavelength of the radiation utilized for the measurements.

2.3.2 The GREAM project

The biological effects of THz radiation are currently arising a growing interest because of their relevance in the medical, security, telecommunications and military areas. After the pioneering proactive studies conducted in the frame of the THz-BRIDGE project in the years 2001- 2009 [2.17], several research groups have addressed various biological endpoints in a wide range of frequencies worldwide to investigate the mechanism of interaction and the presence of specific frequencies, which may induce a response on biological systems.

In the frame of collaboration between the Radiation Source Laboratory and the Army Medical and Veterinary Research Centre - Rome, the Department of Science University of "Roma Tre", and the Department of Clinical Sciences and Translational Medicine - University of

Rome "Tor Vergata", the GREAM project was funded in the years 2013-15 by the Ministry of Defense to evaluate potential genotoxic effects associated with the exposure of living cells "in vitro" to high-frequency electromagnetic radiation, such as microwave and THz radiation.
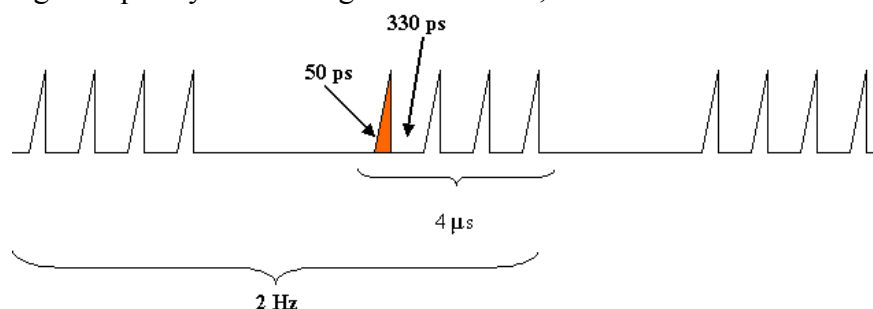

Figure 2.15 - Time structure of the FEL pulses

The GREAM project employs the analysis of cytogenetic and molecular markers, indicators oxidative stress, apoptosis and cell death assays, on two distinct human cellular models (peripheral blood lymphocytes and human fibroblasts). Fibroblasts are particularly important in this study since they are the most common cells of connective tissue in animals. Fibroblasts synthesize the extracellular matrix and collagen and play a critical role in wound healing.

In vitro exposures of human foetal fibroblasts HFFF2 have been performed in a wide band between 100 and 150 GHz using the ENEA Compact Free Electron Laser [2.18]. Due to the specific characteristics of the electron accelerator driving the FEL, the radiation pulse is composed by a "train" of micropulses, each 50 ps long, with 330 ps spacing between adjacent micropulses, as sketched in *Figure 2.15*. The overall duration of the train (macropulse) is 4 μs. Macropulses can be produced at a repetition rate that can be typically varied between 1 and 10 Hz. The peculiar temporal structure of the emitted radiation allows the investigation of the effects of high peak power, while maintaining a low average power, typically few mW, incident on the sample, thus avoiding heating effects. The FEL spectrum consists of several emission lines, spaced at 3 GHz intervals corresponding to the period of the radio-frequency driving the accelerator [2.19].
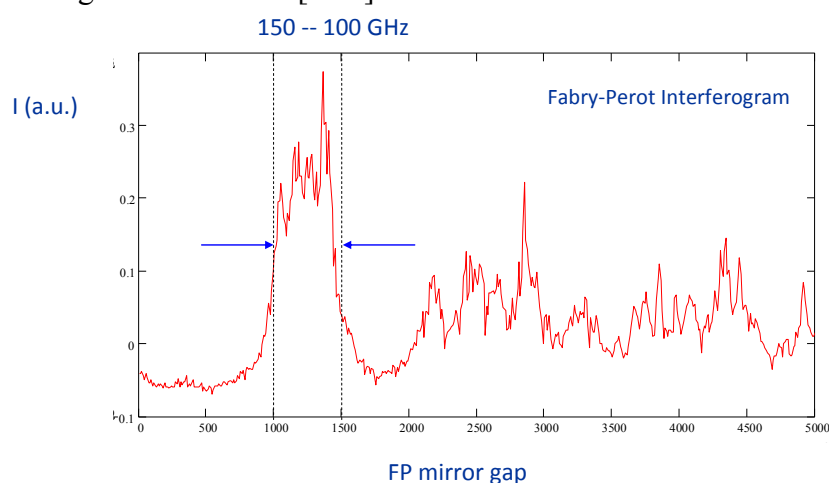

Figure 2.16 - Fabry-Peròt Interferogram of the Compact-FEL wide bandwidth radiation (100 - 150 GHz)

For the irradiation of fibroblasts the Compact-FEL has been operated in the so called "wide-bandwidth" mode, with the emission showing a typical relative bandwidth of around 20% (*Figure 2.16*). A radiation launching device was designed and built for such frequencies in order to provide the necessary expansion to irradiate from below the 5 cm diameter polystyrene Petri dish, containing a monolayer of fibroblasts cells (see *Figure 2.17*).

Sham-exposed samples were placed on the same working plate with the THz exposed samples. During the irradiation experiments the temperature of the sample was monitored by means of an infrared camera FLIR A325.

Various biological endpoints have been addressed: analysis of cytogenetic markers (Micronucleus assay, Comet assay, Chromosome Non-disjunction, telomere length), cell cycle kinetics, protein expression and ultra-structural observations of cells.

In most of the assays no differences were observed between the exposed samples and the control ones, but a significant increase of micronuclei (MN) was observed in irradiated samples, and the MN induction indicated that THz radiation could induce chromosome loss [2.20]. Ultra-structural analysis also showed radiation-induced effects, but such an evidence disappears in samples observed 48h after irradiation, demonstrating that morphological changes revealed immediately after exposure were transitory.
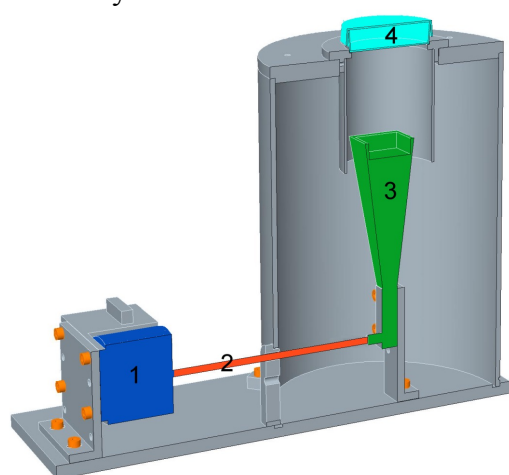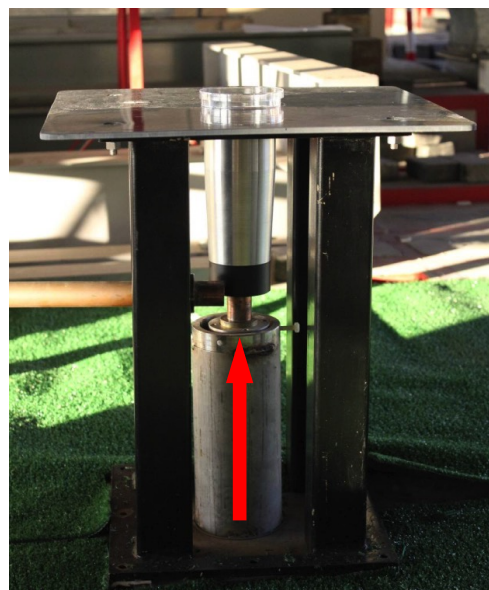

Figure 2.17 - Photo of the exposure set-up installed on the roof of the Compact-FEL, showing the light pipe output, the THz Delivery System (TDS) and the Petri dish containing the biological sample

Figure 2.18 - Layout of the 18-40 GHz exposure set-up. 1) source; 2) transmission line; 3) horn antenna; 4) Petri dish

In order to irradiate samples in the frequency band 18-40 GHz, which is of potential interest in telecommunications, a new CW exposure layout has been set up. In this case a CW source was used: a YIG oscillator, delivering 20 mW output power in the frequency range between 18 and 40 GHz. The layout of the setup is sketched in *Figure 2.18*.

The mm-wave radiation is launched using a horn antenna and the size of the beam naturally expands by diffraction up to the 5.2 cm diameter of the Petri dish.
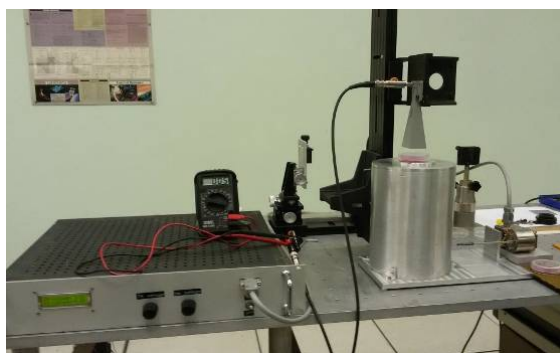
The central emission frequency for irradiation was chosen to be 25.28 GHz.

A picture of the experimental setup is visible in *Figure 2.19*. A collecting horn and a detector are placed over the sample to verify the radiation transmission through the sample itself.

The system was set up in order to obtain a radiation beam profile as uniform as possible

Figure 2.19 - Layout of the 18-40 GHz exposure set-up. 1) source; 2) transmission line; 3) horn antenna; 4) Petri dish

on the sample. The intensity profile of the THz beam at the sample position has been measured by means of a point detector placed on an automated 2D scanning system.

As in the case of the 100 GHz irradiation, Various biological endpoints are being addressed: analysis of cytogenetic markers (Micronucleus assay, Comet assay, Chromosome Non-disjunction, γ-H2AX quantification and Telomere length analysis). Here are reported the preliminary results about Micronucleus assay and γ-H2AX quantification.

A conventional MN test was performed using the Cytokinesis Block Micronucleus (CBMN) technique that permits the analysis of MN in binucleated (BN) cells [2.21]. In *Table 2.1* the results of the induction of MN in HFFF2 cells after exposure to MW radiation from two independent scorers are reported. A significant increase of MN in irradiated cells compared to control cells was observed for both scorer ($\chi^2 < 0.01$) with a mean of 11 MN in 1000 BN in control samples and 21 MN in 1000 BN cells in the irradiated samples.

Table 2.1 - Micronuclei induction after MW treatment of HFFF2 cells

HFFF2	Scorer	Control (MN in 1000 BN)	Treated (MN in 1000 BN)	χ^2
I Exp	1	11	19	*p<0.01*
	2	11	23	*p<0.01*
Mean		11	21	*p<0.01*

To better understand if MW exposure is able to induce direct DNA damage onto HFFF2 cells we have performed the immunofluorescence analysis of phosphorylated histone H2AX foci 30 min, 2 h and 24 h after treatment. No differences were observed between irradiated and control cells at each time after exposure (p>0.05).

2.4 Optics and Quantum Mechanics: symmetry transformations, phase-space representation, optical beams and relativistic wave functions

Cross applications between both classical and quantum mechanics and classical optics are common. Wave optics and Wigner optics, for instance, are areas of classical optics, where concepts and methods from quantum mechanics, like symmetry transformations and phase-space representation, have found a proper interpretation and wide applications.

Central to wave optics is the paraxial wave equation (PWE) [2.22], whereas central to Wigner optics is the Wigner distribution function (WDF) [2.23]. Both are central to my research activity [2.24, 2.25].

The PWE

$$ik_0 \partial_z \psi(x,y,z) = -\frac{1}{2n}[\partial_x^2 + \partial_y^2]\psi(x,y,z), \tag{1}$$

describes the propagation of the slowly-varying complex amplitude $\psi(x,y,z)$ of a monochromatic scalar light field $E(x,y,z) = e^{in(k_0 z - \omega_0 t)}\psi(x,y,z)$ in a homogeneous medium of refractive index n in the close proximity of the z-axis, the main direction of field propagation. Here, $k_0 = \frac{2\pi}{\lambda_0}$ denotes the field wave number in vacuum, corresponding to the frequency $\omega_0 = k_0 c$.

Interest in the PWE typically manifests in the search for new solutions, i.e. optical beams, whose physical relevance is then determined by their features and implementability. Such an issue can benefit from the formal analogy between Eq. (1) and other equations, as for instance the heat equation and the Schrödinger equation, with symmetry transformations and specific solutions, like Appell transformation and Airy wave packet, being transferred from them to the PWE [2.24].

In fact, the note that the (1+1)D free-particle Schrödinger equation admits among its closed-form solutions a wave function evolving from an Airy function [2.26], has found outstanding applications in optics through the (finite-energy) Airy beams [2.27]. These are at the top of

the international research activity since their remarkable properties, i.e. the non-spreading nature and the ability to freely self-bending during propagation and self-healing, make them suitable for several applications such as optical micromanipulation, plasma guidance and light bullet generation [2.28]. The production of Airy beams [2.27] has stimulated an intense and very prolific activity of investigations of specific features of the behavior of such beams as well as more in general of Airy-function related beam. In this connection, a new type of Airy-function
related beams has been proposed in [2.29]. It results from the paraxial free-propagation of the product of four Airy patterns, composed as to display a quadrangle-like shape:

$$\mathcal{A}(x,y) = \frac{c}{w} \text{Ai}\left(\frac{x+y}{\sqrt{2}w} + c_1\right) \text{Ai}\left(-\frac{x+y}{\sqrt{2}w} + c_2\right) \text{Ai}\left(\frac{y-x}{\sqrt{2}w} + c_3\right) \text{Ai}\left(\frac{x-y}{\sqrt{2}w} + c_4\right), \qquad (2)$$

where Ai denotes the Airy function, w a suitable transverse length scale and c_j, $j = 1, \dots, 4$ real arbitrary constants.
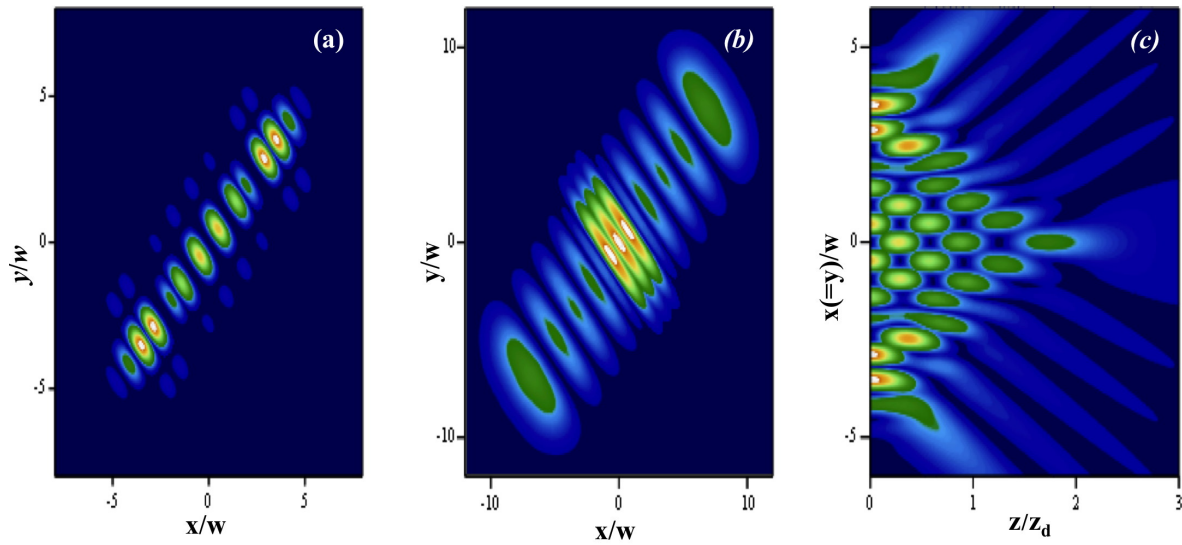

Figure 2.20 - Contour plots of the squared amplitude of the A-generated wave function with $c_1 = c_2 = a_3$ and $c_3 = c_4 = a'_1$ in (a), (b) the plane $\left(\frac{x}{w}, \frac{y}{w}\right)$ at $\frac{z}{z_d} = 0$ and $\frac{z}{z_d} = 1.5$, respectively, and (c) in the plane $\left(\frac{x}{w} = \frac{y}{w}, \frac{z}{z_d}\right)$. The longitudinal coordinate z is scaled by the diffraction length $z_d = kw^2$; also, $a_3 = -5.521$ and $a'_1 = -1.019$ denote the third and first zero respectively of Ai and its derivative Ai'

The structure of the propagated pattern depends on the values of the c_j's. Its peculiarity suggests applications of the proposed beams for optical manipulation and guiding (*Figure 2.20*). Wigner optics bridges between ray and wave optics. It offers the optical phase-space as the proper ambience and the WDF as the tool to accommodate for the two opposite light representations: the localized ray of geometric optics and the non-localized wave function of wave optics.

In fact, the WDF is a basic tool for the hybrid, i.e., space/spatial frequency, representation of optical signals. The "quantum-like" pairs of Fourier conjugate space/spatial-frequency variables span the 4D *wave-optical phase space*, where light signals with the relevant propagation "dynamics" are described by suitable phase-space distribution functions, among which the WDF is definitely the most important one. It represents the wave-optical tool closest to the geometric-optical concept of light ray, due to its localization properties and dynamical behavior [2.25].

In particular, the formalism of the WDF has been elegantly applied to the Lorentz-Gauss vortex beams in [2.30], following the interest of the scientific community in Lorentz beams [2.31] and optical vortices [2.32]. The latter, carrying on orbital angular momentum, find

wide applications in optical micro-manipulation, quantum information processing and phase contrast light microscopy [2.32].
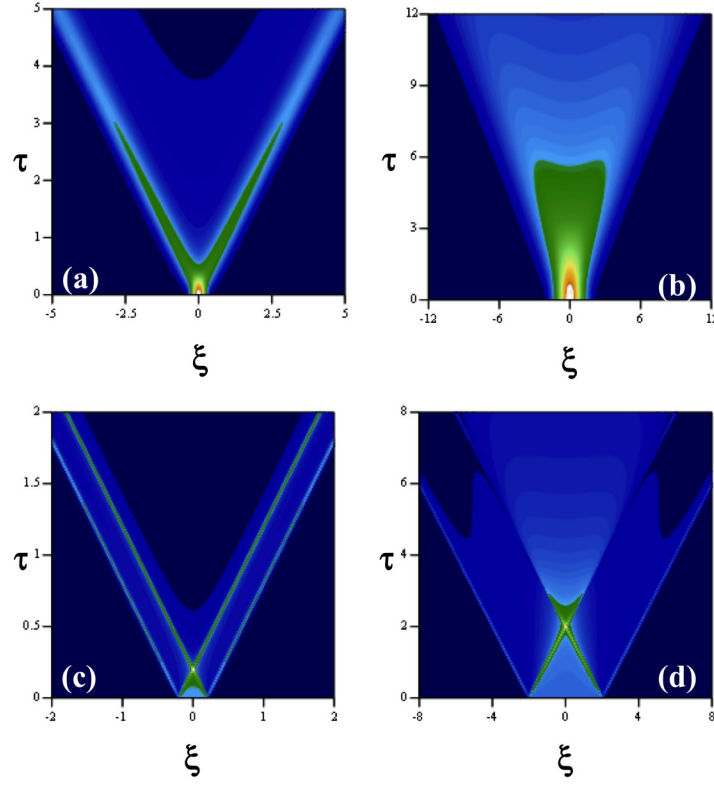

Figure 2.21 - (ξ, τ)-*contour plots of the squared amplitude of the relativistic wave functions, obtained as solutions of Eq. (4) for (a), (b) the Gaussian input* $\frac{1}{\sqrt{2\pi}w}e^{-\frac{\xi^2}{2w^2}}$ *with* $w = 0.002$ *and* $w = 1$, *respectively; and (c), (d) the square input* $\frac{1}{2w}[H(\xi + w) - H(\xi - w)]$, *H denoting the Heaviside step function, with* $w = 0.002$ *and* $w = 2$, *respectively.* ξ *and* τ *represent the convenient dimensionless variables* $\xi = \frac{x}{\lambda_c}$ *and* $\tau = \frac{ct}{\lambda_c}$, *where* $\lambda_c = \frac{\hbar}{mc}$ *is the reduced Compton wavelength. The displayed behavior definitely differs from that of the corresponding non-relativistic wave functions*

The PWE is a primary example of evolution equation, involving a pure differential operator. Many physical processes are well modelled by evolution equations of the same type as heat conduction and non-relativistic quantum particle dynamics. However, many physical processes are equally well modelled by evolution equations involving fractional or pseudo-differential operators. In this connection, work has been devoted to the study of the "(1+1)D relativistic-like heat equation" [2.33]

$$\partial_t \phi(x, t) = -\sqrt{1 - \alpha \partial_x^2}\, \phi(x, t) \tag{3}$$

and the spinless (1+1)D free-particle Salpeter equation, i.e. the relativistic Schrödinger equation [13],

$$i\hbar \partial_t \varphi(x, t) = \sqrt{m^2 c^4 - c^2 \hbar^2 \partial_x^2}\, \varphi(x, t) \tag{4}$$

Here, α plays the role as the thermal diffusivity, whereas m denotes the particle rest mass, c the speed of light in the vacuum, and $\hbar$ the reduced Planck constant. The square root operator, entering Eqs. (3) and (4), is a pseudo-differential operator, which then confers both equations a non-local character.

The Salpeter equation (4) has been the object of a thesis work, carried out under my supervision during an internship at ENEA recently concluded [2.34]. Although Eq. (4) is a simple relativistic version of the Schrödinger equation, it has been the subject of a few analyses unlike the other wave equations of relativistic quantum mechanics, i.e. Klein-Gordon and Dirac equations. This is because of the mathematical complexity one faces due to the aforementioned nonlocal nature of the equation. The recent literature is eventually revealing a thoughtful interest in the Salpeter equation, due to both the recognized advantages it offers with respect to the Klein-Gordon and Dirac equations and to the fact that it stems from the Bethe-Salpeter equation by suitable simplifications and approximations.

In the thesis, several aspects of the matter have been examined: from the analysis of the behaviour of the solutions of the equation (Figure 2.21), both numerically evaluated and asymptotically approximated, to the detailed comparison with the behaviour of the corresponding solutions of the Schrödinger equation in order to both highlight the differences and to possibly understood how the latter "flow" in the former.

Finally, the subject and the character of the activity carried out as a part of the collaboration with other ENEA research teams [2.35, 2.36, 2.37] is described elsewhere in the present Report.

2.5   Fermi FEL Facility at The Elettra-Sincrotrone Trieste Laboratory

Elettra-Sincrotrone Trieste, a multidisciplinary international laboratory of excellence, specialized in generating high quality synchrotron and free-electron laser light and applying it in materials science. The main assets of this research centre are two advanced light sources, the electron storage ring ELETTRA and the free-electron laser (FEL) FERMI, continuously operated (h24) supplying light of the selected frequency and "quality" to more than 30 experimental stations.

FERMI is a unique light source in the world, a seeded FEL, producing photons from the VUV to the soft X-rays with a high degree of coherence and spectral stability [2.38, 2.39]. ENEA has a long term expertise in FEL physics [2.40] and partecipated to the construction and operation of SPARC [2.41] and of other long wavelength FEL sources [2.42]. ENEA is providing support to the FERMI free electron lasers (FELs) machine physics activity.

The development of FEL-1 is in progress since the first lasing in 2010 [2.38]. The FEL was open to external users in December 2012 and it covers the photon energy range between 12 eV and 62 eV with high degree of longitudinal and transverse coherence, tunability, spectral stability with pulses close to the Fourier limit [2.43, 2.44]. The availability of an synchronized Ti:Sa laser with very low time jitter [2.45] and the polarization control [2.46, 2.47], are among the distinguishing features that make this FEL extremely attractive to the scientific community. FEL-1 is a high gain harmonic generation FEL, [2.48, 2.49, 2.50, 2.51, 2.38] where the coherence properties of a (relatively) long-wavelength laser seed (typically 230-260 nm) are transferred to a much shorter-wavelength FEL output pulse. The upshift process begins with the seed interacting with the electron beam in a short undulator (normally called the "modulator") to induce a temporally periodic energy modulation on the beam. The electrons then immediately pass through a chromatic dispersion section that converts this energy modulation into a current density modulation, whose fundamental wavelength is that of the input seed laser but which also has significant harmonic content at shorter wavelengths. The electron beam then enters a longer undulator named "final radiator" tuned such that the resonant wavelength is identical to that of a specific higher harmonic of the seed laser. The light at this upshifted frequency is then amplified and provided to the experimental stations. Special user modes have been developed at FERMI to offer to the scientific community non-

standard operation of the FEL, either at wavelengths below the nominal spectral range[1] (below 20 nm) or new pump-probe schemes with two FEL pulses produced by the same electron beam [2.52, 2.53, 2.54]. These schemes are possible because of the flexible layout of FEL-1 allowing the generation of pairs of FEL pulses with very high degree of coherence. However, special user modes require careful optimization of all systems involved in the FEL process and close collaboration between scientists and machine experts, in order to define the best strategy to achieve the experiment goals. An example is an experiment of coherent control, where the phase correlation of two FEL pulses of two different colours was demonstrated. Light of wavelengths 63.0 and 31.5 nm ionized neon, and by manipulating this phase the asymmetry of the photoelectron angular distribution we controlled with a temporal resolution of only 3 as [2.55].

The EUV to soft X-rays photon energy range at FERMI is covered by the FEL-2 line (62 eV to 310 eV). In order to efficiently seed the electron beam at low wavelengths, FEL-2 is indeed based on a double stage cascaded HGHG scheme (see Fig. 1). An external laser seeds the 1st stage that consists of a modulator (M1) and a two sections radiator (R1); the photon pulse generated in the 1st stage seeds the 2nd stage, made by a second modulator (M2) and a six sections radiator (R2). The magnetic chicane after the 1st stage (DL) delays the electron beam with respect to the photon pulse, to shift the seed generated in the 1st stage onto fresh electrons (see ref. xx for additional details). In other words, FEL-2 is a soft-xray FEL seeded by a VUV FEL, with a similar structure of the one of FEL-1. First lasing of FEL-2 was successfully
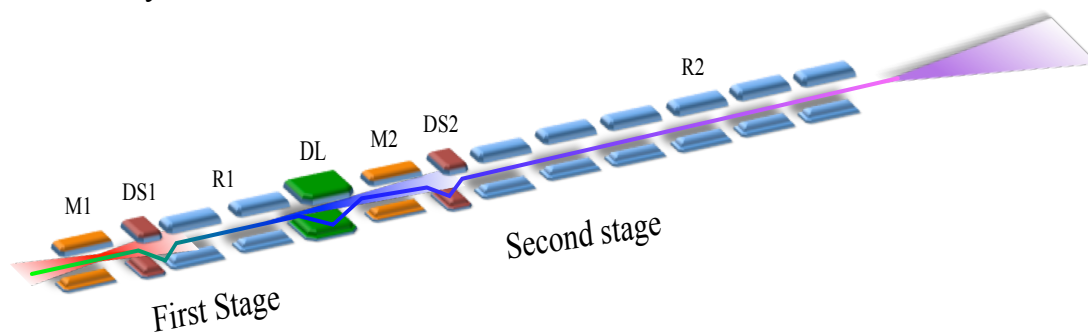

Figure 2.22 - Layout of FERMI FEL-2. Legenda: Modulator of first stage (M1), First dispersive section (DS1), first radiator (R1), delay line (DL), second modulator (M2) second dispersive section (DS2), second and final radiator (R2

demonstrated in October 2012 at 14.4 nm [2.39]. The performances of FEL-2 were extended to progressively lower wavelengths and optimized during further commissioning periods. FEL-2 reached in September 2014 the expected energy per pulse of about 10 μJ at 4 nm [2.56].

The operation of an FEL based on this double stage scheme is more critical than the one of sa ingle stage scheme as FEL-1, and during 2015 a number of critical upgrades aimed at improving the FEL-2 robustness, reliability and flexibility have been identified and the actions to complete these upgrades have been started. The upgrades include an increase of the linac energy, which increases the gain at the shortest wavelengths, the installation of an additional undulator in the first stage (R1 in *Figure 2.22*) which reduces the demands in terms of seed power, and an improved seed system. This includes the addition of a second regenerative amplifier, sharing the same femtosecond oscillator with the existing amplifier, will improve the quality of the laser pulse for seeding FEL-2, leading to an improvement of

---

[1] Special optimization of the electron beam and the FEL parameters allowed generating coherent radiation from FEL-1 at 12 nm, well below the nominal spectral range, to perform user experiments.

the FEL quality and flexibility. The new regenerative amplifier main features are a shorter pulse duration in fixed wavelength (800 nm) mode, i.e. less than 50 fs FWHM, and a central wavelength tunability within ±2%. The wavelength tunability allows a modest tuning of the FEL resonant wavelength without the use of an OPA amplifier, and the shorter pulses allow to use more efficiently the longidudinal distribution of the electron pulse.

2.6 *Free Electron Laser at SPARC- 2015*

2.6.1. Introduction
The Free Electron Laser (FEL) activity at SPARC is operating since about 15 years and is a long term collaboration merging competences which have grown both at ENEA and INFN in the field of accelerator Physics and FEL research and development.

FEL devices are, for many of their aspects, very well established devices, currently exploited in applications. They cover a wide range of frequency interval and can be operated in either Self Amplified Spontaneous Emission (SASE) or oscillator configurations.

The SPARC facility [2.57] has been conceived as a benchmark for testing new aspects of the FEL physics as well as new operating configurations. It is located at the Frascati National Laboratories and originates from a challenging R&D program on FEL physics driven by ultra-brilliant electron beams generated by a photo injector, developed within ENEA and INFN collaboration.

The facility consists of a 150 MeV high brightness electron beam injector [2.58], operating in different configurations including also the velocity bunching configuration [2.59] and a 12 meters long undulator sequence.

The device has provided, during the last years, important contributions to the understanding of the Physics of Free Electron Lasers and has paved the way to innovative scheme of operation.

The most notable achievements have been the proof of non-linear harmonic generation, the harmonic cascade, the seeding, the two colors experiment and the use of a segmented undulator, which has allowed the possibility of simultaneous lasing at two different harmonics.

Observations of FEL radiation in the SASE [2.60], Seeded [2.61] and High Harmonics Generation (HHG) [2.62] modes have been performed from 800 nm down to 40 nm wavelength

During the year 2015 the SPARC FEL activity was mainly devoted to confirm and analyze the results obtained in two colors FEL and in the segmented undulator configurations and in a preparatory phase for using electron bunches generated with Plasma Wake Field Acceleration (PWFA) technique.

From 2015 ENEA has been involved in a Horizon 2020 European project entitled "Design Study on the "European Plasma Research Accelerator with eXcellence In Applications" (EuPRAXIA)

This project will produce a conceptual design report for the worldwide first 5 GeV plasma-based accelerator with industrial beam quality and user areas. The project is aimed at the development of accelerator technology, laser systems and feedbacks for improving the quality of plasma-accelerated beams. Two user areas will be developed for a novel Free Electron Laser and High Energy Physics detector science.

Regarding the FEL the project aims at the design of "ultra-compact" FEL devices allowing a significant reduction of both accelerator and undulator dimensions.

The experimental activity at SPARC LAB has produced a large number of publications in high impact factor international journals and many presentations, part as invited talks, at international conferences.

In particular, in 2015, there have been two publications and a third is being published; there were two presentations to international conferences and an invited talk to a workshop. A detailed list of publications is given below.

2.6.2. Two colors FEL

One of the most significant achievements of 2015 has been the simultaneous operation of the laser on two different colors. Two FEL laser signals were indeed observed in both SASE [2.63] and seeded [2.64] configurations.
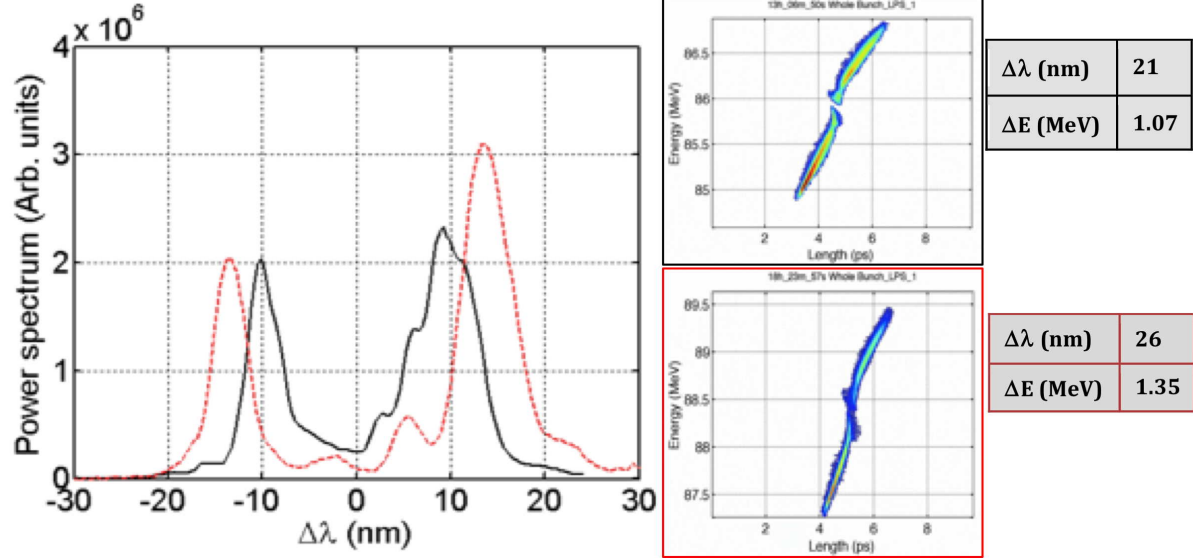

Figure 2.23 - Fine tuning of the spectral distance of the two pulses by varying the energy difference of the two electron bunches

Since the SPARC LINAC operates with a photocathode injector, the use of a multi-peaked laser pulse allows the generation of a multibunch electron beam in a single accelerating phase. A double-peaked electron energy spectrum is obtained by the laser comb technique in the velocity bunching. The electron beam, constituted by two short and balanced bunches, is extracted from the linac accelerating section near the maximum compression.

Arrival time and energy of the two bunches may be controlled by properly tuning the temporal separation at the gun, the phases of the RF-injector and the phases of the accelerations sections (*Figure 2.23*). At maximum compression the two beamlets are temporally superimposed in the longitudinal phase space but split in energy.

The method allows a relatively large tuning range of the time and frequency properties of the FEL emission, suitable for a wide range of applications.

In particular, pump and probe experiments that require an adjustable time delay between the two-color pump and probe pulses. The seeded two colors FEL experiment has been done using a single seed pulse.

Figure 2.24 - Electron phase space composed of two beamlets (a) and (b) compared to the laser chirped distribution (c)

The seed-laser system consists of a Ti:sapphire regenerative amplifier, driven by the same oscillator as the photocathode laser and it has been set to deliver up to 450 μJ at $\lambda_0 = 800$nm.

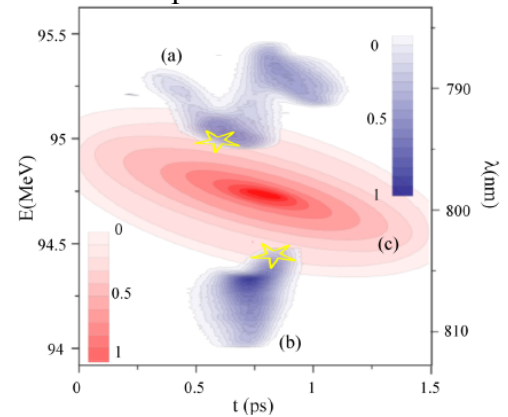The seed is stretched to overlap the bimodal structure of the electrons. A small linear chirp has been introduced to lengthen the seed pulse, ensuring superposition with both the electron bunches and increasing the tolerance for the synchronization with the beam. *Figure 2.24* sketches the superposition of the laser and electron phase spaces and it is evident the role of the laser chirping, allowing an extended temporal and spectral crossing. In *Figure 2.25* a comparison between SASE e seeded operations.
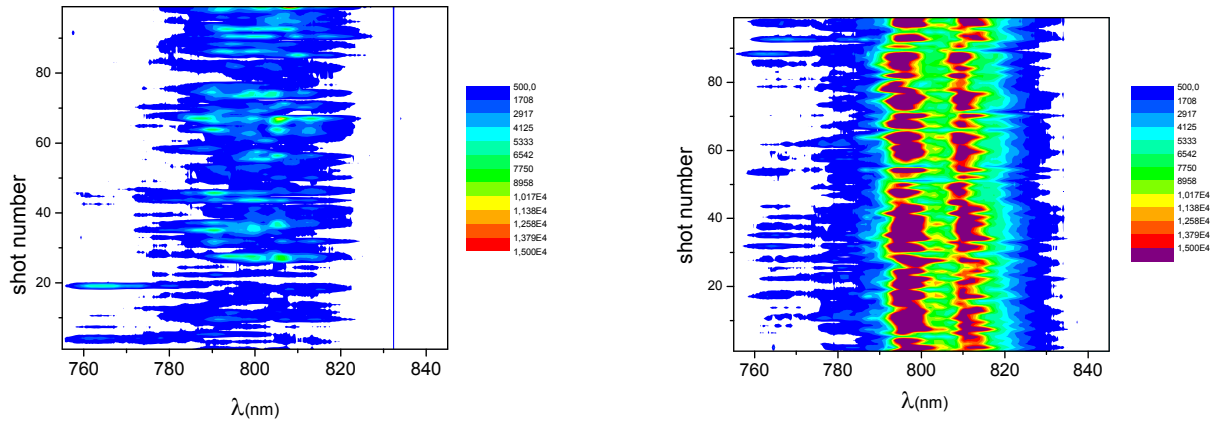

Figure 2.25 - Evidence of radiation stability in seeding configuration. On the left 100 SASE spectrometer measurements, on the right the same amount in seeding regime

This new method produces high quality light signals that could be used in pump & probe experiments. The results have been presented at the Advances in X-ray Free-Electron Lasers Instrumentation III Conference [2.65] and, as invited talk, at the workshop: "Multicolor FEL pulses and coherent control on the attosecond time scale opening new science perspectives" [2.66]. A thorough analysis of the experiment has been published in [2.67] and has been accepted for publication in Phys. Rev. Accel. And Beams [2.68].

2.6.3. Segmented undulator operation

A segmented undulator consists of two sections, arranged to have the second adjusted on a harmonic of the first. Lasing occurs in the second part, due to bunching acquired in the first.
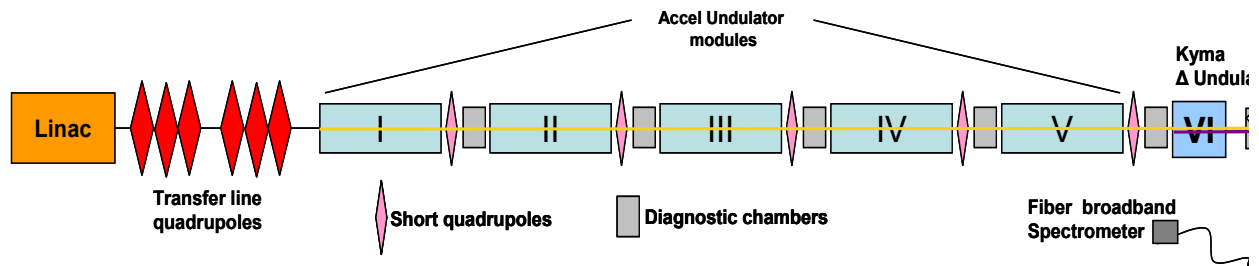

Figure 2.26 - SPARC FEL segmented undulator layout

The segmented SPARC line configuration is reported in *Figure 2.26*. Sections are provided of five undulator modules of the "old" chain, with 2.8 cm period, followed by a short period (1.4 cm) undulator, designed by ENEA SPARC group and realized by KYMA. The KYMA undulator has a quatrefoil structure, a high magnetic field homogeneity and focuses both in vertical and radial directions.

The image of *Figure 2.27* shows a real-time acquisition by the fiber spectrometer that has been used for the direct detection of the light spectral intensity.

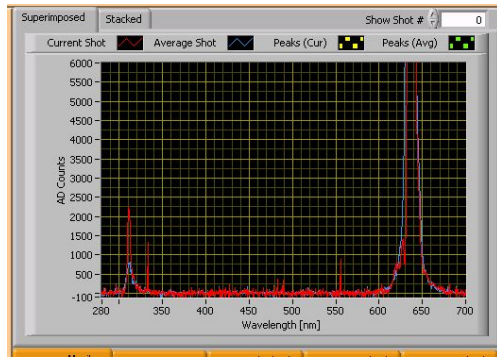The results has been presented at the Advances in X-ray Free-Electron Lasers Instrumentation III Conference [2.69].

Figure 2.27 - Spectrum from Accel undulator modules I-V (630nm) and from Kyma undulator (315nm)

2.6.4. Single spike FEL pulses generated with ultrashort electron beams

As preparatory phase of the LWFA/PWFA experiments for the European project EuPRAXIA, to be performed at SPARC_LAB, electron beams of charge as low as 20pC and rms lengths down to 20 fs have been produced and measured.

After the transport in the undulator, single spike red pulses were observed and detected in the SPARC single-pass FEL. Accurate spectral acquisitions of the radiation were cross checked with the direct measurements of the length of the electron beam, in order to control their mutual consistence. The undulator has been used in the double role of radiation source and supplementary diagnostics for the characterization of the electron beam. The experiment was performed in two shifts (referred to as (1) and (2)), with similar parameters. The procedure started with the photo-generation of a sub-ps electron beam, obtained by illuminating the cathode with a 200fs laser pulse at 266nm. A value of about 20pC of charge was measured with a beam current monitor. The extracted electrons were then propagated along the linac (three S-band cavities) and compressed by means of the velocity bunching. At the maximum compression, corresponding to about 20 fs.

The phase space of case (1) is presented in *Figure 2.28*.

Ultrashort electron bunches has been produced and measured their length. The single spike FEL emission has been studied, giving insight in the superradiant regime. Spectral measurements permit to retrieve the value of the electron length with an optimum agreement. From the diagnostic point of view, we tested the possibility to extend the evaluation of the length of ultrashort electron beams below the limit of rf deflector resolution.

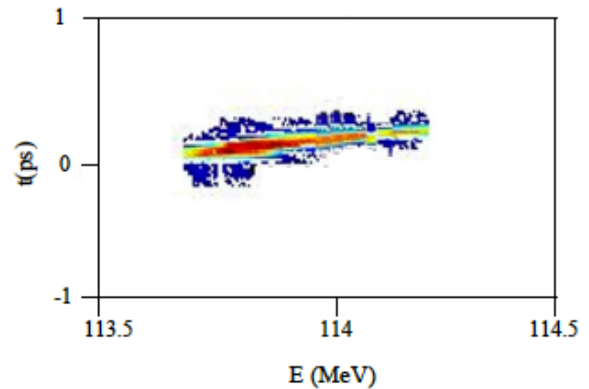The parameters of the electron beam in the two cases are shown in *Table 2.1*.

Figure 2.28 - Compressed trace space in the case of beam (1)

Table 2.2 - Parameters of the electron beams (1) and (2) at the exit of the linac

Electron beam parameters	Beam (1)	Beam (2)
Charge (pC)	20	22
Energy (MeV)	114	111
Projected energy spread (MeV)	< 0.087	< 0.077
Slice Energy Spread (M eV)	< 0.05	< 0.05
Emittance in x (mmmrad)	0.68	0.82
Emittance in y (mmmrad)	1.14	0.76

All data has been shown sharp single spike spectra in nearly 100% of cases, confirming that $\sigma_z < 37$ fs $\times$ c (see *Figure 2.29*).
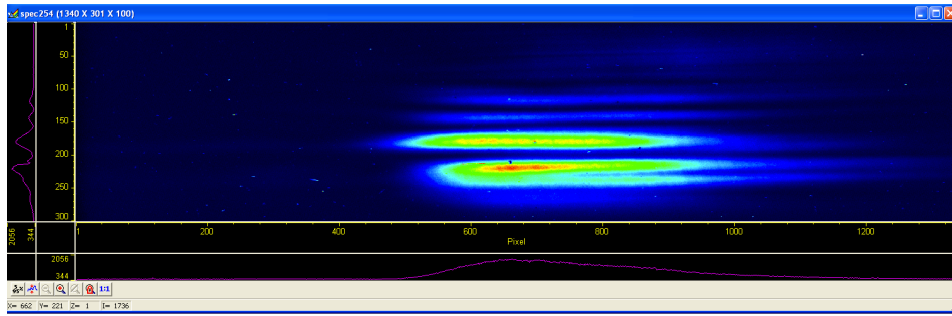
Figure 2.29 - Acquisition from in vacuum spectrometer

The clean shape of the spectral lines demonstrates also that the FEL emission pulses have been acquired at the end of the exponential amplification stage, before the onset of saturation *Figure 2.30*.
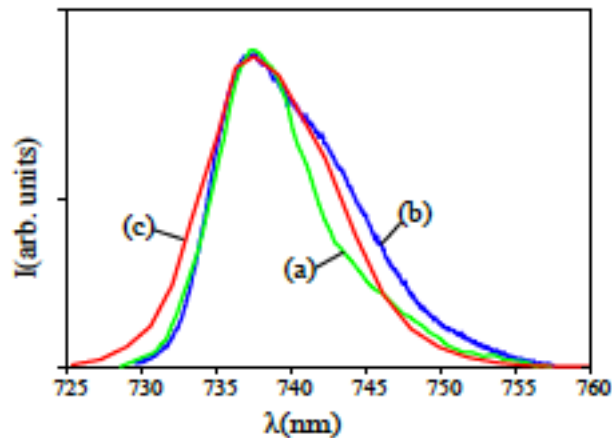

Figure 2.30 - Comparison between spectra for case (1). Green curve (a): fiber spectrometer. Blue curve (b): in vacuum spectrometer. Red curve (c): GENESIS 1.3 simulation

The results are going to be submitted to Physical Review Letters with the title: "Generation, measure and FEL radiation of ultra-short electron beams".

Other Publication 2015
F. Ciocci, G. Dattoli G and E. Sabia "***Transverse Gradient Undulators and FEL operating with large energy spread***" Optics Communications, vol. 356, p. 582-588, ISSN: 0030-4018, doi: 10.1016/j.optcom.2015.08.053 (2015)

References

[2.1] P. Zuppella, A. Reale, A. Ritucci, P. Tucceri, S. Prezioso, F. Flora, L. Mezi, and P. Dunne, "Spectral enhancement of a Xe-based EUV discharge plasma source", Plasma Sources Sci. Tech., **18,** 025014 (2009)

[2.2] L. Mezi, F. Flora, La sorgente DPP di radiazione nell'estremo ultravioletto a scarica elettrica in gas rarefatto, ENEA Technical Report RT/2012/15/ENEA,
http://opac.bologna.enea.it:8991/RT/2012/2012_15_ENEA.pdf

[2.3] S. Bollanti, P. Di Lazzaro, F. Flora, L. Mezi, D. Murra, and A. Torre: "Space- and time-resolved diagnostics of the ENEA EUV discharge-produced-plasma source used for metrology and other applications", High Power Laser Science and Engineering, 3, e29 (2015) doi:10.1017/hpl.2015.30

[2.4] L. Mezi, S. Bollanti, F. Flora, and A. Torre: "ENEA EUV Discharge Produced Plasma Source: Diagnostics, Characterization And Applications", POS (ECPD 2015) 125,
http://pos.sissa.it/archive/conferences/240/125/ECPD2015_125.pdf

[2.5] M. Fagnoni, E. Torti, S. Protti, D. Merli, L. Mezi, G. Della Giustina, G. Brusatin, S. B., F. Flora, A. Torre: "Aryl sulfonates and N,N-disulfonylimides as non ionic photoacid generators for the development of novel photoresists", XXV IUPAC Symposium on Photochemistry, Bordeaux, France, July 13th - 18th, 2014

[2.6] S. Bollanti, P. Di Lazzaro. F. Flora, L. Mezi, D. Murra, A. Torre: "Laser–plasma–source debris-related investigations: an aspect of the ENEA micro-exposure tool", Appl Phys B, 96, 479–490 (2009), DOI 10.1007/s00340-009-3583-z

[2.7] F. Flora, S. Bollanti, D. De Meis, P. Di Lazzaro, A. Fastelli, G. P. Gallerano, L. Mezi, D. Murra, A. Torre, D. Vicca, "High precision electronic solar compass", PCT patent N. WO 2014102841 A1 (3 July 2014)

[2.8] S. Bollanti, D. De Meis, P. Di Lazzaro, A. Fastelli, F. Flora, G.P. Gallerano, L. Mezi, D. Murra, A. Torre, D. Vicca, "Calcolo analitico della posizione del sole per l'allineamento di impianti solari ed altre applicazioni" ENEA Technical Report RT/2012/24/ENEA (2012)

[2.9] S. Bollanti, D. De Meis, P. Di Lazzaro, F. Flora, G.P. Gallerano, L. Mezi, D. Murra, A.Torre, D. Vicca, "Electro-optical sun compass with a very high degree of accuracy"
Opt. Lett. Vol. 40, No. 15, pag. 3619 (August 2015).

[2.10] Aron, Jacob, "Backwards sundial makes useful compass"
New Scientist, 8/8/2015, Vol. 227 Issue 3033, p13
(article appeared on the magazine New Scientist about the ENEA compass, with an interview with Daniele Murra)

[2.11] RAI, program Geo & Geo, 19/10/2015
Interview with Francesco Flora showing the ENEA solar compass.
http://www.enea.it/it/Stampa/eneainonda/19-10-2015-rai-3-aspettando-geo-16-00-durata-00-07.07

[2.12] S. Bollanti, D. De Meis, P. Di Lazzaro, F. Flora, G.P. Gallerano, L. Mezi, D. Murra, A.Torre, D. Vicca, "Test dell'accuratezza della bussola solare Enea in occasione dell'eclissi solare del 20 marzo 2015", ENEA Technical Report RT/2015/24/ENEA (2015).

[2.13] G.P. Gallerano, A. Doria, M. Germini, E. Giovenale, G. Messina, I.P. Spassovsky, J Infrared Milli Terahz Waves (2009) 30:1351–1361

[2.14] [2.3. G.P. Gallerano, A. Doria, E. Giovenale, G. Messina, A. Petralia, I. Spassovsky, K. Fukunaga, I. Hosako, Proc. of the "33rd Int. Conference on Infrared, Millimeter and THz Waves" IRMMW-THz2008, T2G2.1628 (2008)

[2.15] A.Doria, E.Giovenale, G.P.Gallerano, M.Picollo, K.Fukunaga, "A millimeter wave/terahertz 3D scanner for wall painting investigation", Proc. 39th Int. Conf. Infrared, Millimeter, and THz Waves, Tucson, AZ, September 14-19, 2014 - DOI: 10.1109/IRMMW-THz.2014.6956095 (2014)

[2.16] A. Doria, E. Giovenale, G. P. Gallerano, A. Petralia, M. Picollo, K. Fukunaga, "A mm-wave/THz scanner for the THz-ARTE Project", TECHNART 2015 - Catania, April 27 - 30, 2015

[2.17] EU project THz-BRIDGE Tera-Hertz radiation in Biological Research, Investigations on Diagnostics and study on potential Genotoxic Effects, http://www.frascati.enea.it/THz-BRIDGE 2004

[2.18] G.P. Gallerano, A. Doria, E. Giovenale, I. Spassovsky, "High power THz sources and applications at ENEA-Frascati", Journal of Infrared, Millimeter, and Terahertz Waves 35, 17–24 (2014)

[2.19] G.P. Gallerano, A. Doria, E. Giovenale, "The physics of and prospects for THz-Compact FELs", Terahertz Science and Technology, ISSN 1941-7411 7, 160-171 (2014)

[2.20] A. De Amicis, S. De Sanctis, S Di Cristofaro, V. Franchini, F. Lista, E. Regalbuto, E. Giovenale, G.P. Gallerano, P. Nenzi, R. Bei, M. Fantini, M. Benvenuto, L. Masuelli, E. Coluzzi, C. Cicia, A. Sgura, "Biological effects of in vitro THz radiation exposure in human foetal fibroblasts", Mutation Research/Genetic Toxicology and Environmental Mutagenesis, Special Issue - ISCA11 (2014), June 9, 2015; doi:10.1016/j.mrgentox.2015.06.003

[2.21] M. Fenech, The in vitro micronucleus technique, Mutat. Res. 455 (2000) 81-95

*[2.22] M.A. Leontovich and V.A. Fock, Solution of the problem of propagation of electromagnetic waves along the earth's surface by the method of parabolic equations, Sov. J. Phys. **10**, 13-20 (1946)*

*[2.23] E.P. Wigner, On the quantum correction for thermodynamic equilibrium. Phys. Rev. **40**, 749–759 (1932)*

[2.24] A. Torre, Paraxial wave equation: Lie-algebra based approach, in Mathematical: Classical, Quantum, and Computational Methods, eds. V. Lakshminarayanan, M. Calvo and T. Alieva (CRC Press, New York, 2013), Chapter 10, pp. 341-417

[2.25] A. Torre, Linear Ray and Wave Optics in Phase Space (Elsevier, Amsterdam, 2005)

*[2.26] M.V. Berry and N.L. Balazs, Non spreading wave packets, Am. J. Phys. **47**, 264-267 (1979)*

*[2.27] G.A. Siviloglou and D.N. Christodoulides, Accelerating finite energy Airy beams, Opt. Lett. **32**, 979--981 (2007); G.A. Siviloglou, J. Broky, A. Dogariu and D.N. Christodoulides, Observation of accelerating Airy beams, Phys. Rev. Lett. **99**, 213901 (2007)*

[2.28] Y. Hu, G. Siviloglou, P. Zhang, N. Efremidis, D. Christodoulides, and Z. Chen, Self-accelerating Airy beams: generation, control, and applications, in Nonlinear Photonics and Novel Optical Phenomena, Z. Chen and R. Morandotti, eds. (Springer, 2012), vol. 170, pp. 1-46

*[2.29] A. Torre, Propagating Airy wavelet-related patterns, J. Opt. **17**, 075604 (2015)*

[2.30] A. Torre, Wigner distribution function of a Lorentz–Gauss vortex beam: alternative approach, Appl. Phys. B 122, 55 (2016)

*[2.31] O. El Gawhary, S. Severini, Lorentz beams and symmetry properties in paraxial optics. J. Opt. A Pure Appl. Opt. **8**, 409–414 (2006)*

[2.32] J.P. Torres, L. Torner, Twisted Photons. Applications of Light with Orbital Angular Momentum (WILEY-VCH Verlag & Co.KGaA, Weinheim, 2011)

*[2.33] G. Dattoli and A. Torre, Root operators and "evolution" equations, Mathematics **3**, 690-726 (2015);* http://www.mdpi.com/2227-7390/3/3/690

[2.34] A. Lattanzi, Solutions to the Salpeter equation, Thesis, University Roma Tre, 22/3/2016

*[2.35] V. Violante, E. Castagna, S. Lecci, F. Sarto, M. Sansovini, A. Torre, A. La Gatta, R. Duncan, G. Hubler, A. El Boher, O. Aziz, D. Pease, D. Knies and M. McKubre, Review of materials science for studying the Fleischmann and Pons effect, Current Science **108**, 46-64 (2015)*

*[2.36] S. Bollanti, D. De Meis, P. Di Lazzaro, F. Flora, G.P. Gallerano, L. Mezi, D. Murra, A. Torre and D. Vicca, Electro-optical sun compass with a very high degree of accuracy, Opt. Lett. **40**, 3619-3622 (2015)*

*[2.37] S. Bollanti, P. Di Lazzaro, F. Flora, L. Mezi, D. Murra and A. Torre, Space- and time-resolved diagnostics of the ENEA EUV discharge-produced-plasma source used for metrology and other applications, High Power Laser Science and Engineering **3**, (2015) e29*

[2.38] E. Allaria et al., "Highly coherent and stable pulses from the FERMI seeded free-electron laser in the extreme ultraviolet", Nature Photonics 6, 699-704 (2012)

[2.39] E. Allaria et al., "Two-stage seeded soft-X-ray free-electron laser", Nature Photonics 7, 913-918 (2013)

[2.40] G. Dattoli, A. Renieri, A. Torre, Lectures on the Free Electron Laser Theory and Related Topics, World Scientific, (1993)

[2.41] L. Giannessi et al., Phys. Rev. ST Accel. Beams 14, 060712 (2011).

[2.42] G. P. Gallerano, A. Doria, E. Giovenale, I. Spassovsky, Journal of Infrared, Millimeter, and Terahertz Waves, 35, 17-24 (2014)

[2.43] E. Allaria et al., New J. Phys. 14, 113009 (2012)

[2.44] G. De Ninno et al., Single-shot spectro-temporal characterization of xuv pulses from a seeded free-electron laser. Nat Commun, 6, 08 2015

[2.45] M. Danailov et al., Optics Express 22, 12869, (2014)

[2.46] E. Allaria et al., Phys. Rev. X 4, 15 (2014)

[2.47] E. Ferrari et al., Scientific Reports 5, 13531 (2015)

[2.48] I. Boscolo and V. Stagno, The converter and the transverse optical klystron. Nuovo Cimento B 58(2), 267–285 (1980)

[2.49] R. Barbini et al., 80 nm FEL design in an oscillator amplifier configuration, in Proceedings of the Prospects for a 1 A Free Electron Laser, Sag Harbor, New York, ed. by J.C. Gallardo, 22–27 Apr 1990 (BNL 52273)

[2.50] R. Bonifacio et al., Generation of XUV light by resonant frequency tripling in a two-wiggler FEL amplifier, in Proceedings of the Eleventh International Free Electron Laser Conference, Naples, Aug 1989, pp. 787–790

*[2.51] L.H. Yu, Generation of intense uv radiation by subharmonically seeded single-pass free-electron lasers. Phys. Rev. A **44**, 5178 (1991*

[2.52] E. Allaria et al., "Two-colour pump-probe experiments with a twin-pulse-seed extreme ultraviolet free-electron laser", Nature Commun. 4, 2476 (2013)

[2.53] G. De Ninno et al., "Chirped seeded free-electron lasers: Self-standing light sources for two-color pump-probe experiments", Phys. Rev. Lett. 110, 064801 (2013)

[2.54] B. Mahieu et al., "Two-colour generation in a chirped seeded free-electron laser: A close look", Optics Express 21, 22728 – 22741 (2013)

[2.55] K. Prince et al., Nat Photon, 10, 176–179 (2016)

[2.56] E. Allaria et al. The FERMI free-electron lasers. J. Synchrotron Radiation 22, 485–491 (2015)

[2.57] M. Ferrario et al., "SPARC_LAB present and future," Nuclear Instruments and Methods in Physics Research B 309, 183–188 (2013)

[2.58] M. Ferrario et al., "Direct Measurement of the Double Emittance Minimum in the Beam Dynamics of the Sparc High-Brightness Photoinjector," Phys. Rev. Lett. 99, 234801 (2007)

[2.59] M. Ferrario et al., "Experimental Demonstration of Emittance Compensation with Velocity Bunching," Phys. Rev. Lett. 104, 054801 (2010)

[2.60] L. Giannessi et al., "Self-amplified spontaneous emission for a single pass free-electron laser," Physical Review Special Topics. Accelerators And Beams 14 (6), 0607121-8 (2011)

[2.61] L. Giannessi et al., "FEL Experiments at Sparc: Seeding with Harmonics Generated in Gas," Proceedings of the 32th International Free Electron Laser Conference, 294-297 (2010)

[2.62] M. Labatet al., "High-Gain Harmonic-Generation Free-Electron Laser Seeded by Harmonics Generated in Gas," Physical Review Letters 107 (22), 224801-5 (2011)

[2.63] F. Ciocci et al., "Two Color Free-Electron Laser and Frequency Beating" PHYSICAL REVIEW LETTERS, vol. 111; p. 264801-1-264801-5, ISSN: 0031-9007, doi: 10.1103/PhysRevLett.111.264801, (2013)

[2.64] A. Petralia et al., "Two-Color Radiation Generated in a Seeded Free-Electron Laser with Two Electron Beams" PHYSICAL REVIEW LETTERS, vol. 115, p. 014801-1-014801-5, ISSN: 0031-9007, doi: 10.1103/PhysRevLett.115.014801, (2015)

[2.65] F. Villa et al., "Seeded FEL with two energy level electron beam distribution at SPARC_LAB" In: Advances in X-ray Free-Electron Lasers Instrumentation III. PROCEEDINGS OF SPIE, THE INTERNATIONAL SOCIETY FOR OPTICAL ENGINEERING, vol. 9512, p. 95120T-1-95120T-7, Bellingham, WA:SPIE, ISSN: 0277-786X, Prague, Czech Republic , 13–16 April 2015, doi: 10.1117/12.2182160, (2015)

[2.66] F. Ciocci: Two-color FEL at the SPARC test facility. ICTP, Trieste, Italy/ 10-11 Dicember 2015

[2.67] A. Petralia et al., "Two-Color Radiation Generated in a Seeded Free-Electron Laser with Two Electron Beams" Physical Review Letters, vol. 115, p. 014801-1-014801-5, ISSN: 0031-9007, doi: 10.1103/PhysRevLett.115.014801, (2015)

[2.68] M. Carpanese et al., "Seeded free electron laser operating with two colors: Experimental results" Phys. Rev. Accel. And Beams [12] vol. 19 (accepted April 28, 2016)

[2.69] F. Ciocci et al. "Segmented undulator operation at the SPARC-FEL test facility", Proc. SPIE 9512, Advances in X-ray Free-Electron Lasers Instrumentation III, 951203 (May 12, 2015); Prague, Czech Republic , 13–16 April 2015, doi: 10.1117/12.2185099